Phase segregation in Fe-Cu(Ag) and diffusion enhancement in FePt-Cu gas-phase nanoparticles prepared by DC magnetron sputtering

Dissertation

zur Erlangung des akademischen Grades

Doktor der Naturwissenschaften

an der Fakultät für Physik

der Universität Duisburg-Essen

vorgelegt von

Anna Elsukova

Izhevsk, Russische Föderation

Duisburg, July 2014

To my father Evgeny P. Elsukov

Abstract

In this work, properties of binary and ternary gas-phase nanoparticles prepared by DC magnetron sputtering were studied. Formation of metastable alloy phases of immiscible binary systems and their transformation after thermal treatment were investigated in Fe-Cu and Fe-Ag nanoparticles. The stabilization of chemically ordered $L1_0$ phase and suppression of twinned structure formation was investigated in Fe-Pt-Cu particles.

In Fe-Cu nanoparticles - $Fe_{75}Cu_{25}$, $Fe_{60}Cu_{40}$ and $Fe_{25}Cu_{75}$ - formation of metastable Fe-Cu alloys was observed. After thermal treatment iron and copper in $Fe_{60}Cu_{40}$ and $Fe_{75}Cu_{25}$ particles segregated via spinodal decomposition into Fe_{rich} and Cu_{rich} regions. In $Fe_{25}Cu_{75}$ particles phase segregation occurs via nucleation and growth. The thermal stability of Fe-Cu nanoalloys decreases with increasing Cu concentration.

The asymmetrical fully segregated Janus -dumbbell and "raspberry" Fe-Ag particles annealed at 1273 K were produced at 0.5 mbar pressure at different gas flow rates. The particles are unstable over time under atmospheric conditions, and their ageing leads the full or partial encapsulation of silver by iron oxide.

Primary and annealed at 1273 K FePt-Cu nanoparticles with average concentrations of Cu = 5, 7, 11 and 24 at.% were prepared at 0.5 mbar pressure. Adding of 24 at.% Cu led to drastic changes in structure and morphology in both annealed and primary FePt-Cu particles in comparison to FePt nanoparticles prepared under the same conditions. In the primary FePt-Cu sample three different particle morphologies are found: one third of them have single-crystal partially $L1_0$ ordered octahedra, the rest are single crystal fcc disordered cubooctahedra and multi-twinned fcc disordered icosahedra. After annealing at 1273 K approximately 95% particles become single-crystal and at least 40 % of them possess ordered $L1_0$ structure.

Zusammenfassung

In dieser Arbeit wurden die Eigenschaften binärer und ternärer Nanopartikel untersucht. Diese wurden durch DC-Magnetronsputtern aus der Gas-Phase präpariert. Die Bildung metastabiler Legierungsphasen unvermischbarer binärer Systeme und ihre Veränderung nach Hitzebehandlung wurden in Fe-Cu und Fe-Ag Nanopartikeln untersucht. Die Stabilisierung der chemisch geordneten $L1_0$ Phase und die Unterdrückung der Entstehung von Zwillingsstrukturen wurden in Fe-Pt-Cu untersucht.

In Fe-Cu Nanopartikeln, der Zusammensetzungen $Fe_{75}Cu_{25}$, $Fe_{60}Cu_{40}$ und $Fe_{25}Cu_{75}$, wurde die Bildung metastabiler Fe-Cu Legierungen beobachtet. Nach der Hitzebehandlung segregierten die $Fe_{60}Cu_{40}$ und $Fe_{75}Cu_{25}$ Partikel durch spinodale Entmischung in Fe- bzw. Cu-reiche Gebiete. In $Fe_{25}Cu_{75}$-Partikeln geschieht die Entmischung durch Nukleation und Wachstum. Mit steigendem Cu-Anteil verringert sich die thermische Stabilität von FeCu-Nanolegierungen.

Die Fe-Ag Partikel wurden bei 0.5 mbar mit verschiedenen Gasflussraten hergestellt. Nach annealen bei 1273 K zeigten sich diese als vollständig entmischte asymetrische Januspartikel (Dumbbell und Raspberry). Diese Partikel sind unter Normalbedingugen nicht stabil. Nach einer Zeitspane von mehreren Monaten sind diese zu vollständig oder teilweise von Eisenoxid umschlossenen Silberpartikeln gealtert.

Primäre, sowie bei 1273 K annealte FePt-Cu, Nanopartikel wurden mit durchschnittlichen Kupferkonzentrationen von 5, 7, 11, und 24 at.% bei 0.5 mbar hergestellt. Die Präparation mit 24 at.% führte zu massiven Änderungen der Struktur und Morphologie der Partikel. Unter den Primären FePt-Cu-Nanopartikeln fanden sich drei verschiedene Morphologieen: Ein Drittel der Partikel sind einkristalline, teilweise $L1_0$-geordnete Oktaeder, bei den übrigen Partikeln handelt es sich um einkristalline chemisch ungeordnete fcc-Kuboktaeder und mehrfachverzwillingte chemisch ungeordnete fcc Ikosaeder. Nach sintern bei 1273 K verbleiben etwa 95 % einkristalline Partikel, von denen wenigstens 40% eine geordnete $L1_0$ Struktur besitzen.

Abbreviations

bcc   body-centered cubic

DC   Direct Current

DSC   Differential Scanning Calorimetry

EDX   Energy Dispersive X-ray

EELS   Electron Energy Loss Spectroscopy

EFTEM   Energy-filtered Transmission Electron Microscopy

EXAFS   Extended X-Ray Absorption Fine Structure

FC   Field Cooling

fcc   face-centered cubic

fct   face-centered tetragonal

HAADF   High Angle Annular Dark Field

HRTEM   High-resolution Transmission Electron Microscopy

STEM   Scanning Transmission Electron Microscopy

SQUID   Superconducting Quantum Interference Device

ZFC   Zero-Field Cooling

Contents

Chapter 1

Introduction

1.1   Motivation and research objectives.

Synthesis of nanoparticles with controlled properties is an important branch of nanoscale science and engineering. Nanoparticles can be prepared by a variety of methods which can be classified into two main categories: wet-chemical (colloidal) and gas-phase. Both methods have advantages and disadvantages and their suitability depends on the aims of particular investigations.

Gas-phase nanoparticles are formed in a thermodynamically unstable vapor which favors the precipitation of the solid material. Under such conditions, that is supersaturation, particles nucleate homogeneously [1]. Their properties depend on a variety of parameters including supersaturation rate and time particles spend in the nucleation and growth zone. The formation of particles occurs rapidly (milliseconds to seconds) and in a relatively uncontrolled fashion compared to the formation of particles when colloidal methods are used. However, the gas-phase methods are advantageous in several respects. First, the absence of a liquid solution and surface ligands allows to synthesize high-purity composites. Second, thermal treatment of the particles can be included in the preparation process, so that the particles can be annealed in the vapor phase before deposition. This prevents any unwanted agglomeration. Third, in the case of alloy particles, due to the rapid heating-

cooling regime intrinsic to gas-phase preparation, metastable phases with unique properties can also be obtained.

The formation of monometallic particles in the gas phase has been widely studied [2]. However, preparing multi-phase nanoparticles with desired properties can be quite challenging due to the complex and not yet well-understood dependence of the particle's structure, morphology and phase formation behavior on preparation parameters.

This work is on the phase formation and structural properties of three nanoparticles systems Fe-Cu, Fe-Ag and Fe-Pt-Cu prepared by magnetron sputtering. The experimental setup incorporates in-flight annealing of the particles to avoid aggregation, which is usually the case when samples are annealed after deposition on a substrate. The first two systems, Fe-Cu and Fe-Ag, are immiscible in the equilibrium state [3] and phase segregation is expected to occur during in-flight annealing of gas-phase-prepared nanoparticles. Segregation is expected to lead to the formation of various morphologies and structures due to the inhomogeneous compositional distribution of the elements occurring during the annealing stage, including core-shell-like structures having new properties.

The FePt alloy in the $L1_0$ crystallographic phase is known to possess a large magnetic anisotropy energy density K = 7×10^6 J/m^3, large magnetic moment and high oxidation resistance [4], so $L1_0$ FePt nanoparticles are considered to be suitable material for high-density magnetic storage media technology. The main challenge here lies in the preparation of sufficiently small (6-10 nm) nanoparticles and at the same time stable $L1_0$ phase. Although $L1_0$ is a thermodynamically stable structure of bulk FePt at room temperature, this structure does not readily occur in nanoparticles prepared both by wet chemical and gas-phase methods. The transformation to the $L1_0$ phase requires the diffusion of the Fe and Pt atoms and depends on the availability of vacancies over which atoms can exchange positions and acquire their equilibrium positions. If the vacancies are insufficient, diffusion cannot take place, and the particles remain in the metastable disordered fcc state. Another complication arises from the fact that small FePt particles tend to possess a multi-twinned polycrystalline structure [5] and thus become unsuitable for magnetic recording. In order

to enhance the diffusion by lowering the fcc-L10 transition temperature to stabilize the $L1_0$ phase and to suppress the formation of twins, Cu is introduced to FePt. The structural and magnetic properties of such Fe-Pt-Cu nanoparticles were studied.

1.2 Preparation of gas-phase nanoparticles by DC magnetron sputtering.

1.2.1 Basics of DC magnetron sputtering.
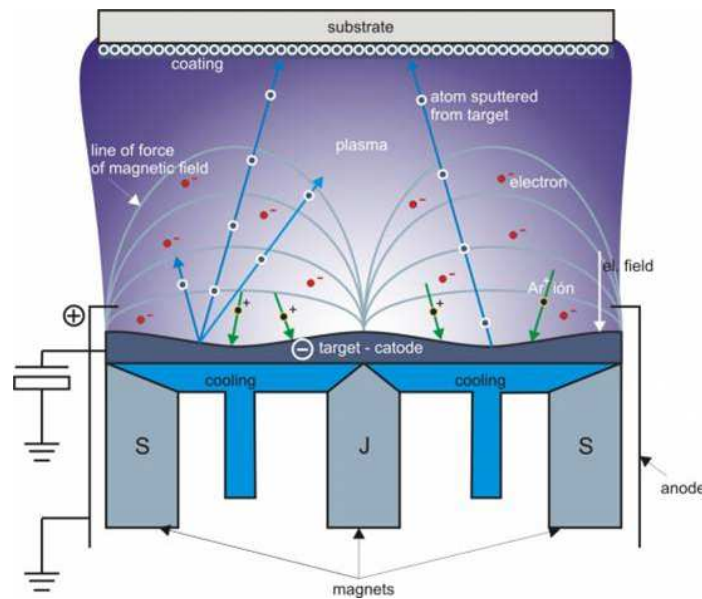
Figure 1.1: Schematic representation of a sputtering system. Source: http://www.polymedia.ch/OpArticles/view/57

Fig.1.1 shows a schematic representation of a sputtering system. The source of the sputtering material (sputtering target) is connected to a DC power supply and serves as a cathode. The target is positioned in a vacuum chamber which is grounded. The sputtering gas (usually, Ar) is introduced into the chamber. If the electric field is strong enough, it creates a glow discharge plasma near the surface of the target which consists of ionized

Ar atoms (Ar^+) and electrons. Ar^+ ions are accelerated towards the target and eventually collide with it, ejecting the target material atoms. The sputtering gas also serves as carrier gas. In magnetron sputtering systems magnets are placed behind the target to trap the electrons and increase the possibility of Ar to ionize, therefore increasing the sputtering yield.

1.2.2 Formation of nanoparticles in the gas-phase.

Nanoparticles produced by magnetron sputtering are formed by the gas-phase conden-sation process. The sputtered material forms a vapor, in which small nuclei begin to form after reaching supersaturation conditions. After the nucleation phase, the nuclei grow into bigger particles either by adding atoms to the surface (surface-growth) or several nuclei merge (coalescence). Several particles may stick together (coagulation) and form agglom-erates ([6], also see Fig.1.2). The nucleation-growth processes depend on vapor conditions, such as number of nuclei, vapor temperature, cooling rate, etc.

1.2.3 Factors influencing the properties of nanoparticles prepared by magnetron sputtering.

The formation and final state of the nanoparticles (structure, size and morphology) is determined by the thermal conditions during particle-formation [7]. The schematic rep-resentation of energy exchange in a magnetron sputtering system is shown in Fig.1.3 (a). Ar^+ ions gain kinetic energy are accelerated by a dc electric field towards the sputter target. Atoms are ejected out of the target with a kinetic energy transferred from the accelerated high-energy Ar^+ ions. When the gas reaches supersaturation, particles begin to form. The particles are then cooled by collisions with neutral Ar atoms. Thus, the Ar gas serves as an energy drain. During the process of particle formation, energy is transferred between low-energy Ar atoms, high-energy Ar^+ ions and nanoparticles.

Investigations given in reference [7] demonstrated that structure and morphology of
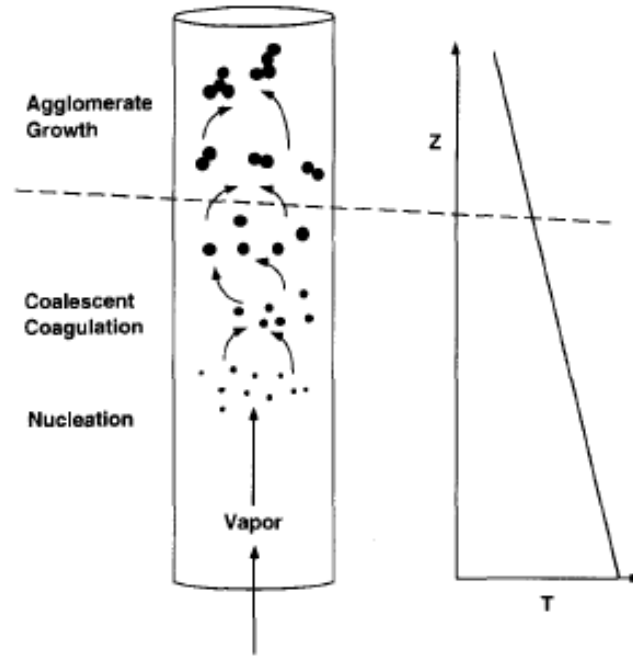
Figure 1.2: Schematic illustration of the processes that contribute to particle growth in gas-phase. Z: distance from the target, T: temperature. Taken from [6].

alloy nanoparticles (in this case FePt) strongly depend on their initial energy, cooling rate and whether particle-formation occurs via surface-growth or coalescence (see Fig.1.3 (b)). The thermal environment can be controlled by the sputtering parameters discussed below.

Sputtering gas and target atoms energies. The average ion energy E_i in a plasma is given by [8]:

$$E_i = 0.733 \times V_{DC} (eV), \tag{1.1}$$

where V_{DC} is the dc target voltage. For a typical voltage-value of 250 V the argon ions have an energy around 183 eV corresponding to a thermal energy of around 2.1×10^6 K. The energy of the sputtered atoms usually varies from 5 to 20 eV (9 eV for iron atom), which corresponds to thermal energies ranging from 5.8×10^4 K to 2.3×10^6 K. The higher the initial energy of Ar^+ ions and target atoms, the lower is the cooling rate. However, the final state of the particles will also depend on the nucleation and growth
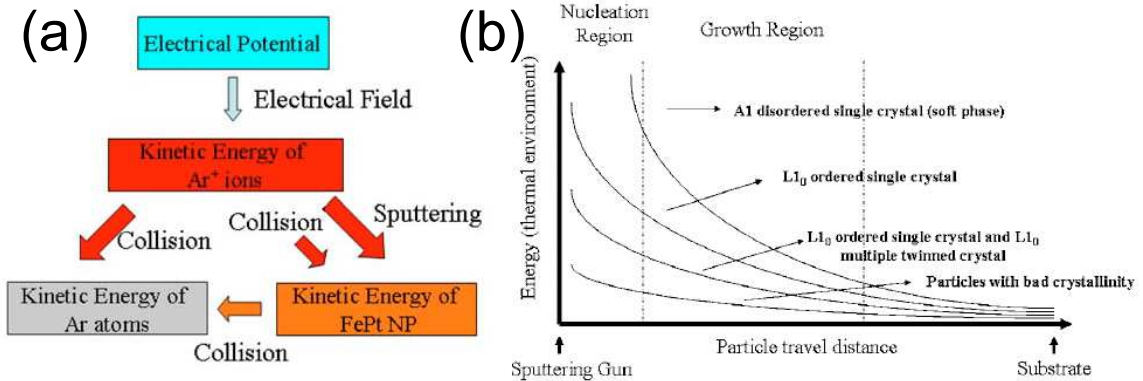
Figure 1.3: (a) Schematic representation of energy exchange in a dc magnetron sputtering system. (b) Thermal environment (energy) during the formation of gas-phase FePt nanoparticles and corresponding resulting structure of particles. The x axis represents the distance from the sputtering gun. Taken from [7].

processes. Particles formed only by surface-growth (before the coalescence starts) have a better size distribution and crystallinity. If the initial kinetic energy is too high, the cooling will proceed too slow and the coalescence phase will start. The thermal environment can be also controlled by adding He to the gas mixture. He lowers the initial ion energy and increases the cooling rate.

Sputter gas flow rate. The flow rate of the sputter gas determines the time for the nanoparticle nucleation and growth processes, also known as the aggregation time or residence time. Longer aggregation times lead to a larger average size of the particles and to a broader size distribution.

Sputter gas pressure. The sputter gas pressure determines the number of ejected target atoms and the collisions between the target atoms and Ar atoms. High gas pressures produce more nucleation sites and faster cooling rates. In general, the higher the gas pressure the broader is the size distribution and larger is the average particle size.

Magnetron plasma. Another important parameter is the density and shape of the magnetron plasma. A magnetic field is used to trap the secondary electrons to increase the probability of Ar to ionize. Thus, the plasma properties strongly correlate with the pro-

file of the magnetic field. The profile strongly depends on the target material; particulary its magnetic permeability. If a ferromagnetic target is used, most of the magnetic flux is trapped inside the target. Therefore, the target should be thin enough to have sufficient magnetic flux for effective sputtering near the target surface.

A high magnetic permeability of the target also leads to a non-uniform distribution of the magnetic flux and plasma density. The typical distribution of the magnetic flux (2D representation) is shown in Fig.1.1 (see also Fig.1.25(c)). The resulting plasma has a toroidal form (see Fig.1.25(a)). The non-uniformity of the plasma density leads to a non-uniform thermal environment during particle-formation, and therefore, to a non-uniform distribution of the particle-properties. Also, prolonged sputtering leads to the formation of a non-uniform erosion profile of the target (Fig.1.1) which means that the magnetic flux distribution (as it depends on target thickness) will also change with time.

In summary. The properties of the particles prepared by magnetron sputtering are very sensitive to sputtering parameters. In general, to achieve a smaller average size and a narrow size distribution, a high gas-flow and a low sputtering gas-pressure should be used. However, the final morphology and crystal structure of the particles strongly depend on the thermal environment and the cooling rate, which have to be adjusted depending on the sputter material. The thermal environment and cooling rates are closely connected to the plasma shape.

1.3   Basics of alloy formation and phase segregation.

1.3.1   Solid solubility of metals. Phase diagrams.

When two or more kinds of metal atoms share sites randomly in a crystal lattice, they form a *solid solution (alloy)*. Whether or not a metal can form an alloy (assuming the system has reached thermodynamic equilibrium) depends on material parameters, relative concentrations and temperature. A graphical representation of the phases of a multicom-

ponent system is called a *phase diagram*. Usually, a temperature-composition (T-x) type of a diagram is used. T-x diagrams of binary Fe-Cu, Fe-Ag and Fe-Pt system are shown in Fig.1.12, Fig.1.18 and Fig.1.20, respectively. Fig.1.27 demonstrates the section of the ternary Fe-Pt-Cu phase diagram at 1000° C. Already, these few diagrams show that solid solubility and its range in temperature and composition vary greatly from system to system. For example, Fe and Pt form an alloy in a large concentration range, while Fe and Ag are almost completely immiscible.

If elements are soluble for all concentrations, they form a *continuous series of solid solutions*. Phases with concentrations close to pure elements are called *primary phases* and usually have the same structure as the dominating element. Others are *intermediate phases* which may possess structures different from the pure elements.

The elements may be randomly distributed in the crystal lattice creating a *random solid solution* (for example, A1 phase of Fe-Pt) or may prefer a certain type of crystal sites forming a *fully or partially ordered solution* ($L1_0$ FePt). The order in solid solution is also called a *superlattice*. It is also possible for atoms of one element to form clusters within the solution which may be randomly scattered or ordered, creating complex structures.

The phase diagram of a multicomponent metallic system is characterized by the extent of the solid solubility of phases, the stability of phases, the temperature dependence of stability and phases structures. The stability and resulting structure of a particular phase in a binary system is determined by the Gibbs energy G_s:

$$\Delta G_S(x_A, x_B; T) = G_S(x_A, x_B; T) - x_A G_A(T) - x_B G_B(T), \qquad (1.2)$$

where G_A and G_B are the molar Gibbs free energies of the pure metals A and B, $G_S(x_A, x_B; T)$ is the Gibbs free energy of the solid solution with atomic concentrations x_A and x_B=1- x_A. The calculated values of Gibbs energies G_A for Fe, Cu, Ag and Pt are presented in Table 1.1.

In absence of intermediate phases the necessary condition for solid solution formation

Table 1.1: Calculated molar Gibbs free energies G_A for Fe, Cu, Ag and Pt at temperature T = 293 K and pressure P = 10^5 Pa [9]

Element	G_A, kJ $\cdot$ mol^{-1}
Fe (bcc)	-1.65
Cu (fcc)	-9.71
Ag (fcc)	-12.47
Pt (fcc)	-12.20

is:

$$\Delta G_S(x_A, x_B; T) < 0. \tag{1.3}$$

In the case when several phases exist, the solid solubility is calculated by comparing $\Delta G_S(x_A, x_B; T)$ with the Gibbs free energies of all possible competing phases $A_\alpha B_\beta$ $\Delta G_{AB}(\alpha, \beta; T)$.

If intermediate phases do not exist, the free energy of formation can be expressed as:

$$\Delta G = \Delta H - T\Delta S, \tag{1.4}$$

where ΔH and ΔS are the enthalpy and entropy of formation, respectively. The entropy of solid solution formation is usually positive and includes contribution from effects such as distribution of magnetic moments, clustering of atoms and long range ordering.

1.3.2 Parameters governing solid solubility.

Systematic studies of phase diagrams for various systems allowed to determine the principles that govern alloy formation. These principles were formulated by Hume-Rothery in 1930 (see [10], chapter 3 and references therein) and are called the *Hume-Rothery rules*.

The first Hume-Rothery rule states that if the atomic sizes of solvent and solute differ by more than 15% the formation of a solid solution is restricted. Waber et al. (see [10], reference *Waber et al. [1963]*) tested this rule on more than 1000 solid solutions and found that 90% of the elemental combinations which should be insoluble actually exhibited a

certain degree of solubility, and on the other hand, only half of the systems predicted to be soluble were actually soluble. For example, Fe and Cu have similar atomic size (126 and 128 pm, respectively), however, these two elements are immiscible in a large concentration range.

The second Hume-Rothery rule states that the electrochemical nature of the two elements must be similar to form a solid solution. In other words, the solid solubility of two metals depends on the difference of electronegativities, $\Delta\varphi=\varphi_A-\varphi_b$, of its components. This difference induces a transfer of electronic charge from the less electronegative to the more electronegative atom until the electronegativities are equalized in the alloy. The smaller the difference in electronegativity, the more likely is the formation of the solid solution.

The third Hume-Rothery rule states that in order to achieve complete solubility, two metals are required to have the similar valency (or valence electron concentration per atom *e/a*). The experimental results on transition metal alloys ([11]) however showed that this rule only worked in 50% of systems. Nevertheless, this rule can be reformulated by broadening the definition of valency considering all s, p and d electrons that are involved in the alloying process. For example, it has been considered for a long time that only the s and p electrons in metals with fully occupied d-bands determine the solubility. However there is the possibility of transferring electrons from the d band to the conduction band and the presence of s-d hybridization during solid solution formation, which makes the situation more complex.

Miedema and coworkers [12] developed an empirical model which proved to be quite successful for predicting solid solubilities of metals [13]. This model is based on a concept of Wigner-Seitz atomic cells. The Wigner-Seitz cell is the smallest polyhedron constructed by bisecting planes perpendicular to the lines joining the atoms in question to their nearest neighbors. The parameters governing the solid solubility of metals A and B are elemental concentrations X_A and X_B, electronegativities φ_A and φ_B, and electron densities at the boundaries of Wigner-Seitz atomic cells $n_b(A)$ and $n_b(B)$. The electron density in the

alloy must be continuous across the boundary between atomic cells of two types of metal atoms. The energy required to smoothen out the difference between electron densities at the atomic cell boundaries is proportional to $(n_b^{1/3}(A) - n_b^{1/3}(B))^2$. The enthalpy of formation of solid solution of metal B in metal A in Miedema model is:

$$\Delta H \propto \Delta h^0, \tag{1.5}$$

where

$$\Delta h^0 = \frac{2V_{A^{2/3}}}{n_b^{1/3}(A) + n_b^{1/3}(B)}[-P(\varphi_A - \varphi_B)^2 + Q(n_b^{1/3}(A) - n_b^{1/3}(B))^2 - R]. \tag{1.6}$$

Here V_A is the volume of atomic cell, P and Q are positive constants determined empirically. R is only different from zero if alloys are formed between transition and non-transition metals.

Fig.1.4 shows a graphical representation of the alloying behavior of Fe (for equiatomic composition) described by Miedema model. The y and x axes represent φ_A-φ_B = $\Delta\varphi$ and $n_b^{1/3}(A)$-$n_b^{1/3}(B)$ = $\Delta n^{1/3}$, respectively. The solid lines separate regions with metals that have a negative enthalpy of alloying (minus signs) with Fe from metals that have a positive enthalpy of alloying (plus signs) with Fe.

The resulting solid solubility depends both on size-mismatch and electronic structure. Fig.1.5 shows the solubility map for iron alloys plotted in thermochemical coordinates [14]: atomic radius vs. enthalpy of formation Δh^0 of an equiatomic compound at room temperature. In general, if Δh^0 is sufficiently negative, the formation of solid solution is favored. As Δh^0 approaches zero, the size effect becomes the deciding factor. Points corresponding to Ag, Cu and Pt are marked by red circles. Data presented in Fig.1.5 shows that good solid solubility (more than 15 %) is expected for Pt, while Ag and Cu do not tend to form solid solution with Fe.
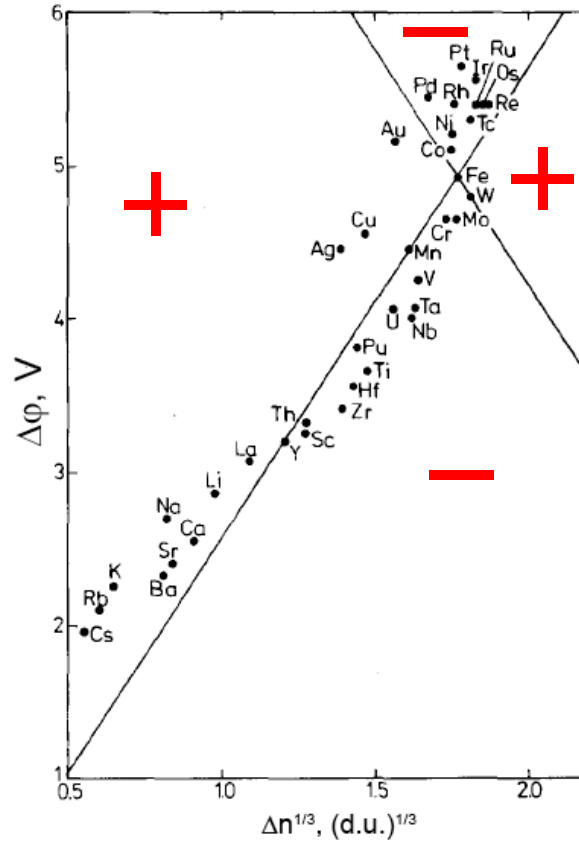
Figure 1.4: Graphical representation of the alloying behaviour of Fe (for equiatomic composition) described by Miedema model. The y and x axes represent φ_A-$\varphi_B = \Delta\varphi$ and $n_b^{1/3}(A)$-$n_b^{1/3}(B) = \Delta n^{1/3}$, respectively. The lines drawn separate metals that have a negative enthalpy of alloying with Fe from metals that have a positive enthalpy of alloying with Fe. Adapted from [12].

1.3.3 Metastable alloys.

The previous section described solid solubilities for alloys in stable thermal equilibrium. However, solubilities for the systems in metastable states (states with a Gibbs free energy higher than the lowest possible value) can be different. The metastable states can be accessed by rapid quenching and usually are characterized by extended solid solubility ([10], chapter 19 and references therein) to a point where two immiscible elements can
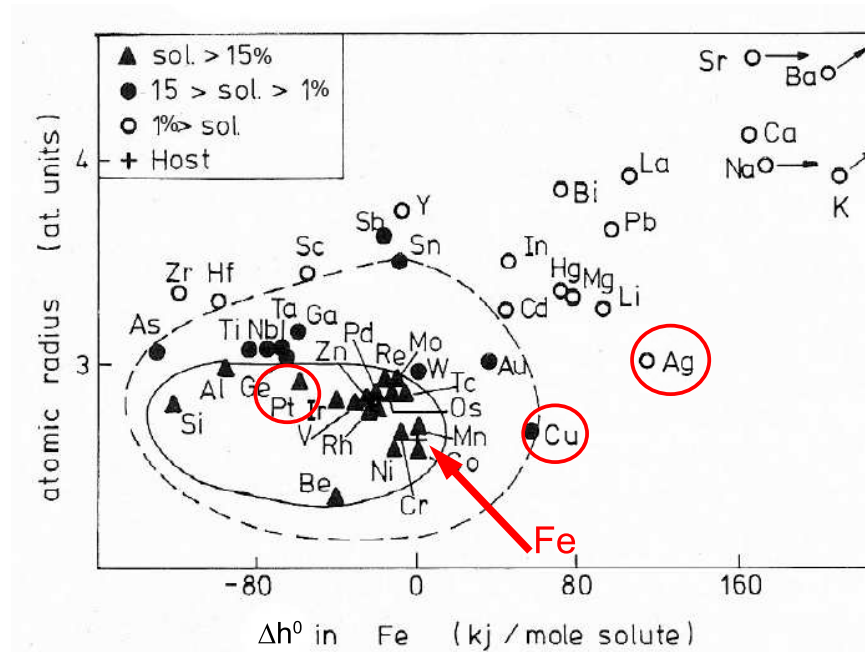
Figure 1.5: Solubility map of Fe alloys using thermochemical coordinates. Data correspond to solubilities at room temperature. Contours of increasing solubility have been drawn. Systems mentioned in the current work are marked with red circles. Adapted from [14].
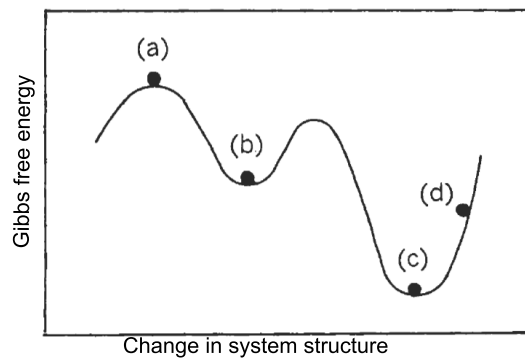
Figure 1.6: A schematic illustration of possible thermodynamic states of alloys: (a) unstable equilibrium (b) metastable equilibrium (c) stable equilibrium and (d) unstable nonequilibrium state. Taken from [10], chapter 19

form an alloy (for example, Fe-Cu, see section 1.5.1).

The nature of metastability can be explained by considering the shape of the Gibbs free energy function which is shown in Fig.1.6. A metastable state is a state where the Gibbs free energy has a local minimum (point (b) in Fig.1.6). The system may stay in this state until a large-enough thermal fluctuation will induce a phase separation (see next section). The state of unstable equilibrium (point (a) in Fig.1.6) can be destroyed by any thermal fluctuation, however small.

1.3.4 Phase separation in metastable systems. Spinodal decomposition.

If a multicomponent systems decomposes into regions with different concentrations of its components, it undergoes a *phase separation*. Phase separation may occur via two mechanisms: (1) nucleation and growth and (2) spinodal decomposition. Nucleation and growth proceeds as follows (see Fig.1.7):

1. initial formation of spherical fragments of the more stable phase,

2. growth of nuclei by diffusion of material from the metastable matrix, followed by coalescence.

The nuclei have a distinct interface with the matrix and their composition is immediately different from the rest of the solution. Nucleation and growth cannot occur spontaneously, and an energy barrier has to be overcome (for example, by large thermal fluctuation).

Unlike nucleation and growth, *spinodal decomposition* starts spontaneously with initial small-amplitude composition fluctuations. The composition amplitude displays a sinusoidal behavior with distance and grows with time (see Fig.1.8). It proceeds homogenously throughout the alloy resulting in a two-phase modulated structure. At the initial stage, all
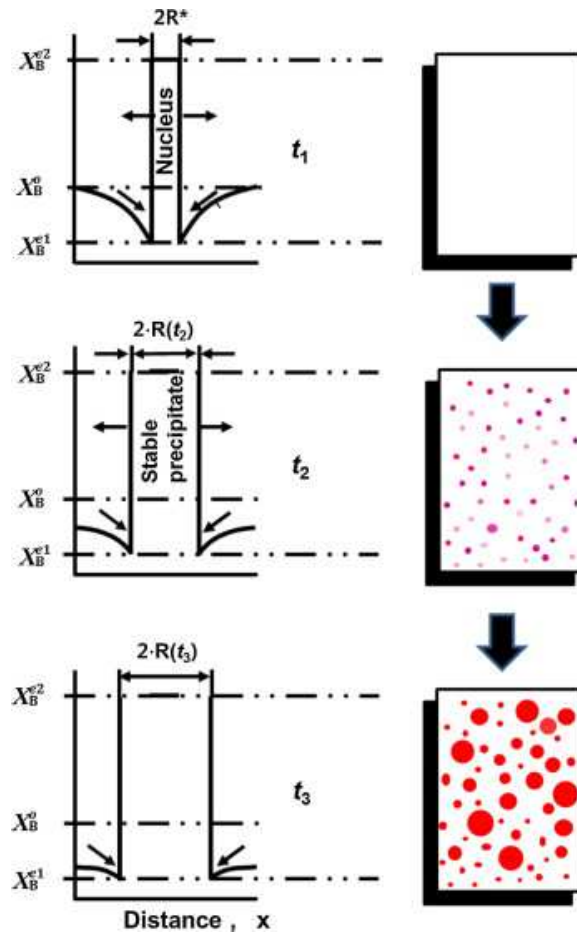
Figure 1.7: Schematic diagrams showing spatial variations in concentration and morphology evolution with time ($t_1 < t_2 < t_3$) during phase separation in metastable system by nucleation and growth mechanism. $X^0{}_B$ and $X^e{}_B$ - metastable and equilibrium concentrations of phase B, respectively. Taken from [15].

regions of solution possess the same structure and there are no pronounced interfaces between them.

Whether phase segregation proceeds via nucleation and growth or spinodal decomposition depends on the cooling rate and the segregation path. Fig.1.9 (a) shows the Gibbs free energy calculated at the temperature T=T$_{cooling}$ for the system AB with a miscibility gap. The phase diagram of the same system is shown in Fig.1.9 (b).
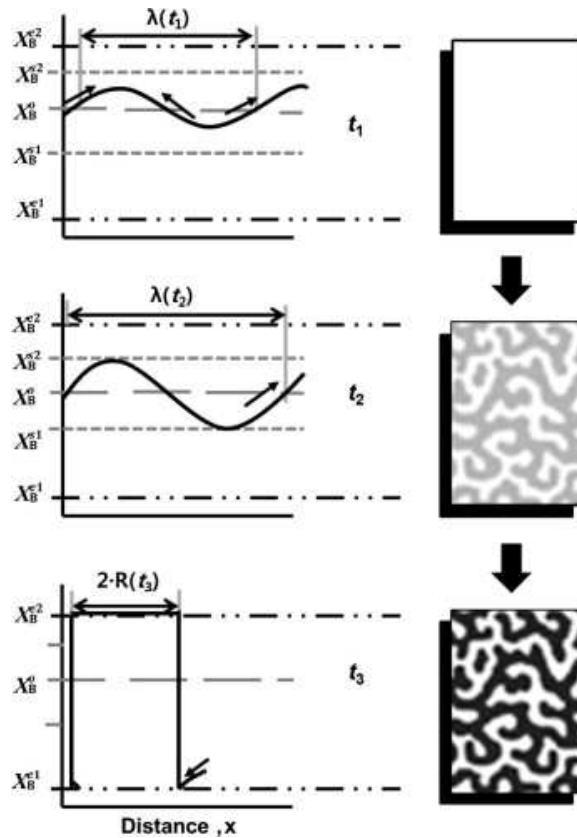
Figure 1.8: Schematic diagrams showing spatial variations in concentration variation and morphology evolution with time ($t_1 < t_2 < t_3$) during phase separation in metastable liquid by spinodal decomposition. $X^0{}_B$, $X^s{}_B$ and $X^e{}_B$ - metastable, spinodal and equilibrium concentrations of phase B, respectively. Arrows represent the direction of diffusion. Taken from [15].

The phase diagram can be divided into three regions: a stable region (outside the miscibility gap), a metastable region and an unstable region, divided by binodal (solid) and spinodal (dashed) lines.

The miscibility gap corresponds to a region of Gibbs free function in the concentration range $X^{e1}{}_B < X_B < X^{e2}{}_B$ (two local minima). Here the boundary between metastable and unstable regions is defined by the sign of the second derivative of the Gibbs energy. In the concentration range $X^{s1}{}_B < X_B < X^{s2}{}_B$ $\partial^2 G/\partial X^2 < 0$ the system is unstable. In this region the system is unbalanced and spinodal decomposition takes place. The Gibbs
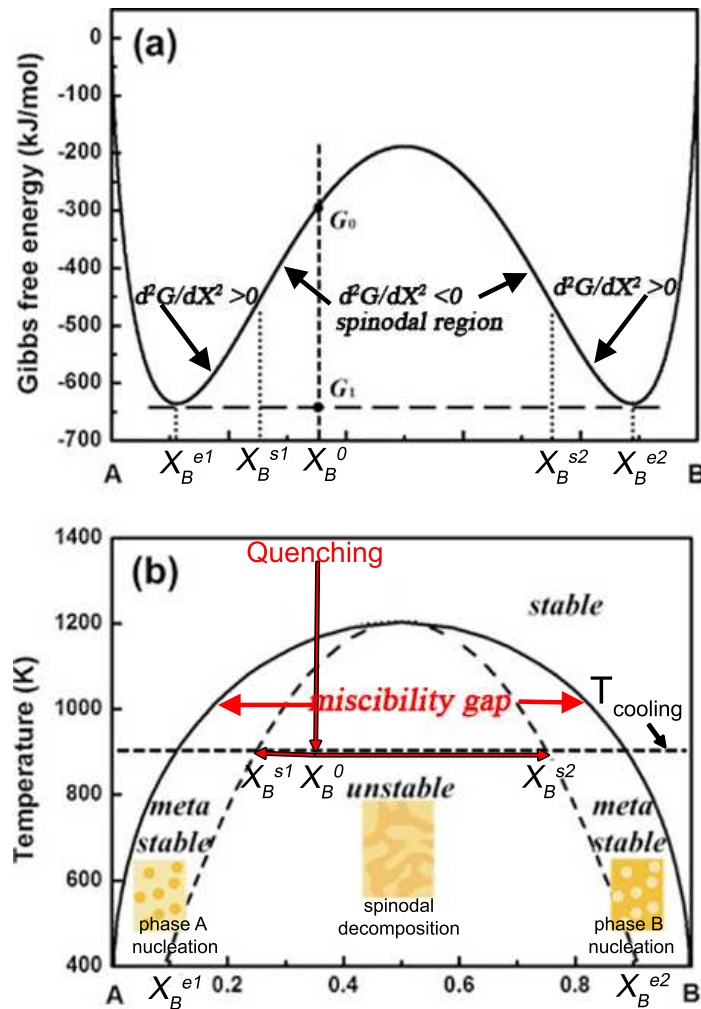
Figure 1.9: (a) Gibbs free energy calculated for the system with the miscibility gap at T=T$_{cooling}$. (b) Phase diagram of the same system with the spinodal lines. Arrows represent the direction of diffusion. Adapted from [15].

free energy second derivative has a positive sign in the concentration ranges $X^{e1}_B < X_B < X^{s1}_B$ and $X^{s2}_B < X_B < X^{e2}_B$, and the system is in a metastable state where phase separation occurs via nucleation and growth.

1.4 Magnetic properties of nanoparticles.

1.4.1 Magnetic moment of the monodomain nanoparticle. Superspin.

If a particle composed of magnetic atoms becomes small enough, single magnetic domain (monodomain) becomes energetically favorable. The critical radius r_c below which a spherical particle becomes a monodomain is given as ([16]):

$$r_c \approx 9 \frac{(AK_u)^{1/2}}{\mu_0 M_s^2},\tag{1.7}$$

where A is the exchange constant, K_u is the magnetic anisotropy energy density constant, μ_0 is the magnetic permeability of vacuum, M_s is the saturation magnetization. The typical values of critical radii vary from 15 to 750 nm. In superparamagnetic theory [17] it is assumed that magnetic moments of the particle's atoms rotate coherently, so the magnetic behavior of the particle is described by a single magnetic moment (macrospin or superspin) with a magnitude of $\mu = \mu_{at}N$, where μ_{at} is the atomic magnetic moment and N is the number of the atoms in the particle.

1.4.2 Magnetic anisotropy.

Magnetic anisotropy is the dependence of the internal energy on the direction of spontaneous magnetization. The direction of magnetization in which the energy of the system is minimum is called the *easy axis*. The maximum energy is reached when the magnetization lies in the direction called the *hard axis*. In bulk materials, the main sources of anisotropy are magnetocrystalline and magnetostatic energies. In nanosized materials, contributions of shape and surface anisotropies have to be taken into consideration.

Magnetocrystalline anisotropy. Magnetocrystalline anisotropy is the contribution to the magnetic anisotropy that depends on the magnetization direction with respect to the crystal lattice. Its origin is the the spin-orbit interaction and the crystal symmetry of the sample. The simplest form of crystal anisotropy is the *uniaxial* anisotropy, which is described by a

single stable orientation (easy-axis) of the internal magnetization. The magnetocrystalline uniaxial anisotropy energy is given by:

$$E_{uni} = K_2 V sin^2\theta + K_4 V sin^4\theta, \tag{1.8}$$

where K_2 and K_4 are anisotropy constants, V is the particle volume and θ is the angle between the symmetry axis and the magnetization. In the case of ferromagnetic materials, K_4 and high-order coefficients are often small in comparison to K_2, and the anisotropy energy is written as:

$$E_{uni} = KV sin^2\theta, \tag{1.9}$$

.

where K is the effective uniaxial anisotropy energy density constant. At temperatures much lower the Curie point, K is assumed to be temperature independent.

Shape anisotropy. Shape anisotropy results from the anisotropy of the demagnetizing factors and is defined by the shape of the specimen. For example, the shape anisotropy of an ellipsoidal specimen is uniaxial and its energy can be expressed as:

$$E_{shape} = \frac{1}{2}\mu_0 V M_s^2 (N_x - N_z)sin^2\theta, \tag{1.10}$$

where V is the volume of the particle, M_s is saturation magnetization, N_x and N_z are demagnetization factors relative to the x and z axes, respectively.

Strain anisotropy. Strain anisotropy [16] is a magnetostrictive effect and its energy is described as:

$$E_{strain} = -\frac{3}{2}\lambda_s \sigma S cos^2\theta, \tag{1.11}$$

where λ_s is the saturation magnetostriction, σ is the strain per area, S is the particle surface and θ is the angle between the magnetization and the strain axis.

Surface anisotropy. Surface anisotropy is caused by the reduction of the coordination number at the surface. Surface anisotropy enhances the total anisotropy of small nanoparticles since, with decreasing particle-size the magnetic contributions from the surface increases. In the case of spherical particles with diameter d, the effective magnetic anisotropy energy density is expressed as:

$$K_{eff} = K_v + \frac{S}{V}K_s = K_v + \frac{6}{d}K_s, \qquad (1.12)$$

where $S = \pi d^2$, $V = \pi d^3/6$ are the surface area and the volume of the particle, respectively.

1.4.3 Relaxation behavior of magnetic particle ensembles. Superparamagnetism.

The magnetic energy of a single domain particle with uniaxial anisotropy is expressed as:

$$E = KV sin^2\theta - \mu H cos(\alpha - \theta), \qquad (1.13)$$

where K - is anisotropy energy density, V is the particle volume, H is the applied magnetic field, μ is the particle's magnetic moment, α and θ are the angles between the easy axis and magnetization and magnetic field, respectively [17] (see Fig.1.10).

Fig.1.10 (b) (continuous line) shows the dependence of the particle free energy divided by KV on the angle θ between magnetization and easy-axis in the absence of a magnetic field. The energy minima (θ= 0 and π) are separated by the an energy barriers KV. This dependence shows that without external magnetic field, the particle magnetization can be in both equilibrium states (parallel to easy axis).

The relaxation behaviour of the magnetization is described by the Arrhenius law:

$$M(t) = M_0 exp(-t/\tau), \qquad (1.14)$$
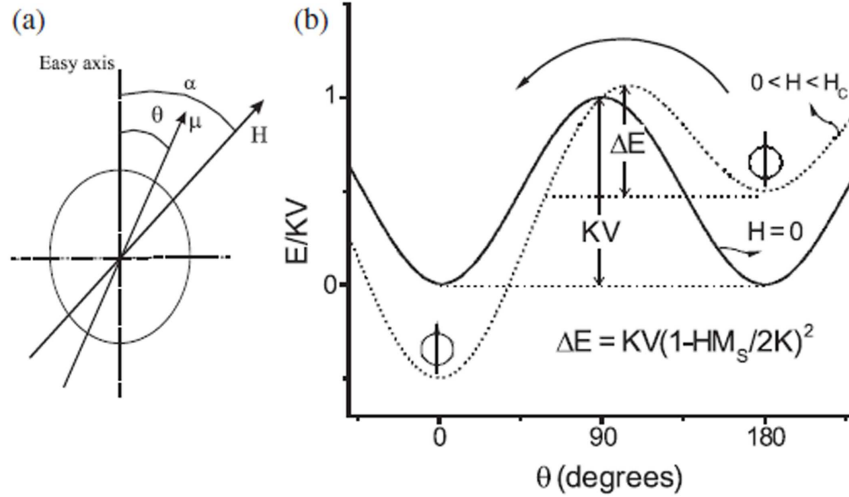
Figure 1.10: (a) Axis system for a fine particle. (b) The angular dependence of the energy barrier for zero external field (continuous line) and for a field value lower then the coercive field (dashed line). Taken from [17].

where M_0 is the initial magnetization and τ is the characteristic relaxation time. This relaxation time depends on temperature and energy barrier according to:

$$\tau = \tau_0 exp(KV/k_B T), \tag{1.15}$$

where k_B is the Boltzmann constant and τ_0 is a value inversely proportional to the jump attempt frequency of the particle magnetic moment between two opposite directions parallel to the magnetization easy axis. The values of τ_0 vary in the range 10^{-9}-10^{-10} s ([17]). If a magnetic field is applied, the energy barrier for the easy axis direction, coinciding with the direction of the magnetic field, dectrases.

The behavior of the magnetization strongly depends on the time window τ_m of the particular experimental technique with respect to the intrinsic relaxation time τ.

In case when $\tau_m \gg \tau$ the relaxation of the system occurs faster then observed in this time window, the system reaches thermodynamical equilibrium. The particles are in the

superparamagnetic regime.

If $\tau_m \ll \tau$, the system relaxation proceeds slowly and quasistatic properties as in an ordered magnetic systems are observed. In this case particles are considered to be in the *blocked regime*.

For a fixed measurement time-window, the magnetic behavior depends on the temperature. The temperature that divides superparamagnetic and blocked regimes ($\tau_m = \tau$) is called the blocking temperature T_{Bl}.

For identical particles, the blocking temperature is defined as:

$$ln\tau = ln\tau_0 + \frac{KV}{k_B T_{Bl}},$$ (1.16)

For conventional (for instance, SQUID) magnetometry, $\tau_m = 100$ s and T_{Bl} is given by

$$T_{Bl} \approx \frac{KV}{25 k_B}.$$ (1.17)

Using the same procedure the critical value of the particle volume can be obtained:

$$V_{crit} \approx \frac{25 k_B T}{K}.$$ (1.18)

1.4.4 Superparamagnetic and blocked regimes. Initial susceptibility.

The analytical description of the magnetic behavior of the ensemble of nanoparticles is a complex problem. The exact solutions exist only in two extreme cases: for $T = 0$, when particles are in a fully blocked state, and $T \gg T_{Bl}$ for a superparamagnetic ensemble. In both cases, it is assumed that there are no magnetic interactions between the particles.

If the particle is superparamagnetic, its magnetization is described by the Langevin function:

$$\frac{M}{M_S} = coth(\frac{\mu H}{k_B T}) - \frac{k_B T}{\mu H} = L(\frac{\mu H}{k_B T}).$$ (1.19)

In a range of small fields the magnetization is given as:

$$M = M_S \frac{\mu H}{3k_B T} = \frac{N \mu^2 H}{3k_B T} \tag{1.20}$$

and the initial susceptibility χ_{sp} = M/H is given as:

$$\chi_{sp} = \frac{N \mu^2}{3k_B T} = \frac{M_s^2 V^2}{3k_B T} = \frac{M_s^2 V}{3k_B T}. \tag{1.21}$$

The values of magnetization for fully blocked identical nanoparticles were calculated by E. C. Stoner and E. P. Wohlfarth [18] by minimizing Eq.1.13. For each fixed angle between magnetic field and easy axis α, hysteresis loops were calculated. Afterwards, all loops were averaged ,thus obtaining the hysteresis loop for an ensemble of particles with randomly distributed anisotropy axes. The expression for initial susceptibility was calculated as:

$$\chi_{bl} = (2/3) \frac{M_S}{H_a}, \tag{1.22}$$

where H_a is the anisotropy field H_a=$2K/M_S$. Therefore, the value of the initial susceptibility is:

$$\chi_{bl} = \frac{M_S^2}{3K}. \tag{1.23}$$

1.4.5 Distribution of energy barriers in ensembles of NPs.

The distribution of energy barriers in a granular system can be determined by measuring the magnetization as a function of temperature in small fields. The procedure is called ZFC-FC (zero-field-cooling - field-cooling) magnetization measurement. The ZFC magnetization is measured in a small field (20 - 300 Oe) after cooling down the demagnetized sample in zero field. The FC magnetization is measured after cooling the sample in the same field.
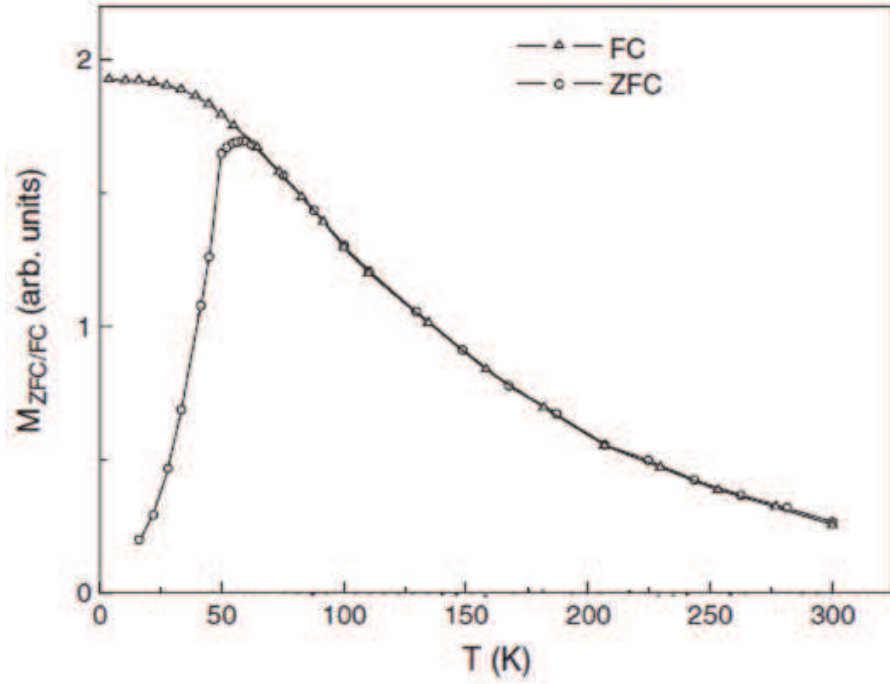
Figure 1.11: Typical ZFC-FC magnetization curves measured for the sample of magnetic non-interacting nanoparticles with size distribution. Taken from [17].

Fig.1.11 shows the typical ZFC-FC magnetization curves measured for a sample of magnetic non-interacting nanoparticles with a size distribution. The FC magnetization monotonously decreases with increasing temperature, while the ZFC curve has a maximum at a temperature which is, as proven by Tournus et al. [19, 20], the blocking temperature T_{Bl}.

The ZFC magnetization is expressed as [19, 20]:

$$M_{ZFC}/H = \int\limits_{0}^{Vcrit} \chi_{\text{sp}} V D(V) dV + \int\limits_{Vcrit}^{\infty} \chi_{\text{bl}} V D(V) dV, \qquad (1.24)$$

,

where $V_{crit} = \frac{k_B T}{K_{eff}} ln\frac{\tau}{\tau_0}$ is the critical volume between superparamagnetic and blocked nanoparticles. Here K_{eff} is an effective magnetocrystalline anisotropy energy density.

$D(V)$ is the particle-volume distribution function. The first part of Eq.1.24 is the fraction of superparamagnetic particles, the second is the fraction of ferromagnetically blocked particles. Taking into consideration expressions for χ_{sp} and χ_{bl} Eq.1.21 and Eq.1.23, the values of M_{ZFC}/H are written as:

$$M_{ZFC}/H = \frac{M_S^2}{3k_BT} \int\limits_0^{Vcrit} V^2D(V)dV + \frac{M_S^2}{3K_{eff}} \int\limits_{Vcrit}^{\infty} VD(V)dV. \qquad (1.25)$$

1.5   Preparation and phase segregation in metastable alloys: Fe-Cu system.

1.5.1   Solid solubility in the Fe-Cu system. Metastable Fe-Cu alloys.
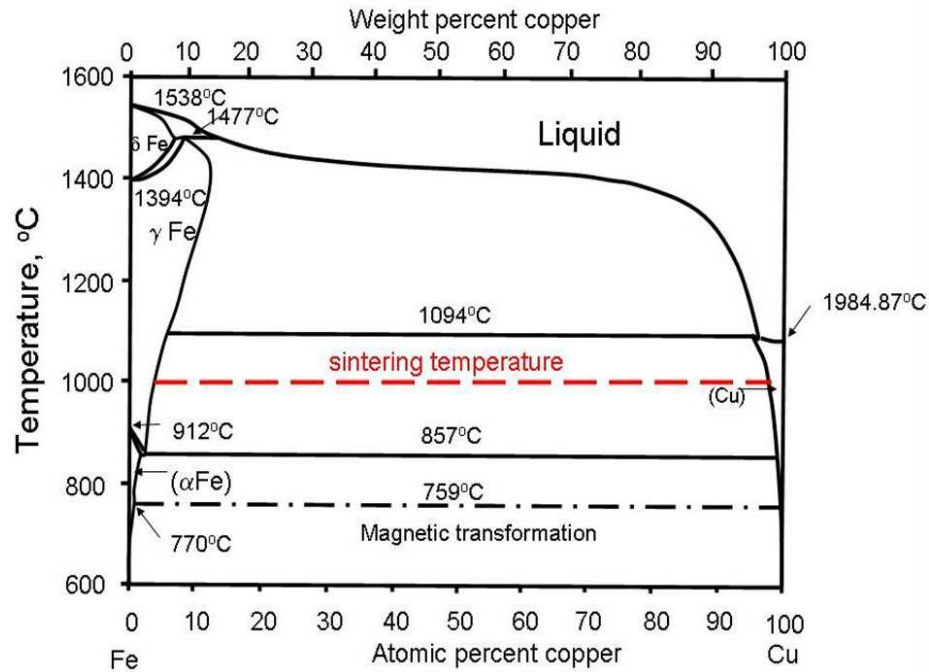
Figure 1.12: Fe-Cu phase diagram. Taken from [3].
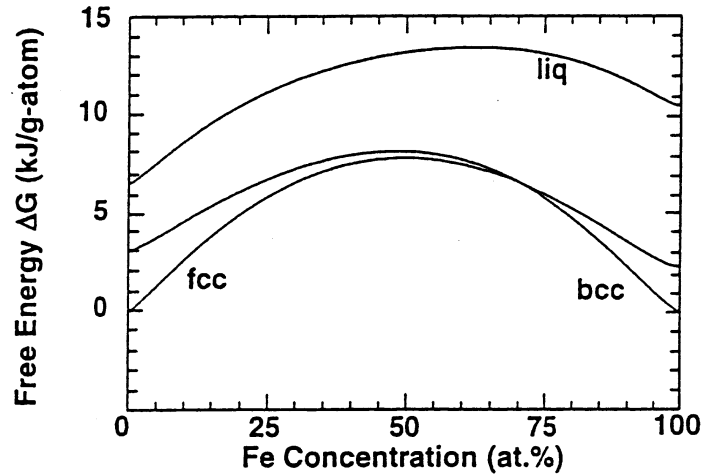
Figure 1.13: Free energy functions at 673 K in the FeCu system calculated in reference [21].

The Fe-Cu equilibrium phase diagram is characterized by a large miscibility gap (see Fig.1.12). The Fe-Cu system has a positive free energy of mixing which is concentration dependent and reaches a maximum in $Fe_{50}Cu_{50}$ (7.5 kJ/g-atom at 673 K) (see Fig.1.13) [21–24]. Despite this, the preparation of Fe-Cu metastable alloys is possible by means of various techniques (mechanical alloying, liquid quenching, thermal evaporation and sputtering). Fig.1.14 shows a schematic diagram of the metastable alloys structures obtained by various methods. Typically, the diagram contains two single phase alloy areas: bcc Fe-rich and fcc Cu-rich. The concentration range of these areas depends on the method of preparation.

1.5.2   Fe-Cu binary phase diagram for nanometer-sized particles.

The effect of size reduction on the Fe-Cu phase diagram was studied in references [29, 30] . Authors of reference [30] calculated various thermodynamical parameters using phenomenological models for the Gibbs energy of various Fe-Cu phases. These parameters were used by X. J. Liu et. al ([29]) to calculate the Fe-Cu binary phase diagram taking size effects into consideration (Fig.1.15). This diagram shows that the size of the single
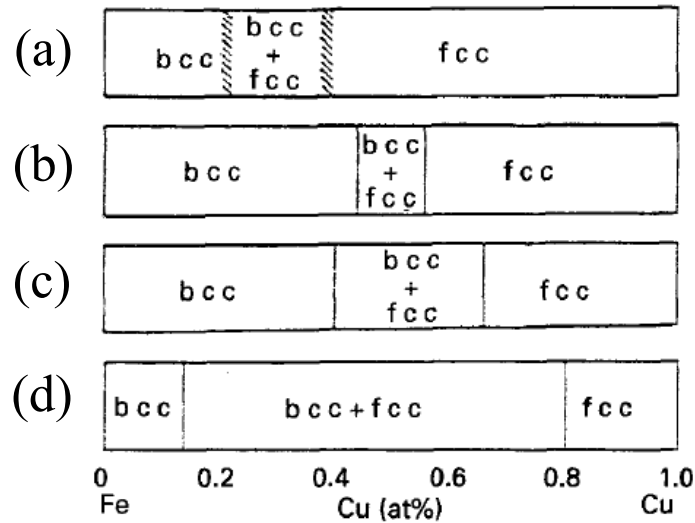
Figure 1.14: Schematic diagram of the Fe-Cu metastable alloys structure obtained by (a) mechanical alloying [25], (b) sputtering [26], (c) thermal evaporation [27], (d) liquid quenching [28]. Taken from [25]

phase alloy regions is size dependent and expands with decreasing diameter of the grain or nanoparticle. In other words, in small particles or grains, the formation of a single bcc or fcc phase is more favorable.

The lattice constants of bcc and fcc Fe-Cu alloys prepared by sputtering, thermal evaporation and liquid quenching are shown in Fig.1.16.

1.5.3   Thermal stability and diffusion in Fe-Cu alloys.

The thermal stability of the Fe-Cu alloys has been extensively investigated ([32–38]). Hornbogen [32] studied Fe-Cu alloys prepared by vapor deposition with Cu concentration up to 50 at.%. The alloys were subsequently annealed at temperatures up to 830^oC for 3 min at each temperature. The as-prepared alloys possessed a bcc structure with a grain sizes of 2-10 nm. Annealing at temperatures higher than 250^oC led to Cu segregation to the grain boundaries and increasing of the grain size up to 20-40 nm.

Nakamura et. al [33] prepared $Fe_{33}Cu_{67}$ metastable fcc alloy by RF sputtering which
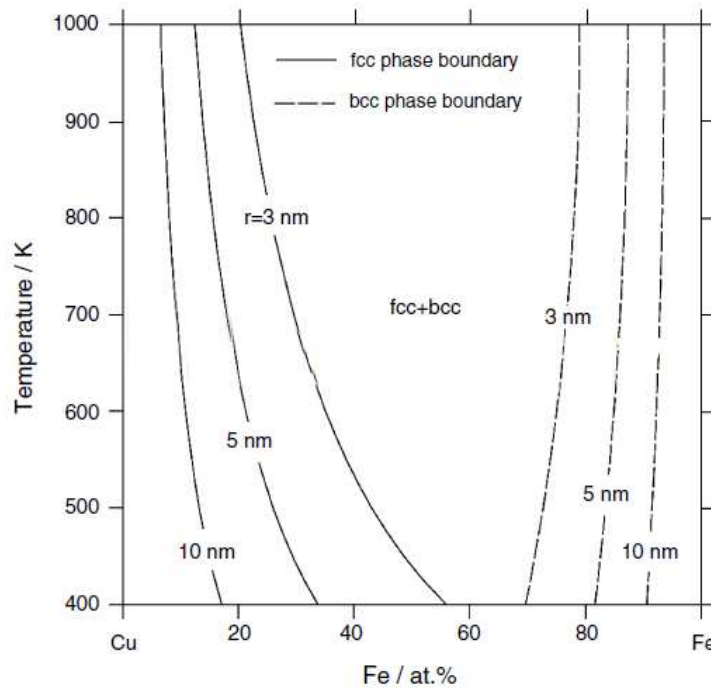
Figure 1.15: Fe-Cu binary phase diagram for nanometer-sized particles. Taken from [29].

was subsequently annealed at 400 ^{o}C for 1 hour. Mössbauer spectra showed that annealing led to Fe precipitation as fcc particles. These precipitates remained coherent until the grain size reached 20 nm and then transformed to the bcc α-Fe phase.

Eckert et al. [34–36] prepared metastable Fe_x-Cu_{100-x} alloys in the broad concentration range $5 \leq x \leq 95$ at.% by mechanical alloying. As-prepared alloys with x < 60 at.% and x > 80 at.% exhibited single-phase fcc and bcc structures, respectively. For $60 \leq x \leq 80$ at.% both phases coexisted. Thermal analysis was performed by means of differential scanning calorimetry (DSC) at a heating rate of 20 K/min in a temperature range from 300 to 900K. The conclusions on phase segregation in alloys were drawn by analyzing maximum temperatures of DSC peaks, changes in grain size and atomic level strains. The pure fcc and bcc single phase alloys were found to be more stable than the ones with two coexisting phases. Additions of Fe in single-phase fcc alloys improved the thermal stability,
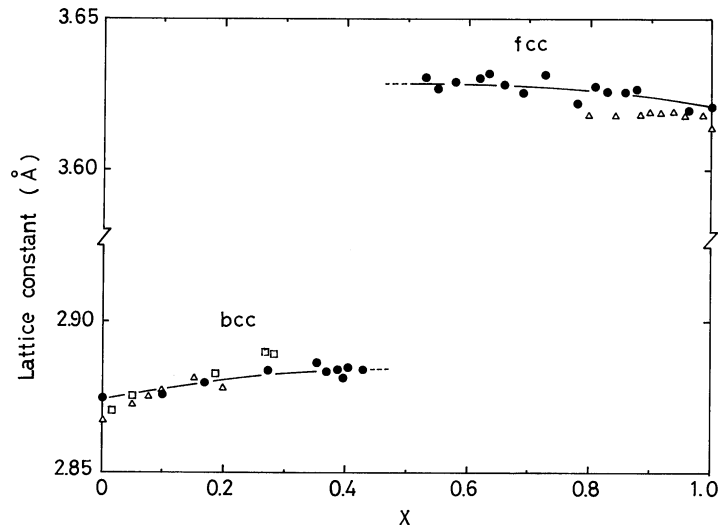
Figure 1.16: Lattice constant of $Fe_{1-x}Cu_x$ alloy at room temperature prepared by ●: sputtering, □: thermal evaporation, △: liquid quenching. Taken from [26].

however adding Cu did not affect the stability in single-phase bcc solid solutions. The phase separation of fcc and bcc phases proceeded by different mechanisms: the fcc phase decomposed by formation of bcc Fe particles, while in bcc solid solutions, Cu segregated to the bcc grain boundaries forming a layer of almost pure Cu and then nucleating into the Cu particles.

On the other hand, Crespo et al. [37, 38] discovered anomalous magnetic magnetic behavior of Fe-Cu alloys during decomposition which could not be explained by the simple decomposition of the system into the stable bcc (Fe) and fcc (Cu) phases. Metastable bcc $Fe_{70}Cu_{30}$, and fcc $Fe_{50}Cu_{50}$ and $Fe_{30}Cu_{70}$ alloys were prepared by mechanical alloying and subsequently annealed with a heating rate of 20K/min at temperatures in the range of 300-900 K. The x-ray diffraction data showed no formation of a new crystal phase and change of grain size up to 723 K for all samples. Crespo et al. observed drastic decrease of the magnetic moment per iron atom after annealing indicated presence of magnetic phases with a broad range of Curie temperatures. An explanation was found by assuming that the phase separation at the early stages proceeds via spinodal decomposition. For example, spinodal
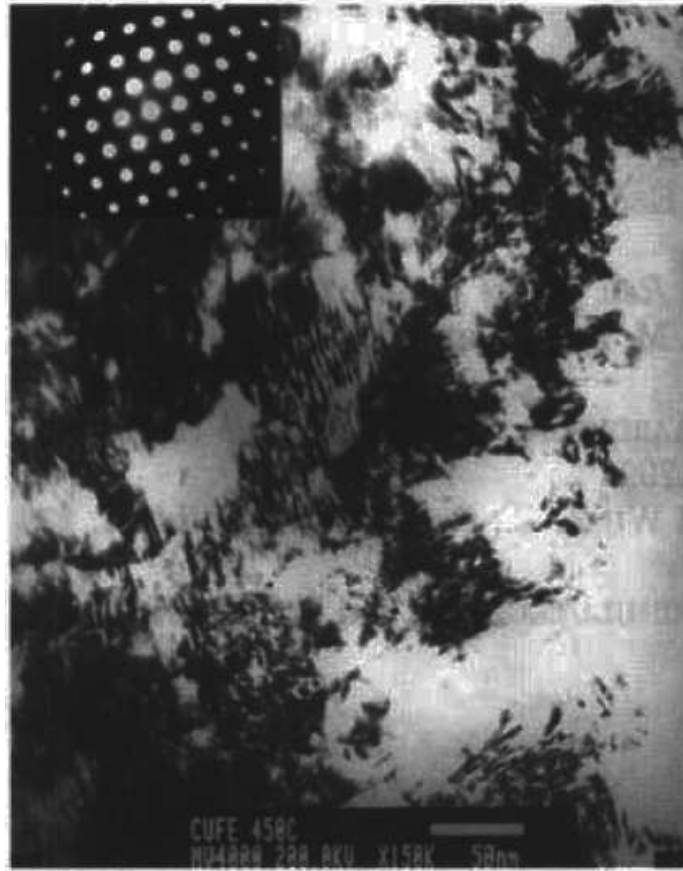
Figure 1.17: TEM image of a fcc $Fe_{50}Cu_{50}$ alloy prepared by mechanical alloying and annealed at 723 K. Taken from [31].

segregation in the fcc Fe-Cu alloy takes place in the following way:

fcc Fe-Cu $\rightarrow$ fcc $Fe_{rich}Cu_{poor}$ + fcc $Fe_{poor}Cu_{rich}$,

and further goes as:

fcc $Fe_{rich}Cu_{poor}$ + fcc $Fe_{poor}Cu_{rich}$ $\rightarrow$ bcc $Fe_{rich}Cu_{poor}$ + fcc $Fe_{poor}Cu_{rich}$ $\rightarrow$

$\rightarrow$ bcc Fe + fcc Cu.
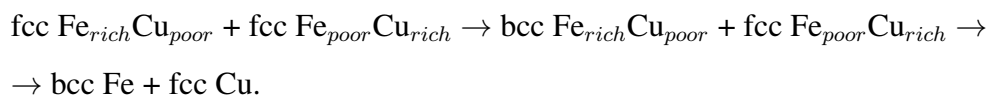
The assumption was supported by Mössbauer [39], EXAFS [40] and TEM [31] measurements for $Fe_{50}Cu_{50}$ alloy. Fig.1.17 shows bright image TEM image of a fcc $Fe_{50}Cu_{50}$ alloy prepared by mechanical alloying and annealed at 723 K. The TEM image shows the contrast modulation with a periodicity of about 2-3 nm. The diffraction pattern shown in

the inset is taken from a 20 nm area.

1.6 Binary Fe-Ag system

.
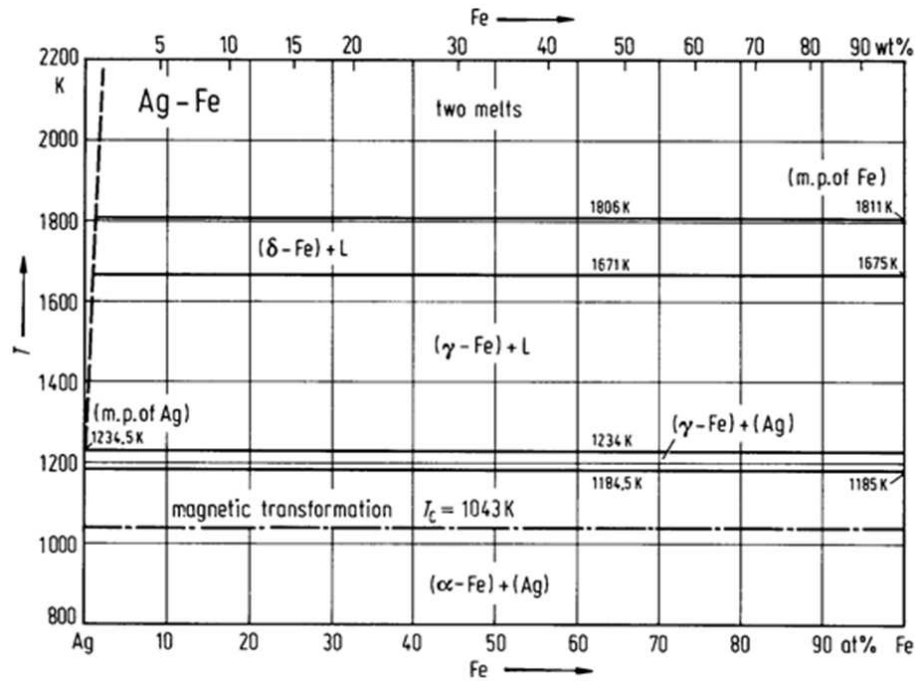
Figure 1.18: Ag-Fe phase diagram. Taken from [41]

The equilibrium phase diagram of the Ag-Fe system is shown in Fig.1.18. The equilibrium phases of the Ag-Fe system are the liquid, the bcc solid solution based on low-temperature α-Fe as well as high-temperature δ-Fe (bcc allotrope), and the fcc phase with a large miscibility gap. The mutual solubility of Ag and Fe is very low in both solid and liquid states. The solubility of Ag in solid Fe reaches a maximum of approximately 0.022 at.% at 1671 K. Iron and silver have a large positive free energy of mixing of approximately 25.5 kJ mol^{-1} [41].

1.7 Janus nanoparticles and their applications.

The term "Janus nanoparticle"was used for the first time in 1991 in the Nobel lecture of Pierre-Gilles de Gennes to describe particles consisting of two hemispheres possessing different chemical properties. Such particles were named in honor of the Roman two-faced god Janus who was depicted with two heads placed back to back so he could look in two opposite directions at the same time [42]. Today the "Janus nanoparticle"term is used to describe any asymmetric, biphasic and polyphasic particle. During the last twenty years, Janus particles with various morphologies (such as dumbbell, snowman, acorn and half-raspberry, etc.) (see Fig.1.19) were produced and proved to be very promising in regard of numerous applications such as:

1. stabilization of water-in-oil (oil-in-water) emulsions (the combination of a hydrophilic hemisphere with a hydrophobic one) [43];

2. local light switches (Au/fluorescent polystyrene particles) [44, 45];

3. microscopic probe devices to study the physicochemical environment in organic surface chemistry [46];

4. biomedical imaging applications (combination of of the magnetically active part (Fe_3O_4, FePt) and the noble metal(Au, Ag) that exhibit strong surface plasmon resonance absorption) [47–49];

5. targeting cancer cells (Fe_2O_3 and semiconductor nanocrystal or quantum dot (CdSe)) [50–52];

6. catalysis (Au- Fe_3O_4 nanoparticles) [53–55].

Janus nanoparticles provide the possibility not only to combine various functionalities but also to tune them. Interfacial interactions in these systems lead to changes in the physical and chemical properties of the separated single-phase nanoparticles such as surface plasmon absorption [56, 57] and magnetic properties [56, 58].
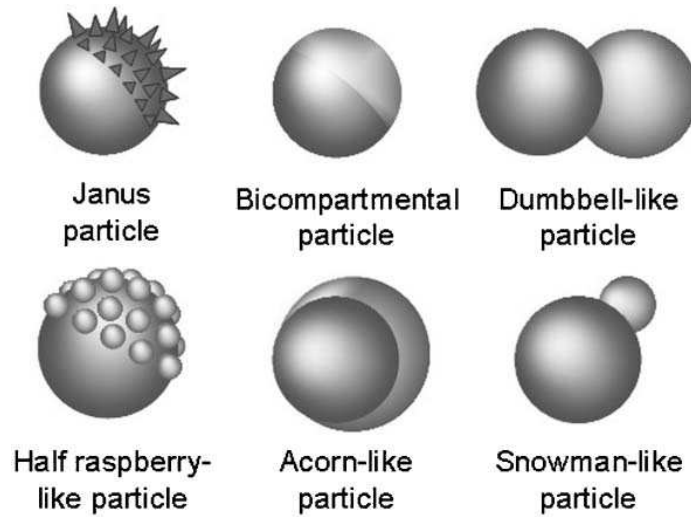
Figure 1.19: Schematic representation of Janus nanoparticles (Note: spheres and diamonds symbolise particles and chemical functions, respectively). Taken from [42]

1.8 Stabilization of $L1_0$ ordered phase in FePt nanoparticles.

1.8.1 General properties of Fe-Pt alloys.

Fe-Pt phase diagram. The equilibrium phase diagram of the Fe-Pt system is shown in Fig.1.20. The high temperature phase is a chemically disordered fcc solid solution A1 phase. At temperatures below 1300 ^{o}C, Fe-Pt alloys with Pt concentrations close to 35-55 at.% exhibit an disorder-order transformation from the A1-type structure to the $L1_0$-type superstructure. This phase is chemically ordered and its crystal lattice in case of perfect equiatomic stoichiometry ($Fe_{50}Pt_{50}$) consists of Fe and Pt planes stacked in [001] crystal orientation. As the difference between atomic radii of Fe and Pt is about 10%, the compression of the crystal lattice in the stacking direction occurs during disorder-order transition, resulting in face centered tetragonal (fct) lattice. The $L1_0$ phase is thus characterized by two different lattice constants a and c. A1 and $L1_0$ crystal structures are shown in Fig.1.21.
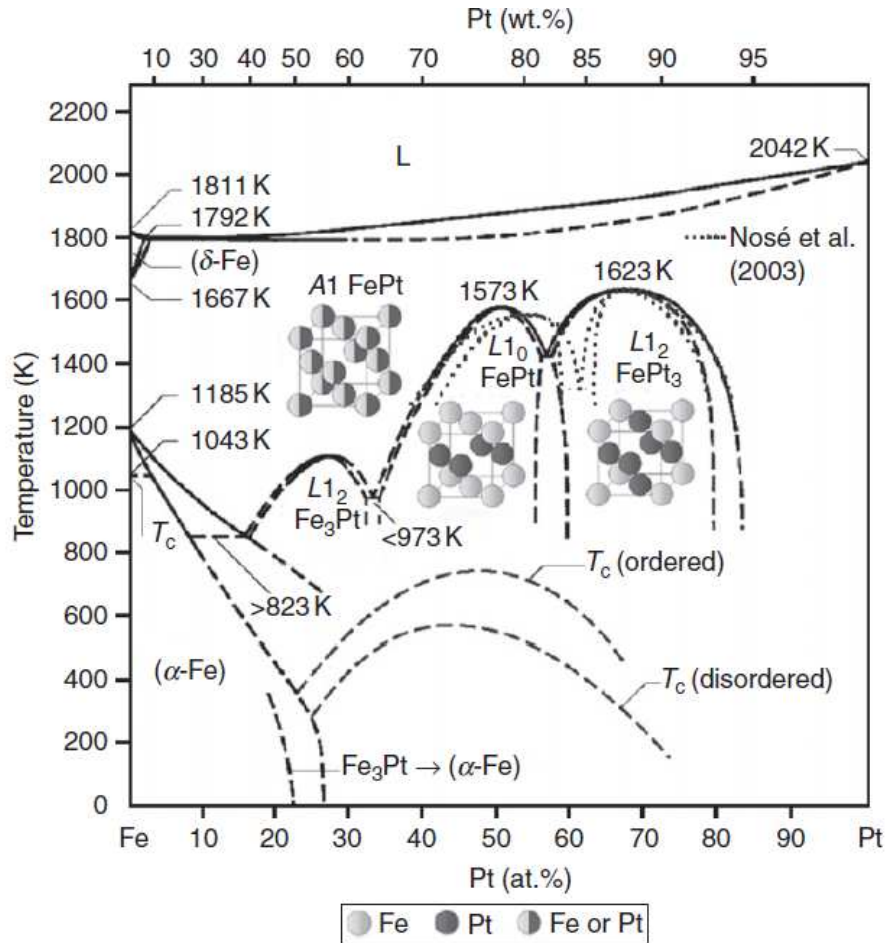
Figure 1.20: Equilibrium phase diagram of the Fe-Pt system (taken from [4], chapter 5). Crystallographic structures of the corresponding phases are shown schematically.

The lattice constants along with tetragonal distortion ratio *c/a* depend on both alloy concentration and degree of ordering (see below). In fully ordered $Fe_{50}Pt_{50}$ alloy a=0.385 nm, c=0.371 nm and *c/a*=0.96; in a disordered $Fe_{50}Pt_{50}$ alloy a=0.380 nm. The *c/a* ratio in $L1_0$-ordered FePt alloys varies from 0.96 to 0.98 ([60–62]).

Chemical ordering in FePt. A perfectly $L1_0$-type ordered FePt alloy consists of consecutive Fe and Pt planes with Pt atoms occupying (0 0 0) and ($\frac{1}{2}$ $\frac{1}{2}$ 0) sites and Fe atoms occupying ($\frac{1}{2}$ 0 $\frac{1}{2}$) and (0 $\frac{1}{2}$ $\frac{1}{2}$) sites. The degree of ordering is characterized by the fractions
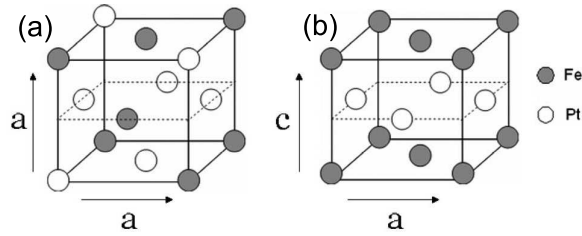
Figure 1.21: Crystal phases of Fe-Pt. (a) A1, chemically disordered face centered cubic phase. (b) L1$_0$, chemically ordered face centered tetragonal phase. (Taken from [59].)

of Fe and Pt sites (r_{Fe} and r_{Pt}, respectively) occupied by the correct atom. The degree of long-range chemical order S is defined as [63]:

$$S = r_{Pt} + r_{Fe} - 1 = (r_{Pt} - c_{Pt})/y_{Fe} = (r_{Fe} - c_{Fe})/y_{Pt}, \qquad (1.26)$$

where $c_{Pt(Fe)}$ is the fraction of Pt(Fe) atoms $y_{Pt(Fe)}$ is the fraction of Pt(Fe) sites. If ordering is perfect, $S=1$, while in case of full disorder $S=0$. For non-stoichiometric alloys S is always less than 1 and its maximum value is a function of alloy composition defined as $S = 1 - 2|\Delta x|$, where Δx is a deviation of atom fraction from 0.5.

Determination of long-range order parameter by powder diffraction.
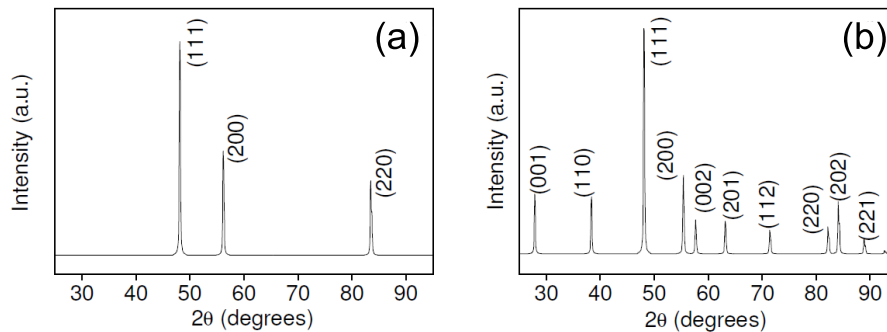
Figure 1.22: Calculated x-ray diffraction patterns for (a) disordered A1 Fe-Pt and (b) completely ordered L1$_0$ Fe-Pt phase. (Taken from [64].)

Powder diffraction is often used to determine the long-range order parameter in L1$_0$-

type structure. Fig.1.22 (a) shows a calculated x-ray diffraction pattern for the fully disordered A1 Fe-Pt alloy. The A1 phase produces fundamental reflections (111), (200) and (220). Ordering leads to the splitting of the fundamental reflections and produces additional superstructure reflections (001), (110), (201), (112) and (221).

The long-range order parameter can be estimated as [63]:

$$S = (\frac{I_s/I_f}{I_s^0/I_f^0})^{\frac{1}{2}}, \tag{1.27}$$

where I_s and I_f are the intensities of the superstructure and and corresponding fundamental peaks, respectively, and $I^0{}_s$ and $I^0{}_f$ are the corresponding intensities in case of the completely ordered alloy of the same composition.

Magnetic properties. Pt metal is paramagnetic. In the FePt, Pt atoms carry an induced magnetic moment, while the magnetic moment of Fe-sites is enhanced compared to bcc Fe. In $Fe_{50}Pt_{50}$ the values of total magnetic moments of Fe and Pt sites are μ_t(Fe)=2.83μ_B and μ_t(Pt)=0.41μ_B ([64] and [4], chapter 5. Enhanced magnetic moments along with large values of magnetocrystalline anisotropy are associated with the hybridization of Fe *3d* and Pt *5d* states and the large spin-orbit coupling in Pt [65]. The magnetocrystalline anisotropy is closely connected to the symmetry of the tetragonal lattice as well as chemical ordering, which increases linearly with the long range order parameter according to [66–68] and [69]. However, a lattice tetragonal distortion is caused by ordering itself, so it is not entirely clear how to separate their influences on anisotropy ([64]).

The Curie temperature T_c depends on the exchange interactions between the atoms, which, in turn, depend on the number of different types of nearest-neighbors atomic pairs and the distance between the atoms. Therefore, T_c is influenced by both chemical ordering [68, 70] and alloy composition [64, 71–73]. The dependence of Curie temperature on alloy composition [73] is shown on the Fe-Pt phase diagram in Fig.1.20. T_c of the ordered alloys reaches maximum (750K) near equiatomic composition, while the maximum of T_c for the disordered alloys (585 K) lies near 40 at.% Pt. The values of T_c estimated in various works (see [4], Table 5.4) are scattered, as might be attributed to different degrees of order in the

measured alloys. The Curie temperature is sensitive to chemical ordering within the alloy, as was shown by Rong et al. [70], and increases with increasing degree of order.

Unlike the Curie temperature, the saturation magnetization M_s of $L1_0$ FePt alloys was reported to be independent of the degree of order at fixed alloy composition. The total magnetization was found to increase with increasing content of Fe [67, 68].

1.8.2 Gas-phase $L1_0$-ordered FePt nanoparticles.

Structure and morphology.
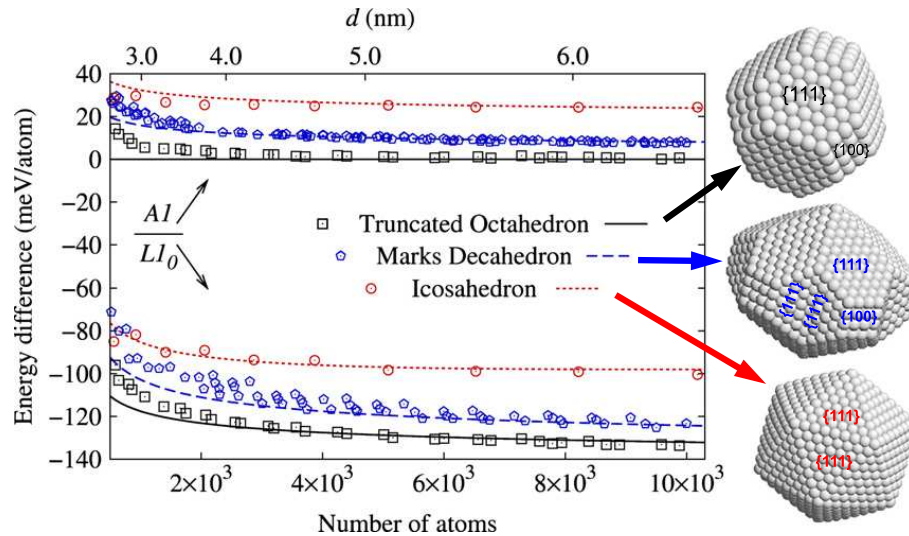
Figure 1.23: Average potential energies for disordered and $L1_0$ ordered FePt particles in different morphologies.(Adapted from [5].)

Due to the large contribution of the surface energy to the total energy, the structures of FePt nanoparticles significantly differ from the bulk alloy. In order to minimize the surface energy the FePt nanoparticles tend to possess the morphologies with densely packed $\{111\}$ facets which exhibit the lowest surface energy [74]. Müller et al. [5] studied size and morphology dependence of the total energy in equiatomic FePt particles. Fig.1.23 shows calculated size dependence of the averaged potential energy for A1-disordered and $L1_0$-

ordered FePt nanoparticles of different morphologies, namely truncated octahedron, Marks decahedron and icosahedron. Truncated octahedra particles are single crystal. Icosahedral particles are multi-twinned and consist of 12 tetrahedra and each tetrahedron forms 72° twin-boundaries with every neighbor. A decahedron consists of five regular tetrahedra sharing a common edge in [110] direction and each contributing two {111} facets to the surface of the decahedron. A more energetically favorable shape (Marks decahedron) is obtained by truncating the decahedron along the edges, exposing {100} and {111} facets. Fig.1.23 demonstrates that for both A1 and $L1_0$ phase the truncated octahedron is the most stable structure. However, the energy difference between different shapes is greatly reduced in small clusters.

The morphologies of the gas-phase prepared particles are expected to be close to theoretical predictions. Indeed, icosahedral and decahedral multi-twinned structures are frequently observed for small particles(less than 8 nm) [7, 60, 75–82].

Theoretical calculations also predict that the stability of the tetragonal $L1_0$ phase significantly decreases with decreasing particle size [83]. This effect is enhanced if segregation of Pt atoms takes place. Several studies confirmed the existence of a critical particle size below which the formation of the $L1_0$ phase is not possible. In reference [84], the order parameter S sharply drops below d = 3 nm and decreases to zero for d $\leq$ 2 nm, while in FePt nanoparticles investigated in [85] and [86], the ordering did not proceed when the particle size was smaller than 4 nm. The indication of segregation of Pt to the surface of nanoparticles was found in [80] and [81], where HRTEM analysis of FePt icosahedral particles showed significant expansion of the lattice constant in the surface layers due to the local Pt enrichment. A similar surface lattice relaxation was observed in single-crystal $L1_0$-ordered FePt particles and attributed to Pt segregation towards the Pt surface ([4], reference *Pohl et al.(2010)*).

Another complication arises from the fact that many of the nanoparticles preparation techniques are kinetically controlled, so initially, the fcc disordered phase is formed and additional annealing is required. Also, the nucleation sites are required for the ordering to

originate. In FePt, thin-film grain boundaries and crystal defects serve as such nucleations sites for the phase transformation. However, small FePt nanoparticles do neither have conventional grain boundaries nor defects.

Magnetic properties.

In order to apply the FePt nanoparticles as a perpendicular magnetic recording media, the following features of their hysteresis loop are required [59]:

1. unity remanent squareness M_r/M_s,

2. unity slope at coercivity point (dM/dH),

3. relatively large negative nucleation field $H_n \leq 2000$ Oe,

4. small switching field distribution $\Delta H_k/H_k \sim 5\%$,

5. high coercivity (CoPtCr alloys, which are currently used as magnetic recording media, have a coercive field of 14 kOe [87]),

6. high saturation field (CoPtCr alloys have a saturation magnetization of 300 emu/cm^3).

Gas-phase prepared FePt particles often possess low coercivity and hysteresis loops with poor squareness and a broad switching field distribution (i.e. non-rectangular shape). This is attributed to:

(a) a number of different morphologies of the particles with large a fraction of multi-twinned particles. Zhang et al. [88] calculated the anisotropy distribution in the twinned FePt particles and found that the averaged anisotropy field of a twinned structure is much smaller than that of the single-crystal.

(b) Inhomogeneous alloying in the particles, leading to the presence of several phases with different degree of order (confirmed in EXAFS measurements by Antoniak et al. [89]).

(c) Aforementioned reduced thermodynamical stability of the tetragonal $L1_0$ phase in small particles and Pt segregation to the surface [80, 83–86].

Several methods to enhance the $L1_0$ ordering in gas-phase FePt nanoparticles were proposed.

Post-deposition annealing. Castaldi et al. [90] deposited equiatomic FePt particles by electron-beam co-evaporation of Fe and Pt on Si substrates, at substrate temperatures T_s between 300 and 700°C. The highest coercive field (measured at room temperature) of 10 kOe was obtained for the sample deposited on a substrate held at 600°C. However, the particle-size varied from 2 to 40 nm. Ito et al. [91] have prepared FePt octahedral particles by sputtering. The particles were deposited onto a MgO(001) substrate with pre-deposited MgO film. During deposition of nanoparticles, the substrate was held at 780°C. The room temperature coercivities of the samples with various thicknesses of MgO film varied near 60 kOe. The average particles size varied from 10 to 20 nm. Size distributions were not presented in the paper, however SEM and TEM images show that particle were agglomerated. To preserve uniformity of particles size, Elkins et. al [92] mixed as-prepared fcc FePt particles with salt powders and annealed them at 700°C. Later, the samples were washed in water and salts were removed from the particles. Coercivities up to 30 kOe were obtained, however the shape of hysteresis loops was not rectangular and showed kinks and relatively low saturation magnetizations. The large fractions of polycrystalline particles were found in the annealed samples.

In-flight annealing. Authors of [77, 93, 94] implemented an in-flight heating stage into the experimental setup to avoid post-deposition annealing. FePt particles prepared by magnetron sputtering were heated by four quartz halogen projector bulbs before deposition onto a Si substrate [94]. While the particles size distribution remained relatively narrow (4-12 nm), the coercive field was found to be significantly lower (2500 Oe at room temperature) than those discussed above. Chen et al. [93] prepared FePt particles by magnetron sputtering varying the temperature of the particle-forming chamber and the temperature of the in-flight annealing stage. They found that both parameters affected the microstructure

and magnetic properties. The FePt particles annealed at 800^oC possessed improved crystallinity and an enhanced coercive field compared to particles prepared without in-flight heating. Still, even the highest coercive field was quite low (600 Oe) and several different particle-morphologies were present in the samples. Rellinghaus et al. [77] studied the effect of in-flight annealing on the magnetic and structural properties of equiatomic FePt particles prepared by magnetron sputtering with various gas pressures. Particles prepared at low pressure (p_{prep}=0.5 mbar) possessed icosahedral multi-twinned structure and even the highest annealing temperatures could not suppress the twin formation. As a result, the particles remained superparamagnetic at room temperature. Particles prepared at p_{prep}=1.5 mbar transformed to the $L1_0$ ordered phase, with coercive field of 2500 Oe at room temperature, after annealing. However, increasing the gas pressure also lead to a broadening of the size-distribution.

Results discussed above show that while in-flight annealing allows the FePt particles to preserve a narrow size distribution, it provides only a slight enhancement of magnetic anisotropy. Probably, the time that the particle spends in the heating stage is not sufficient to suppress twinned structure formation and induce full $L1_0$ ordering.
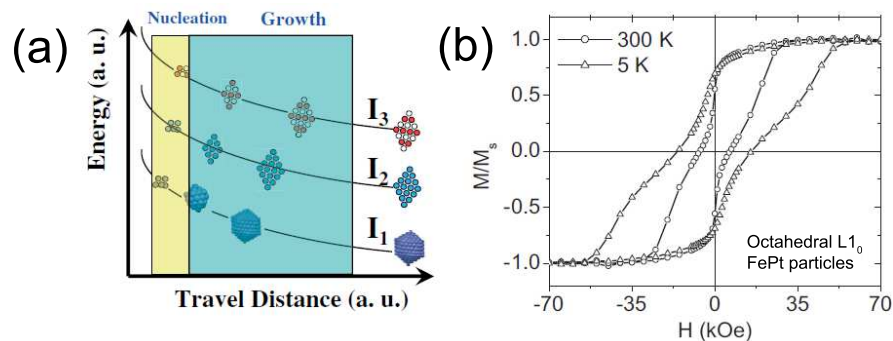
Control of plasma parameters.

Figure 1.24: FePt prepared by magnetron sputtering in [76] (details discussed in the text). (a)Schematic overview of particles morphologies prepared at different discharge currents (I1<I2<I3). (b)Magnetic hysteresis loops of octahedral $L1_0$ FePt nanoparticles measured at both 300 K ($\circ$) and 5 K ($\triangle$).

An alternative way to prepare the $L1_0$ ordered FePt nanoparticles is to control the thermal environment during the nucleation and growth stage [59, 76]. Qiu et al. [76] tuned the FePt morphologies by regulating the magnetron discharge current,and thus manipulating the density of the magnetron plasma. The density of magnetron plasma determines the density and energy of argon atoms and therefore the energy of sputtered metal atoms. High discharge currents provide more dense plasma and higher argon energies. Sputtered metal atoms gain more energy from the argon atoms and, as a result the surface growth proceeds at elevated temperatures. Additionally, the energy dissipation rate of the metal atoms is reduced which results in a slower cooling rate. The overview of the particle-structures prepared in reference [76] is shown in Fig.1.24(a). Increasing the discharge current leads to a suppression of the icosahedral twinned structure and induces the $L1_0$ ordering. The hysteresis loops of the octahedral $L1_0$ FePt particles is presented in Fig.1.24(b). The "wasp-waisted"shape of the hysteresis loop indicates the presence of disordered and ordered particles, which reverse at different magnetic fields.

Liu and Wang [7, 59] assumed that the coexistence of ordered and disordered phases comes from the non-uniformity of the thermal environment during the formation of particles caused by the toroidal shape of the plasma in a conventional magnetron sputtering setups. In order to adjust the surface magnetic field distribution and, thus, the plasma shape, they put a soft iron ring and a cone piece on the alloy target (Fig.1.25(a,b)). Iron was used because of its high permeability value (Fig.1.25(c,d)). The high-resolution TEM image of the octahedral $L1_0$ FePt nanoparticle along with the hysteresis loop measured at room temperature are shown in Fig.1.25(e,f). The particles exhibit a high coercivity of 8.25 kOe and a relatively good squareness. The small kink on the loop is still observed and might be attributed to a remaining fraction of disordered particles or to the influence of surface anisotropy [8].

Reactive sputtering. A further method used to stabilize the $L1_0$ phase in FePt nanoparticles is sputtering in the presence of oxygen or nitrogen.

Oxygen has two main effects on the surface of fcc metals:
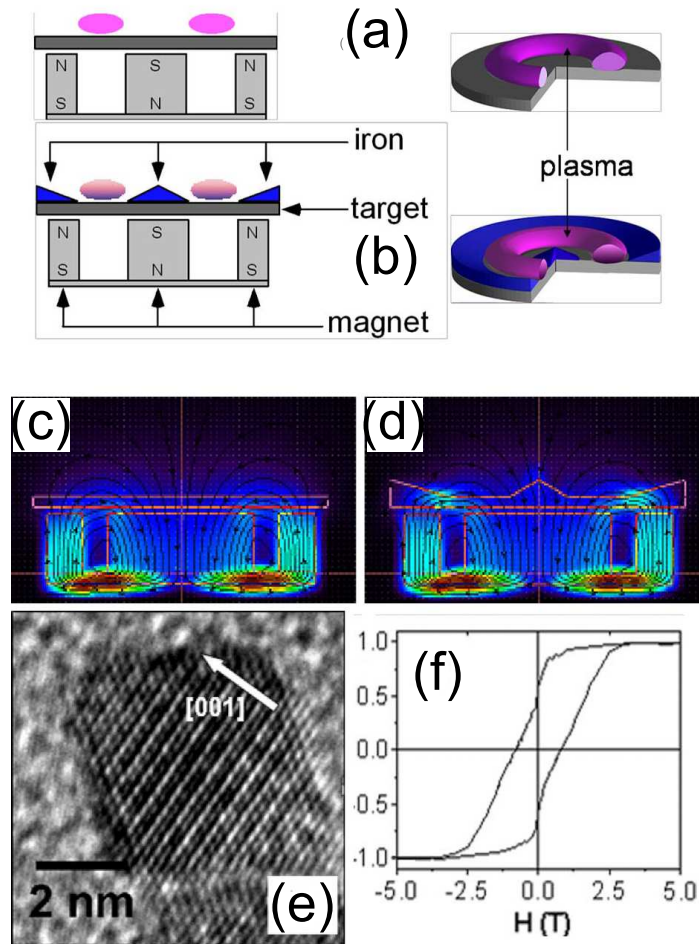
Figure 1.25: FePt prepared by magnetron sputtering in [59]. (a),(b) Schematic illustrations of the modification of the sputter gun head. (c),(d) Magnetic field distribution of the magnetron configurations shown in (a) and (b), respectively. (e) High-resolution TEM image of an octahedral FePt nanoparticle. (f) Corresponding hysteresis loop measured at 300 K.

1. oxygen increases the activation energy for surface diffusion (for example, in Cu and Pt [96, 97]);

2. oxygen can also reduce the surface free energy of metals (for example, Cu, γ-Fe, Ni [97–99]).
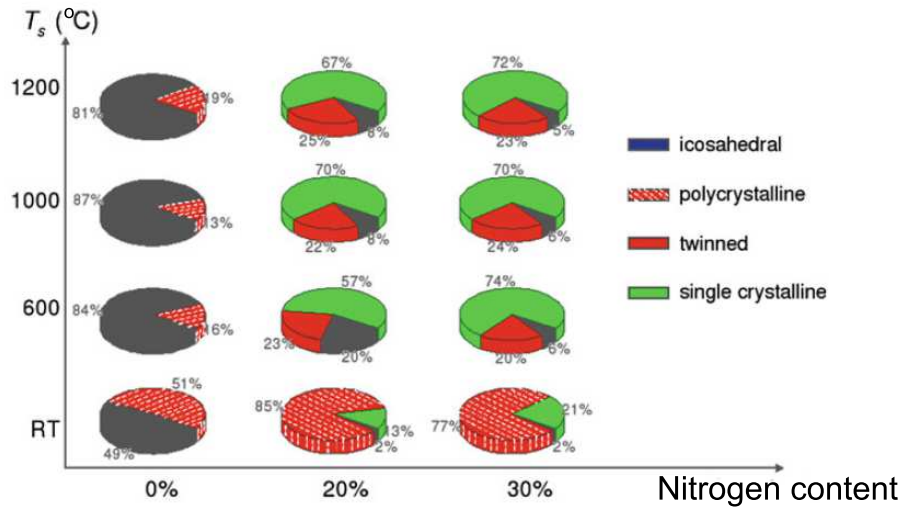
Figure 1.26: The morphology diagram of FePt nanoparticles prepared by reactive nitrogen sputtering in [75, 95].

Effect (1) decreases the average particle size, while effect (2) suppresses the formation of the twin structure. Stappert et al. [79] prepared FePt particles by magnetron sputtering (p_{prep}=1.0 mbar) adding different amounts of oxygen to the gas mixture. The particles were also annealed in-flight at 600° C. They found that at high oxygen concentration (6.6 % of gas mixture), the twin structure was almost completely suppressed and the majority of FePt nanoparticles had a cuboctahedral morphology and single crystal fcc structure. However, the formation of the $L1_0$ phase was not observed.

If nitrogen is introduced into FePt nanoparticles during their growth (nitriding), it will be incorporated in the octahedral interstitial sites of the crystal lattice. During in-flight annealing nitrogen will effuse out of the particles agitating the lattice and enhancing the mobility of Fe and Pt atoms. This effect induces the formation of the $L1_0$ phase. Dmitrieva et al. [75, 95] prepared FePt nanoparticles at p_{prep}=0.5 mbar at various annealing temperatures. They showed that after adding nitrogen to the gas mixture a significant fraction of FePt particles were single-crystal (see Fig.1.26). The authors estimated that approximately 70 % of single-crystal and polycrystalline particles had $L1_0$ structure.

1.8.3 Stabilization of L10 phase in gas-phase FePt nanoparticles by adding a substitutional element.

Several works explored the influence of the third element on the structural and magnetic properties of FePt alloys, thin films and nanoparticles.

FePt-M (M=P, B, Pd, Cu) alloys. Kündig et al. [100] studied the properties of $Fe_{35}Pt_{35}P_{30}$ alloy prepared by melt spinning. In the as-prepared state it consisted of A1 FePt and PtP_2 phases. Annealing led to a microstructure consisting of the $L1_0$ and paramagnetic PtP_2 phases with increased coercivity (about 25 kOe). $Fe_{80-x}Pt_xB_{20}$ amorphous alloys prepared by rapid quenching ([101]) and subsequently annealed at 798 K were found to be consist of $L1_0$ FePt, A1 FePt and Fe_2B phases with average grain size of the phases of about 20 nm.
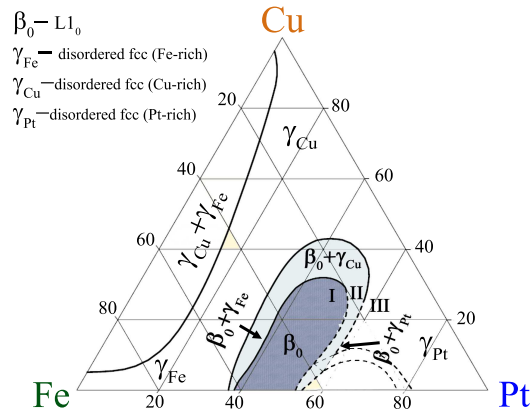
Figure 1.27: Isothermal sections of the phase diagram for iron-platinum-copper alloys at 1000^oC (adapted from [102]). The axes are labelled in at.%.

Willoughby et al. [103] reported the positive energy of mixing in bulk Fe-Pt-Pd alloy. However homogeneous Fe-Pt-Pd alloy thin films and particles were prepared (see below). Lyubina et al. [104] showed that it is possible to obtain high amounts of $L1_0$ phase in such alloys. In Fe-Pd alloys the A1 to $L1_0$ transformation starts at higher temperature which results in a lower driving force for the formation of the $L1_0$ phase. However, the migration

enthalpy for atoms is lower than in Fe-Pt alloys and the growth of the $L1_0$ phase proceeds faster.

The Fe-Pt-Cu alloy has a negative energy of mixing almost in the whole concentration range [105]. The isothermal section of the ternary phase diagram of Fe-Pt-Cu alloys at 1000^oC is shown in Fig.1.27.

Effect of underlayer on FePt films. Hu et. al [106] prepared FePt thin films with MgO underlayer by magnetron sputtering at 300^oC with subsequent annealing at temperatures from 200 to 350^oC. The observed increase of the coercivity (from 5 to 10 kOe) after annealing was attributed to a diffusion of MgO from the underlayer through FePt grain boundaries. Zhu et. al [107] demonstrated the reduction of the ordering temperature in 5 nm thick FePt films with 9 nm equiatomic AuCu underlayer. Xu et. al [108] compared the influence of Ag and Cu underlayers on the magnetic properties of FePt films prepared by magnetron sputtering and annealed at 550^oC. While Cu had little effect on the FePt coercivity, an Ag underlayer was able to reduce the ordering temperature and increase the coercivity of the FePt film up to 10 kOe. Authors attributed it to an expansion of the FePt unit cell induced by Ag. However, other works [109–112] showed that a Cu underlayer is capable to reduce the ordering temperature, induce the $L1_0$ phase formation and increase FePt coercivity. The Cu underlayer effect on FePt coercivity is attributed to the diffusion of Cu into FePt layer creating crystal defects which serve as additional sites for $L1_0$ growth. The effect also depends on the relative thickness of layers and the epitaxial relationship between Cu and FePt layers.

FePt-X films and nanoparticles. In [113] B. Wang systematically studied the influence of various additives (Au, Ag, Ni, Cu, Mn, Mg, V, and B) in FePt films (with varying Pt and additive concentrations) on A1 to $L1_0$ transformation. Several parameters (kinetic ordering temperature, transformation enthalpy, transformation activation energy and Curie temperature) were measured for $L1_0$ ternary and binary films. The results showed that all additions except Cu lead to an increase of kinetic ordering temperature compared to the binary films with the same Pt concentration. The transformation enthalpy was found to

be unaffected by additives except for the case of Au. Adding Ni, Mn, V and B increased the activation energy, while the rest of the additives had no effect on it. Ni, Cu, Mn and Mg lowered the Curie temperature of the ternary film, while in case of other additives it remained unchanged.

Barmak and Berry [71] conducted similar research for FePt-Ni and FePt-Cu alloys. They found that both Cu (up to 20 at.%) and Ni (up to 25 at.%) lower the Curie temperature of the $L1_0$ alloys. Cu had no effect on the kinetic ordering temperature, while addition of Ni increased it. Both additives increased the activation energy of A1 to $L1_0$ transformation, while having no effect on the transformation enthalpy.

The magnetic properties of $Fe_{55-x}Ni_xPt_{45}$ ($0 \leqslant x \leqslant 55$ at.%) alloy films were studied by Thiele et. al [114]. Films were epitaxially grown on single crystal MgO(100) substrates at 550^oC. The Curie temperatures decreased with increasing Ni concentration. The magnetocrystalline anisotropy energy density K stayed constant up to x=10 at.% and then dropped rapidly from 4.6×10^7 erg/cm^3 to 0.6×10^7 erg/cm^3 at x=15 at.% followed by a steady decrease with Ni content.

Kanazawa et al. [115] investigated magnetic properties of $FePt_xPd_{1-x}$ ($0 \leqslant x \leqslant 1$) films prepared by magnetron sputtering and subsequently annealed at 400^oC, 500^oC and 600^oC. The coercive fields decreased with increasing Pd content and decreasing annealing temperature.

Platt et al. [116] compared the magnetic behavior of $(FePt)_{1-x}M_x$ (M=Cu, Ag, Au; x = 10,20,30,40) films deposited on Si(100) substrate with MgO buffer layer and subsequently annealed at 350^oC, 450^oC, 550^oC and 650^oC. The coercivities of the films increased with the annealing temperature but were independent on the Ag and Au content, while copper had a significant influence on coercivity (see Fig.1.28). The coercivities of FePt-Ag and FePt-Au films were negligible up to 450^oC, while a FePt-Cu film exhibited high coercivity at 350 and 450^oC, which indicates that the addition of Cu lowers the ordering temperature compared to the binary FePt alloy. The same behavior was reported by Maeda et. al [117] for FePt-Ag and FePt-Cu films prepared by dc sputtering. Films were deposited on glass
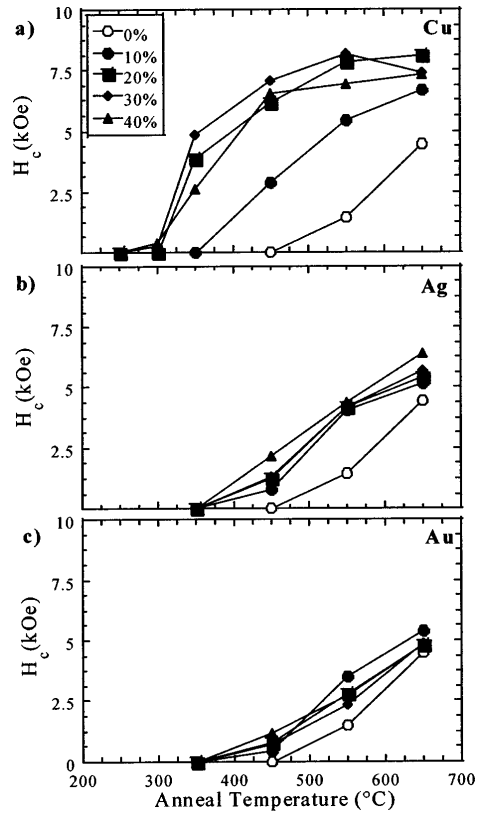
Figure 1.28: Coercive field H_c vs. annealing temperature of (a) FePt-Cu, (b) FePt-Ag and (c) FePt-Au films studied in [116].

substrates and subsequently annealed at temperatures in the 300-700°C range. Fig.1.29,(a) shows the dependence of the coercive field on annealing temperature and shows that Cu reduces the temperature of L1$_0$ ordering, while Ag has no such effect. The dependencies of the coercivity on Cu and Ag concentrations of the films annealed at 300°C is presented in Fig.1.29,(b). The coercive field of the FePtAg films remains constant, while the coercivity of FePtCu films rapidly increases and has a maximum near 15 at.%.

The decrease of the ordering temperature by adding Cu to FePt alloy was also confirmed in [118,119]. Aimuta et. al [118] reported that adding 3 at.% of Ag also leads to a decrease of ordering temperatures which contradicts the aforementioned results.

All works demonstrated that Cu formed a stable ternary alloy with FePt, while Ag (and

Figure 1.29: (a) Coercive field H_c as a function of annealing temperature of FePt, $(FePt)_{85}Cu_{15}$, $(FePt)_{82}Ag_{18}$ f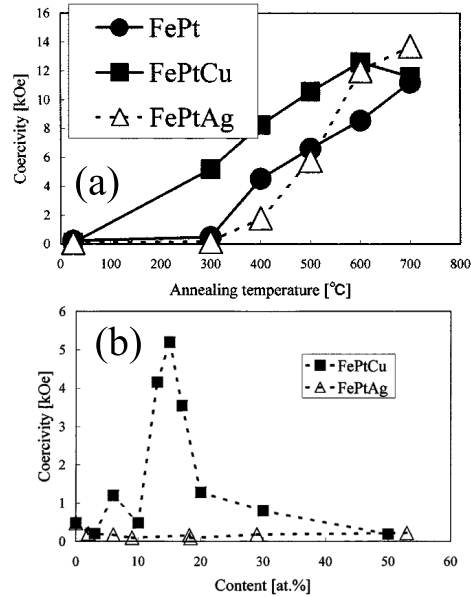ilms. (b)Coercive field H_c of FePtCu and FePtAg films as a function of the content of Cu and Ag after annealing at 300^oC. Taken from [117].

Au) segregated to the surface or to the interface between the substrate and the film after annealing. Aimuta et. al [118] considered the Ag segregation during annealing to be the reason for the reduction of the ordering temperature. The effect of Cu on the ordering temperature can be attributed both to enhanced diffusivity [119] and the smaller Gibbs energy of the FePtCu alloy providing the enhanced driving force for the A1 to $L1_0$ transformation [117].

Theoretical calculations predict segregation in FePt for Cu, Ag and Au with Cu segregation being the weakest [120]. The authors of [120] also found that Cu and Ag substitutions at Fe sites is energetically more favorable than substitutions at Pt sites, while for Au, both cases are approximately equal.

FePt-X particles (X= Cr [121, 122], Co [123], Zr [124], Mn [125], Au [122, 126, 127], Ag [122, 128], Pd [122, 129], Cu [122, 127, 130–136]) exhibit the same behaviour as thin films. The coercive fields increase with the annealing temperature reaching a maximum

near 10 kOe. The concentration dependencies usually have a peak near 20 at.% of additive.

Chapter 2

Experimental techniques

2.1 Magnetron sputtering

All samples were prepared by the inert-gas condensation method based on DC magnetron sputtering. The experimental setup consists of a liquid nitrogen cooled nucleation chamber, a furnace and a deposition chamber. Continuous flow of Ar (sputtering gas) and He is introduced into the nucleation chamber which contains a sputtering target. Primary particles generated in the nucleation chamber travel with the Ar/He gas-flow through a furnace and subsequently are deposited on substrates held at liquid nitrogen temperature. The furnace is operated in the case when in-flight annealing is desired.

The schematic representation of the setup is shown in Fig.2.1. The essential elements are:

1. nucleation chamber equipped with DC sputter gun (SG), sputtering target (T) and cooling shield (CS),

2. in-flight annealing section consisting of quartz tube positioned in a three-zone furnace (F),

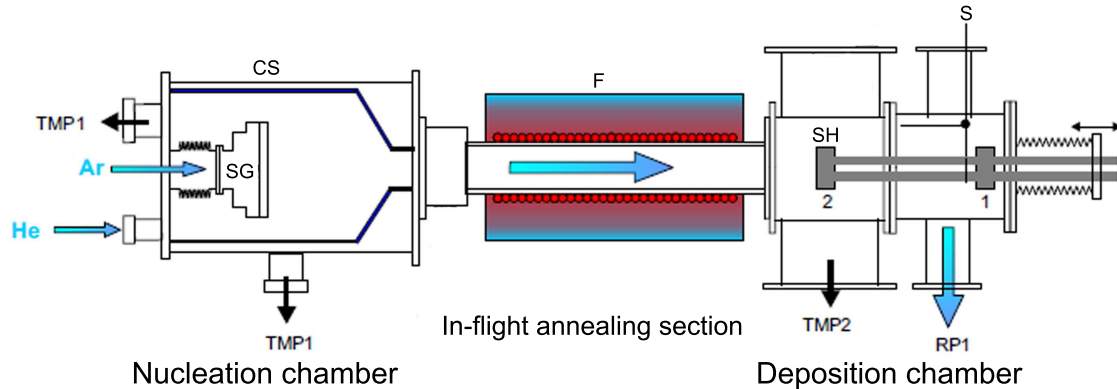3. deposition chamber containing a sample holder (SH).

Figure 2.1: Schematic representation of the experimental setup consisting of nucleation chamber, in-flight annealing section and deposition chamber. Essential components are the DC sputter source (SG), the cooling shield (CS), the three-zone furnace (F), sample holder shutter (S), the sample holder (SH), the turbo-molecular pumps (TMP1 TMP2) and the roots pump (RP1). Adapted from [137].

The gas flow and vacuum system. To avoid contamination of nanoparticles during preparation clean manufacturing conditions are necessary. They are provided by a base pressure in the high vacuum region and the use of high-purity gases.

The vacuum is attained by two turbo-molecular pumping stations (TMP1 and TMP2) connected to the nucleation and deposition chambers. They produce a base pressure of $p_{base} \leq 10^{-7}$ mbar. During sample preparation continuous flow of gas is created by the roots pump connected to the deposition chamber. To prevent oil from entering the deposition chamber a cold trap cooled with liquid nitrogen is placed between the pump and the chamber.

High-purity (99.999%) Ar and He gases are introduced into the nucleation chamber during preparation. The gas control system consists of a capacitive pressure sensor and a total of four mass flow controllers. Argon is introduced through the inlet in the sputtering source, so it flows directly over the sputtering target. Helium is introduced through the additional inlet (see Fig.2.1). The total gas pressure is set by changing the pumping capacity of the roots pump through a control valve situated between the pump and the deposition cham-

ber. For a more detailed description of the gas control system, see reference [137]). The actual volume flow of the gas $f_{Nucleation}$ in the nucleation chamber depends on the gas pressure so that $f_{Nucleation} = f_{set} \frac{1bar}{p_{sputter}}$, where f_{set} is the gas flow at atmospheric pressure and $p_{sputter}$ is the gas pressure. The volume flow in the furnace $f_{furnace}$ increases by a factor of $T_{furnace}/293$ K with increasing temperature, so it is defined as $f_{furnace} = f_{set} \frac{1bar}{p_{sputter}} \frac{T_{furnace}}{293K}$.

Nucleation chamber.
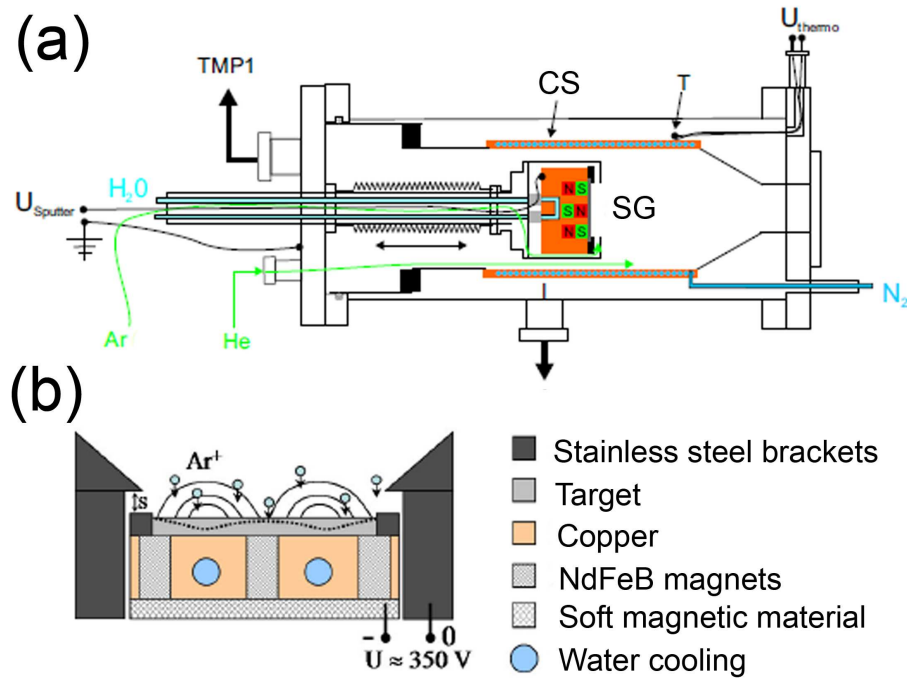
Figure 2.2: (a) Schematic representation of the nucleation chamber [137].(b) Schematic illustration of the magnetron sputtering gun. The color-coded areas are explained in the right image. The dashed line shows the sputter erosion profile of the sputter target. The black lines show the magnetic field lines. Adapted from [95].

The schematic representation of the nucleation chamber is shown in Fig.2.2(a). It contains the magnetron sputtering gun SG (type AJA A320) operated in DC mode. The schematic illustration of the sputtering gun is shown in Fig.2.2(b). The arrangement of the Nd-Fe-B magnets is chosen to provide an efficient sputter yield for magnetic materials.

The inner part of the nucleation chamber consists of copper blocks incorporated between the magnets and the target holder. A negative voltage of about 350 V is applied between the target and the outer sheath which is grounded. The gap width s between the target holder and the sheath is approximately 2 mm. The sputtering gas (argon) is introduced directly to the sputtering source. The gas molecules are ionized in the plasma of the sputter source, and the argon ions are accelerated in an electric field towards the target. The measured current is about 0.7 A. Thus, the sputtering power is about 250 W. In order to avoid the heating of the target and the magnets and the copper block are cooled with water.

During sputtering, the gas mixture is cooled by the liquid nitrogen shielding. This leads to supersaturation and nucleation. The shield is made of copper in order to ensure optimum thermal conductivity.

Both the temperature gradient as well as the residence time of the nanoparticles in the cooled area (i.e., the length of the nucleation zone) are important parameters for the particle growth process. In order to vary the length of the nucleation zone, the position of the sputtering source can be changed. To enable this, the sputtering source is attached to a stainless steel bellows tube. The effective length of nucleation zone is the distance from the sputtering target to the end of the cooling plate. It can be varied in the range between 3 cm and 23 cm. In the current work, the nucleation zone length is set to 15 cm.

In-flight annealing section. During in-flight annealing the gas mixture with the primary particles flows through a tube (made of heat-resistant oxide-ceramic material- Degussit AL23) which is located within a three-zone furnace (TZF Carbolite). Annealing temperatures up to 1473 K can be achieved. The inner diameter of the tube is 4.7 cm, and the heated region is 70 cm long. Thus, the volume of gas flowing through the furnace is 1.22 l.

Deposition chamber. After nucleation and in-flight annealing the particles are deposited on a sample holder mounted perpendicular to the direction of gas flow. The sample holder with the substrates is cooled with liquid nitrogen in order to obtain a higher amount of deposition of the particles.

The gas mixture is pumped by a roots pump, so the pressure gradient generated along

the entire route is about 0.2 mbar. Cu grids covered with carbon film (TEM grids) of diameter 3.05 mm and silicon substrates of dimensions 4 x 4 x 0.5 mm^3 with naturally oxidized surface can be attached to the sample holder.

Sputtering targets. Fe-Cu, FePt-Cu and Fe-Ag sputtering targets were manufactured by patching iron or FePt disk targets with diameter 50.8 mm and thickness 1.5 mm with copper or silver pieces of diameter 3 mm inserted into the target. Patches are placed symmetrically in the centre of the iron or FePt erosion zone. The number of patches was calculated to achieve the desired nominal composition of the particles. An image of the Fe-Cu sputtering target is shown is Fig.2.3.

Figure 2.3: Fe-Cu sputtering target.

Calculating time of in-flight annealing. The time that particles spend in the furnace τ_s is calculated as:

$$\tau_s = \frac{V_{furnace}}{f_{furnace}} = \frac{\pi (d_{furnace}/2)^2 l_{furnace}}{f_{set}\frac{1bar}{p_{sputtering}}\frac{T_S}{293K}}, \tag{2.1}$$

where $\mathrm{d}_{furnace}$ = 4.7 cm and $\mathrm{l}_{furnace}$ = 70 cm are the diameter and the length of the

furnace tube, respecively.

2.2 Transmission electron microscopy

Morphological and structural properties of the nanoparticles were studied by means of High Resolution Transmission Electron Microscopy (HRTEM). The elemental analysis was conducted using TEM combined with Energy Dispersive X-ray (EDX) spectroscopy and Energy-Loss Electron Spectroscopy (EELS). The detailed description of these techniques can be found in [138].

2.2.1 High-Resolution Transmission Electron Microscopy (HRTEM)

The essential elements of TEMs are the electron source, the condenser lens system, the sample, the objective lens system, the imaging system and the CCD camera. A schematic of an electron microscope is presented in Fig.2.4.

The electron source is a tungsten or single-crystal LaB_6 cathode (also called electron gun) connected to a high voltage source of typically 100-300 kV. The electrons are ejected from the gun by means of thermionic or field emission and accelerated by the high voltage. The field emission cathodes (or field emission guns, FEG) are more suitable for high resolution measurements as they have have a narrow electron energy spread.

The electron source is placed in the upper part of the microscope. The part below is a microscope column which consists of a set of converging magnetic lenses. The condenser lens system generates a defined beam from the accelerated electrons. It consists of two condenser lenses and two condenser apertures. Below the condenser system two objective lenses are positioned with the sample situated between them. The sample has to be transparent for the electrons, so its maximum thickness should be about 100 nm or less. The electron beam is diffracted by the crystal lattice of the sample. The diffracted beams are focused by the second objective lens in its back focal plane into a diffraction pattern. In the image plane of the objective lens the intermediate image is formed. The spheri-
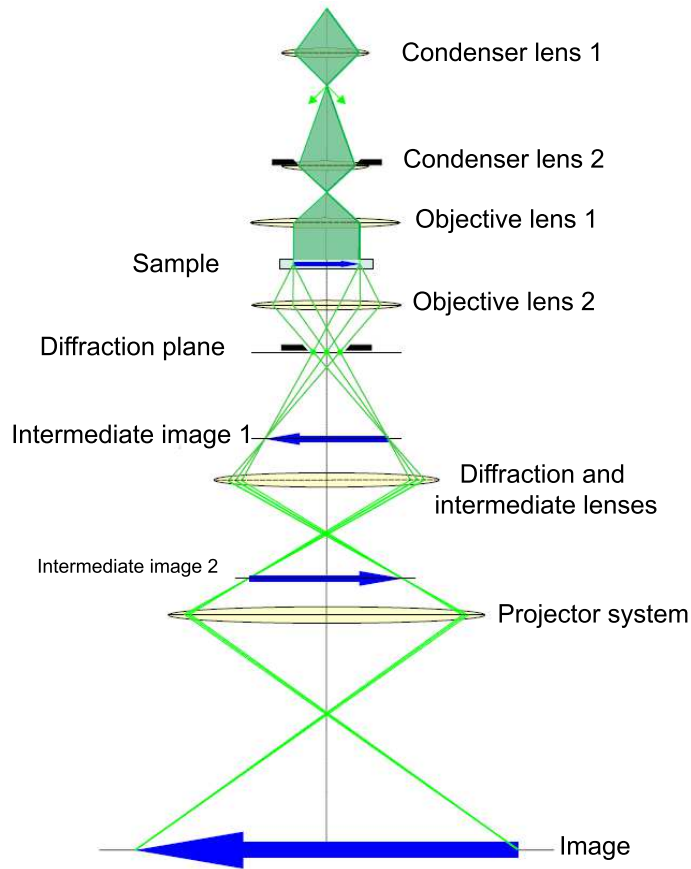
Figure 2.4: A schematic of a transmission electron microscope. Adapted from [137].

cal abberation coefficients C_s of condenser and objective lenses determine the resolution of the microscope. The imaging system consists of intermediate and projector lenses and serves to magnify the diffraction or the intermediate image. The image is projected onto fluorescent screen or CCD camera.

Image formation in the electron microscope

The interaction of an electron wave with a thin specimen results in a change of the amplitude and phase shift of the electron wave. The phase shift occurs due to the difference in inner potential of the material with respect to the vacuum. If an object is thin enough, it

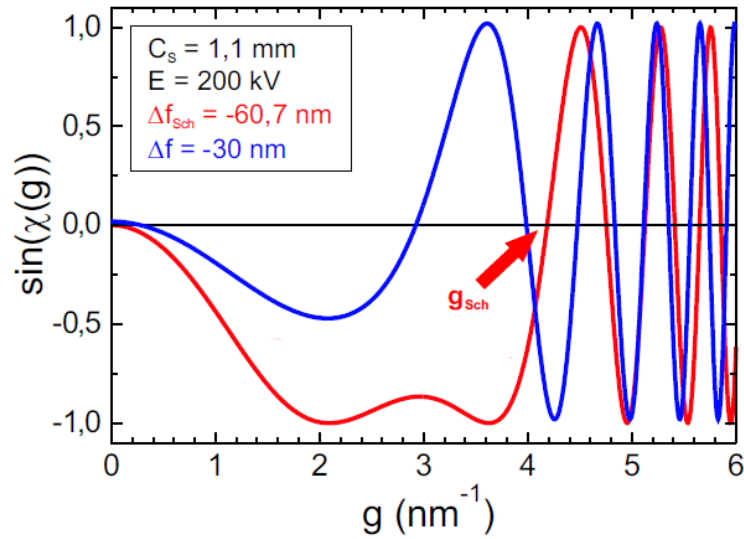Figure 2.5: Phase transfer functions of a microscope with an accelerating voltage of 200 kV and a spherical aberration coefficient C_s = 1.1 mm for two defocus Δf values. Adapted from [137].

only produces a phase shift to the wave at its exit plane and is called a *phase object*. The image contrast produced by such objects is called *phase contrast*.

The HRTEM image quality strongly depends on the imaging system of the microscope. The imaging system is described with the so-called contrast transfer function (CTF) *H(**g**)*, where ***g*** is a spatial frequency in the reciprocal space. The CTF is defined by lens aberration, focus, and apertures and can be expressed as $H(g) = A(g)E(g)2sin\chi(g)$, where A(**g**) is the aperture function, E(**g**) describes properties of the lenses and χ(**g**) is an aberration function (also called phase transfer function). Spherical aberration is the main factor determining image quality. Fig.2.5 shows the phase transfer functions of a microscope with an accelerating voltage of 200 kV and a spherical aberration coefficient C_s = 1.1 mm for two defocus Δf values. Negative values of the phase transfer function correspond to the positive phase contrast, at which the atoms appear dark and the background is bright. For positive values, i.e. a negative phase contrast, the atoms appear bright and the background

is dark. To interpret the HRTEM images, one has to operate in a spatial frequency range in which the phase transfer function does not change sign. In the so-called Scherzer defocus Δf_{Sch} (red curve), the phase transfer function has the same sign at a large spatial frequency range. The point g_{Sch}, where $\sin\chi(\mathbf{g}) = 0$ ($\Delta f = \Delta f_{Sch}$) for the first time, defines the so-called point resolution $1/g_{Sch}$ of the microscope. At $g > g_{Sch}$ the phase contrast transfer function oscillates and the HRTEM image cannot be interpreted.
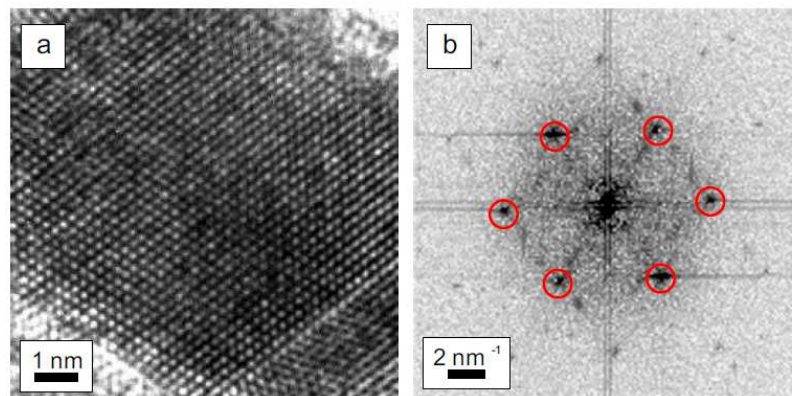
Figure 2.6: (a) HRTEM image of an FePt nanoaprticle with (b) corresponding FFT image. Diffraction spots are marked with red circles. Adapted from [137].

The HRTEM image is taken with a CCD camera and the corresponding fast Fourier-transformed image (FFT) can be calculated. This image corresponds to the diffraction pattern of the sample region in the HRTEM image. The analysis of the FFT image provides the structural information. An example of this is shown in Fig.2.6. The HRTEM image (Fig.2.6 (a)) shows the FePt nanoparticle on an amorphous carbon film. In Fig.2.6 (b) the corresponding FFT image is presented. The reflections marked with red circles can be attributed to the fcc crystal structure of FePt.

Figure 2.7: Electron-specimen interactions in TEM. Taken from [138].

2.2.2 High-Angle Annular Dark-Field Scanning Transmission Electron Microscopy (HAADF-STEM)
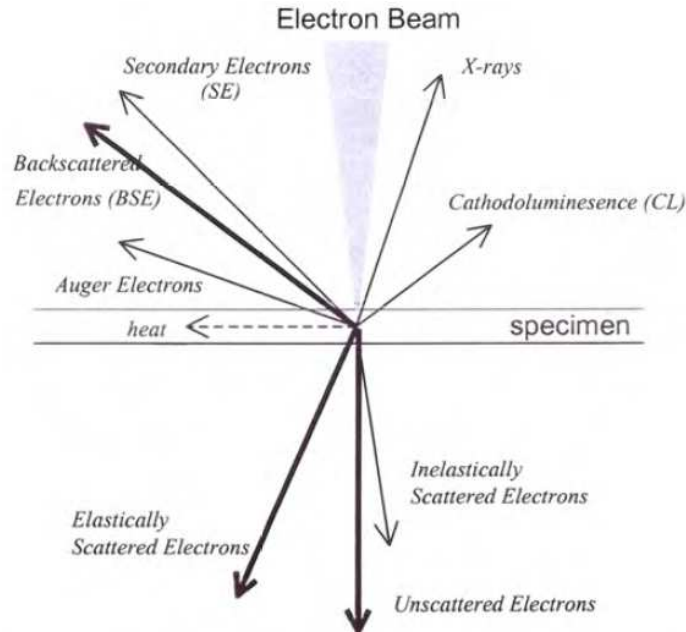
The HAADF-STEM method combines two techniques: high-angle annular dark-field imaging, which is highly sensitive to atomic-number contrast, and scanning electron microscopy.

When an electron enters the specimen it interacts with its atoms. Atomic and nuclear electrostatic potentials affect the speed and/or direction of the electron. If only the direction changes, the electron undergoes *elastic scattering*. In case of *inelastic scattering* the change of speed is involved. The incident electron does not pass its energy to the atom during an elastic scattering process, while the inelastic scattering process involves the energy exchange between the incident electron and the specimen atoms. Other specimen-electron interactions include emission of X-rays, Auger electrons, cathodoluminesence etc. They

are summarized in Fig.2.7.

The bright-field TEM images are produced by electrons scattered elastically through the small angles (so-called Bragg scattering). The bright-field contrast depends both on specimen material, its structure and orientation with respect to the beam. In contrast, HAADF technique provides images produced by electrons scattered at high angles (4-11°). These electrons undergo so-called Rutherford forward scattering which is the consequence of interaction between the electrons and the atomic nuclei of the specimen. The scattering cross section, and thus the contrast in the HAADF images, is directly proportional to Z^2. In other words, HAADF contrast, also called Z-contrast, directly reflects the distribution of chemical elements in the sample.

The STEM technique involves the electron beam being focused down to a small spot ($\leq$ 1 nm) and scanned through the sample. The principal schemaic of the HAADF-STEM is showed in Fig.2.8.

2.2.3 Element specific analysis in TEM

Energy Dispersive X-ray (EDX) Spectroscopy

When an incident electron of the electron beam hits an atom in the specimen, there is a probability to transfer its energy to the electron shell and ionize the atom. The ionised atom now has an electron vacancy in a shell. The electrons in outer levels will jump into this vacancy to restore the stationary state of the atom. During this process, an X-ray with an energy equal to the energy difference between the levels is emitted (Fig.2.9 (a)). Each element has a unique electron shell structure, so the X-rays generated by the specimen are *characteristic*. In other words, the X-rays have specific energies or wavelengths characteristic of elements and are called *characteristic radiation*. Each type of atom produces several peaks in the spectrum corresponding to the transitions between different energy levels. For example, electrons in two of three energy levels in the L shell may jump into the K shell. These are called $K_{\alpha 1}$ and $K_{\alpha 2}$ lines. Jumping to K shell creates K lines, to L
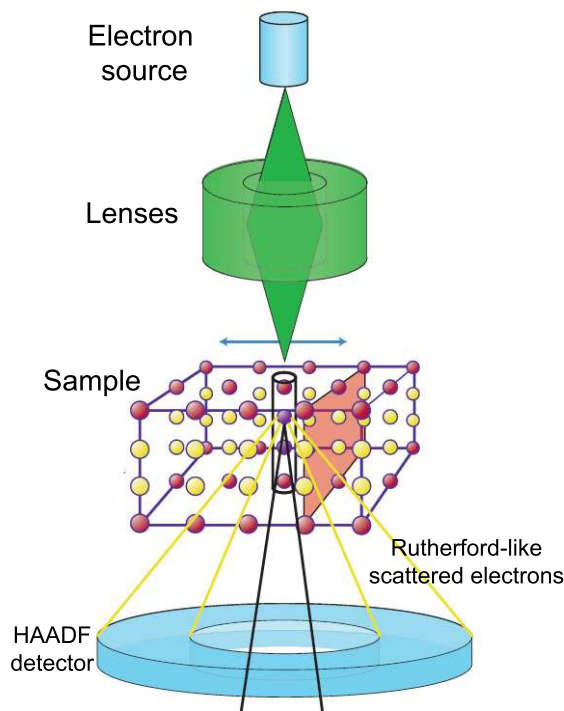
Figure 2.8: Major elements of a scanning transmission electron microscope. Magnetic lenses focus the beam to a small spot size, which is scanned across the sample. Rutherford-like scattered electrons are collected by the high-angular annular dark-field (HAADF) detector. Adapted from [139].

shell creates L lines, and so on. Fig.2.9 (b) shows an EDX spectrum with peaks labeled by the respective elements and electronic transitions. By comparing the weighted integrated intensities of the peaks, the concentration ratio of the elements can be determined.

The X-ray radiation is detected by a side-mounted detector. An X-ray photon is absorbed in the sensitive semiconductor material of the detector and creates a certain number of electron-hole pairs proportional to the energy of the photon. In this work a Si(Li) detector is used with the energy resolution of about 150 eV. The elemental composition can be determined with an accuracy of about $\pm$ 2-3 at.%.

EDX spectroscopy measurements performed in STEM mode also allow to determine the elemental distribution within the sample along a chosen line (so called *line scan*) or to
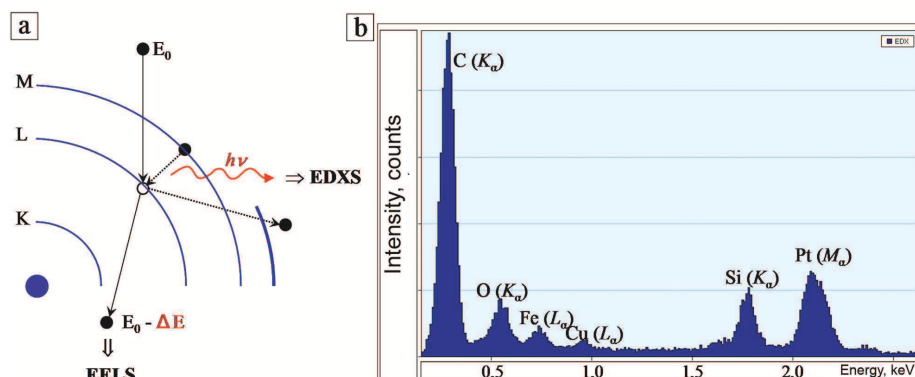
Figure 2.9: (a) Schematic representation of the inelastic interaction between the electron with the initial energy E_0 and an atom. (b) An EDX spectrum. Adapted from [137].

obtain a two dimensional elemental map.

Electron Energy Loss Spectroscopy (EELS)

Electron energy loss spectroscopy (EELS) utilizes the electrons which undergo inelastic scattering and lose energy after the interaction with the specimen. The amount of energy loss, measured using an electron spectrometer, provides information about chemical composition of the sample. In the current work, the Gatan Image Filter (GIF) system is used to obtain and process the spectra. A schematic diagram of the Gatan electron spectrometer is shown in Fig.2.10. The incident electrons are selected by an entrance aperture and pass through a prism magnet. The magnetic prism deflects the electrons through $\geq 90°$ and spatially separates the electrons according to their energies into a electron energy loss spectrum in the energy dispersive plane (a process analogous to the dispersion of white light by a glass prism). A retractable slit and a series of lenses are positioned between the prism and the energy dispersion plane (not shown in the image). The GIF system can be operated in imaging and spectroscopy modes. In the imaging mode the lenses restore the image at the entrance aperture so it can be viewed on a CCD camera. In the spectroscopy mode the energy dispersive plane is projected onto the CCD camera and the EEL spectrum

is acquired.
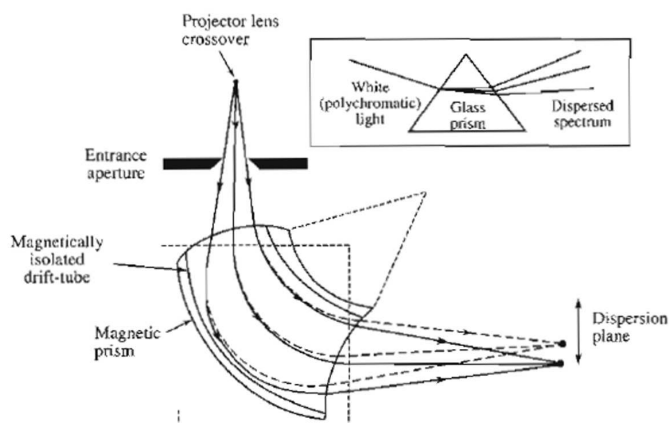
Figure 2.10: Schematic diagram of the Gatan electron spectrometer taken from [138].

An EEL spectrum consists of a distribution of electron counts versus energy loss and has three principal regions:

1. The zero-loss peak, which consists of elastically scattered electrons.

2. The low-loss region ($\leq$ 50 eV) contains plasmon losses and losses associated with the weakly bound outer-shell electrons in the specimen atoms.

3. The high-loss region (100 eV - 2000 eV), which contains electron-loss peaks (also called edges) associated with inner-shell excitations. This is the region which provides the information on the chemical composition of the sample. The high-loss regions of EEL spectra of Fe, Cu and Ag are shown in Fig.2.11.

Energy filtered TEM (EFTEM)

A retractable slit positioned in front of the energy dispersion plane in the GIF spectrometer allows to select electrons with energies within a certain window ΔE (usually,

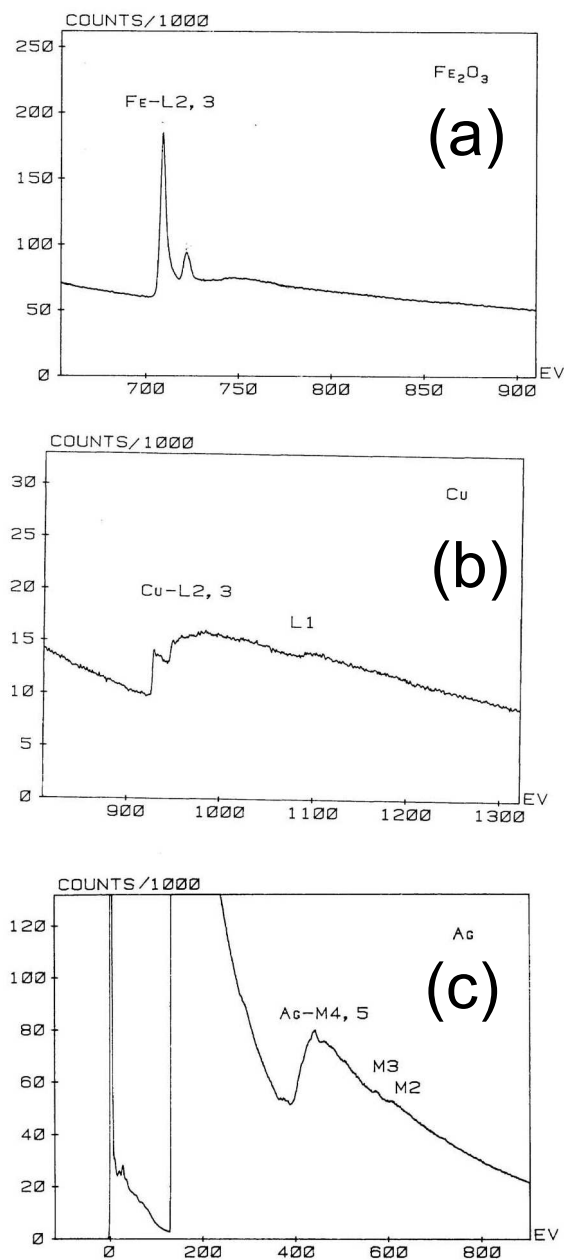Figure 2.11: (a) Fe $L_{2,3}$ (b) Cu $L_{2,3}$ and (c) Ag $M_{4,5}$ EELS edges. Taken from [140].

10-50 eV). The series of multipole lenses allows to reconstruct the image produced exclusively by selected electrons (a filtered image). However, in order to obtain the elemental map, removing the background contribution to the image intensity is crucial. In the current work a three-window method to subtract the background is used. Two energy-filtered background images in front of the ionization edge (pre-edge images) and one image at the edge (post-edge image) of the element of interest are acquired (see Fig.2.12). Afterwards, the extrapolated background image is calculated and subtracted from the ionization edge image. The net image is an elemental map.
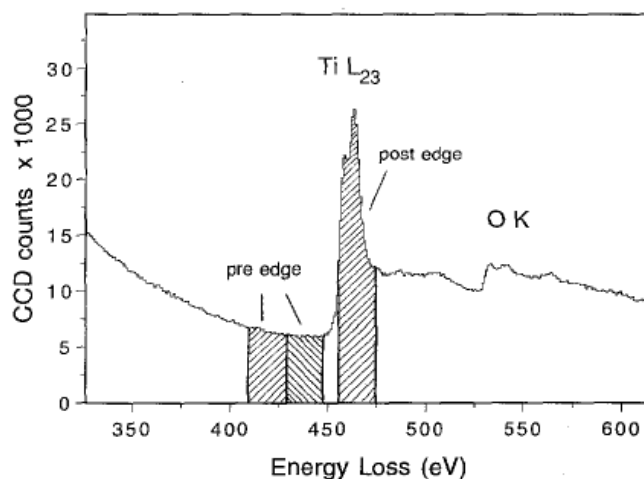
Figure 2.12: Typical EEL-spectrum showing an inner-shell ionization edge of Ti; positions of energy-filtered images for background subtraction are indicated by shaded areas. Taken from [141].

Comparison of EDX and EFTEM methods

Both EDX and EFTEM methods can be applied to investigate elemental distribution in nanoparticles. However, both methods have their advantages and disadvantages. The EDX method allows simple and more precise calculation of elemental concentrations and is quite straightforward and more reliable. The EFTEM method is sensitive to the sample

parameters (thickness, shape, orientation) and can produce a number of artefacts. However, EDX mapping requires from 40 minutes to 1 hour, while EFTEM map can be obtained just in a few minutes. In other words, EFTEM is preferable for the samples which are unstable under the beam. In the case of EFTEM, the edge shape has to be taken into account. For instance, Cu $L_{2,3}$ edge is not so well pronounced as Fe and Ag edges (see Fig.2.11 (b)) which means that a correct estimation of the Cu distribution in the sample with low Cu concentration can be difficult.

3D tomography

Conventional TEM provides two-dimensional projections of the specimen. To study the three-dimensional morphology of the object, the 3D tomography method is used. The sample is tilted around the tilt axis of the microscope goniometer, typically over a range of -70° to +70°, recording images at 1-2° intervals. These images are called tilt-series. After acquisition, the images are aligned with each other by the software and then are processed by the reconstruction program, which reconstructs a three-dimensional volume of the object.

2.2.4   FEI Tecnai F20 TEM

In this work, morphology, chemical composition and crystalline structure of gas-phase nanoparticles were predominantly studied using FEI Tecnai F20 TEM operated at 200 kV with a point resolution of 0.23 nm. The microscope is equipped with a Schottky field emission gun, a super twin lens, an EDX Si(Li) detector, a HAADF detector and a Gatan image filter system. For TEM measurements, particles were deposited on a copper or nickel TEM grid coated with amorphous carbon.

2.3   Magnetization measurements.

Magnetization measurements were performed using SQUID (Superconducting QUantum Interference Design)-magnetometer manufactured by Quantum Design (model MPMS-XL5).

Chapter 3

Phase segregation in metastable alloy Fe-Cu nanoparticles

In this chapter phase segregation in metastable alloy Fe-Cu nanoparticles is studied. Fe sputtering targets patched with 3, 6 and 12 Cu pieces (see Fig.2.3) were used to prepare Fe-Cu nanoparticles with Fe(Cu) nominal concentrations 80, 60 and 20 at.%, respectively. For all samples Ar and He were introduced into the nucleation chamber at 50 sccm. The total gas pressure was adjusted to 1 mbar. For each concentration two samples were prepared: the primary particles, produced without in-flight annealing, and particles in-flight annealed at 1273 K. The in-flight annealing time is 0.32 s (equation 2.1).

3.1   Structure and morphology of Fe-Cu nanoparticles

3.1.1   Average elemental concentrations in Fe-Cu nanoparticles

The composition of the Fe-Cu samples was determined by means of EDX spectroscopy. Spectra for each sample were obtained from 10 different regions of about 250 nm in diameter, and the average elemental concentrations were determined (Table 3.1). The EDX analysis were also performed on single nanocomposites that confirmed the presence of both

Fe and Cu within the particles.

Table 3.1: Elemental concentrations in Fe-Cu nanoparticles

Sample		Fe, at.%	Cu, at.%	Error, at.%
$Fe_{75}Cu_{25}$	primary	75	25	
	annealed	74	26	
$Fe_{60}Cu_{40}$	primary	65	35	3
	annealed	62	38	
$Fe_{25}Cu_{75}$	primary	27	73	
	annealed	25	75	

3.1.2 Morphology and size distribution of Fe-Cu nanoparticles

Figure 3.1: TEM micrographs of (a) primary and (c) in-flight annealed $Fe_{75}Cu_{25}$ nanoparticles with their respective size distributions (b,d).

The micrographs of primary and in-flight annealed $\underline{Fe_{75}Cu_{25}}$ particles with corresponding size distributions are shown in Fig.3.1(a-d). The primary particle-size ranges from 5 to about 60 nm, and for the in-flight annealed particles, from 8 to 50 nm.

Primary particles have cubic and spherical morphologies, whereas all in-flight annealed particles appear to be spherical. The number of cubic primary particles was estimated to be approximately 10% of the total number of particles.
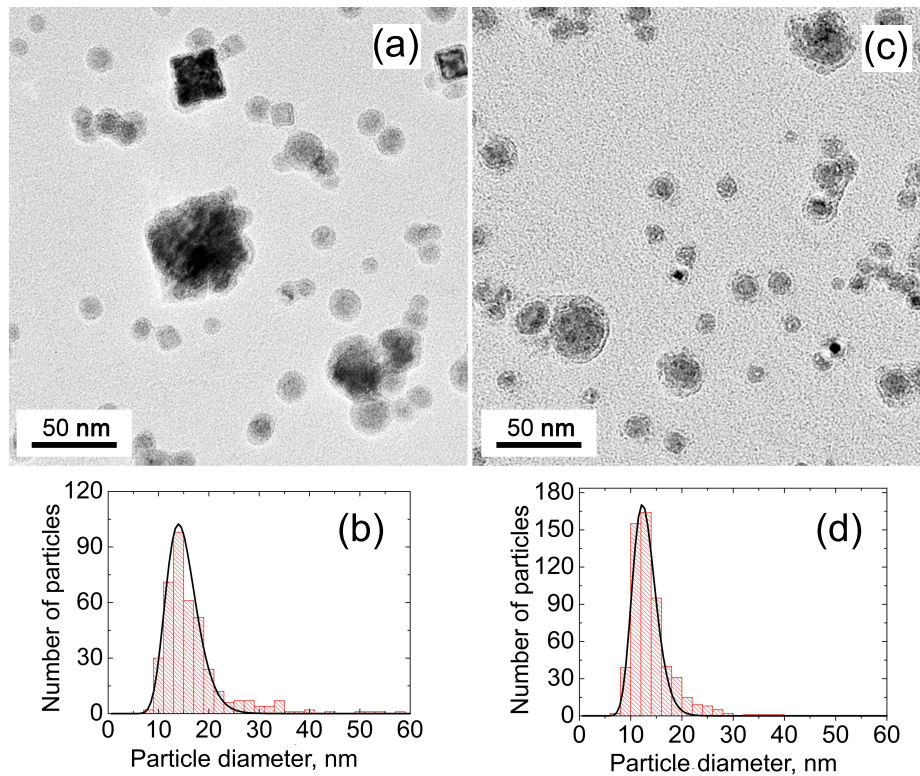

Figure 3.2: TEM micrographs of (a) primary and (c) in-flight annealed $Fe_{60}Cu_{40}$ nanoparticles with their respective size distributions (b,d).

The micrographs of primary and in-flight annealed $\underline{Fe_{60}Cu_{40}}$ particles with corresponding size distributions are shown in Fig.3.2(a-d). As in the previous case, approximately 10% of the primary nanoparticles had a cubic shape. The primary particle-size ranges from 5 to about 60 nm, and for in-flight annealed particles, from 8 to 70 nm.

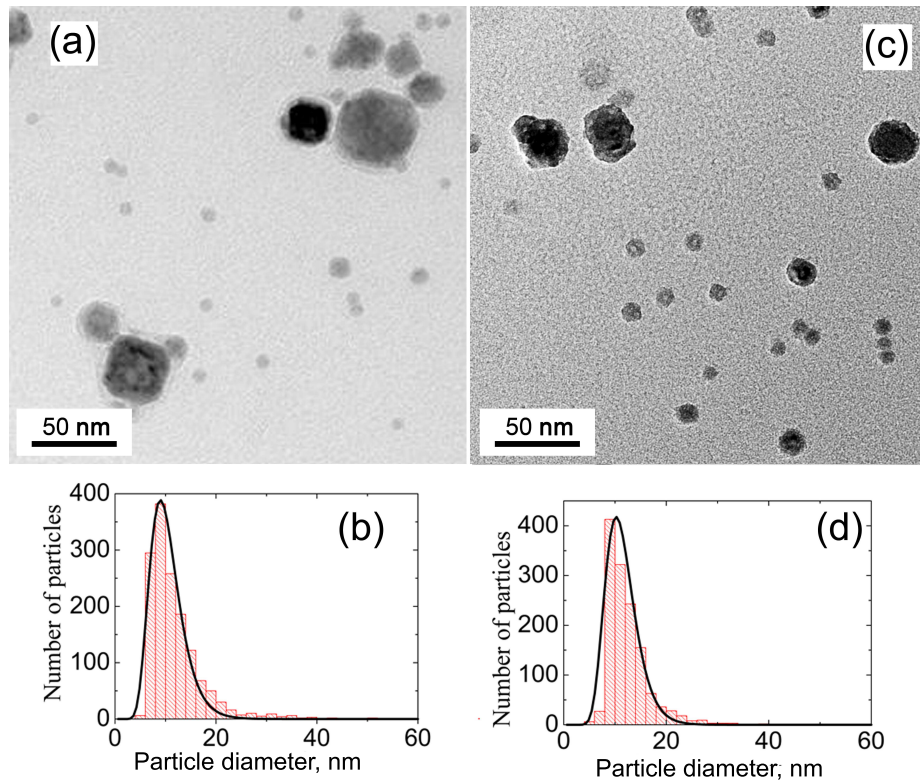The micrographs of primary and in-flight annealed $\underline{Fe_{25}Cu_{75}}$ particles with correspond-
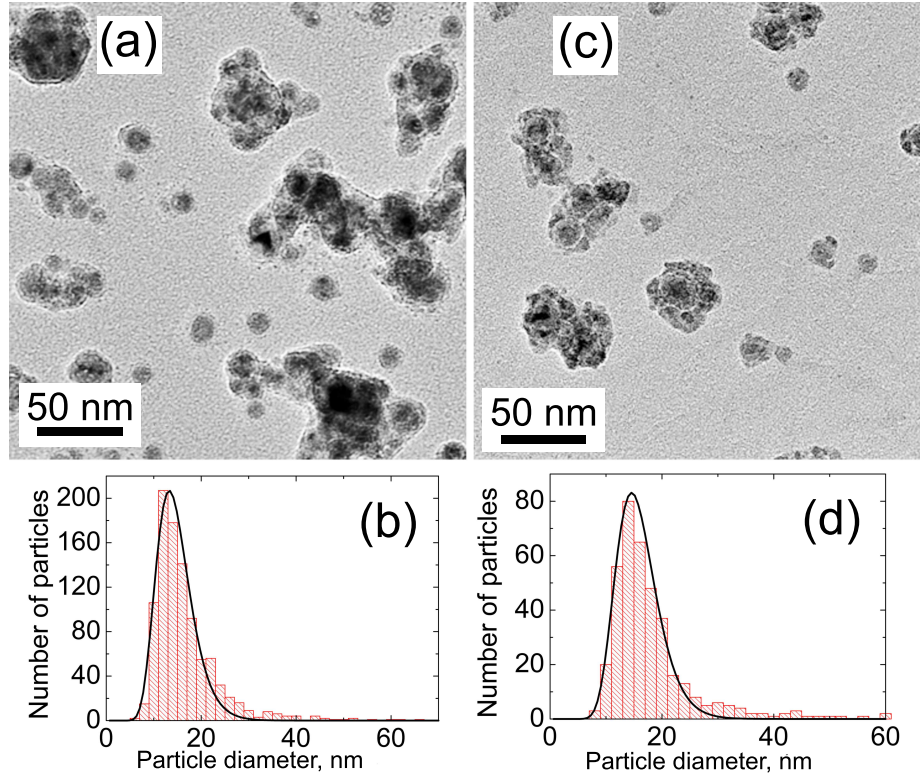
Figure 3.3: TEM micrographs of (a) primary and (c) in-flight annealed $Fe_{25}Cu_{75}$ nanoparticles with their respective size distributions (b,d).

ing size distributions are shown in Fig.3.3(a-d). The primary $Fe_{25}Cu_{75}$ particle-size ranges from 5 to 70 nm (Fig.3.3(a)), whereas the size of the in-flight annealed $Fe_{25}Cu_{75}$ particles ranges from 8 to 60 nm. Unlike as in the previous cases, $Fe_{25}Cu_{75}$ particles appear to form aggregates of spherical shape both before and after in-flight annealing.

All size distributions were fitted by the log-normal distribution function:

$$f(D) = \frac{e^{\frac{-ln^2(D/D_m)}{2\sigma^2}}}{D\sigma\sqrt{2\pi}}.$$

(3.1)

Here, parameters $ln(D_m)$ and σ denote the geometric mean particle diameter and geometric standard deviation, respectively. Average diameter $<d>$ and standard deviation Δ

are calculated as:

$$< d >= e^{(ln(D_m)+\sigma^2/2)}, \tag{3.2}$$

$$\Delta = (e^{\sigma^2} - 1)e^{2ln(D_m)+\sigma^2}. \tag{3.3}$$

The distributions were obtained only for isolated spherical particles. The size-distribution parameters are presented in Table 3.2.

Table 3.2: Size distribution parameters of Fe-Cu nanoparticles

Sample		D_m, nm	σ	<d>, nm	Δ, nm
$Fe_{75}Cu_{25}$	primary	14.7 ± 0.5	0.21 ± 0.01	15 ± 1	3.19 ± 0.03
	annealed	12.7 ± 0.5	0.18 ± 0.01	13 ± 1	2.34 ± 0.01
$Fe_{60}Cu_{40}$	primary	9.9 ± 0.5	0.31 ± 0.01	10 ± 1	3.29 ± 0.02
	annealed	10.1 ± 0.5	0.27 ± 0.01	10 ± 1	2.89 ± 0.02
$Fe_{25}Cu_{75}$	primary	14.2 ± 0.5	0.26 ± 0.01	15 ± 1	3.88 ± 0.04
	annealed	15.5 ± 0.5	0.24 ± 0.01	16 ± 1	3.87 ± 0.03

3.1.3   Structure of Fe-Cu nanoparticles

The crystal structure of the particles was determined by electron diffraction. The diffractograms were calibrated using a gold film sample measured under the same beam conditions as reference. The powder diffraction patterns for primary and in-flight annealed $Fe_{75}Cu_{25}$ nanoparticles are shown in Fig.3.4. The structural data are collected in Table 3.3. The analysis of diffraction rings (Fig.3.4) shows a good agreement with bcc α-Fe. Diffraction patterns of primary and in-flight annealed particles are quasi identical, which indicates that annealing does not affect the crystal structure of $Fe_{75}Cu_{25}$ nanoparticles.

The powder diffraction patterns of primary and in-flight annealed $Fe_{60}Cu_{40}$ nanoparticles are presented in Fig.3.5, and the results are collected in Table 3.4. The diffraction pattern of primary $Fe_{60}Cu_{40}$ nanoparticles consists of bright pronounced rings corresponding to the bcc structure. There are also three weak rings associated with fcc Cu, marked by
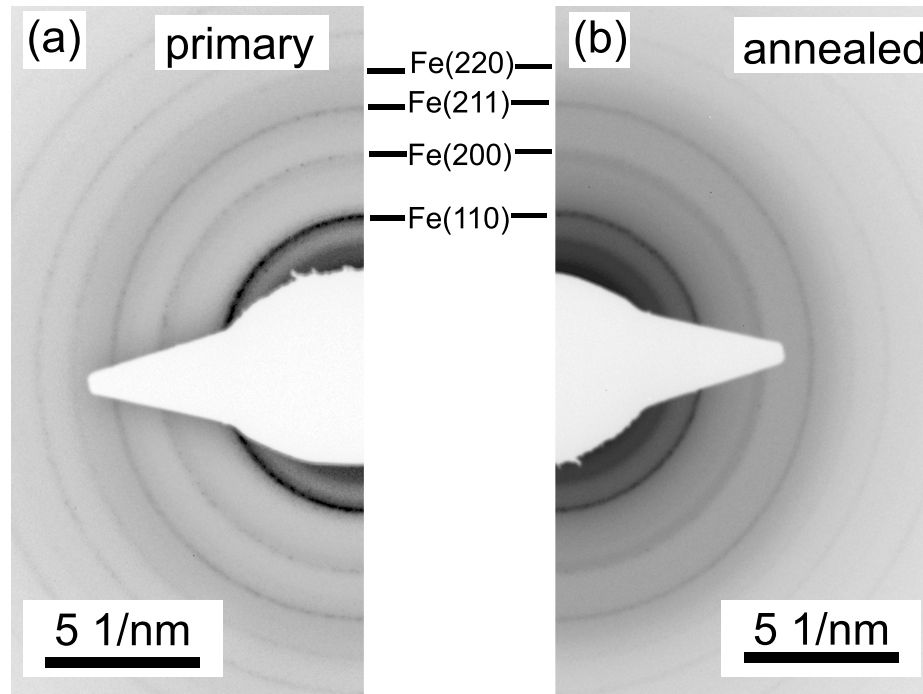
Figure 3.4: Powder diffraction pattern of (a) primary and (b) in-flight annealed $Fe_{75}Cu_{25}$ nanoparticles.

Table 3.3: Powder diffraction analysis for primary and in-flight annealed $Fe_{75}Cu_{25}$ nanoparticles

$Fe_{75}Cu_{25}$ primary	$Fe_{75}Cu_{25}$ annealed	bcc Fe [142] (a=0.287 nm)	
d,$\pm$ 0.002 nm	d,$\pm$ 0.002 nm	plane	d,nm
0.201	0.201	(110)	0.202
0.142	0.143	(200)	0.143
0.115	0.116	(211)	0.117
0.101	0.102	(220)	0.101

violet arrows in Fig.3.5(a). The diffraction pattern of in-flight annealed $Fe_{60}Cu_{40}$ particles (Fig.3.5(b)) contains pronounced rings corresponding both to bcc and fcc structures. The results show that in-flight annealing has a significant impact on the structure of $Fe_{60}Cu_{40}$ nanoparticles and promotes the formation of the fcc structure.

In the case of $Fe_{25}Cu_{75}$ nanocomposites, in-flight annealing has substantial impact on
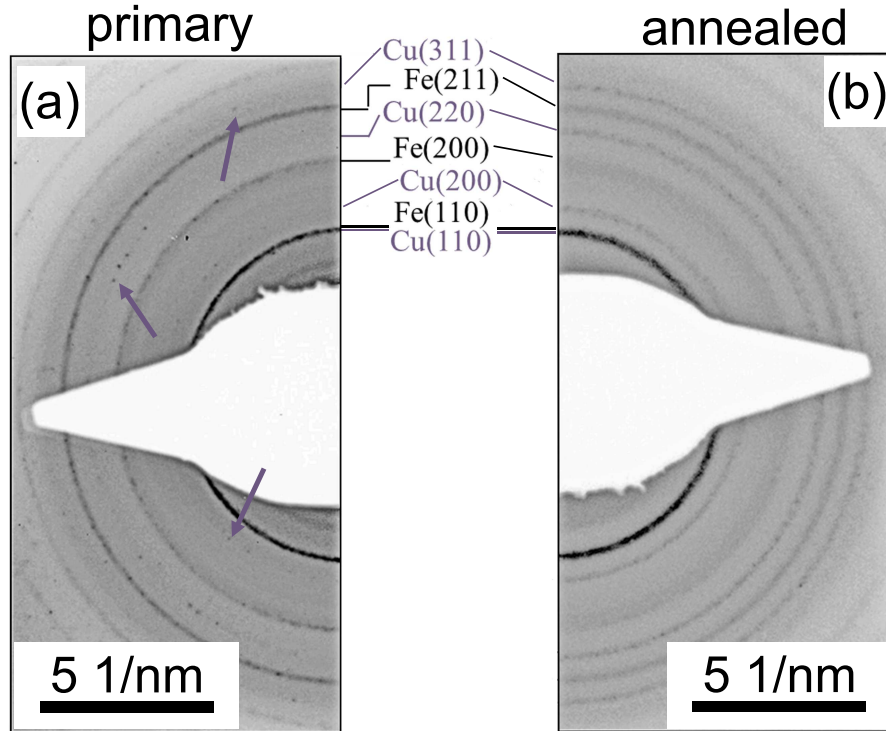
Figure 3.5: Powder diffraction pattern of (a) primary and (b) in-flight annealed $Fe_{60}Cu_{40}$ nanoparticles.

Table 3.4: Powder diffraction analysis for primary and in-flight annealed $Fe_{60}Cu_{40}$ nanoparticles. Red color indicates the weak reflection.

$Fe_{60}Cu_{40}$ primary	$Fe_{60}Cu_{40}$ annealed	bcc Fe [142] (a=0.287 nm)		fcc Cu [143] (a=0.362 nm)	
d,$\pm$ 0.002 nm	d,$\pm$ 0.002 nm	plane	d,nm	plane	d,nm
0.208	0.209	(110)	0.202	(111)	0.208
0.181	0.184			(200)	0.180
0.147	0.147	(200)	0.143		
0.131	0.130			(220)	0.128
0.120	0.119	(211)	0.117		
0.111	0.111			(311)	0.109

weak reflections

the crystal structure as discussed here. The diffraction pattern of primary $Fe_{25}Cu_{75}$ particles (Fig.3.6(a)) corresponds to the fcc Cu structure (see Table 3.5), while the diffraction

pattern of in-flight annealed particles consists of rings corresponding both to bcc α-Fe and fcc Cu and oxide (Table 3.5 and Fig.3.6(b)). The oxide is labeled as Cu_2O, however the formation of copper ferrite, $Fe_xCu_yO_z$, cannot be excluded, since d-spacings of iron oxides and copper ferrites are very close to each other (see [144]).
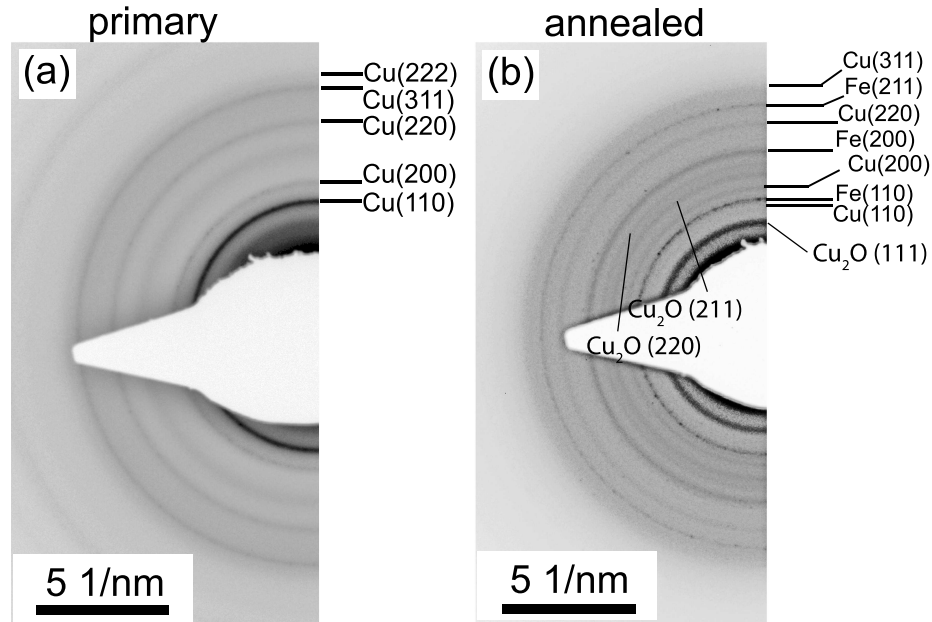
Figure 3.6: Powder diffraction pattern of (a) primary and (b) in-flight annealed $Fe_{25}Cu_{75}$ nanoparticles.

Fig.3.7 shows a typical HRTEM micrographs of primary $Fe_{75}Cu_{25}$ nanoparticles with different shapes. Fig. 3.7(b) shows the FFT image obtained from the area of Fig. 3.7(a) shown with the white square. The FFT image corresponds to bcc iron. The d-spacing was determined to be 0.204 ± 0.005 nm which corresponds to the interplane distance d_{110} of bcc iron (Table 3.3).

Fig.3.7(c) shows the HRTEM image of the primary spherical $Fe_{75}Cu_{25}$ nanoparticle. The FFT image (Fig.3.7(d)) corresponds to overlapping patterns of bcc iron and Fe_3O_4/γ-Fe_2O_3. The d-spacings were determined to be 0.202 ± 0.005 nm (reflections marked by white circles) and 0.294 ± 0.005 nm (reflections marked by yellow circles) which corre-

Table 3.5: Powder diffraction analysis for primary and in-flight annealed $Fe_{25}Cu_{75}$ nanoparticles.

$Fe_{25}Cu_{75}$ primary	$Fe_{25}Cu_{75}$ annealed	bcc Fe [142] (a=0.287 nm)		fcc Cu [143] (a=0.362 nm)		Cu_2O [145] (a=0.427 nm)	
d,$\pm$ 0.002 nm	d,$\pm$ 0.002 nm	plane	d,nm	plane	d,nm	plane	d,nm
	0.247					(111)	0.247
0.207	0.204	(110)	0.202	(111)	0.208	(200)	0.213
0.182	0.186			(200)	0.180		
	0.171					(211)	0.174
	0.160					(220)	0.151
	0.146	(200)	0.143				
0.128	0.128			(220)	0.128		
	0.119	(211)	0.117				
0.108	0.110			(311)	0.109		

spond to interplane distances d_{110} of bcc iron (d_{400} of iron oxide) and d_{220} of iron oxide, respectively. The literature values are d_{220}= 0.295 nm of γ-Fe_2O_3 and d_{220} = 0.296 nm of Fe_3O_4, d_{400} = 0.208 nm for γ-Fe_2O_3, and d_{400} = 0.209 nm for Fe_3O_4) [146], [147].

A similar result was obtained for the in-flight annealed $Fe_{75}Cu_{25}$ nanoparticles shown in (Fig.3.7(e)). Fig.3.7(f) shows the FFT image obtained from Fig.3.7(e). The FFT image also corresponds to overlapping patterns of bcc iron and Fe_3O_4/γ-Fe_2O_3. The d-spacings were determined to be 0.201 $\pm$ 0.005 (reflections marked by white circles) and 0.297 $\pm$ 0.005 nm (reflections marked by yellow circles).

In all cases the particles are viewed along the [001] zone axis. HRTEM micrographs show that all particles have a single-crystal core and an oxide shell.

The TEM image of the cubic primary $Fe_{60}Cu_{40}$ nanoparticle is shown in Fig.3.8(a). The HRTEM image obtained from the particle-area marked with the red square is shown in Fig.3.8(b) with the corresponding FFT inmage shown in Fig.3.8(c) which corresponds to a bcc Fe structure overlapped with the one of iron oxides (Fe_3O_4 or γ-Fe_2O_3). The measured d-spacings d = 0.202 $\pm$ 0.005 nm (reflections marked by white circles) and 0.293 $\pm$ 0.005 (reflections marked by yellow circles) correspond to the interplane distances d_{110} of bcc Fe (d_{400} of iron oxide) and d_{220} of iron oxide, respectively. The particle is viewed along [001]
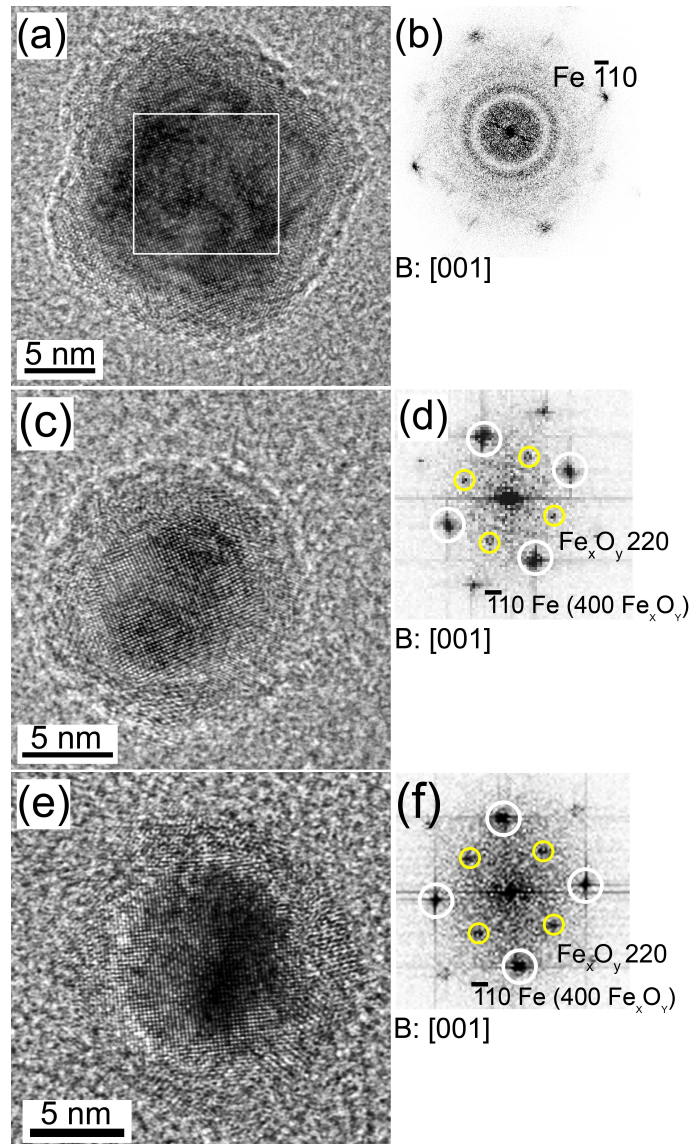
Figure 3.7: HRTEM micrographs of cubic (a) and spherical (c) primary $Fe_{75}Cu_{25}$ nanoparticles. (e) HRTEM micrograph of in-flight annealed $Fe_{75}Cu_{25}$ nanoparticle. (b) FFT image obtained from the area in image (a) marked with white square. (d) FFT image obtained from image (c). (f) FFT image obtained from image (e).

direction.

The spherical primary $Fe_{60}Cu_{40}$ nanoparticles (Fig.3.8(d)) has a bcc Fe structure with d-spacing $d = 0.203 \pm 0.005$ nm (Fig.3.8(e)). The particle is viewed along the [111] direction.

Figure 3.8: (a) TEM micrograph of the cubic primary $Fe_{60}Cu_{40}$ nanoparticle. (b) HRTEM image of the area marked with the red square in image (a). (c) FFT image obtained from image (b). Fe_xO_y corresponds to one of the iron o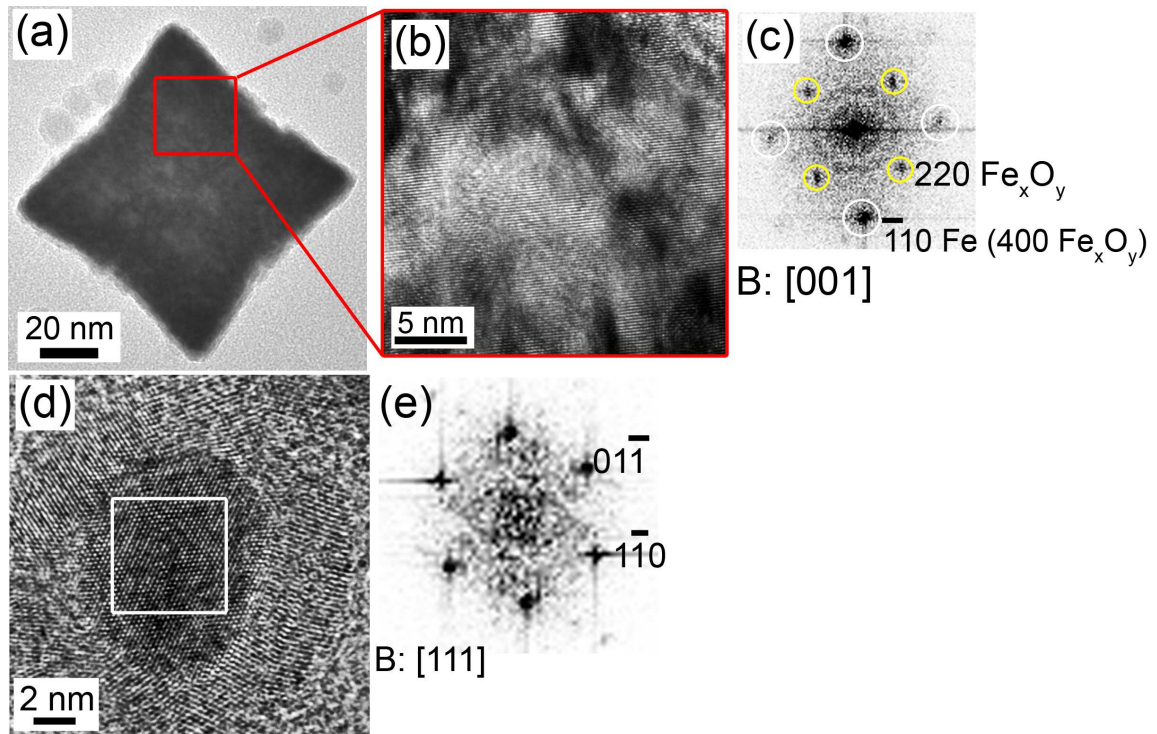xides: Fe_3O_4 or γ-Fe_2O_3. (d) HRTEM image of the spherical primary $Fe_{60}Cu_{40}$ nanoparticle. (e) FFT image obtained from area marked with the white square in image (d).

As in the case of $Fe_{75}Cu_{25}$, primary $Fe_{60}Cu_{40}$ nanoparticles consist of a single-crystal core and a polycrystalline shell.

The TEM image of the in-flight annealed $Fe_{60}Cu_{40}$ nanoparticle is shown in Fig.3.9(a). The HRTEM image of the particle's core (area marked with the red square in image (a)) is presented in Fig.3.9(b). The corresponding FFT image (Fig.3.9(c)) shows reflections (red circles) corresponding to the fcc Cu structure viewed along the [001] direction. The d-spacings d $= 0.182 \pm 0.005$ nm correspond to (200) planes of Cu (see Table 3.3). The reflections marked with blue circles may either correspond to iron oxide (Fe_3O_4 or γ-Fe_2O_3) or result from the overlapping of bcc Fe and iron oxide patterns. The d-spacings are 0.204
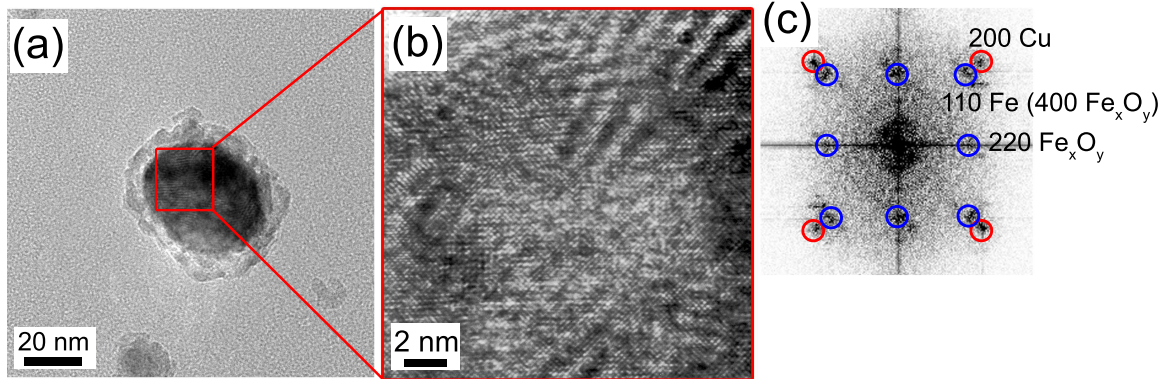
Figure 3.9: (a) TEM micrograph of the in-flight annealed $Fe_{60}Cu_{40}$ nanoparticle. (b) HRTEM image of the area marked with the red square in image (a). (c) FFT image obtained from image (b). Fe_xO_y corresponds to one of the iron oxides: Fe_3O_4 or γ-Fe_2O_3.

$\pm$ 0.005 and 0.295 $\pm$ 0.005 nm correspond to the (110) planes of bcc Fe ((400) planes of iron oxide) and (220) planes of iron oxide, respectively. Two interpretations of the FFT image are possible:

1. Particles consist of an fcc core and an iron oxide shell,

2. Particle consists of a granular fcc+bcc core and iron oxide shell.

The first option, however, appears to be more likely. The particle-core (as seen in Fig.3.9(b)) is single-crystal. Though minor crystal defects are present, no pronounced grain boundaries can be seen.

Another in-flight annealed $Fe_{60}Cu_{40}$ particles is shown in Fig.3.10 (a). The reflections in the corresponding FFT image (Fig.3.10 (b)) marked with the white and yellow circles belong to bcc Fe structure overlapped with iron oxide (measured d-spacings d = 0.207 $\pm$ 0.005 nm and 0.299 $\pm$ 0.005). In this case the set of reflections marked with blue arrows (d = 0.260 $\pm$ 0.005 nm) allows to identify the iron oxide as γ-Fe_2O_3 ([148], also see Fig.4.3).

Fig.3.11(a) shows the HRTEM image of a primary a $Fe_{25}Cu_{75}$ nanoparticle. The FFT image obtained from the area marked by the white square is presented in Fig.3.11(b). The

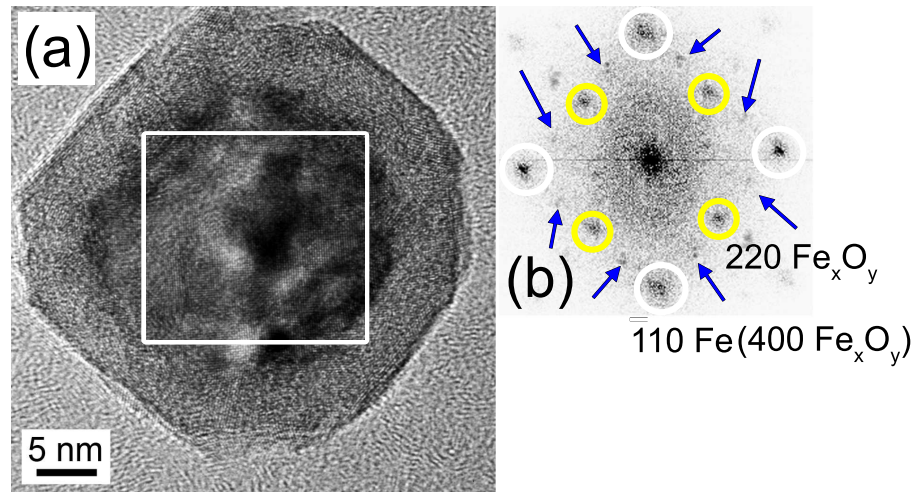Figure 3.10: (a) HRTEM image of the in-flight annealed $Fe_{60}Cu_{40}$ nanoparticle. (b) FFT image obtained from the area in image (a) marked with white square. Fe_xO_y corresponds to one of the iron oxides: Fe_3O_4 or γ-Fe_2O_3.
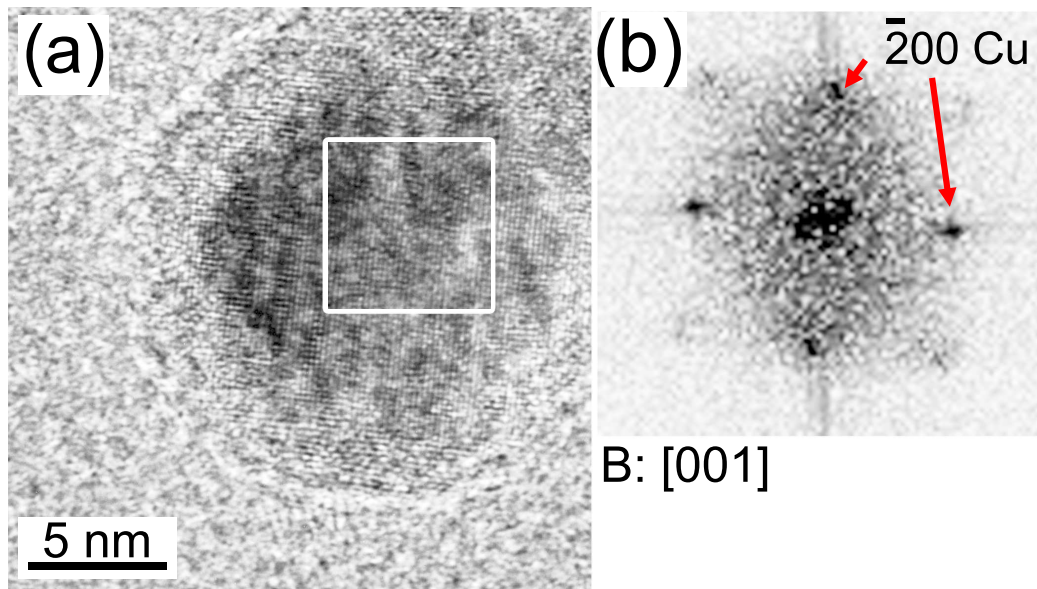
Figure 3.11: (a) HRTEM micrograph of a primary $Fe_{25}Cu_{75}$ nanoparticle. (b) FFT image obtained from the area marked with the white square in image (a).

FFT image corresponds to the fcc Cu structure viewed along the [001] zone axis. The measured d-spacing d = 0.184 ± 0.005 nm corresponds to (200) planes of Cu (see Table 3.3).
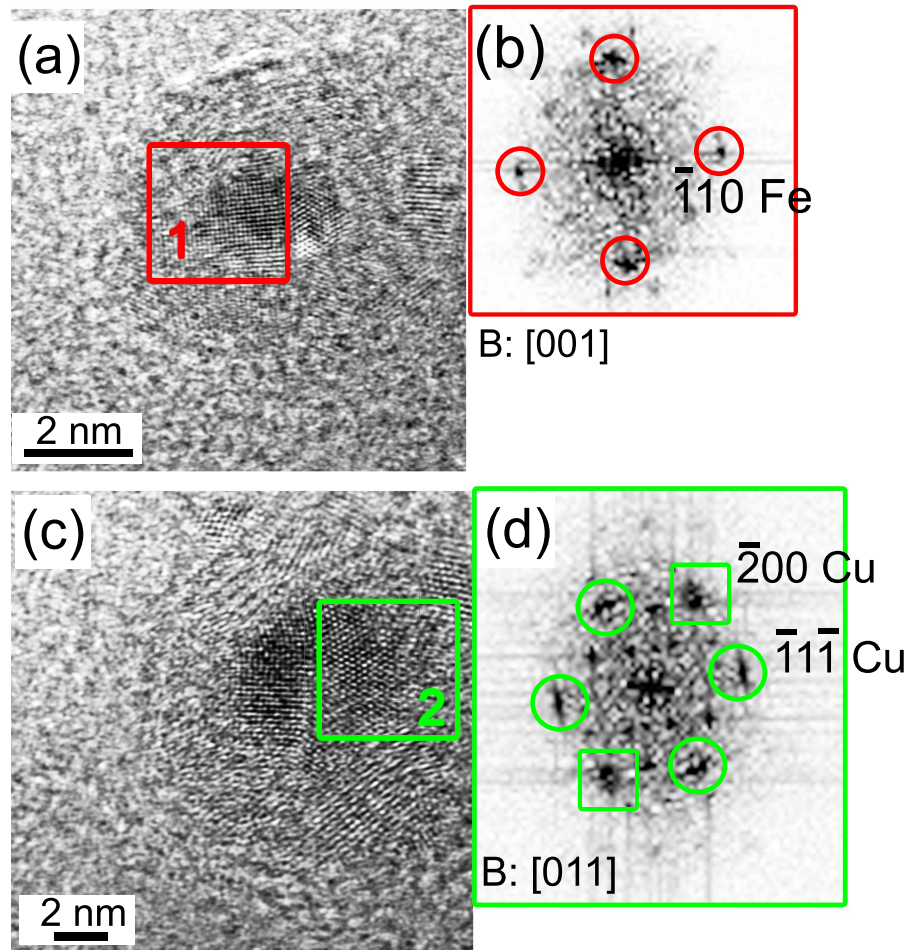
Figure 3.12: (a,c) HRTEM micrographs of the same in-flight annealed $Fe_{25}Cu_{75}$ nanoparticle obtained under different beam conditions. (b) FFT image of the area in the image (a) marked with red square "1". (d) FFT image of the area in the image (c) marked with green square "2".

After in-flight annealing, $Fe_{25}Cu_{75}$ particles are found to become polycrystalline and consist of bcc and fcc crystals. HRTEM images of the same in-flight annealed $Fe_{25}Cu_{75}$ particle measured under different beam conditions (focus and magnification) are presented

in Fig.3.12(a). The contrast variation in the images indicates that the particle consists of an oxide shell and a polycrystalline core. The core itself consists of two crystallites marked by red and green squares. Fig.3.12(b) shows the FFT image obtained from the area marked by the red square in Fig.3.12(a) (crystallite **1**) which corresponds to bcc Fe viewed along the [001] zone axis. Also, weak oxide reflections can be seen. The measured d-spacings is d = 0.202 ± 0.005 nm correspond to (110) planes of bcc iron.

Fig.3.12(d) shows the FFT image obtained from the area in Fig.3.12(c) marked with the green square (crystallite 2) . The diffraction pattern corresponds to fcc Cu viewed along [011] zone axis. The d-spacings are d = 0.185 ± 0.005 and 0.210 ± 0.005 nm corresponding to the (200) and (111) planes of fcc Cu.

3.2 Phase segregation in metastable primary and in-flight annealed Fe-Cu nanoparticles

The elemental distribution within individual Fe-Cu particles was studied by means of spatially resolved EDXS line scans, 2D EDXS maps, and EFTEM mapping experiments.

3.2.1 $Fe_{75}Cu_{25}$

Fig.3.13(a) shows a HAADF STEM image of the primary spherical $Fe_{75}Cu_{25}$ particle. The corresponding EDX line-scan profile is presented Fig.3.13(b). One finds that iron and copper are both present and relatively uniformly distributed in the particle core − the region with the brighter contrast in Fig.3.13(a). The particle shell contains only iron and no copper.

The HAADF STEM image of a in-flight annealed $Fe_{75}Cu_{25}$ nanoparticle is presented in Fig.3.13(c). The corresponding EDX line scan (Fig.3.13(d)) demonstrates a clear maximum in Cu K-line profile indicating the formation of a copper-enriched region within the particle.
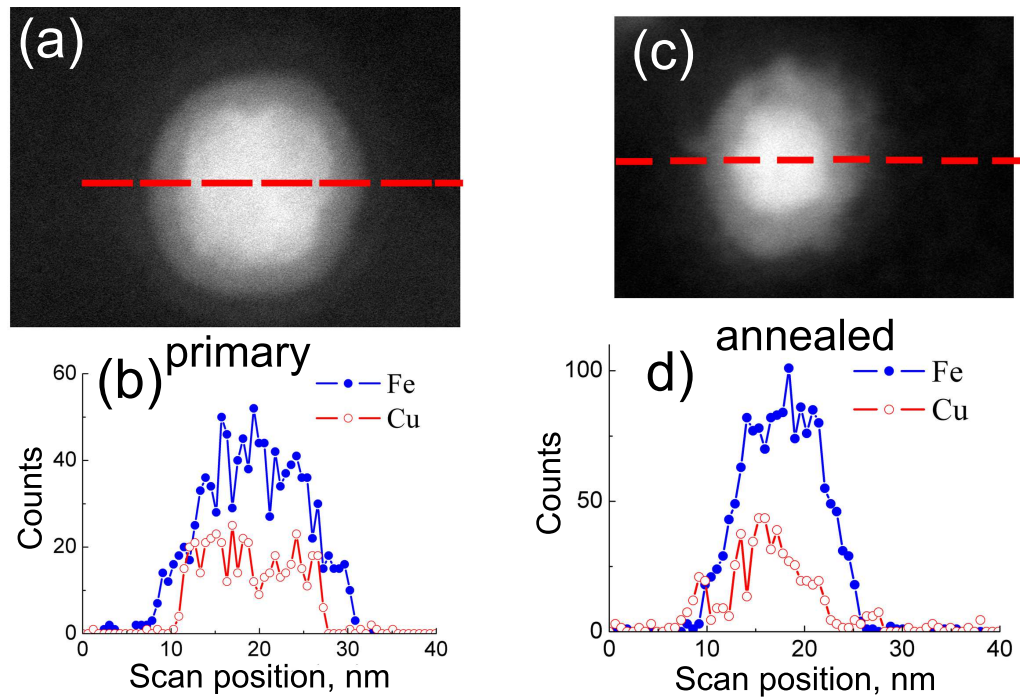
Figure 3.13: HAADF STEM images of (a) primary and (c) in-flight annealed $Fe_{75}Cu_{25}$ nanoparticles. The red lines indicate the paths of electron beam during the scan. (b,d) Line-scan profiles of characteristic x-ray absorption Fe and Cu K-lines as a function of electron probe position on the particles in images (a) and (c), respectively.

HAADF STEM images of cubic and spherical primary $Fe_{75}Cu_{25}$ particles with corresponding two-dimensional distributions of x-ray Fe and Cu K-lines are shown in Fig.3.14(a) and (b), respectively. In both cases (cubic and spherical) $Fe_{75}Cu_{25}$ primary nanoparticles consist of an Fe-rich shell and a Fe-Cu core. The Fe-rich shell is actually iron oxide as concluded from HRTEM analysis and as indicated by a weaker Z-contrast in the STEM image.

EDX mapping experiments performed on in-flight annealed $Fe_{75}Cu_{25}$ particles (Fig.3.15) confirm a less uniform distribution of copper within in-flight annealed particles compared to the primary particles. The Cu EDX map in Fig.3.15 shows two Cu-enriched areas in particle's core, marked by red arrows, and one Cu-enriched area in the particle's shell marked by the white arrow. However, HRTEM analysis showed that both primary and in-flight
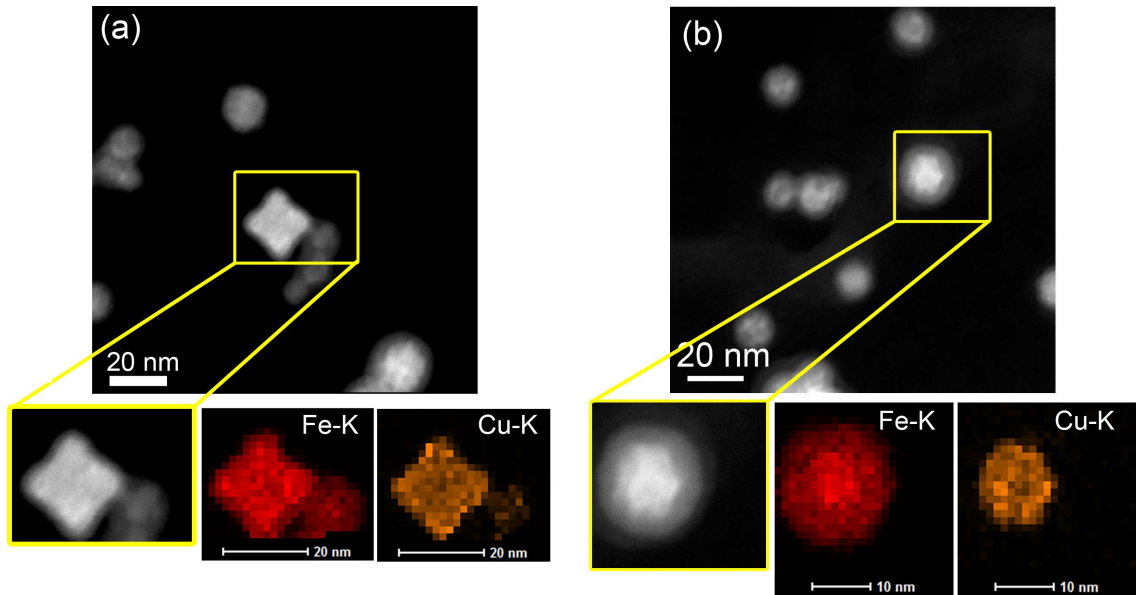
Figure 3.14: HAADF STEM images of the primary (a) cubic and (b) spherical $Fe_{75}Cu_{25}$ nanoparticles with corresponding elemental maps of characteristic x-ray absorption Fe and Cu K-lines.

annealed particles have a single-crystal bcc core, which means that segregation in the core part proceeds via spinodal decomposition [15].

3.2.2 $Fe_{60}Cu_{40}$

The HAADF STEM images of the primary and in-flight annealed $Fe_{60}Cu_{40}$ spherical nanoparticles are presented Fig.3.16(a) and (c), along with corresponding line-scan profiles of characteristic x-ray Fe and Cu K-lines shown in Fig.3.16(b) and (d) (lower parts), respectively. The upper parts of Fig.3.16(b) and (d) show the local compositions of Fe and Cu calculated from EDX spectra obtained for the line-scans. The uncertainty is about 3 at.%. The local Fe and Cu concentration distributions in the central parts of the particles clearly show oscillations with a local maximum of Fe concentration at positions corresponding to a local minimum in Cu concentration. The amplitude of oscillations is larger in the in-flight annealed particle.
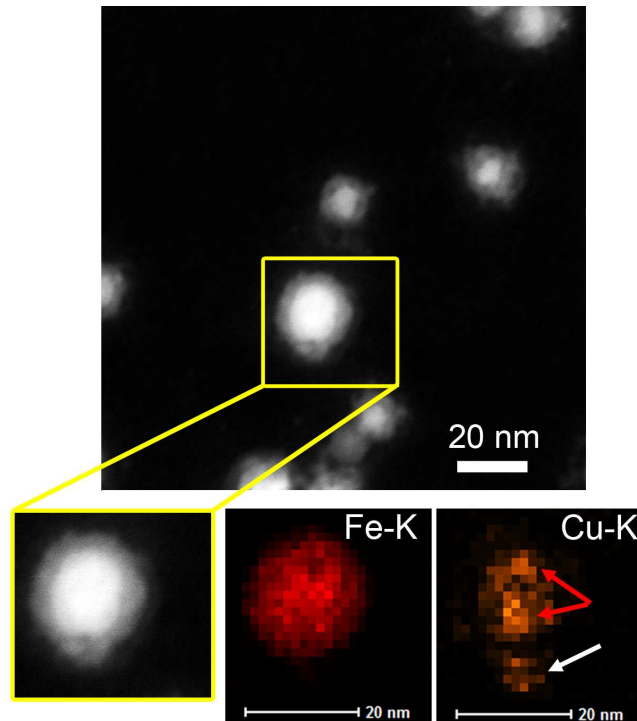
Figure 3.15: HAADF STEM image of the in-flight annealed $Fe_{75}Cu_{25}$ nanoparticle with corresponding elemental maps of characteristic x-ray Fe and Cu K-lines.

The line-scans also demonstrate that the primary particle's shell mostly consists of iron, while in the in-flight annealed particle copper appears to segregate to the surface. However, as it will be shown below, this is not common for all particles.

The elemental distribution within $Fe_{60}Cu_{40}$ nanoparticles was further investigated by means of EDX spectroscopy and EFTEM mappings. Fig.3.17 shows HAADF STEM images and corresponding two-dimensional distributions of x-ray Fe and Cu K-lines of primary $Fe_{60}Cu_{40}$ particles. Fig.3.18 shows zero-loss images of primary $Fe_{60}Cu_{40}$ particles with corresponding EFTEM elemental maps of Fe and Cu obtained at Fe and Cu $L_{2,3}$-edges. EDX and EFTEM elemental maps obtained for cubic primary $Fe_{60}Cu_{40}$ particles (Fig.3.17(a) and Fig.3.18(a,b,c)) show an uniform distribution of Fe and Cu within the particles. However, in spherical nanoparticles (Fig.3.17(b), Fig.3.18(d,e,f) and (g,h,i)) phase segregation and co-existence of Fe-rich and Cu-rich regions can be clearly seen, which
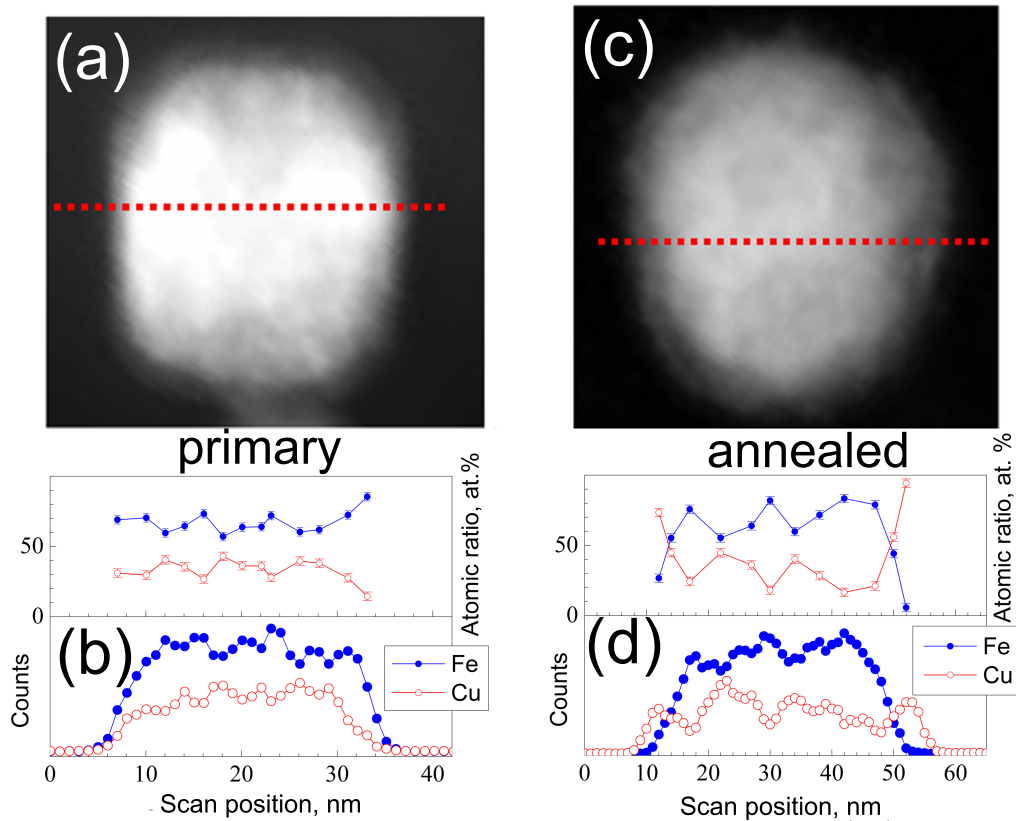
Figure 3.16: HAADF STEM images of (a) primary (spherical) and (c) in-flight annealed $Fe_{60}Cu_{60}$ nanoparticles. The red lines indicate the path of electron beam during the scan. (b,d)(Lower part) line-scan profiles of characteristic x-ray Fe and Cu K-lines and (upper part) local composition of Fe and Cu as a function of electron probe position on the particles in images (a) and (c), respectively.

means that phase segregation occurs through spinodal decomposition as in case of $Fe_{75}Cu_{25}$ nanocomposites. EDX and EFTEM maps also show that particles' shells mostly consist of iron.

The elemental maps obtained for in-flight annealed $Fe_{60}Cu_{40}$ nanoparticles showed that annealing promotes further segregation of iron and copper, also via spinodal decomposition. However, segregation becomes size-dependent. Fig.3.19 shows HAADF STEM images and two-dimensional distributions of x-ray Fe and Cu K-lines in in-flight annealed
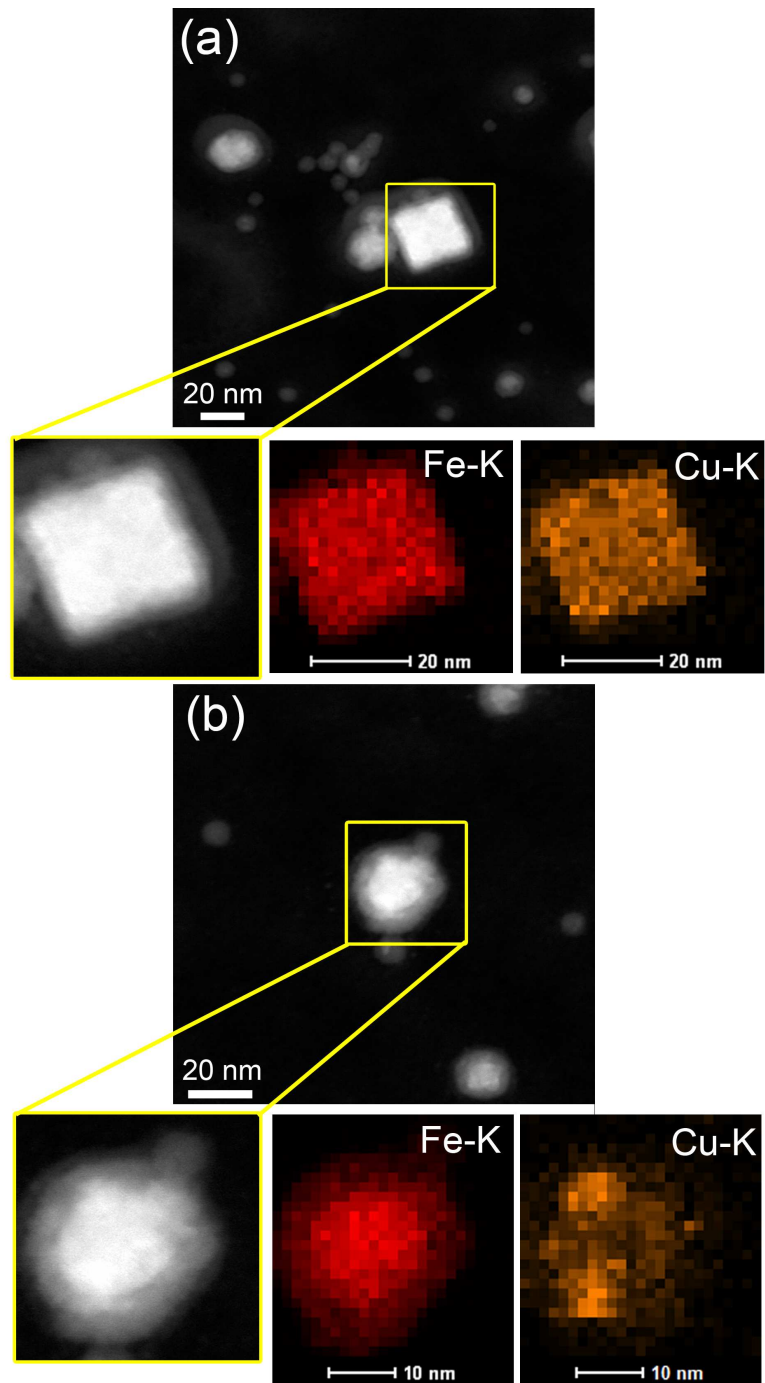
Figure 3.17: HAADF STEM images of the primary (a) cubic and (b) spherical $Fe_{60}Cu_{40}$ nanoparticles with corresponding elemental maps of characteristic x-ray Fe and Cu K-lines.

Figure 3.18: (a),(d),(g) Zero-loss images of primary $Fe_{60}Cu_{40}$ nanoparticles. (b),(e),(h) Corresponding Fe-$L_{2,3}$ elemental maps. (c),(f), (i) Corresponding Cu-$L_{2,3}$ elemental maps. Elemental maps are presented in false colors.

particles with particle-size close to 20 nm. In both particles, separation of Fe-rich and Cu-rich regions is observed. The contrast difference in elemental maps is more pronounced than in the case of primary $Fe_{60}Cu_{40}$ and in-flight annealed $Fe_{75}Cu_{25}$ nanoparticles. However, copper is only observed in the particle core. It must be also noted that in the particle shown in Fig.3.19(a), there are several, though interconnected, Cu-rich regions, while in Fig.3.19(b), the nanoparticle's *core* consists of a Cu-rich area surrounded by an Fe-rich part.

Fig.3.20 shows a zero-loss image with corresponding EFTEM elemental maps of Fe and Cu obtained at Fe and Cu $L_{2,3}$ edges of a in-flight annealed $Fe_{60}Cu_{40}$ particle with a size of
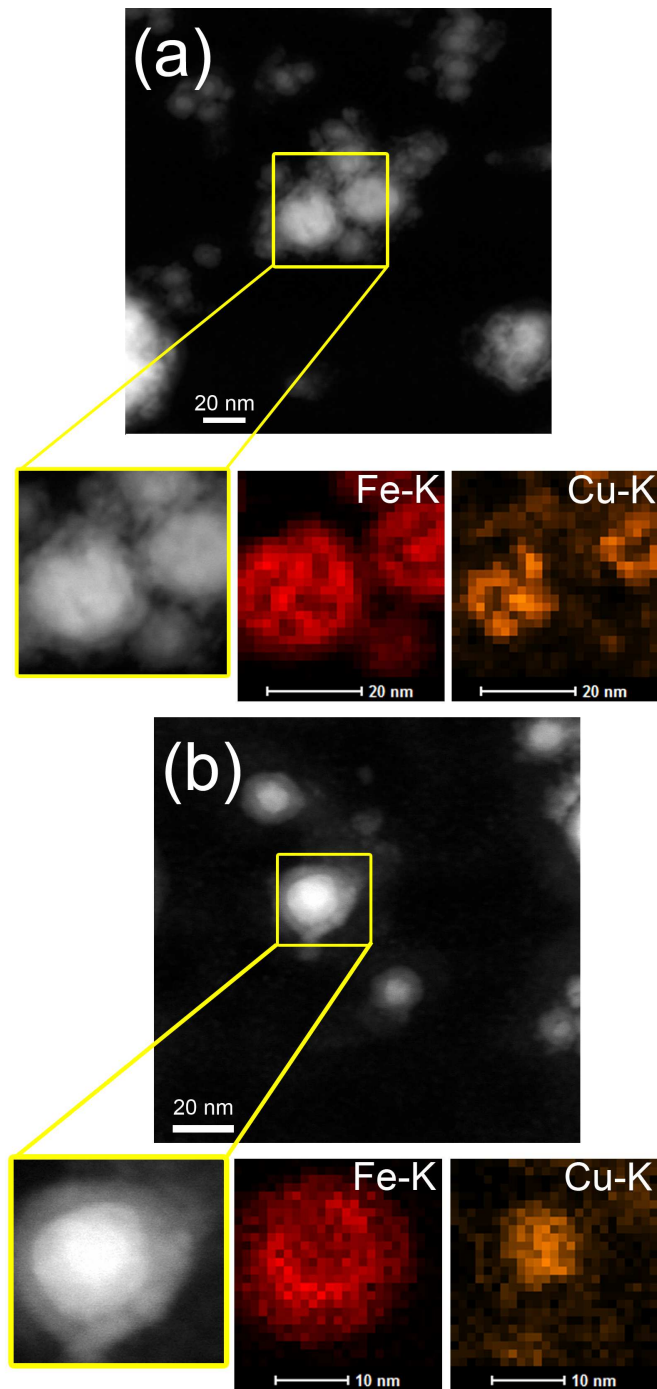
Figure 3.19: (a),(b)HAADF STEM images of the in-flight annealed $Fe_{60}Cu_{40}$ nanoparticles with corresponding elemental maps of characteristic x-ray Fe and Cu K-lines.

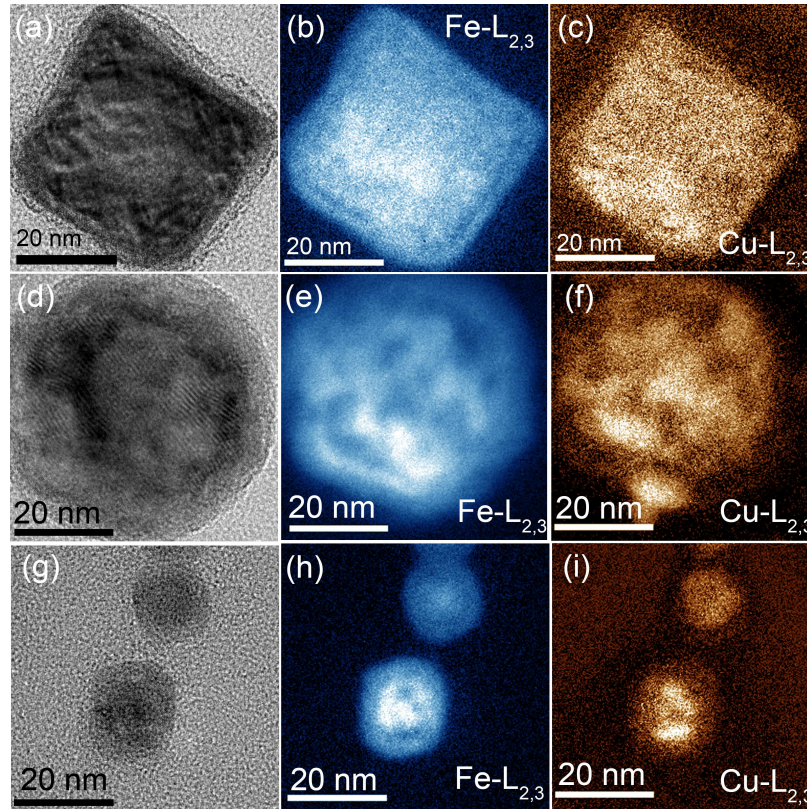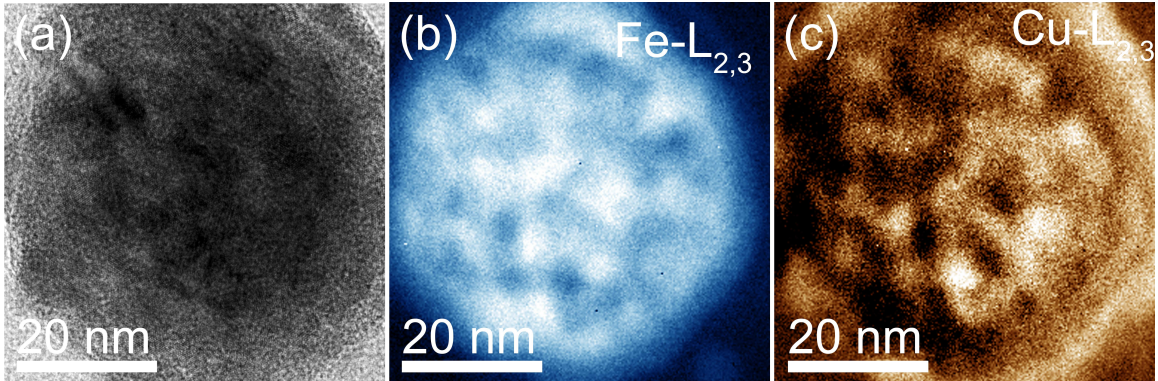Figure 3.20: (a) Zero-loss image of in-flight annealed $Fe_{60}Cu_{40}$ nanoparticle. (b) Corresponding Fe-$L_{2,3}$ elemental map. (c) Corresponding Cu-$L_{2,3}$ elemental map. Elemental maps are presented in false colors.

60 nm. The elemental maps show that while the particle core also consists of Fe-rich and Cu-rich regions, some amount of copper segregates to the surface. This is consistent with the line-scan shown in Fig.3.16(d) for a in-flight annealed $Fe_{60}Cu_{40}$ particle (Fig.3.16(c)) with a size of 50 nm.

3.2.3 $Fe_{25}Cu_{75}$

The HAADF image of the primary $Fe_{25}Cu_{75}$ nanoparticle and line-scan profile of the characteristic x-ray Fe and Cu K-lines as a function of electron probe position on the particle are shown in Fig.3.21(a) and (b). The line-scan indicates a relatively uniform distribution of iron and copper within the particle.

The HAADF image and line-scan profile of the in-flight annealed $Fe_{25}Cu_{75}$ particle are presented in Fig.3.21(c) and (d). The iron K-line intensity has a single broad peak which means that iron is not equally distributed within the particle and forms a large cluster within the particle.

Fig.3.22(a) and (d) show zero-loss images of primary $Fe_{25}Cu_{75}$ particles with corresponding EFTEM elemental maps of Fe (Fig.3.22(b) and (e)) and Cu (Fig.3.22(c) and (f)).
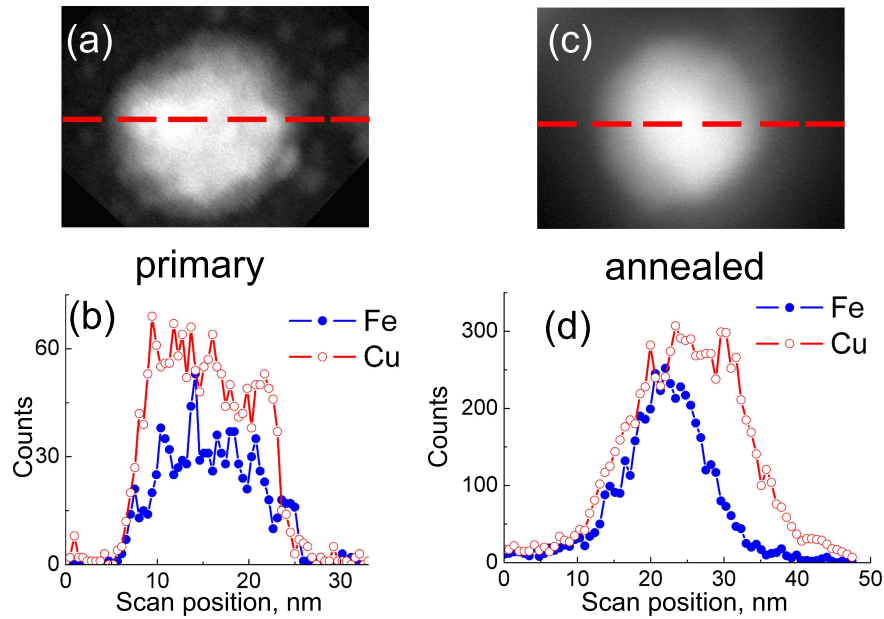
Figure 3.21: HAADF STEM images of (a) primary and (c) in-flight annealed $Fe_{25}Cu_{75}$ nanoparticles. The red lines indicate the path of electron beam during the scan. (b,d) Line-scan profiles of characteristic x-ray Fe and Cu K-lines as a function of electron probe position on the particles in images (a) and (c), respectively.

EFTEM maps confirm the relatively uniform distribution of Fe and Cu in the primary particles. Also, some small pure Cu particles are present (e.g., the particle marked by the white line in Fig.3.22(d)).

In in-flight annealed particles, for which the zero-loss images are shown in Fig.3.23(a) and (d), either an iron-rich core and a copper-rich shell are formed (Fig.3.23(a,b,c)), or copper segregates in one direction and an asymmetrical particle is formed (Fig.3.23(d,e,f)). Large in-flight annealed $Fe_{25}Cu_{75}$ particles may consist of several copper and iron clusters (Fig.3.23(g,h,i)).
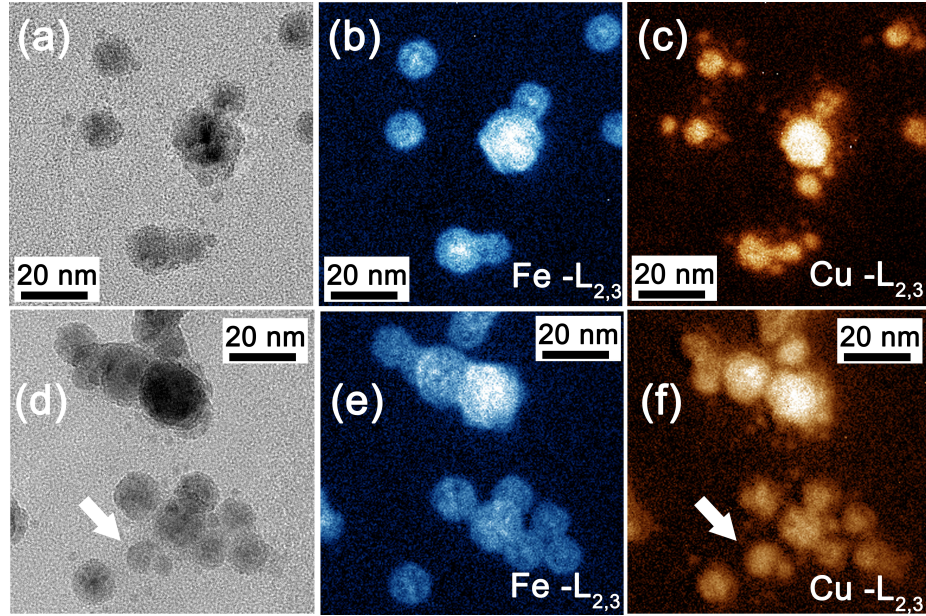
Figure 3.22: (a),(d) Zero-loss images of primary $Fe_{25}Cu_{75}$ nanoparticles. (b),(e) Corresponding Fe-$L_{2,3}$ elemental maps. (c),(f) Corresponding Cu-$L_{2,3}$ elemental maps. Elemental maps are presented in false colours.

3.3 Fe-Cu nanoparticles: summary and discussion

Structure of primary Fe-Cu nanoparticles. The majority of primary Fe-Cu nanoparticles consist of s single-crystal core and polycrystalline (oxide) shell. 90% of primary $Fe_{75}Cu_{25}$ and $Fe_{60}Cu_{40}$ particles have spherical shape and the rest 10% are cubic. All $Fe_{25}Cu_{75}$ particles are spherical. Iron-rich $Fe_{75}Cu_{25}$ nanoparticles (both cubic and spherical) have a bcc alloy core, while copper-rich $Fe_{25}Cu_{75}$ are fcc. The HRTEM analysis showed that the core of $Fe_{60}Cu_{40}$ particles has a bcc structure. However, powder diffraction shows weak rings corresponding to fcc structure (Fig.3.5 (a)). Either small amount of particles has fcc structure, or fcc diffraction rings are produced by Cu clusters in the oxide shell. The observed structures coincide with the ones expected from the phase diagram of metastable Fe-Cu alloys prepared by sputter deposition (Fig.1.14 (b)).

Oxide shells of $Fe_{75}Cu_{25}$ and $Fe_{60}Cu_{40}$ particles are predominantly iron-rich, though
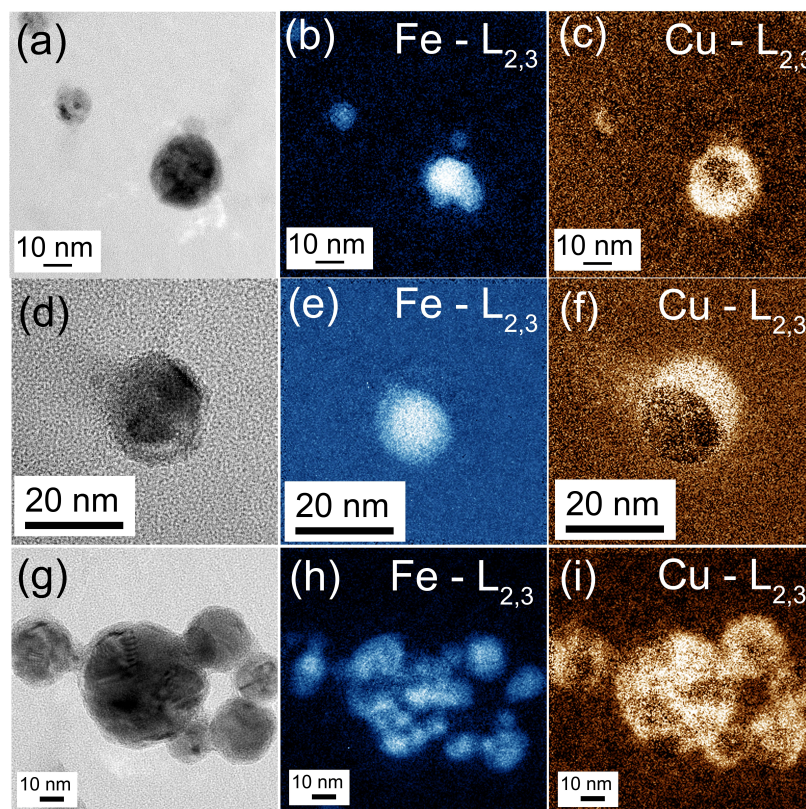
Figure 3.23: (a),(d),(g) Zero-loss images of in-flight annealed $Fe_{25}Cu_{75}$ nanoparticles. (b),(e),(h) Corresponding Fe-$L_{2,3}$ elemental maps. (c),(f), (i) Corresponding Cu-$L_{2,3}$ elemental maps. Elemental maps are presented in false colors.

Cu clusters are also present. Both Fe and Cu are present in the oxide shells of $Fe_{25}Cu_{75}$ particles. This result is consistent with the investigation of of air oxidation of Fe-Cu alloys presented in reference [150].

Structure of in-flight annealed Fe-Cu nanoparticles. After in-flight annealing $Fe_{75}Cu_{25}$ particles preserve their bcc single-crystal core. The annealed $Fe_{25}Cu_{75}$ particles are polycrystalline and consist of bcc and fcc clusters. The annealed $Fe_{60}Cu_{40}$ particles have a single-crystal core, however, particle with both fcc and bcc cores are found. All in-flight annealed particles have spherical shape.

Phase segregation in Fe-Cu nanoparticles. Thermal treatment at 1273 K for 0.32 s
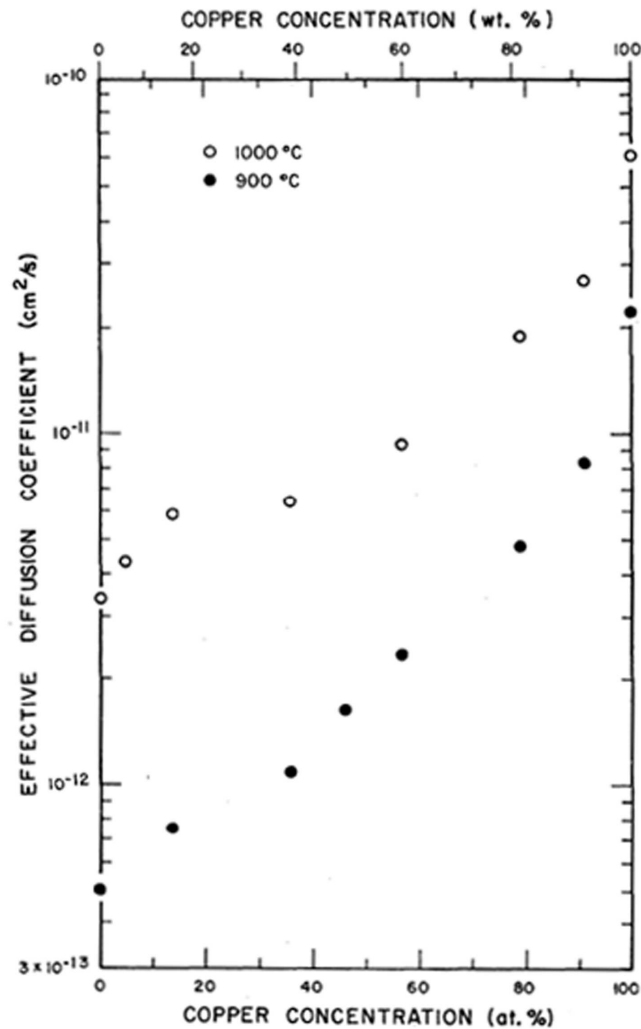
Figure 3.24: Effective diffusion coefficients of Fe as a function of Cu concentration in Fe-Cu alloys at 1000°C (white circles) and 900°C (black circles) [149].

promotes phase segregation in all samples, though its effect depends on the Cu concentration.The phase segregation in Fe$_{75}$Cu$_{25}$ and Fe$_{60}$Cu$_{40}$ proceeds via spinodal decomposition. In Fe$_{60}$Cu$_{40}$ the typical concentration oscillation and presence of Fe$_{rich}$-Cu and Fe - Cu$_{rich}$ is observed even in primary spherical particles. After in-flight annealing the amplitude of oscillation increases and particles become less homogeneous. In most cases particle's

core consist of several intertwined iron-rich and copper-rich regions. However, in some in-flight annealed $Fe_{60}Cu_{40}$ particles segregation occurs by forming a copper-rich core surrounded by iron-rich shell (Fig.3.19 (b)); the latter is oxidized after exposing samples to the atmospheric conditions. In the in-flight annealed $Fe_{25}Cu_{75}$ particles, almost complete segregation of iron and copper is observed, which means that phase segregation proceeds via nucleation and growth.

Apparently, the thermal stability of Fe-Cu nanoalloys decreases with increasing Cu concentration. This can be explained by the increasing of iron diffusion rate in the Fe-Cu alloy with copper concentration. Fig.3.24 shows the effective diffusion coefficients of Fe as a function of Cu concentration in Fe-Cu alloys at 1000^oC (white circles) and 900^oC (black circles). The values of the diffusion coefficients for $Fe_{75}Cu_{25}$, $Fe_{60}Cu_{40}$ and $Fe_{25}Cu_{75}$ are: $D_{Fe \to Fe_{75}Cu_{25}} = 6.18 \cdot 10^{-12}$ cm^2/s, $D_{Fe \to Fe_{60}Cu_{40}} = 6.36 \cdot 10^{-12}$ cm^2/s, $D_{Fe \to Fe_{25}Cu_{75}} = 1.77 \cdot 10^{-11}$ cm^2/s [149].

Several features like the presence of cubic nanoparticles in primary $Fe_{75}Cu_{25}$ and $Fe_{60}Cu_{40}$ samples, different ways of segregation in in-flight annealed $Fe_{60}Cu_{40}$ and $Fe_{25}Cu_{75}$ nanoparticles of the same size (see Fig.3.19 and Fig.3.23), and the presence of small pure Cu nanoparticles in the $Fe_{25}Cu_{75}$ sample can be explained by non-uniformity of plasma density (see *Introduction: Factors influencing the properties of nanoparticles prepared by magnetron sputtering.*). For example, the cubic primary $Fe_{60}Cu_{40}$ particles have uniform distribution of Fe and Cu, while the spherical one show oscillation of Fe and Cu concentration. It means that cubic particles are formed in a different thermal environment and are cooled down faster. As a result the more homogeneous Fe-Cu alloy phase is stabilized before segregation takes place.

Chapter 4

Structure, morphology, and ageing of Fe-Ag Janus nanoparticles

In this chapter the structural properties and ageing of Janus Fe-Ag nanoparticles prepared by DC magnetron sputtering with in-flight annealing at 1273 K are studied. The two types of Janus Fe-Ag nanoparticles - dumbbell and "raspberry" (with corresponding primary particles prepared under the same conditions but without annealing) were obtained under preparation parameters listed in table 4.1.

Table 4.1: Preparation parameters of Fe-Ag nanoparticles

Sample	Sputtering target	Nominal composition	Total gas pressure	Gas mixture (flow rate)	Annealing temperature
dumbbell	Iron target patched with six silver pieces (see Fig.2.3)	Fe: 80 at.% Ag: 20 at.%	0.5 mbar	Ar (50 sccm) + He (50 sccm)	1273 K
"raspberry"				Ar (50 sccm)	
primary$_{dumbbell}$				Ar (50 sccm) + He (50 sccm)	room temperature
primary$_{"raspberry"}$				Ar (50 sccm)	

4.1   Dumbbell Fe-Ag nanoparticles

4.1.1   As-prepared in-flight annealed Fe-Ag nanoparticles

Fig.4.1(a-d) shows four typical high resolution TEM micrographs of as-prepared Fe-Ag nanoparticles produced in a gas mixture of Ar and He (introduced at a flow rate of f_{Ar}=f_{He}=50 sccm) and in-flight annealed at 1273 K. The distinct contrast in the images reveals the dumbbell-like shape of the nanoparticles consisting of one faceted part and another part with a core-shell structure. The average particle dimensions (see Fig.4.1(d)) were determined to be **a** = 10 ± 0.5 nm and **b** = 6 ± 0.5 nm (faceted part), **c** = 12 ± 0.5 nm and **d** = 8 ± 0.5 nm (spherical core-shell part).

The contrast in Fig.4.1(a-d) indicates that the dark faceted part consists of or has a high silver concentration due to the fact that the heavier element produces a darker contrast in TEM bright field images. Consequently, the brighter spherical part is expected to have a lower Ag concentration.

Fig.4.2(a) shows a HRTEM micrograph of Fe-Ag nanoparticle. FFT images obtained from areas **1**(faceted part) and **2**(core of the spherical part) marked with white squares on the micrograph are shown in Fig.4.2(b, c), respectively. The d-spacings determined from the FFT image in Fig.4.2(b) are 0.243 ± 0.005 nm and 0.206 ± 0.005 nm, which correspond, respectively, to the d-spacings of the {111} (white-encircled) and {200} (white-framed) planes of fcc Ag. The lattice parameter is obtained as 0.408 ± 0.007 nm, which agrees well with that of fcc Ag [151]. The beam direction **B** is parallel to [011].

The FFT image in Fig.4.2(c) can be interpreted as the sum of two overlapping diffraction patterns. The first pattern belongs to bcc Fe viewed in the [001] direction: white-encircled spots give a d-spacing of 0.206 ± 0.005 nm, which corresponds to the spacing between {110} bcc iron planes. This gives a lattice parameter of 0.290 ± 0.003 nm [152]. Thus, the Ag and Fe parts are found to lie epitaxially on the (001) plane (see Fig.4.2(d)), whereby the Fe part is rotated by 45° around an axis perpendicular to the Ag lattice. The Ag(001)<100>‖Fe(001)<110>epitaxial relationship is quite common, as it has a small
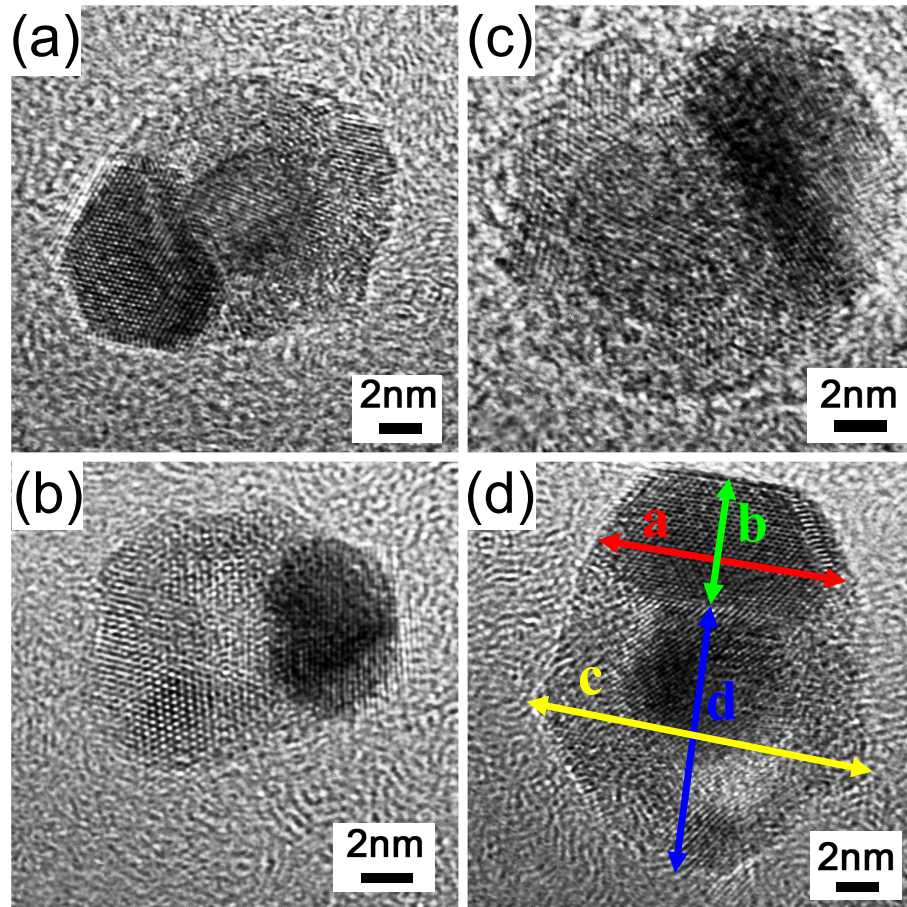
Figure 4.1: (a-d) Typical TEM micrographs of as-prepared Fe-Ag nanoparticles in-flight annealed at 1273 K. The dimensions **a,b,c,d** are shown on (d) by colored arrows.

in-plane mismatch of about 0.8% [153].

The yellow-encircled spots with d-spacings 0.287 ± 0.005 nm correspond to the {220} family of planes of iron oxide (either maghemite γ-Fe_2O_3 or magnetite Fe_3O_4) [147, 148]. The spots corresponding to {400} oxide planes overlap with the spots corresponding to {110} planes of bcc Fe. The spots marked with red arrows allow to identify the iron oxide as γ-Fe_2O_3 as they correspond to {130} planes which are only visible in the diffraction pattern of maghemite. This is proved by CrystalMaker$^{\circledR}$ simulations of Fe_3O_4 and γ-Fe_2O_3 diffraction patterns taken with the electron beam parallel to the [001] direction (Fig.4.3). The measured d-spacing is 0.268 ± 0.005 nm is in agreement with the literature value of

Figure 4.2: (a) HRTEM micrograph of an as-prepared in-flight annealed Fe-Ag nanoparticle. (b) FFT image obtained from area "1" marked with the white square in the image (a). (c) FFT image obtained from area "2" marked with the white square in the image (a). White and yellow circles mark γ-Fe$_2$O$_3$ {400} (Fe {110}) and {220} plane families, respectively. Red arrows mark the γ-Fe$_2$O$_3$ {130} plane family. (d) HRTEM micrograph of an as-prepared Fe-Ag nanoparticle with facets shown with colored lines.

0.264 nm [148], as well as the angle between (-130) and (-310) planes (measured value: $\alpha_{(130)} = 52 \pm 1°$, expected value: 53°). The epitaxial relationship between Fe and γ-Fe$_2$O$_3$ is Fe(011)<100>∥γ-Fe$_2$O$_3$(001)<100>.

The structural analysis of the shell of the spherical part of the Fe-Ag nanocomposite in
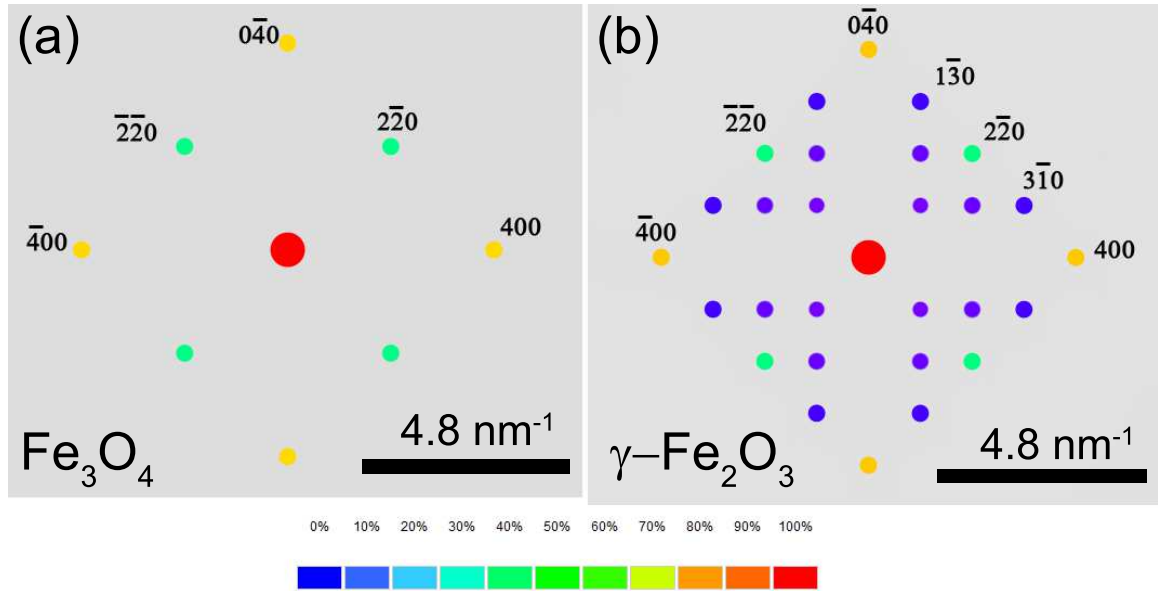
Figure 4.3: CrystalMaker$^{\circledR}$ -simulated diffraction patterns of (a) Fe_3O_4 and (b) γ-Fe_2O_3. The beam direction **B** is [001]. Diffraction spots are color coded by intensity from red (the highest) to blue (the lowest).

Fig.4.4(a),(b) reveals that its structure also corresponds to γ-Fe_2O_3 and Fe_3O_4. The measured d-spacings 0.205 ± 0.005 nm and 0.255 ± 0.005 nm correspond to $\{400\}$ and $\{311\}$ planes of γ-Fe_2O_3/Fe_3O_4 [147, 148], respectively. The measured angles $\alpha = 35 \pm 1°$, $\beta = 72 \pm 1°$ correspond to the angle between (-1-31) and (1-31) planes, and the angle between (1-31) and (400) planes, respectively (see Fig.4.4(c), which shows the CrystalMaker$^{\circledR}$ -simulated diffraction patterns of maghemite and magnetite with the beam in the [031] direction). The spots corresponding to the $\{130\}$ planes of maghemite are not visible in the diffraction pattern in Fig.4.4(b). However, their absence does not exclude the possibility of maghemite formation.

The average chemical composition of the particles was measured to be $C_{Ag} = 21 \pm 3$ at.%, $C_{Fe} = 79 \pm 3$ at.%. Spectra were taken from 10 different particles.

To probe the local compositional distribution within the individual nanoparticles, spatially resolved EDXS line-scans were performed on the Fe-Ag particles using a focused
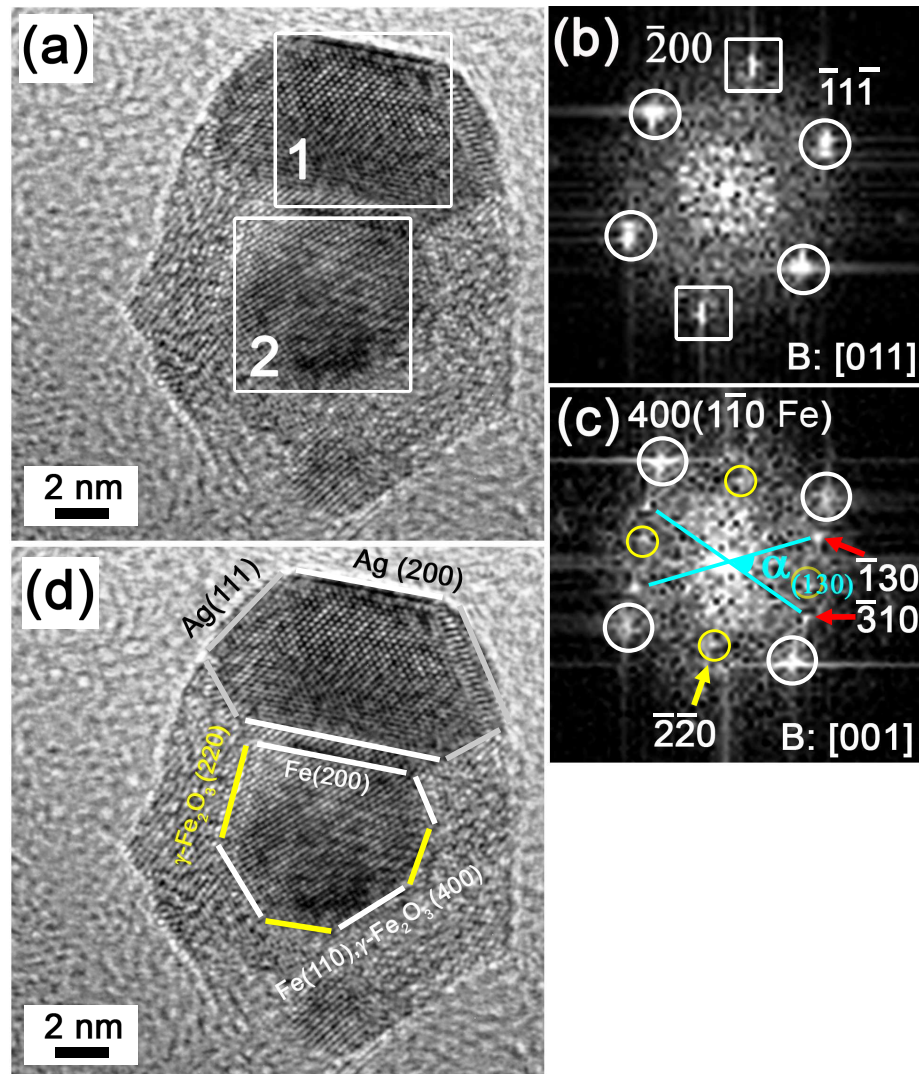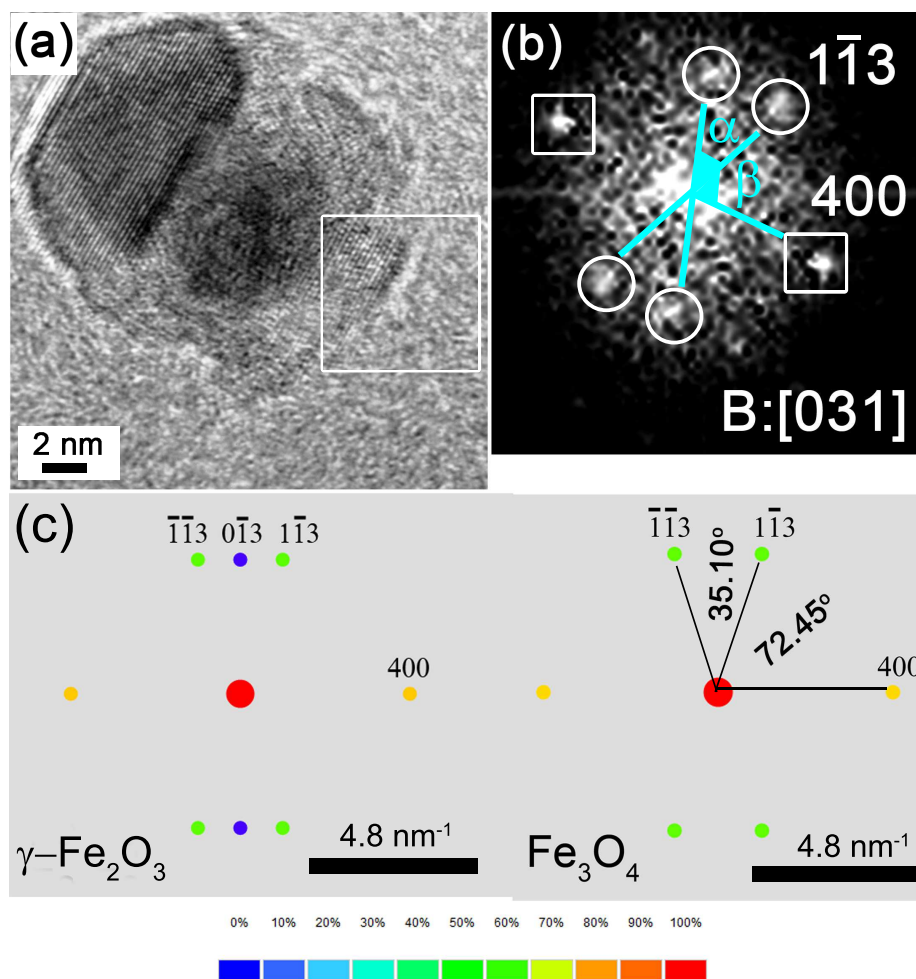
Figure 4.4: (a) HRTEM micrograph of an as-prepared in-flight annealed Fe-Ag nanoparticle. (b) FFT image obtained from the area marked with the white square in image (a). White circles and squares mark iron oxide {113} and {400} plane families, respectively. (c) CrystalMaker® -simulated diffraction patterns of γ-Fe_2O_3 and Fe_3O_4. The beam direction **B** is [031]. Diffraction spots are color coded by intensity. The most intense reflections are colored red, the least intense are colored blue (see inset).

electron probe of $\sim$1 nm in the STEM mode. Fig.4.5(a) shows the HAADF STEM image of two as-prepared dumbbell-shaped Fe-Ag nanoparticles. The contrast in HAADF STEM images is highly sensitive to the atomic number of the scattering atoms, allowing to identify the brighter part of the particle as silver and the less bright part as iron and iron oxides. This is confirmed by EDX line-scans. The path of the electron probe is indicated by the arrow

(Fig.4.5(a)). The extracted characteristic x-ray line-scan profiles are plotted in Fig.4.5(b). The profile shows almost full segregation of silver and iron with a small overlap, which may also be due to the finite size of the electron probe or to the non-parallel orientation of the Fe-Ag interface with the electron beam.
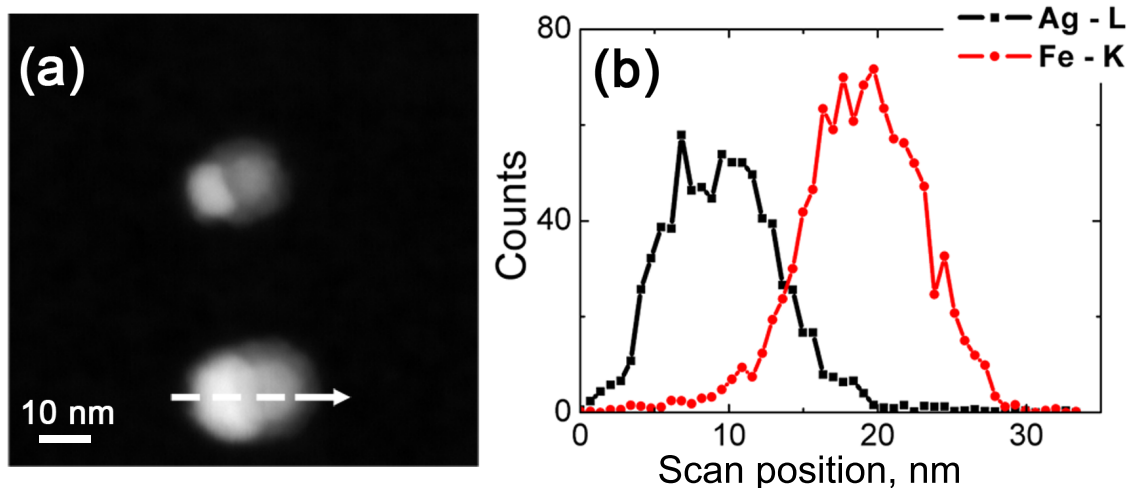
Figure 4.5: (a) HAADF STEM image of as-prepared Fe-Ag particles. The white dashed arrow shows the path of the electron beam during the scan. (b) Line-scan profile of characteristic x-ray Fe-K and Ag-L lines as a function of electron probe position on the particle.

The EDX spectra were obtained from various parts of the particles. Fig.4.5(a) shows the HAADF STEM image of the as-prepared Fe-Ag nanoparticle. Red points mark the areas from which EDX spectra (Fig.4.5(b),(c)) were taken. EDX spectrum obtained from the area corresponding to the bright Ag part (Fig.4.5(b)) shows the absence of iron peaks, while the EDX spectrum obtained from the core-shell area (Fig.4.5(c)) has no peaks corresponding to silver.

These results indicate that full segregation of iron and silver occurs within the particle. However, since the EDX method is limited to $\sim$2 % compositional accuracy [138], up to 2 at.% Ag could reside inside the Fe and Fe-oxide part (and vice versa).
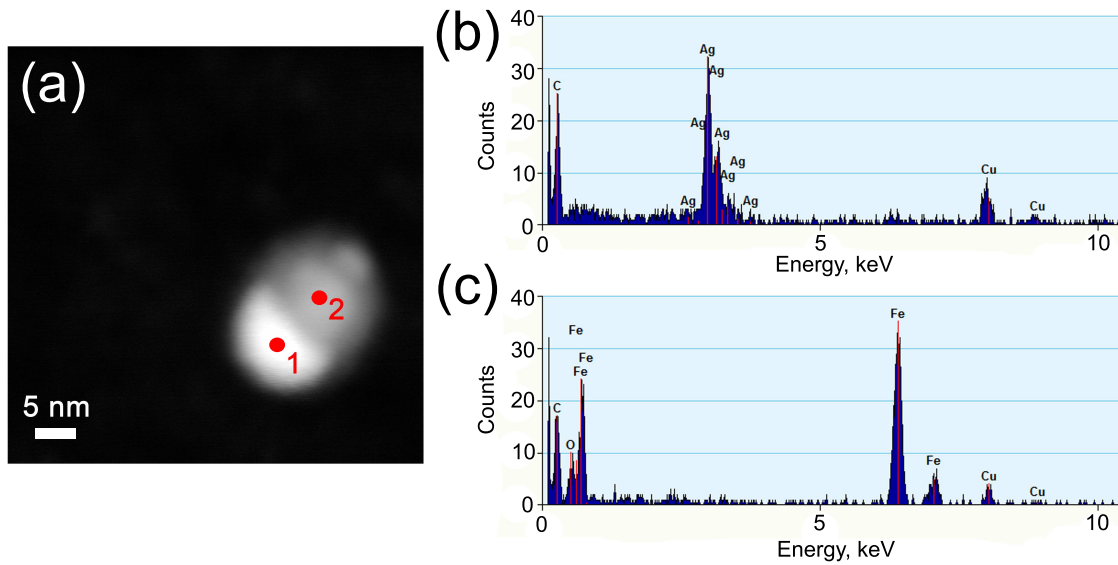
Figure 4.6: (a) HAADF STEM image of an as-prepared Fe-Ag particle.(b) EDX spectrum obtained from point "1" in the image (a). (c) EDX spectrum obtained from point "2" in the image (a).

4.1.2   Primary$_{dumbbell}$ **Fe-Ag nanoparticles**

Fig.4.7(a-d) shows four typical HRTEM micrographs of Fe-Ag particles prepared under the same conditions as the particles described above, but without in-flight annealing (primary$_{dumbbell}$ particles). HRTEM micrographs show that the particles are polycrystalline, spherical and partially oxidized. In some particles small clusters with Ag fcc structure could be identified. The inset in Fig.4.7(a) shows the FFT image obtained from the area marked with the white square. The diffraction pattern in this FFT image corresponds to fcc Ag viewed in [011] direction. The particle-size was found to vary from 14 to 23 nm and the mean diameter was estimated to be $\bar{d} = 20.8 \pm 0.5$ nm.

EDX measurements showed that both iron and silver are present within the particle, and the average concentrations C of silver and iron were found to be $C_{Ag} = 23 \pm 3$ at.%, $C_{Fe} = 77 \pm 3$ at.%. Spectra were measured for 10 different particles. EDX line-scans shown in Fig.4.8(b,d) reveal partial segregation of Fe and Ag within the particles.
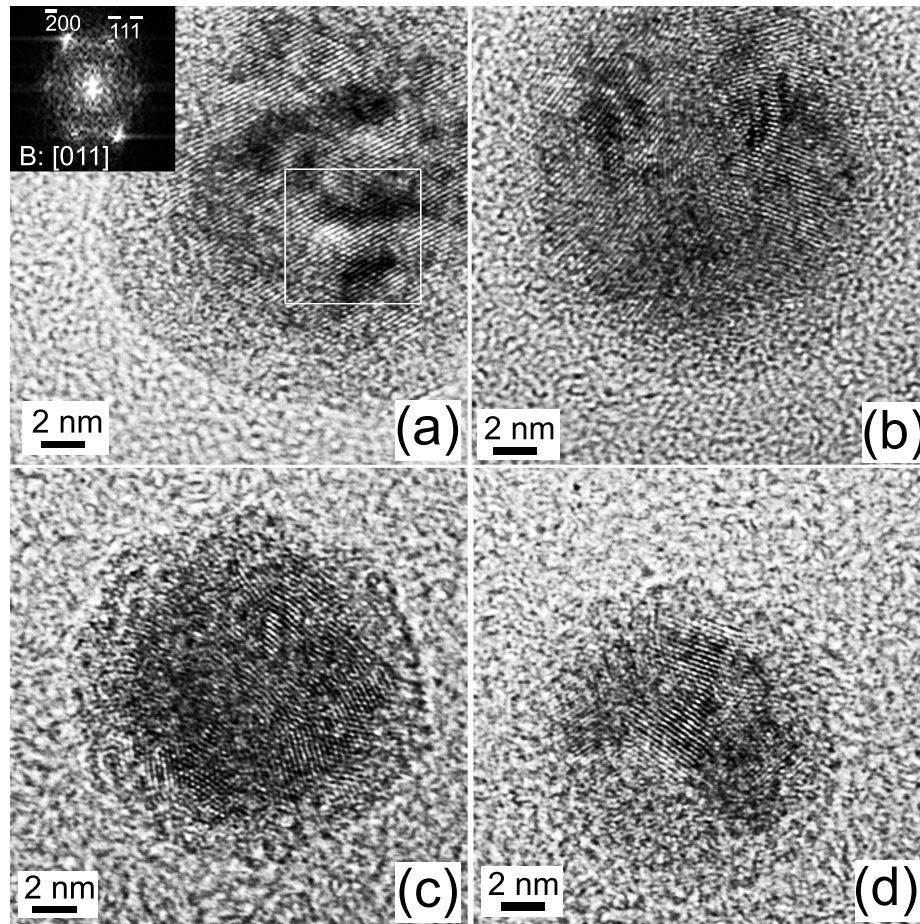
Figure 4.7: (a-d)Typical TEM micrographs of as-prepared primary$_{dumbbell}$ Fe-Ag nanoparticles. (a, inset) FFT image obtained from the area of the image (a) marked with the white square.

4.1.3 Aged in-flight annealed dumbbell Fe-Ag nanoparticles

Fe-Ag nanoparticles in-flight annealed at 1273 K were also analyzed after storage for 5 months under ambient atmospheric conditions. Fig.4.9 shows two typical micrographs of the aged Fe-Ag in-flight annealed particles. After ageing, some particles have divided into two parts (Fig.4.9(a)) and others still possess the dumbbell morphology (Fig.4.9(b)). The contrast distribution in Fig.4.9(b) indicates void formation inside the particle.

HRTEM micrographs of Fe-Ag nanoparticles with corresponding FFT images are shown in Fig.4.10. The FFT image (Fig.4.10(c)) obtained from area "1" in Fig.4.10(a) shows the
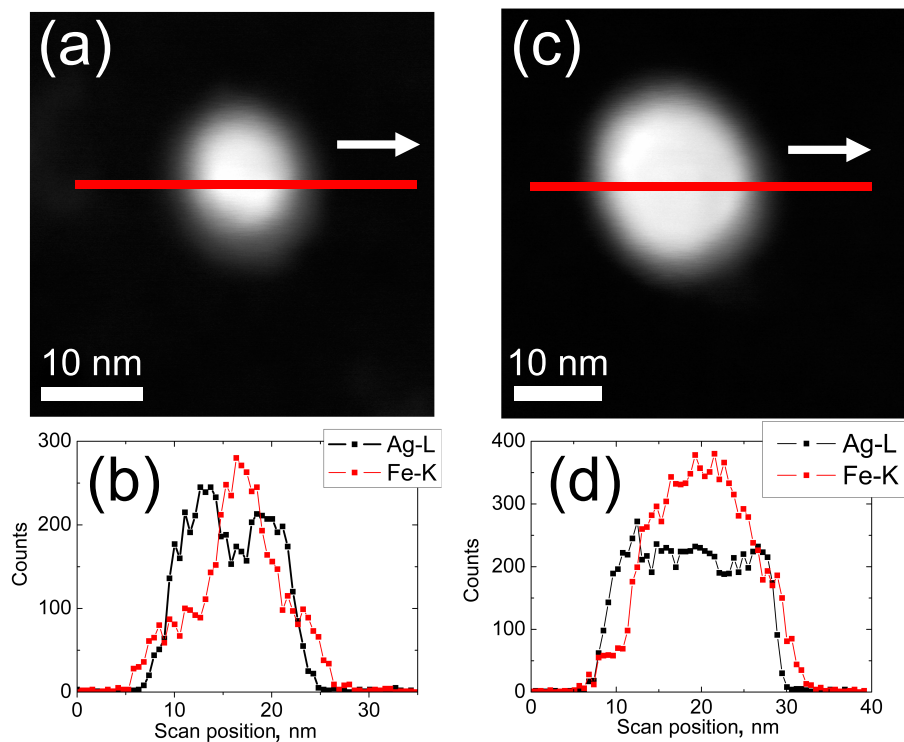
Figure 4.8: (a,c) HAADF STEM images of as-prepared primary$_{dumbbell}$ Fe-Ag particles. The red lines indicate the path of the electron beam during the scan. The scan direction is shown by white arrows. (b,d) Line-scan profiles of characteristic x-ray Fe-K and Ag-L lines as a function of electron probe position on the particles in images (a) and (c), respectively.
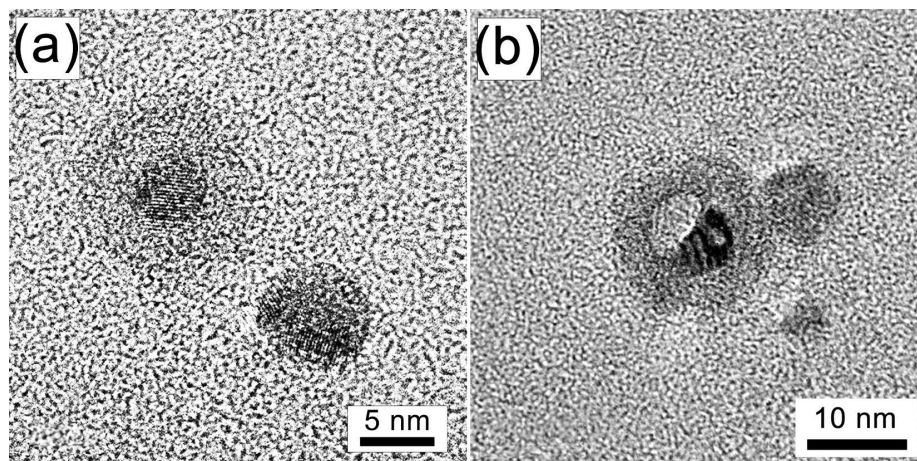
Figure 4.9: Dumbbell Fe-Ag nanoparticles after ageing. (a), (b) TEM micrographs of the aged in-flight annealed dumbbell Fe-Ag nanoparticles.
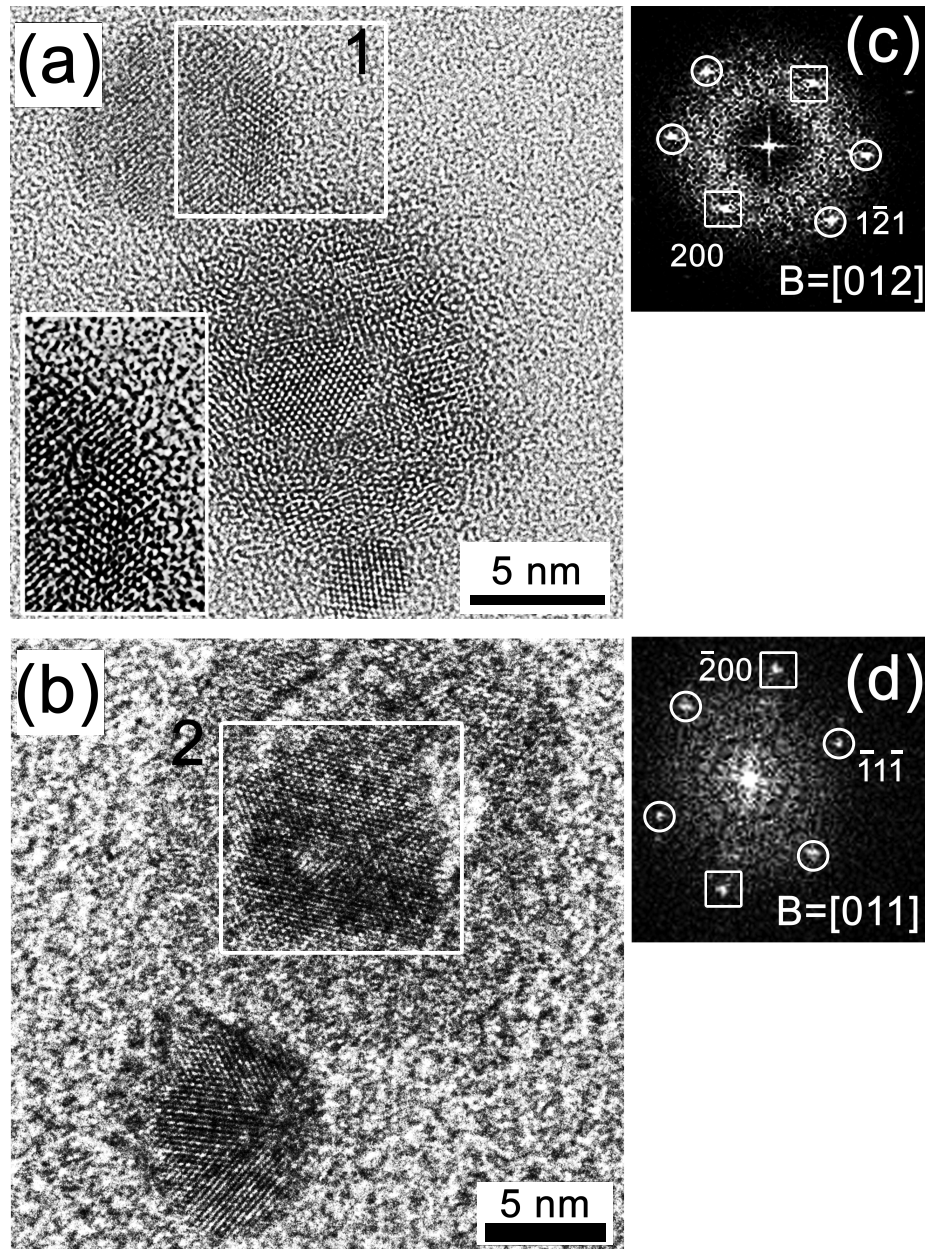
Figure 4.10: Dumbbell Fe-Ag nanoparticles after ageing. (a), (b) HRTEM micrographs of the aged Fe-Ag nanoparticles. (c) FFT image obtained from area "1" in the image (a). (d) FFT image obtained from area "2" in the image (b). (a, inset) Magnified image of area "1".

spots corresponding to $\{200\}$ (white-squared) and $\{121\}$ (white-circled) planes with d-spacings 0.234 ± 0.005 nm and 0.192 ± 0.005 nm (literature values are $d_{200} = 0.236$ nm, $d_{121} = 0.193$ nm) giving a lattice parameter of 0.472 ± 0.007 nm, which matches well with

the lattice parameter of Ag_2O with a = 0.473 nm [154]. Fig.4.11 shows the crystal structure of silver oxide and the CrystalMaker$^{\circledR}$ -simulated diffraction pattern (beam direction **B** is parallel to [012]).
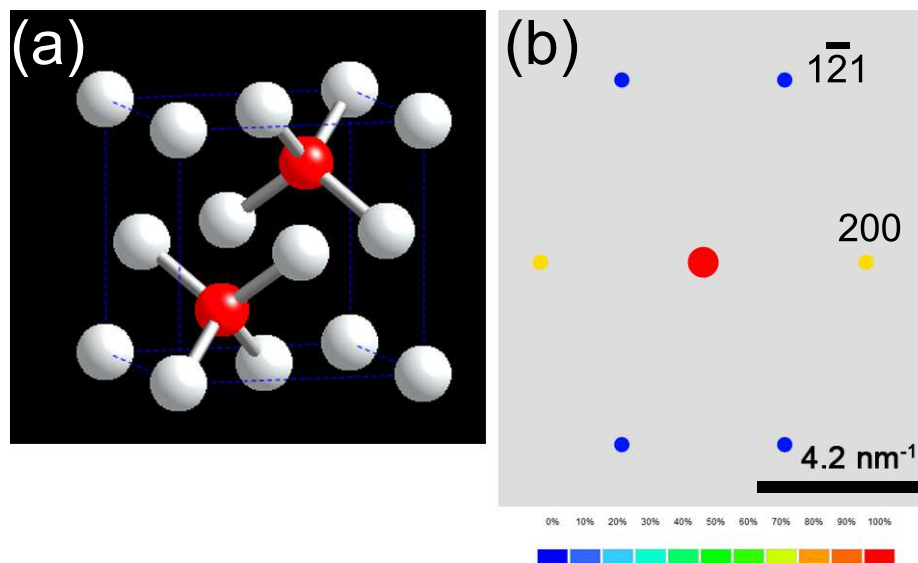
Figure 4.11: (a) Crystal structure of Ag_2O. White spheres correspond to Ag, red to O atoms. (b) CrystalMaker$^{\circledR}$ -simulated diffraction pattern with beam direction **B** in [012]

The results show that the faceted fcc Ag parts of as-prepared dumbbell composites evolve into spherical Ag_2O particles, and in some cases, they are separated entirely from the rest of the composite. The Ag_2O particles are not single-crystalline but possess a twin structure. The diffraction pattern in the FFT image in Fig.4.10(d) is identical to the one in Fig.4.2(b) and shows that the core part corresponding to area "2" in Fig.4.10(b) is fcc Ag. The Ag part in the core is single crystalline.

HRTEM images indicate that the larger part of the nanocomposite has a core-void-shell structure with the shell thickness varying from 2.4 to 4 nm, as will become more evident from EDX analysis results presented below.

Fig.4.12(a) and (b) show HAADF STEM images of two aged Fe-Ag particles with corresponding EDX line-scan profiles in Fig.4.12(c) and (d). Fig.4.13(b) and (c) show two-dimensional maps of x-ray Fe and Ag lines in the aged Ag-Fe particle in Fig.4.13(a). The
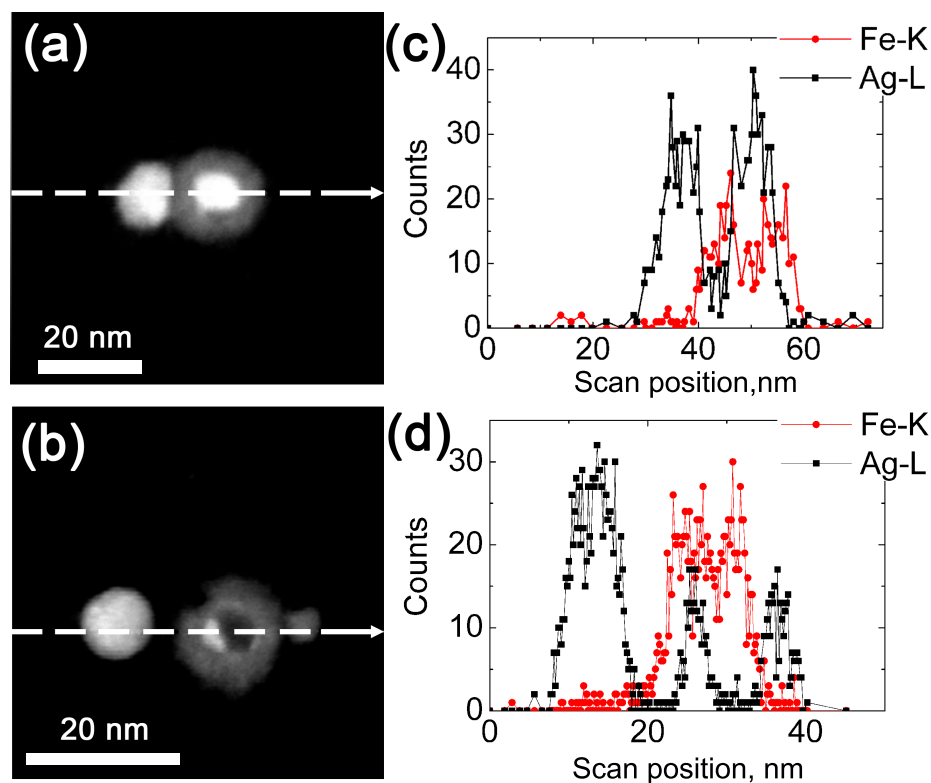
Figure 4.12: Dumbbell Fe-Ag nanoparticles after ageing. (a),(b) HAADF STEM images of the aged Fe-Ag particles. The white dashed arrows show the path of the electron beam during the scan. (c),(d) Corresponding line-scan profiles of characteristic x-ray Fe-K and Ag-L lines as a function of electron probe position on the particle. The brighter parts correspond to Ag. The darker parts correspond to iron oxide.

RGB image constructed by superimposing Fe and Ag maps is presented in Fig.4.13(d). The measurements were performed using a double Cs-corrected JEOL JEM-2200FS microscope [155]. According to the line-scans and the elemental mapping, the bright regions in Fig.4.12(a) and (b) correspond to silver, and the darker regions consist of iron. This is consistent with the HRTEM analysis and confirm the aforementioned assumptions on structure and morphology of the aged particles.

However, HRTEM images and EDX line-scans provide only a two-dimensional projection of the nanocomposites, so it is possible that the silver part is located on top of the iron oxide particle. To prove that the Ag-void core is indeed situated inside the coated Fe-oxide shell, the three-dimensional morphology of a particle was studied by means of 3D electron
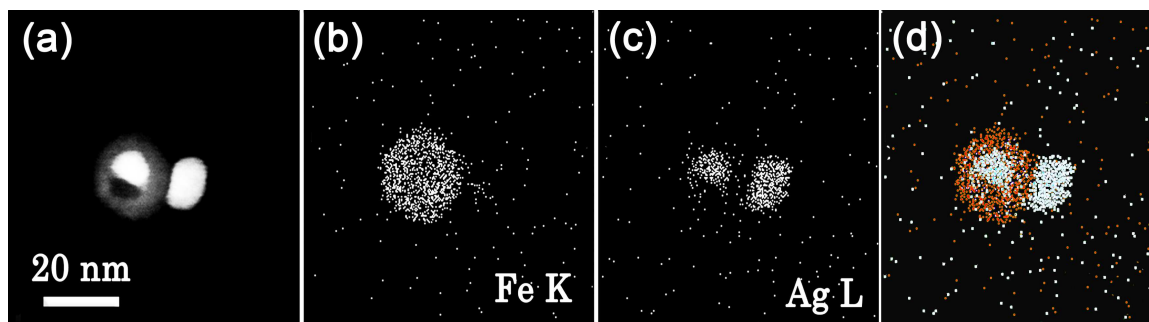
Figure 4.13: Dumbbell Fe-Ag nanoparticles after ageing. (a) HAADF STEM images of an aged Fe-Ag particle. (b)Corresponding elemental map of the characteristic x-ray Fe-K line. (c) Corresponding elemental map of characteristic x-ray Ag-L line. (d) RGB image constructed by superimposing Fe and Ag maps.
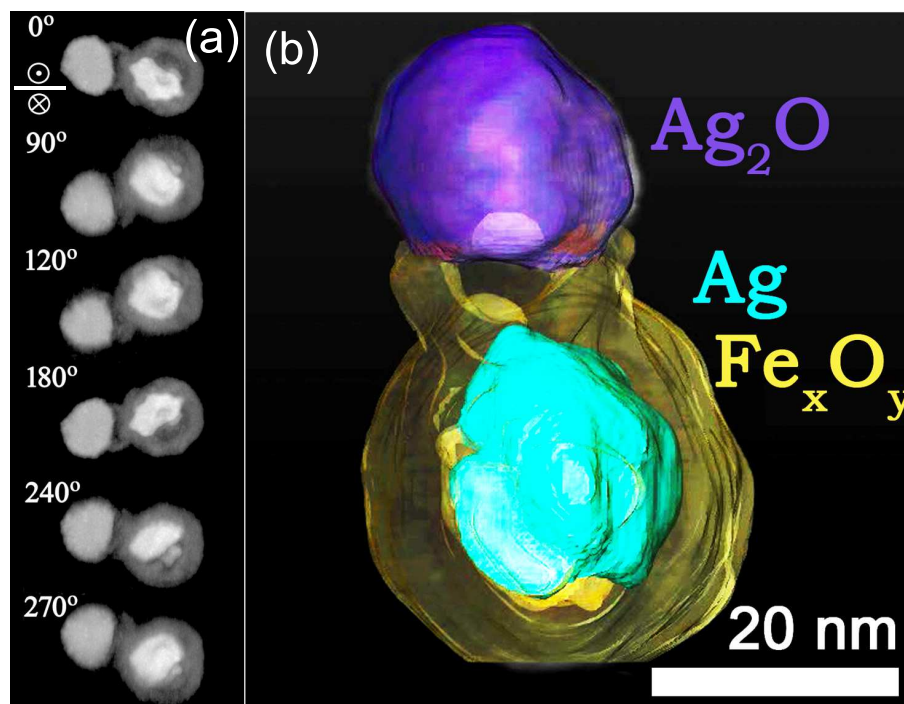
Figure 4.14: Dumbbell Fe-Ag nanoparticles after ageing. (a) Tilt series images of an aged Fe-Ag particle. The particle is rotated around a horizontal axis, lying in the plane of the figure, in the direction shown with the arrow 'head' and 'nock'. The brighter part corresponds to Ag. The less bright part is iron and iron oxide. (b) 3D reconstructed image of an aged Fe-Ag particle with color segmentation.

tomography. A tilt-series of images of the aged Fe-Ag nanoparticles rotated in $2°$ tilt-steps in a $\pm 65°$ angle-range was acquired with a FEI TEAM 1 microscope at the National Center for Electron Microscopy, Berkeley, CA [155]. Fig.4.14 (a) shows a 3D reconstruction for six projections of an aged Fe-Ag particle rotated around the horizontal axis lying in the plane of the figure in the direction shown with the arrow 'head' and 'nock'. Fig.4.14 (b) presents a 3D reconstructed image of an aged Fe-Ag particle with color segmentation, where the 3D features stand out more clearly. The colors were assigned to silver, silver oxide and iron oxide parts of the particles taking into consideration HAADF STEM contrast and results of EDX spectroscopy measurements. A video showing the continuous rotation of the particle and the details of the 3D morphology of the particle is attached to this thesis. The results of the tomography measurements prove that the silver cluster (bright part) is positioned inside the iron oxide shell. The silver cluster possesses an irregular morphology.

4.2 Fe-Ag nanoparticles with "raspberry" morphology

4.2.1 As-prepared in-flight annealed Fe-Ag nanoparticles

Fig.4.15 shows a TEM micrograph of as-prepared Fe-Ag particles in-flight annealed at 1273 K with corresponding size distribution (inset). These particles were produced in the presence of Ar with a flow rate of f_{Ar} = 50 sccm. The contrast in Fig.4.15 (for example, particles 1, 2 and 3) indicates that particles consist of a spherical part and a small amount of material located on its top; the so-called "raspberry" morphology [42]. The best fit for the particle size distribution, measured for the spherical part of the nanocomposite, is given by a normal distribution:

$$f_D = \frac{1}{\sigma\sqrt{2\pi}} e^{-\frac{1}{2}\left(\frac{D-D_m}{\sigma}\right)^2}. \tag{4.1}$$

Here, parameters D_m and σ denote the geometric mean particle diameter and geometric standard deviation, respectively. The expected value <d> ("average"particle diameter) is
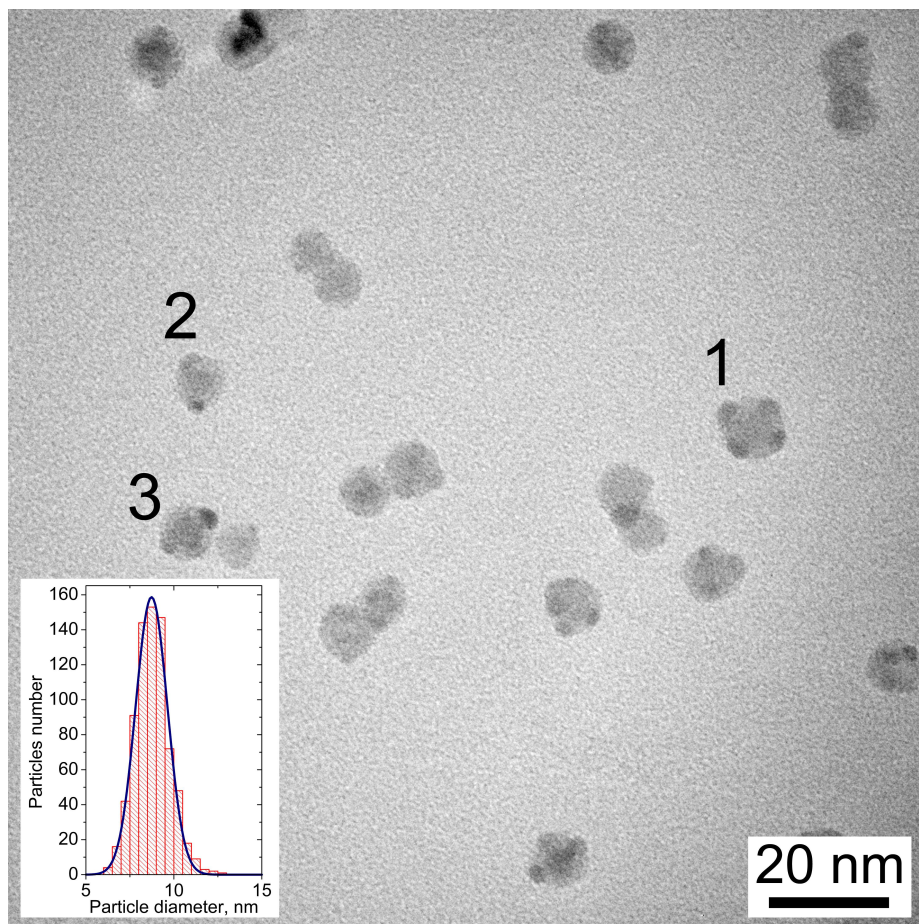
Figure 4.15: TEM micrograph of as-prepared in-flight annealed "raspberry" Fe-Ag nanoparticles. The inset shows the particle-size distribution.

equal to D_m, and the standard deviation $\Delta = \sigma^2$. The value of the geometric mean particle diameter, which in this case is the average diameter, is $D_m=<d>=9 \pm 1$ nm. The geometric standard deviation and the standard deviation are found to be $\sigma = 0.9 \pm 0.5$ nm $^{\frac{1}{2}}$ and Δ=0.8 ± 0.1 nm, respectively.

The size of the small silver parts of the "raspberry" was measured using HRTEM images (approximately 25) and varied from 2.5 to 4 nm. The size varied not only from particle to particle, but also within a single particle.

The typical HRTEM image of a "raspberry" Fe-Ag particle is shown in Fig.4.16(a).
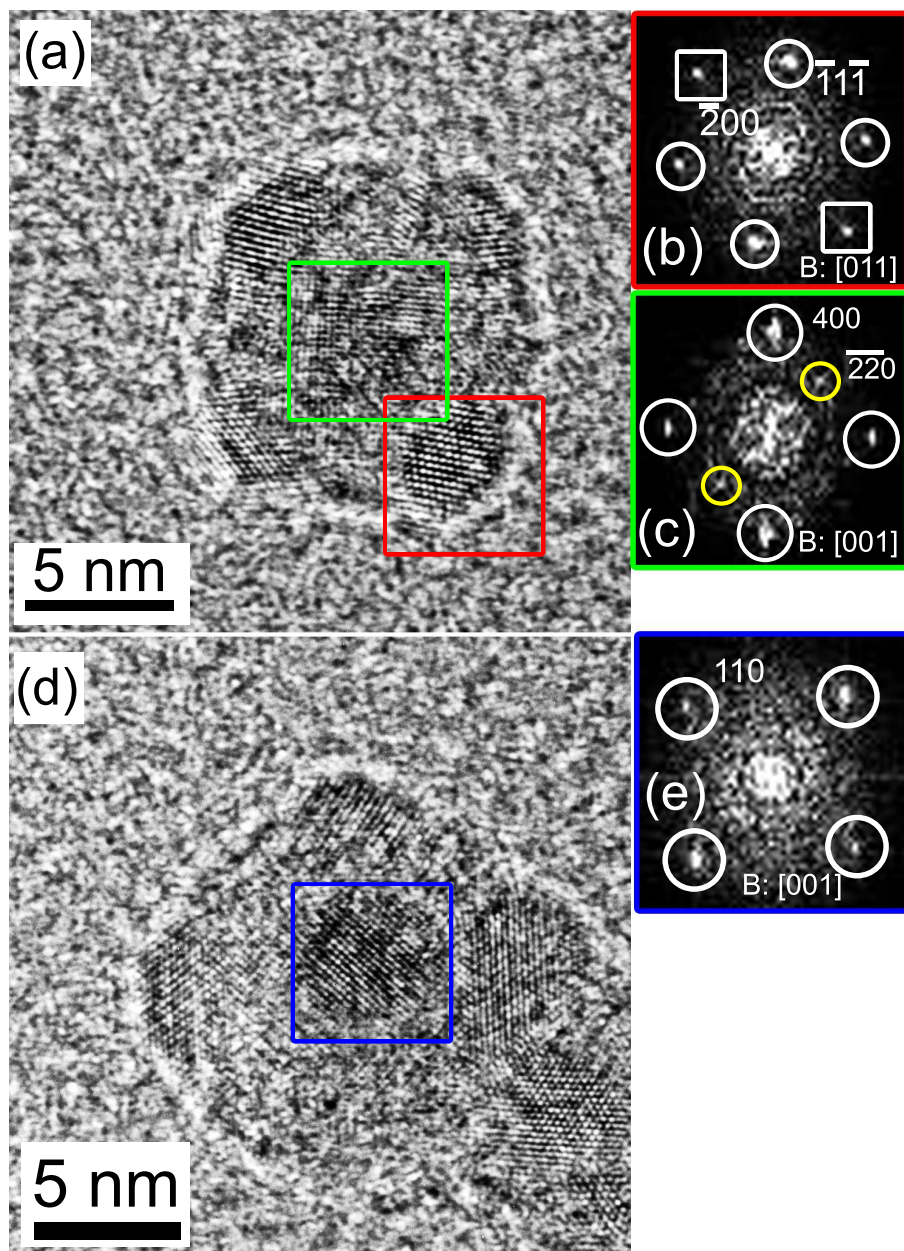
Figure 4.16: (a),(d) Typical HRTEM micrographs of as-prepared in-flight annealed "raspberry" Fe-Ag nanoparticles. (b) FFT image obtained from the area marked with the red square in the image (a). (c) FFT image obtained from the area marked with the green square in the image (a). (e) FFT image obtained from the area marked with the blue square in the image (d).

Here also, the contrast indicates four small parts surrounding the core-material (one of them marked with the red square). The FFT image obtained from the area marked with the red square is shown in Fig.4.16(b). The measured d-spacings are 0.237 ± 0.005 nm (white-encircled spots) and 0.207 ± 0.005 nm (spots marked with white squares) and correspond to $\{111\}$ and $\{200\}$ planes of fcc Ag, respectively. The lattice parameter is found to be 0.410 ± 0.007 nm, which agrees well with the literature value for fcc Ag [151]. The beam direction is parallel to [011].

The FFT image obtained from the "core" of the particle (area marked with the green square) is shown in Fig.4.16(c). The d-spacings corresponding to the diffraction spots marked with white circles are estimated to be 0.211 ± 0.005 nm (corresponding to $\{400\}$ planes of Fe_3O_4/γ-Fe_2O_3) and 0.298 ± 0.005 nm for reflections marked with yellow circles (corresponding to $\{220\}$ planes of Fe_3O_4/γ-Fe_2O_3). The beam direction is parallel to [001]. The FFT image in Fig.4.16(c) may be interpreted as the sum of two overlapping bcc Fe and Fe_3O_4/γ-Fe_2O_3 diffraction patterns. The particle in Fig.4.16(a) may consist of an Fe core and a Fe_3O_4/γ-Fe_2O_3 shell with silver parts on top or the Fe part may be completely oxidised. The latter is, however, less likely because fully oxidized Fe particles of such size would have pores [156] (see discussion section). TEM investigation showed no such pore formation at any magnification.

Fig.4.16(d) shows another HRTEM micrograph of a "raspberry" Fe-Ag particle. The FFT image obtained from the area marked with the blue square in Fig.4.16(d) is presented in Fig.4.16(e). The d-spacings corresponding to the diffraction spots marked with white circles are 0.207 ± 0.005 nm which is in good agreement with the d-spacing values for bcc Fe $\{110\}$ planes [152]. The absence of spots which would correspond to $\{220\}$ planes of iron oxide confirms the presence of a pure iron core.

The chemical composition of the particles was determined to be $C_{Ag} = 16 \pm 3$ at.%, $C_{Fe} = 84 \pm 3$ at.%. Spectra were taken from 10 different regions of about 250 nm in diameter and the average was determined. The investigation of the elemental concentration distribution within the particle was not possible because Fe-Ag particles were found to be

unstable under the high intensity electron beam which is required for EDX and EFTEM line-scans and mapping. Still, HRTEM analysis along with the fact that particles contained both silver and iron allows to assume that as-prepared in-flight annealed Fe-Ag particles prepared without He possess the "raspberry" morphology: small silver pieces attached to the iron-iron oxide core-shell spherical part.

4.2.2   Aged in-flight annealed Fe-Ag nanoparticles
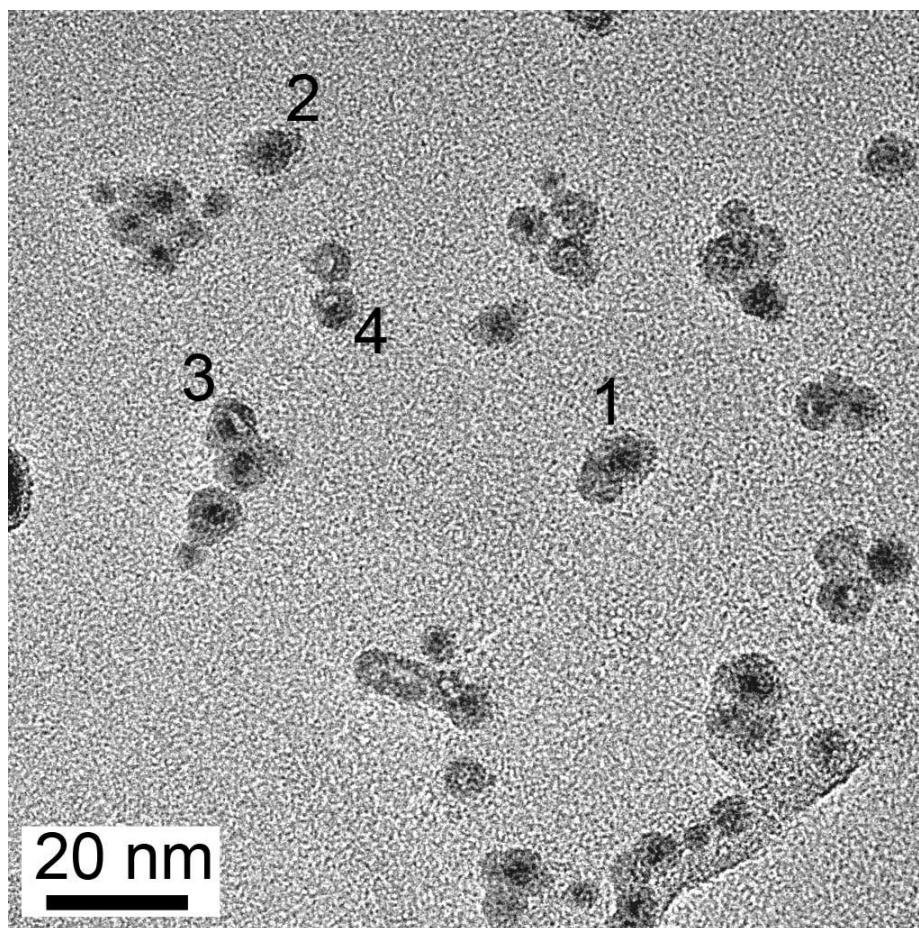
Figure 4.17: "Raspberry" Fe-Ag nanoparticles after ageing. TEM micrograph of aged in-flight annealed Fe-Ag nanoparticles.

The "raspberry" Fe-Ag particles were stored under the same conditions as the dumbbell

ones, but it was found that the raspberry particles attained their aged state more rapidly than the dumbell particles. While dumbbell particles preserved their morphology and structure for at least two months, the "raspberry" nanocomposites aged completely during this time.

The TEM image of the aged Fe-Ag nanoparticles is shown in Fig.4.17. These are spherical with a core-shell structure (e.g. particles 1 and 2) and a void formation is also seen within the particles (e.g. particles 3 and 4). The shell is polycrystalline with thickness varying from 2.3 to 3.7 nm. The thickness is also nonuniform within a single particle.

Two typical HRTEM images of aged Fe-Ag particles are presented in Fig.4.16(a) and (d). Particles in Fig.4.16(d) are spherical core-shell composites, while Fig.4.16(a) shows a void inside the particle. The FFT image obtained from the area marked with the white square in Fig.4.16(a) is shown in Fig.4.16(b). The measured d-spacings are estimated to be 0.258 ± 0.005 nm (reflections marked with yellow circles), 0.302 ± 0.005 nm (reflections marked with white squares), and 0.245 ± 0.005 nm (reflections marked with blue circles) which correspond to $\{311\}$ planes (0.253 nm), $\{220\}$ planes (0.297 nm), and $\{222\}$ planes (0.242 nm) of Fe_3O_4, respectively. The values of the angles α and β were measured to be $64 \pm 1°$ and $59 \pm 1°$. Fig.4.16(c) shows a CrystalMaker$^{®}$ -simulated diffraction pattern of Fe_3O_4 with the electron beam in [112] direction. It is identical to the diffraction pattern in Fig.4.16(b).

The FFT image obtained from the "core" part of the particle shown in Fig.4.16(d) is presented in Fig.4.16(e). The FFT image corresponds to fcc Ag viewed in the [011] direction. The measured d-spacings 0.205 ± 0.005 nm and 0.239 ± 0.005 correspond to the $\{200\}$ and $\{111\}$ planes, respectively).

The elemental distribution within the particles were investigated by means of EDX line-scans and EFTEM mapping. Fig.4.19(a) and (c) show HAADF STEM images of the aged Fe-Ag nanoparticles. The contrast indicates a core-shell structure. EDX line-scans were performed on nanocomposites marked with yellow squares in Fig.4.19(a) and (c), and the respective line-scan profiles are shown in Fig.4.19(b) and (d). Both line-scans indicate that the bright parts correspond to silver, and the grey parts to iron. This is consistent with data
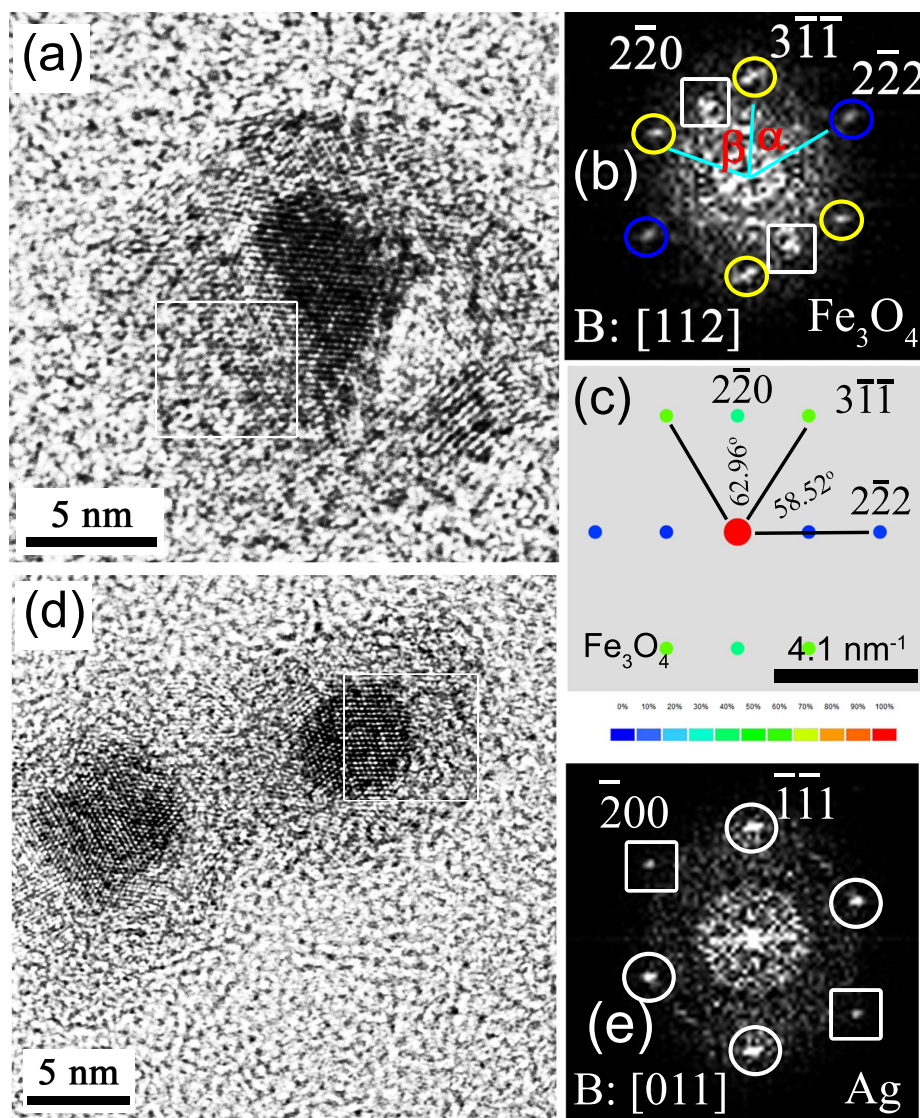
Figure 4.18: "Raspberry" Fe-Ag nanoparticles after ageing. (a),(d) HRTEM micrographs of aged "raspberry" Fe-Ag nanoparticles, (b) FFT images obtained from the area marked with the white square in the image (a), (c)CrystalMaker$^{\circledR}$ -simulated diffraction pattern of Fe_3O_4. The beam direction is [112]. Diffraction spots are color coded by intensity. The most intense reflections are colored red, the least intense are colored blue (see inset). (e) FFT image obtained from the area marked with the white square in image (d).

obtained from HRTEM images. The small dark spot seen in the upper left particle in the enlarged area of Fig.4.19(c)is due to void formation within the particle.
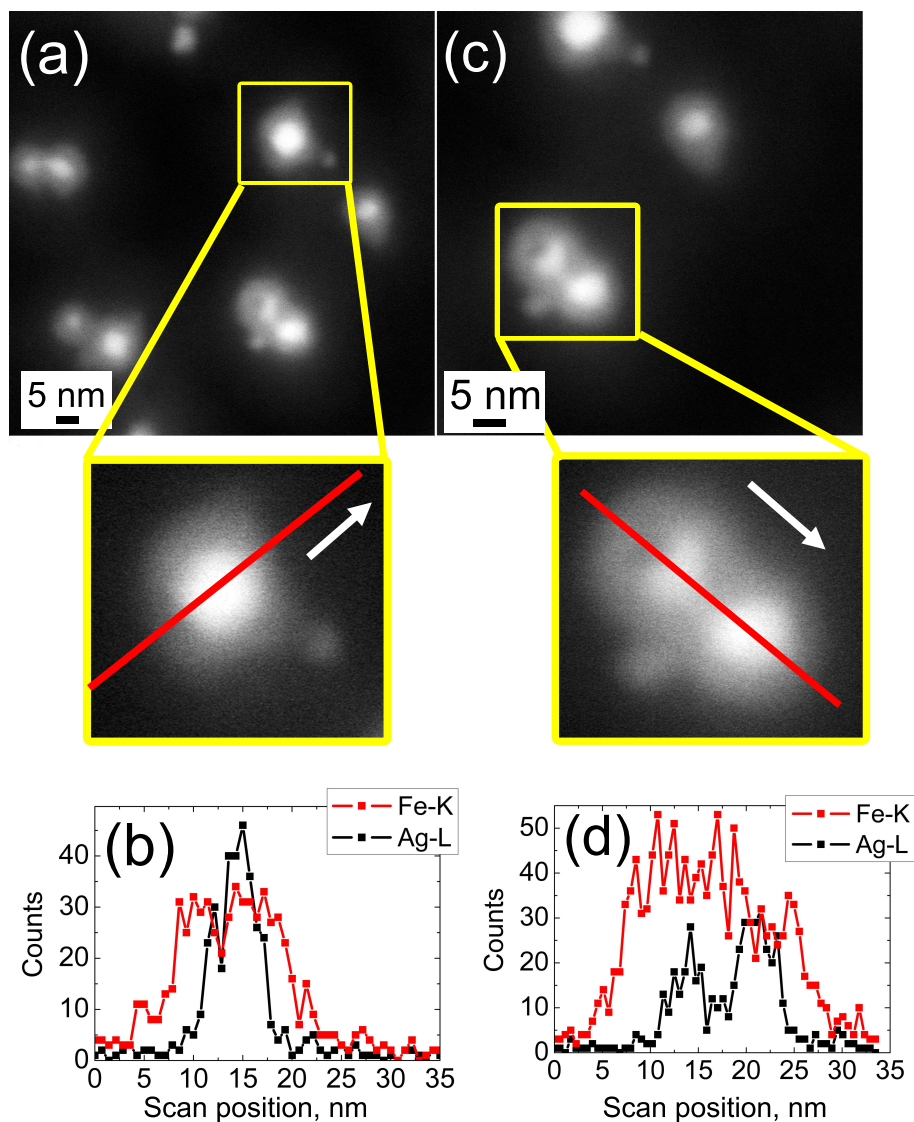
Figure 4.19: "Raspberry" Fe-Ag nanoparticles after ageing. (a),(c) HAADF STEM images of aged "raspberry" Ag-Fe nanoparticles. The particles on which the line-scans were performed are marked with the yellow squares. The red lines indicate the path of electron beam during the scan. The scan directions are shown with white arrows. (b),(d) Line-scan profiles of characteristic x-ray Fe-K and Ag-L lines as a function of electron probe position in images (a) and (c).

Two-dimensional elemental maps of the aged Fe-Ag nanoparticles were obtained by means of EFTEM. Fig.4.20(a) and (e) show the zero-loss images of aged raspberry Fe-Ag particles. Corresponding Fe-$L_{2,3}$ and Ag-$M_{4,5}$ elemental maps are presented in Fig.4.20(b)
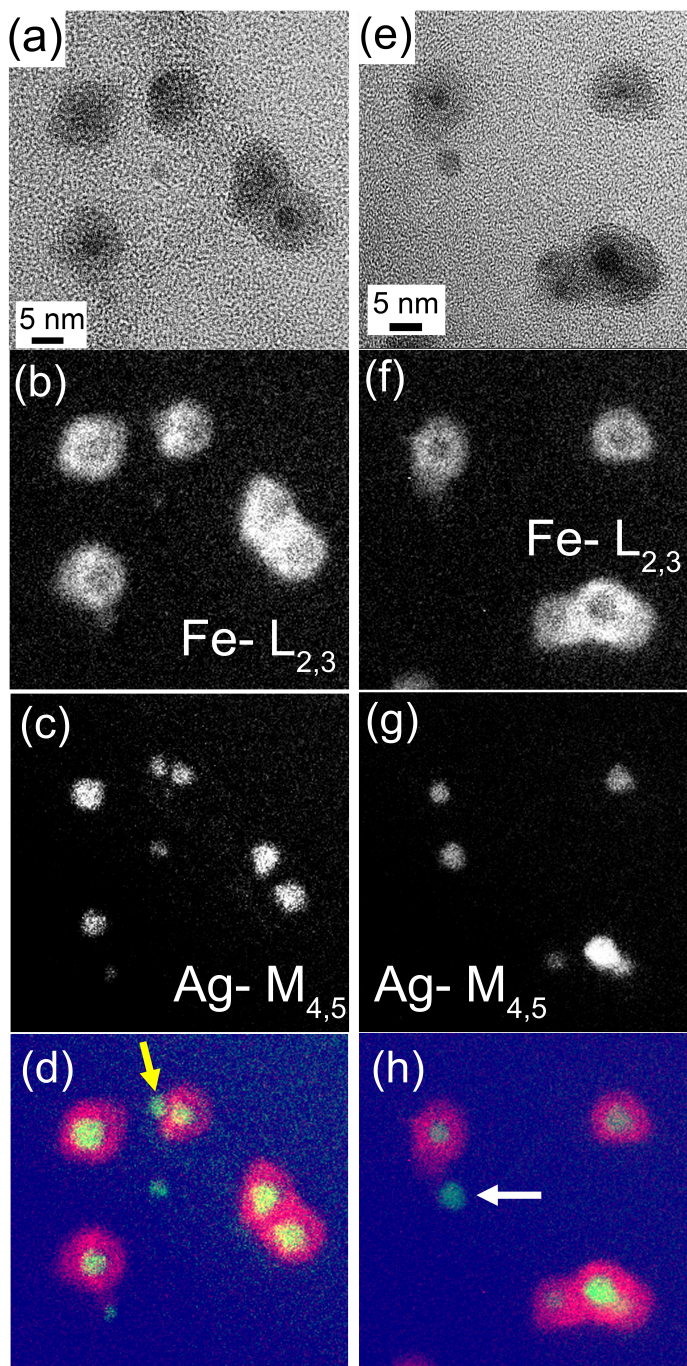
Figure 4.20: "Raspberry" Fe-Ag nanoparticles after ageing. (a),(e) Zero-loss images of the aged "raspberry" Fe-Ag particles. (b),(f) The corresponding Fe-$L_{2,3}$ elemental maps. (c),(g) The corresponding Ag-$M_{4,5}$ elemental maps. (d),(h) RGB images constructed by superimposing Fe and Ag maps.

and (f), and Fig.4.20,(c) and (g). Fig.4.20,(d) and (h) show RGB images constructed by superimposing Fe and Ag maps.

The EFTEM data are consistent with HRTEM and EDX data and show that particles mostly have a core-shell structure with silver as the core. However, some silver pieces remain on the surface of the particles (marked with the yellow arrow in Fig.4.20(d)), and some are completely separated form the nanocomposite (marked with the yellow arrow in Fig.4.20(h)).

4.3 Formation and ageing of dumbbell and "raspberry" Ag-Fe nanoparticles

4.3.1 Segregation and Janus morphology formation in as-prepared dumbbell and "raspberry" Ag-Fe particles

The results obtained for primary$_{dumbbell}$ Fe-Ag nanoparticles (Fig.4.7 and 4.8) indicate that segregation of Fe and Ag starts already as the particles exit the plasma. Dumbbell and "raspberry" Fe-Ag nanoparticles are annealed at 1273 K which is higher than the melting point of Ag (T_m=1235 K). This means that during annealing Ag and Ag-rich clusters are in the liquid state and segregate to the surface. In order to prove that the annealing time is enough for complete segregation, even in the case when Ag is dissolved inside the Fe-rich cluster, the mean atomic diffusion length λ was calculated. λ is a function of the annealing time τ_s and the diffusion coefficient D [157]:

$$\lambda = \sqrt{D\tau_s} \tag{4.2}$$

The diffusion coefficient D, in turn, depends on the diffusion constant D_0, the activation

energy for diffusion E_a, and annnealing temperature T_S [157]:

$$D = D_0 \exp(-\frac{E_a}{k_B T_S})$$

(4.3)

The bulk values D_0 = 1950 cm^2 s^{-1} and E_a=2.99 eV for volume diffusion of Ag in Fe ([157] was used to calculate the mean atomic diffusion length λ for the particles exposed to the annealing temperature T_S = 1273 K for τ_s = 0.16 s. τ_s is calculated according to equation 2.1. The calculated value λ= 137 nm is much larger than the particle size, so full segregation occurs.

To understand the behavior of the molten Ag on the Fe surface, contact angle can be considered. The assumed geometry of the liquid, solid and vapor phases is shown in Fig.4.21. It consists of a liquid drop in contact with a flat substrate − the so-called sessile drop configuration. The contact angle is defined by three interfacial energies: $\gamma_{l/v}$, $\gamma_{s/v}$, $\gamma_{s/l}$ which are the liquid-vapor, solid-vapor and solid-liquid interface energies, respectively. Assuming, that the solid surface is flat and smooth and the surface energy anisotropy is weak, which is the case for metals [158], the model gives the Young's equation:

$$\gamma_{s/v} = \gamma_{s/l} + \gamma_{l/v} \cos \theta,$$

(4.4)

where θ is a contact angle. Situations with θ >90° are referred to as poor wetting and those with θ <90° as good wetting.

In reference [159], the wetting behavior of liquid Ag on polycrystalline Fe substrates was studied. The contact angle was found to decrease from approximately 45° to 10° as the temperature was increased from 1233 K to 1423 K. This means that at 1273 K silver should wet iron quite well. However, in the case of gas-phase-prepared nanoparticles, gravitational effects and curved rough surfaces cannot be neglected. The liquid phase tends to form a drop with a higher contact angle on curved and rough surfaces (the latter is known as Lotus Leaf effect) [160]. Therefore, a Janus particle (dumbbell or "raspberry") rather than a core-shell particle is obtained.
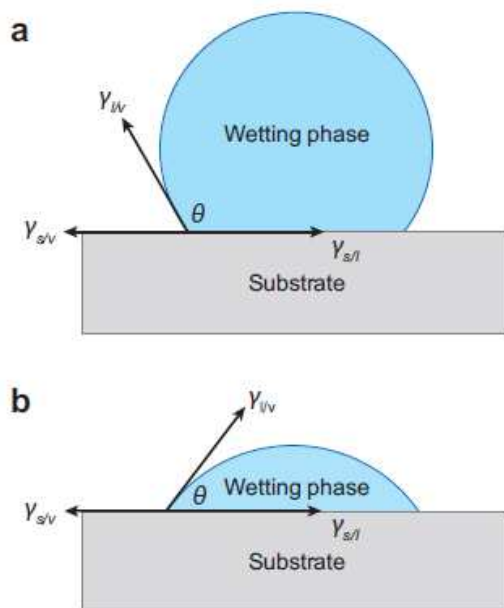
Figure 4.21: Illustration showing the wetting equilibria of a drop on a flat substrate when the interfacial energies are isotropic.(a) Poor wetting and (b) good wetting. Gravitational effects are neglected. Taken from [158]

The resulting Janus morphology of the particles (dumbbell or "raspberry") depends on whether He is present in the gas mixture during particle preparation (see table 4.1). He, as discussed in the introductory chapter, enhances the cooling rate and creates a steep temperature gradient (see Fig.4.22). The results obtained for primary$_{dumbbell}$ Fe-Ag particles prepared in the presence of He (Fig.4.7 and 4.8) show the formation of large Ag-rich clusters. The primary particles prepared with the same parameters used for the "raspberry" particles (primary$_{"raspberry"}$) could not be analyzed as they possessed poor crystallinity and immediately decayed even under low-intensity electron beam conditions. However, it can be assumed that a higher Ar energy and a flatter temperature gradient leads to a more uniform distribution of Ag within the particle. During the annealing, Ag also segregates more uniformly which results not in one, but several small Ag clusters located on the top of Fe/oxide, thus creating "raspberry" morphology(see Fig.4.22).
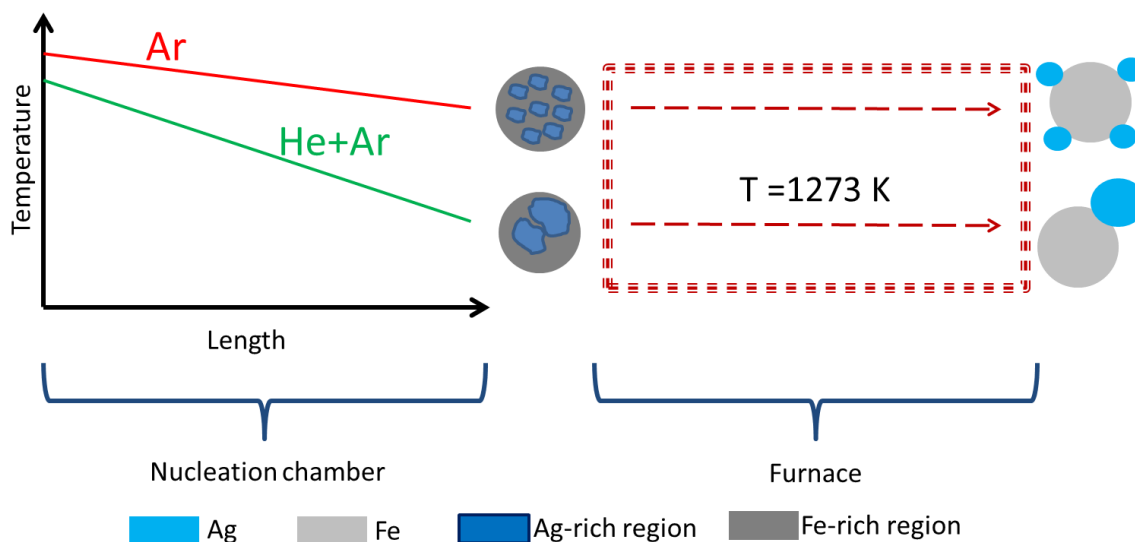
Figure 4.22: Formation of Fe-Ag nanoparticles with dumbbell and "raspberry" morphologies.

4.3.2 Ageing of dumbbell and "raspberry" Fe-Ag particles

In order to understand the mechanism of ageing, the main factors responsible for the change of structure and morphology of Fe-Ag nanoparticles have to be identified. Formation of voids within the particles is the first indication that oxidation plays a central role in the changes of morphology during the ageing process [161, 162]. Two experimental works dedicated to the study of oxidation of Fe/Ag bilayers [163] and ageing of Ag-Au nanocomposites [164] confirm this assumption. Apart from oxidation, interfacial interactions between Ag and iron/iron-oxide have to be taken into account.

This section provides the overview of oxidation of metals and interfacial interactions of nanostructured metal and oxide surfaces along with the results of references [163] and [164]. Finally, a mechanism for ageing of dumbbell and "raspberry" nanoparticles is proposed.

Overview of driving forces behind Fe-Ag nanoparticles ageing

Low-temperature oxidation of metals. Low-temperature oxidation is a reaction occurring at or below room temperature between solid and gas. It is described by the generalized Cabrera-Mott theory ([165–167]).

The first stage of oxidation involves adsorption of the oxygen molecule by the metal surface. This is considered to involve dissociation and at least partial ionization of oxygen followed by the incorporation of oxygen into the metal surface; presumably by a place-exchange mechanism. The initial oxidation is completed when a thin continuous layer of stable oxide is formed. From this point on, the metal is separated from the gas by the oxide barrier. The central assumption of the Cabrera-Mott theory is that electrons pass through oxide layers from the metal to the oxygen atoms by thermionic excitation from the metal into the conduction levels of the oxide or by electron tunnelling through the oxide barrier. At low temperatures the latter mechanism prevails. The oxygen ions formed on the surface by dissociation of oxygen molecules and the capture of tunnelling electrons are partially incorporated in the oxide surface and set up a potential across the film which provides a driving force for continued oxidation. The field created across the oxide lowers the potential barriers for ions to migrate: the barrier at the oxide-air interface is lowered for the anions, and the barrier at the metal-oxide interface is lowered for the cations. Oxide growth at this stage is a slow logarithmic process. In the case of Fe, it takes 40 s to form a 2 nm thick oxide layer on a freshly exposed iron surface, 40 weeks for a film of 3 nm, and 600 years for a film of 4 nm [168]. Depending on metal/metal oxide system either cation or anion migration process predominates, determining the migration of lattice defects. The mass and charge transport mechanisms during oxidation are shown in Fig.4.23.

Oxidation of small gas-phase Fe nanoparticles at room temperature In reference [161] showed that the generalized Cabrera-Mott theory can be used for a qualitative description of oxidation in metal nanoparticles. Oxidation of small gas-phase Fe nanoparticles of various sizes at room temperature was studied in reference [162], and it was found that particles with a diameter of less than 8 nm were fully oxidized and contained voids. Partially oxi-
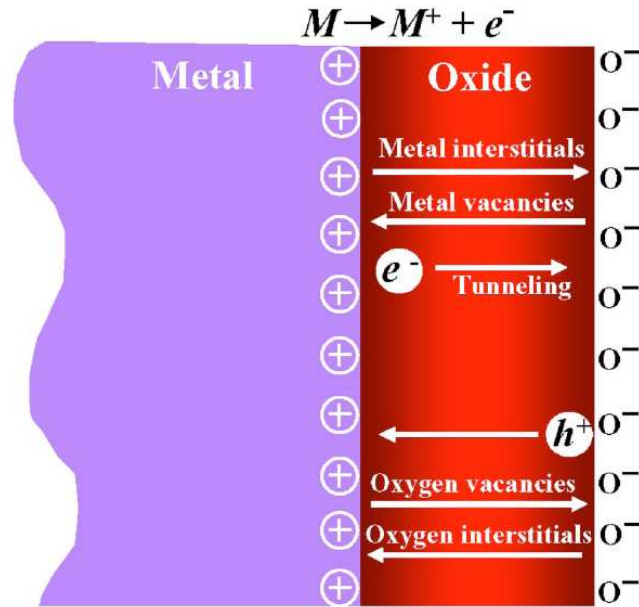
Figure 4.23: Low-temperature oxidation of metals. The schematic drawing shows the possible mass and charge transport mechanism during oxidation. Taken from [162].

dized particles consisted of an oxide shell, an iron core, and several voids spatially located at the interface between the Fe core and the oxide shell (see Fig.4.24).

The void formation can be explained as follows. Generally the iron oxidation product is Fe:FeO:Fe_3O_4:Fe_3O_4 + γ-Fe_2O_3: γ-Fe_2O_3. The thickness or presence of different oxides depends on oxidation conditions (oxygen pressure and temperature). During low-temperature oxidation of Fe in air the FeO layer is either not present of quite thin comparing to Fe_3O_4 and γ-Fe_2O_3 [169]. The outward diffusion of the Fe cations is the dominant mass transport process of Fe_3O_4 growth [169, 170]. Outward diffusion of Fe cations means inward diffusion of vacancies which coalesce near the iron/iron oxide interface.

Interfacial interaction of nanostructured metal and oxide surface. Nanostructured metal-oxide surface interaction is a complicated phenomenon which includes interfacial charge redistribution and/or mass transport at the interface. This is determined by the nature of both the metal and the oxide (surface and interfacial energies, band structure, crystallo-
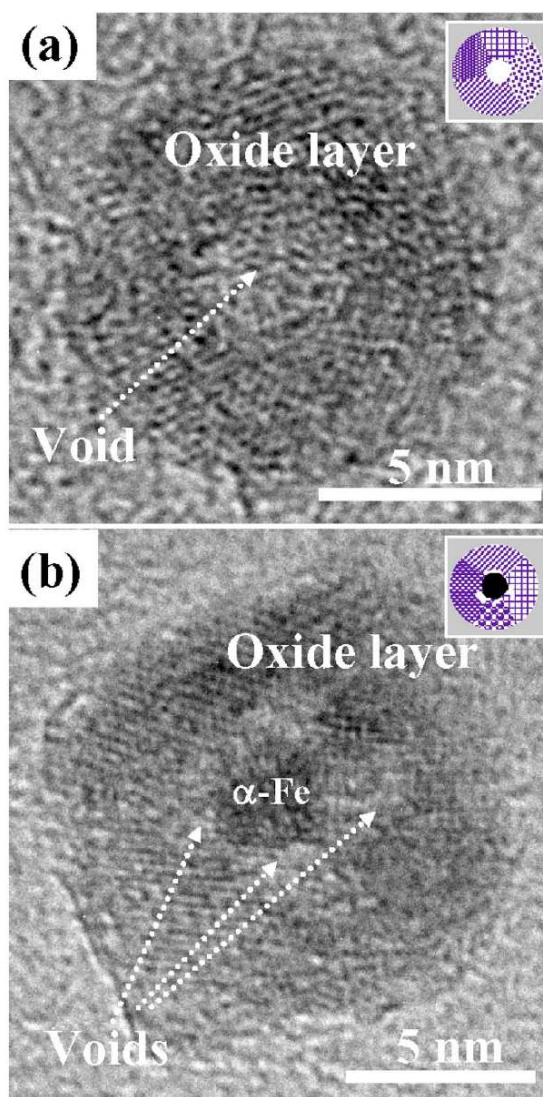
Figure 4.24: HRTEM images showing (a) a fully oxidized 8 nm particle with a void in the center of the particle and (b) trapping of the cluster of voids at the interface between the Fe core and the oxide shell for a 10 nm particle. The inset in each image is a schematic illustration of the particle structure. Taken from [162].

graphic orientation, etc.) and ambient conditions . The chemical interaction can be classified by the final product into four categories ([171] and references therein):

1. *Redox reaction*, which occurs at the metal/oxide interface ($Me^{I} \parallel Me^{II}O_x$) by oxidiz-

ing the metal and reducing the the oxide surface. The reaction can be schematically written as:

$\mathrm{Me}^I \parallel \mathrm{Me}^{II}\mathrm{O}_x \rightarrow \mathrm{Me}^{IO} \parallel \mathrm{Me}^{II}\mathrm{O}_{x-y}$. This reaction is attributed to mass transport in the form of oxygen diffusion.

2. *Alloy formation*. Formation of stable intermetallic compounds:

$\mathrm{Me}^I \parallel \mathrm{Me}^{II}\mathrm{O}_x \rightarrow \mathrm{Me}^I\mathrm{Me}^{II}{}_y \parallel \mathrm{Me}^{II}\mathrm{O}_z$

or

$\mathrm{Me}^I \parallel \mathrm{Me}^{II}\mathrm{O}_x \rightarrow \mathrm{Me}^I\mathrm{O}_y \parallel \mathrm{Me}^I\mathrm{Me}^{II}{}_z \parallel \mathrm{Me}^{II}\mathrm{O}_x$.
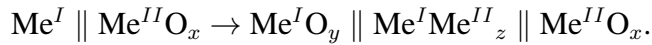
In the alloy formation process, cations are assumed to be extracted from the oxide layer and incorporated into the metal overlayer.

3. *Encapsulation.* The encapsulation reaction involves mass transport from the oxide surface to the surface of the metal particle and requires the outward diffusion of cations from the oxide onto the metal particle (see Fig.4.25). The main driving force for the encapsulation is the minimization of surface energy in case when the metal surface energy is higher than that of the oxide surface, which is the case for noble metals. As a result, the particle is covered by thin layer of oxide $\mathrm{Me}^{II}\mathrm{O}_x$:

$\mathrm{Me}^I \parallel \mathrm{Me}^{II}\mathrm{O}_x \rightarrow \mathrm{Me}^{II}\mathrm{O}_{x-\delta} \parallel \mathrm{Me}^I \parallel \mathrm{Me}^{II}\mathrm{O}_z$
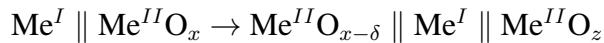
4. *Interdiffusion.* The metal may diffuse into the oxide layer and vice versa. As a result, a mixed oxide can form:

$\mathrm{Me}^I \parallel \mathrm{Me}^{II}\mathrm{O}_x \rightarrow \mathrm{Me}^I\mathrm{Me}^{II}\mathrm{O}_y$.
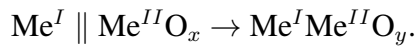
Oxidation of Fe/Ag bilayers. The authors of reference [163] studied the oxidation of a bilayer consisting of 20 nm Ag deposited on 20 nm Fe. The layers were epitaxially grown on the (001) plane. On annealing at 200°C, voids with diameters of 100-200 nm were found in the Ag layer. In samples annealed at the same temperature but under pure oxygen atmosphere, rapid oxidation of the Fe layer was observed and the iron oxide layer was
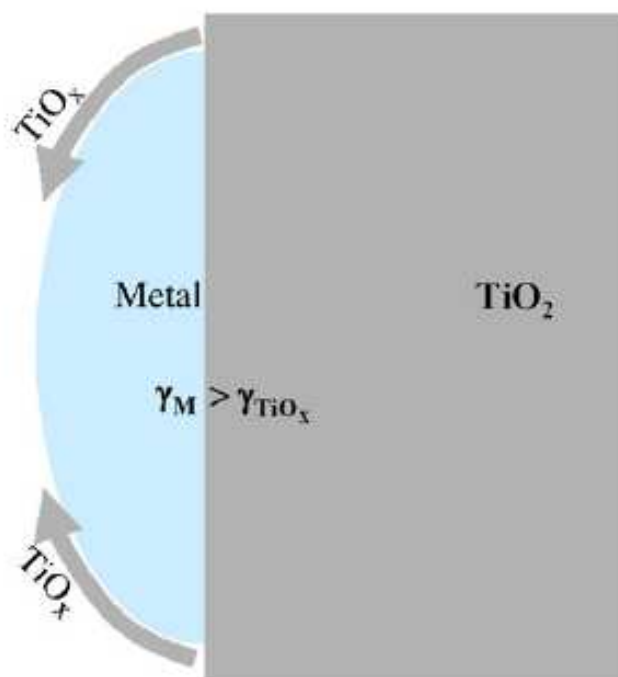
Figure 4.25: Interfacial interaction of nanostructured metal and oxide surface. Schematics showing the mass migration of oxide onto metal clusters driven by the minimization of surface energy of the whole system [171].

formed on the Ag layer. The formation of voids was explained by the presence of small FeO patches at the Fe/Ag interface. The voids in the Ag layer were formed as Ag retracted from FeO due to higher surface energy.

Ageing of Ag-Au nanocomposites. D. Belić studied the structural properties of $Ag_{85}Au_{15}$ nanoclusters prepared by the inert gas aggregation method [164]. The as-prepared nanoclusters possessed spherical morphology and had a uniform distribution of Au and Ag. After being stored for 52 days under ambient conditions, particles experienced a change in their structure and morphology. Some of them exhibited the (Au-Ag)@(Ag$_2$O) core-shell morphology, while the others formed a dumbbell Janus structure with Au-Ag and Ag$_2$O parts. After a period of 12-18 months some of the Janus nanoparticles separated into two Au-rich and Ag-rich fragments, another showed the formation of a neck between the two

parts (see Fig.4.26).
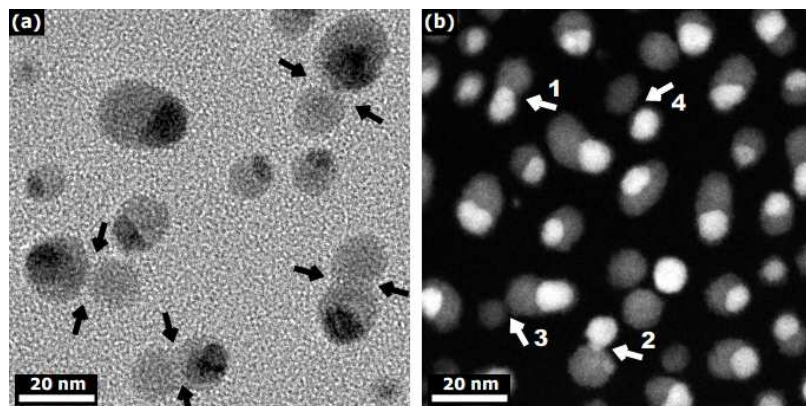
Figure 4.26: Ageing of Ag-Au nanocomposites. (a) TEM image of an aged $Ag_{85}Au_{15}$ sample (t_{ageing} = 18 months, average particle size D = 6 nm). (b) HAADF STEM image of another aged $Ag_{85}Au_{15}$ sample (t_{ageing} = 12 months, average particle size D = 3 nm) showing nanoclusters at various stages of segregation: 1 - neck formation; 2 - neck narrowing; 3 - neck breaking; 4 - separate clusters. Taken from [164].

It was assumed that after the initially homogeneously alloyed Ag-Au nanoclusters were exposed to air, they began to oxidize. The oxidation process is not stoichiometric, and Ag_xO is formed on the surface of the clusters. The incorporation of oxygen lowers the energetic barrier for the surface diffusion of Ag due to a high mobility of Ag_xO. The particle tries to minimize its surface energy, and forms an elongated Janus composite, which later separates into distinct clusters. This occurs for all Ag-Au particles regardless of their size.

Ageing of the dumbbell and "raspberry" Fe-Ag nanoparticles

The ageing of Fe-Ag nanoparticles is mainly caused by the following factors:

1. further slow oxidation after the initial oxidation of the iron/iron oxide part of the particle

2. interaction of the silver/iron oxide surface and minimization of surface energy.

Ageing of "raspberry" Fe-Ag nanoparticles. As no Fe-Ag compounds, no Ag oxide or no ternary Fe-Ag-O was found in aged particles, the main driving forces for the ageing of Fe-Ag particles are the minimization of surface energy and the mass transport at the Ag/iron oxide interface. As the iron/iron oxide part continues to oxidize, the voids are formed and silver begins to diffuse inside the particle through the void/Fe(Fe-oxide) interface. As silver diffuses inside, the aggregation and recrystallization of silver clusters occurs. Finally, when the particle is fully oxidized, small voids coalesce into a single large void at the center of the particle, and silver is encapsulated inside. The process representing the ageing of "raspberry" particles is shown in Fig.4.27.
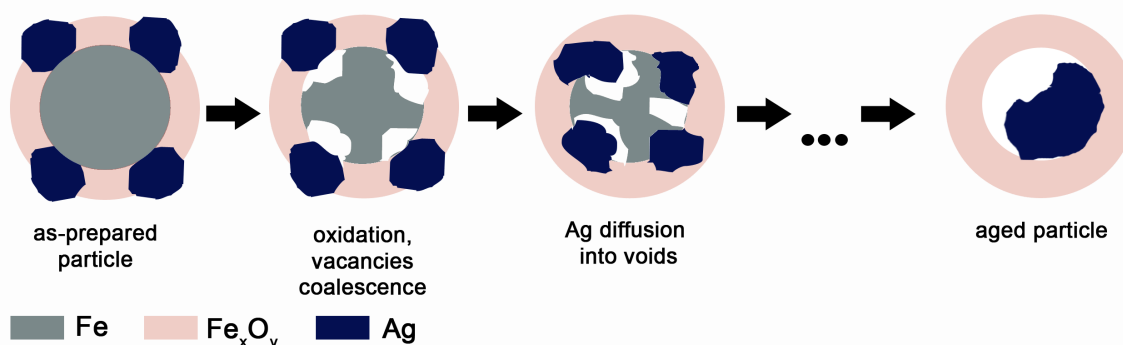
Figure 4.27: Ageing of "raspberry" Ag-Fe nanoparticles.

Ageing of dumbbell Fe-Ag nanoparticles. Apparently, in the case of aged dumbbell nanoparticles, silver is only partially encapsulated by the iron oxide shell. The possible ageing scenario for dumbbell nanoparticles is the following: During the oxidation of the iron part, the oxide thickness increases and so does the oxide/silver interface. As the system minimizes its surface energy, not only silver diffuses into voids in the iron part, but small pores appear in silver as well. These pores create the route for surface diffusion of iron oxide inside the silver part, and finally, the silver piece is divided in two halves. One half is encapsulated inside oxide shell, the other remains outside. In some cases it separates completely from the rest of the composite to minimize the interfacial energy. The outer

silver part then oxidizes while encapsulated silver is protected from oxidation by the iron oxide shell.

We note that in our case even when the size of the iron/iron oxide part of the particle is more than 8 nm (critical size for full oxidation [162]) the shell becomes fully oxidized. This can be explained by two factors: first, oxidation was studied on a time scale of several weeks in the current study. This means, that the oxide layer formed during the initial stage of passivation (even for particles more than 8 nm) is not enough to restrain oxidation completely, and it proceeds slowly. Second, it is known that silver has a higher oxygen permeability than most metals [172]. The transport of oxygen through Ag proceeds through dissociative adsorption of molecular oxygen at the surface. This occurs by the dissolution of atomic oxygen into the particle, and the subsequent migration of the atoms between octahedral sites of the lattice (or through defects) until they arrive at the interface between silver and iron/iron oxide. Therefore, the silver parts may serve as an additional source of oxygen for the iron particles and promote further oxidation. The ageing of dumbbell particles is shown schematically in Fig.4.28.
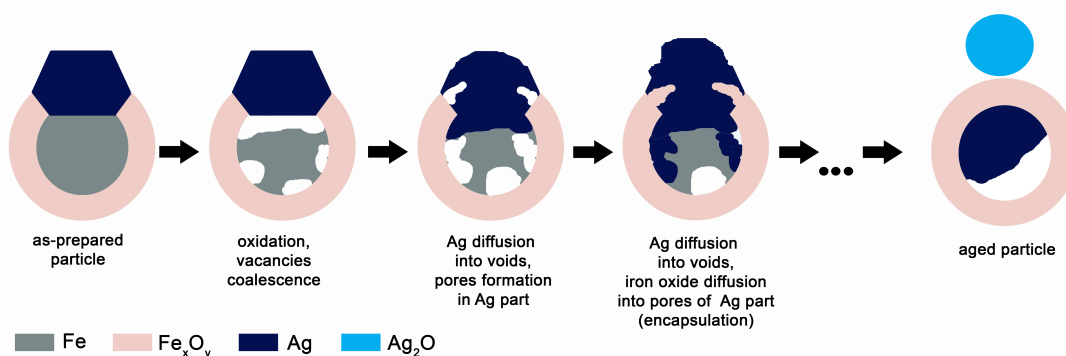
Figure 4.28: Ageing of dumbbell Fe-Ag nanoparticles. The thickening of the iron oxide shell during oxidation is not depicted.

Chapter 5

Stabilization of L1$_0$ phase and suppression of twin structures in FePt-Cu nanoparticles

In this chapter structure, morphology and magnetic properties of Fe-Pt-Cu nanoparticles are studied. The influence of Cu on stabilization of the ordered L1$_0$ phase and suppression of twin structures is investigated.

By varying the number of Cu patches (3, 6, 12 and 18) in the Fe$_{50}$Pt$_{50}$ target samples with different Cu concentrations (5 at.%, 7 at.%, 11 at.% and 25 at.%, respectively) were prepared. For all samples Ar and He were introduced into the nucleation chamber at 50 sccm. The total gas pressure was adjusted to 0.5 mbar. For each concentration two samples were prepared: the primary particles, produced without in-flight annealing, and particles in-flight annealed at 1273 K. The in-flight annealing time is 0.16 s (equation 2.1).
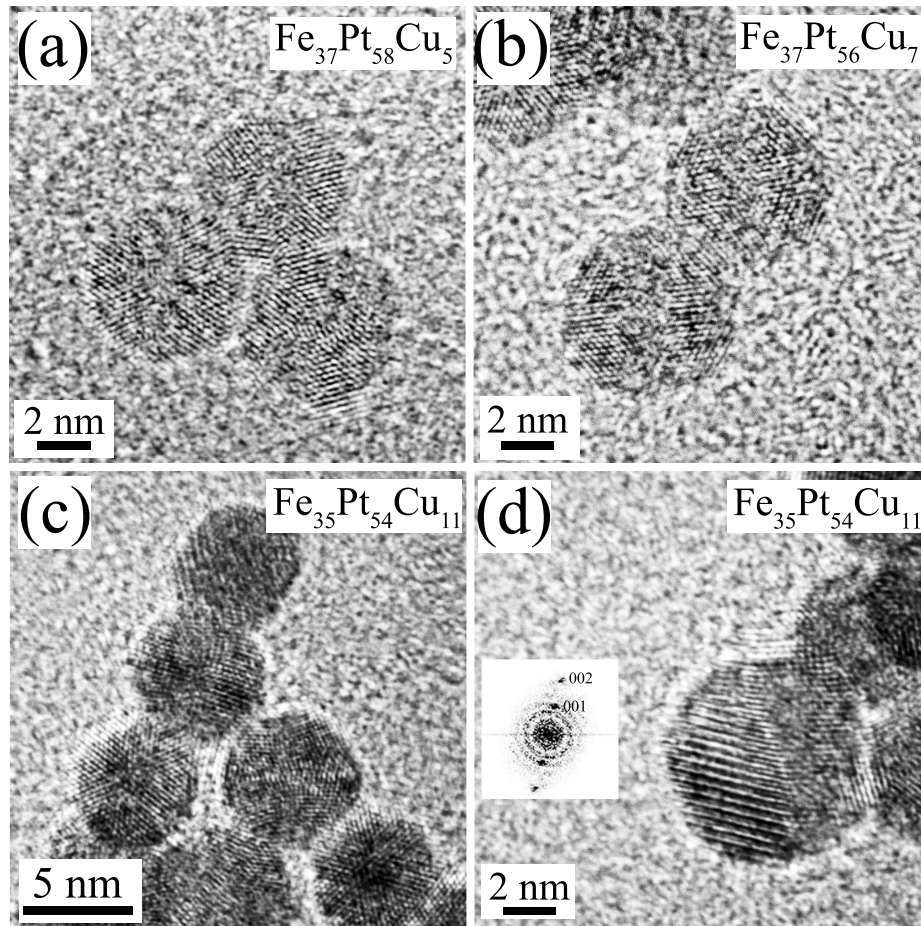
Figure 5.1: Fe-Pt-Cu nanoparticles with low Cu concentration. Typical HRTEM micrographs of in-flight annealed (a) $Fe_{37}Pt_{58}Cu_5$ nanoparticles, (b) $Fe_{37}Pt_{56}Cu_7$ nanoparticles, and (c) $Fe_{35}Pt_{54}Cu_{11}$ nanoparticles. (d) Double twinned $Fe_{35}Pt_{54}Cu_{11}$ nanoparticle with corresponding FFT image (inset).

5.1 In-flight annealed Fe-Pt-Cu nanoparticles with low Cu concentration

Fig.5.1(a-c) show typical TEM micrographs of in-flight annealed Fe-Pt-Cu nanoparticles with average Cu concentrations 5 at.%, 7 at.%, and 11 at.%, respectively. The image contrast is typical for multiply twinned icosahedral crystals [60]. No indication of formation of the ordered face-centered tetragonal (fct) structure L1$_0$ as well as single crystal

particles are found for the in-flight annealed samples with average Cu concentrations 5 and 7 at.%. For the in-flight annealed sample with 11 at.% Cu, approximately 90% of the particles are also multi-twinned and icosahedral (Fig.5.1(c)). The rest of the nanocomposites (Fig.5.1(d)) possess double-twinned morphology and the L1$_0$ structure. The FFT image obtained from the particle in Fig.5.1(d) shows the presence of a superstructure (001) reflection. The measured d-spacing is 0.374 ± 0.005 nm and corresponds to the literature value of 0.371 nm [137]). This proves the formation of the L1$_0$ phase.

5.2 Primary and in-flight annealed Fe-Pt$_2$-Cu nanoparticles
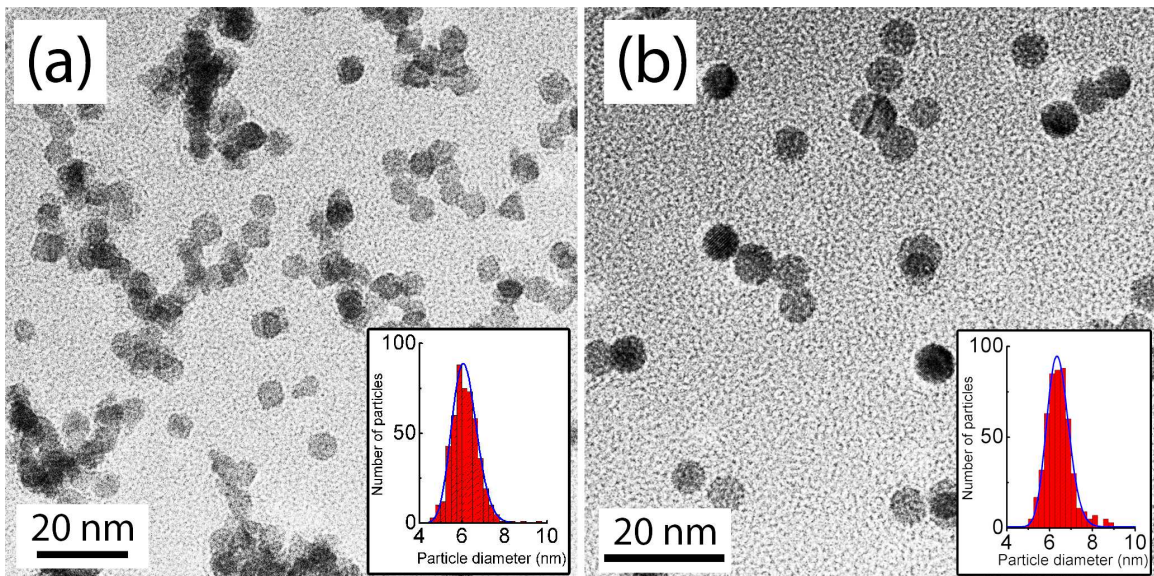
Figure 5.2: TEM micrographs of (a) primary and (b) in-flight annealed FePt$_2$Cu nanoparticles. Insets present corresponding particle size distributions.

TEM micrographs of primary particles and particles in-flight annealed at 1273 K are presented in Fig.5.2(a) and (b), respectively. In-flight annealed particles are more separated from each other compared to the primary particles which tend to form large aggregates.

Table 5.1: Size distribution parameters of FePt$_2$Cu nanoparticles

Sample	D$_m$, nm	σ	$<$d$>$, nm	Δ, nm
FePt$_2$Cu primary	6.1 ± 0.5	0.09 ± 0.01	6 ± 1	0.6 ± 0.1
FePt$_2$Cu in-flight annealed	6.4 ± 0.5	0.08 ± 0.01	6 ± 1	0.5 ± 0.1

Insets in Fig.5.2(a) and (b) show corresponding size distributions of primary and in-flight annealed particles.

The size distributions are fitted by the log-normal distribution function. Values of geometric mean particle diameter, geometric standard deviation, average particle diameter and standard deviation are listed in table 5.1.

Table 5.2: Elemental concentrations in FePt$_2$Cu nanoparticles

Sample	Fe, at.%	Cu, at.%	Pt, at.%	Error, at.%
FePt$_2$Cu in-flight annealed	26	24	50	3
FePt$_2$Cu primary	26	21	53	3

The compositions of the Fe-Pt-Cu nanoparticles were measured by EDX spectroscopy. Spectra for each sample were taken from 10 different regions of about 250 nm in diameter. The average concentration is calculated from each spectra, and the results are presented in table 5.2. Taking into account an error of 3%, the composition is close to Fe$_{25}$Pt$_{50}$Cu$_{25}$ (further referred to as FePt$_2$Cu).

To examine the crystal structure of the particles, the electron diffraction patterns were obtained (Fig. 5.3). The patterning was calibrated with a gold film sample measured under the same beam conditions. The results of the analysis of the patterns are collected in table 5.3. According to table 5.3 the positions of the rings in the diffraction pattern of primary particles (Fig. 5.3(a)) correspond to the planes associated with cubic fcc structure. The lattice parameter is estimated to be a=0.372 $\pm$ 0.003 nm. The diffraction pattern of in-flight annealed particles (Fig.5.3(b)) shows the formation of nanoparticles with ordered face-centered tetragonal (fct) structure L1$_0$. This is indicated by the appearance of $\{011\}$ and $\{210\}$ superstructure rings marked by red lines in Fig.5.3(b), and the splitting of the rings corresponding to the families of $\{002\}$ and $\{220\}$ planes.
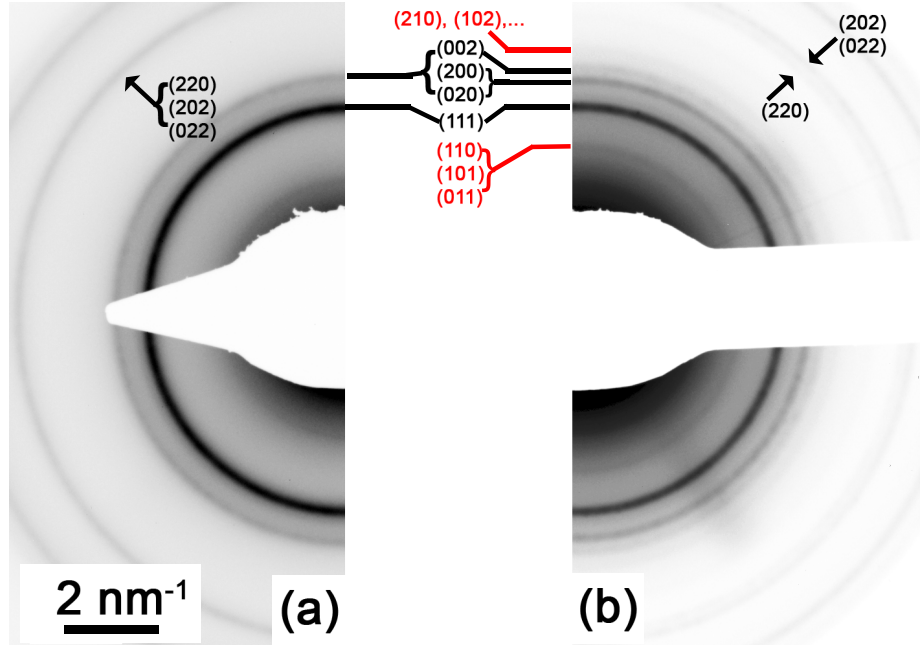
Figure 5.3: Powder diffraction pattern of (a) primary and (b) in-flight annealed FePt$_2$Cu nanoparticles.

The lattice constants are estimated to be a = 0.388 ± 0.004 nm and c = 0.366 ± 0.004 nm. The calculated value of the tetragonal distortion is (c/a) = 0.94 ± 0.01. The literature data for ordered FePt particles give a (c/a) ratio in the range 0.96 < c/a < 0.98 ([60–62]), while the values for bulk L1$_0$ Fe-Pt-Cu alloys are reported to be 0.91 < c/a < 0.94 [102, 173–176].

From the obtained c/a, the average order parameter S for the FePt$_2$Cu nanoparticles can be estimated using the following expression [67]:

$$S^2 = \frac{1 - \frac{c}{a}}{1 - \left(\frac{c}{a}\right)_{ordered}},\tag{5.1}$$

where $\left(\frac{c}{a}\right)_{ordered}$ is the tetragonal distortion ratio for the perfectly ordered alloy with the same elements concentration. The value of $\left(\frac{c}{a}\right)_{ordered} = 0.92$ for the fully ordered FePt$_2$Cu alloy was taken from reference [102]. The order parameter for in-flight annealed FePt$_2$Cu nanoparticles is estimated to be 0.87 ± 0.02.

Table 5.3: Powder diffraction analysis for primary and in-flight annealed FePt$_2$Cu nanoparticles

FePt$_2$Cu primary particles	FePt$_2$Cu in-flight annealed particles	FePt fcc structure [137] (a=0.380 nm)		FePt L1$_0$ structure [137] (a=0.385 nm c=0.371 nm)	
d,$\pm$ 0.002 nm	d,$\pm$ 0.002 nm	hkl	d, nm	hkl	d, nm
	0.275	110 101 011		110 101 011	0.272
0.217	0.219	111	0.219	111	0.219
0.189	0.194 0.183	200 020 002	0.190	200 020 002	0.193 0.193 0.186
	0.171	102 012 201 021 210 120		102 012 201 021 210 120	0.167 0.167 0.171 0.171 0.172 0.172
0.133	0.134 0.136	220 202 022	0.134	220 202 022	0.136 0.134 0.134

Another way of estimating the order parameter is to calculate the integrated intensities ratio of the superlattice and the corresponding fundamental peaks in the powder diffraction (see equation 1.27).

The diffraction pattern Fig.5.3(b) was processed using DiffTools script [177] written for Digital Micrograph ^{TM}. The obtained intensity versus scattering vector ($2\pi/d_{hkl}$) profile is shown in Fig.5.4(a). The background is fitted by the spline function and subtracted. The resulting integrated intensity profile is fitted by the sum of Gaussian peaks (Fig.5.4 (b)).

For estimation of order parameter the (110) and (220) superlattice and fundamental peaks were used. Taking into account their multiplicity which is 1 and 3, respectively, the
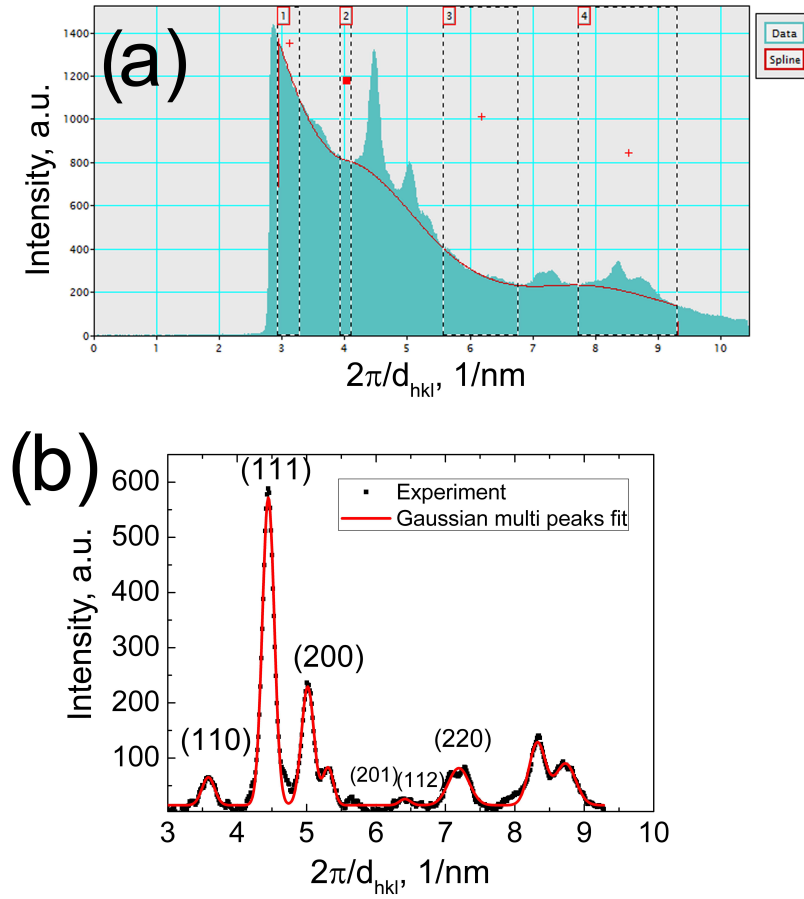
Figure 5.4: In-flight annealed FePt$_2$Cu nanoparticles. (a) Powder diffraction intensity profile. Background is fitted by spline function (red line). (b) Integrated powder diffraction intensity profile with subtracted background (black line) fitted with multiple Gaussian peaks (red line).

following expression is obtained [178]:

$$S^2 = \left(\frac{3I_{110}/I_{220}}{I^0_{110}/I^0_{220}}\right). \tag{5.2}$$

The theoretical value of I$^0_{110}$/I$^0_{220}$ = 1.78 was taken from [179]. The order parameter S is found to be 0.87 ± 0.05. It must be noted that the degree of ordering may vary from nanoparticle to nanoparticle, so both methods (equations 5.1 and 5.2) provide only a crude

approximation of the *average* order parameter S.
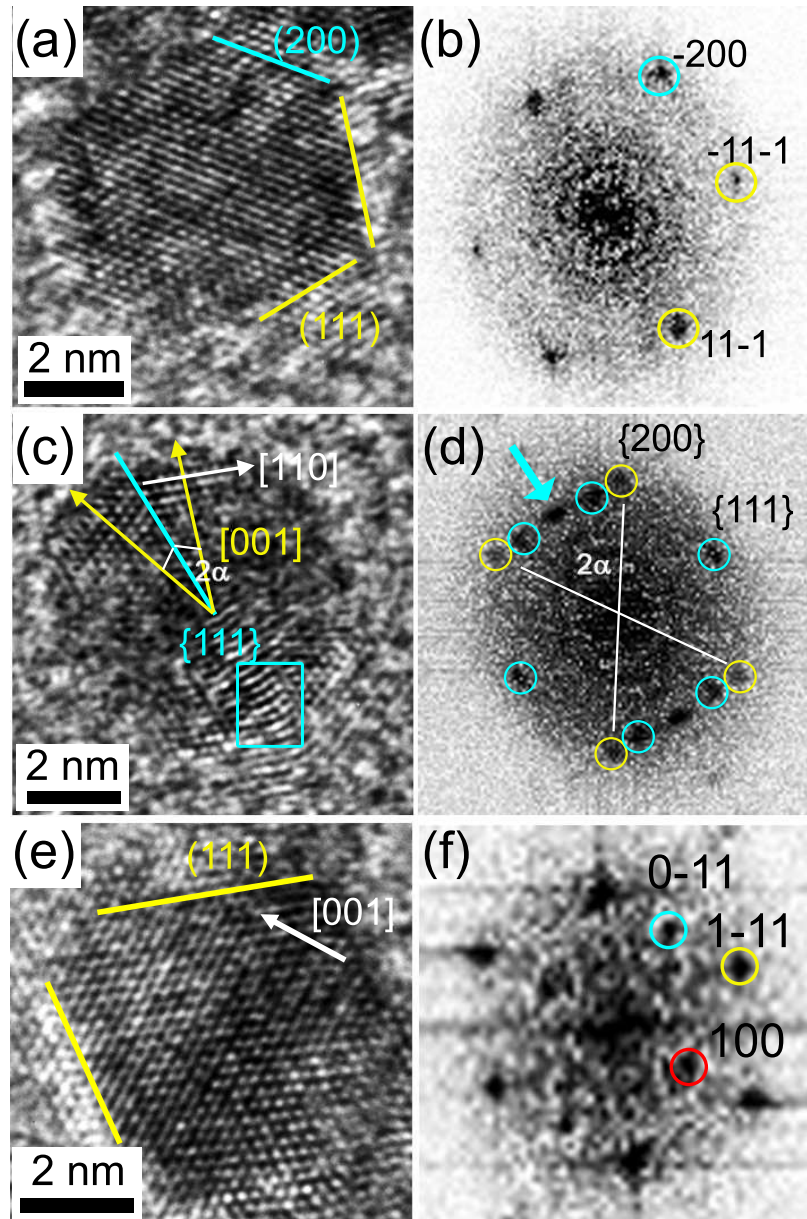
Figure 5.5: Primary FePt$_2$Cu nanoparticles. Typical HRTEM images of primary (a) single crystal cubooctahedral, (c) multiple twin icosahedral and (e) single crystal truncated octahedral FePt$_2$Cu particles with corresponding FFT images (b), (d), (f).

5.2.1   HRTEM analysis of primary FePt$_2$Cu nanoparticles

The morphology and crystal structure of individual particles were studied by HRTEM analysis. For primary particles, three types of morphologies approximately in equal proportions were observed. Typical high resolution images for each case are shown in Figs.5.5(a),(c) and (e). The particle in Fig.5.5(a) is a single crystal and possesses the fcc structure as indicated by the corresponding FFT image in Fig.5.5(b). The particle is viewed along the <011> zone axis. The colored circles and lines mark the plane families in the FFT image and the corresponding facets of the particle. The measured d-spacings are 0.218 ± 0.005 nm and 0.194 ± 0.005 nm corresponding to {111} and {200} planes of FePt (see table 5.3). The facet configuration indicates a cubooctahedral shape [180].

A typical image of the particle of the second type is presented in Fig.5.5 (c), and its FFT image is shown in Fig.5.5(d). The image contrast and the diffraction pattern in the FFT image are typical for multiply twinned icosahedral crystals [60]. Such particles consist of 12 tetrahedra and each tetrahedron forms 72° twin-boundaries with each neighbor [79].

The particle seen in Fig.5.5,(c) is viewed along its 2-fold symmetry axis. The FFT image consists of diffraction patterns of two crystallites tilted towards each other at an angle of $2\alpha \cong 70^o$, both viewed along the <011> zone axis. The twin boundary between crystallites runs along the 111-plane and is marked in Fig.5.5(c) by the blue line. [001] and [110] directions are marked by yellow and white arrows respectively. Reflections corresponding to {200} and {111} planes are shown with yellow and blue circles on the FFT image. The additional {111} reflection in the FFT image marked by the blue arrow in Fig.5.5(d) arises from the truncated part of the particle marked by the blue square in Fig.5.5(c).

The particles of the third type have an octahedral shape. For approximately two thirds of this kind of particles no indication of L1$_0$ phase formation was observed. The rest exhibit ordering in the center of the particle. Fig.5.5(e) shows a typical HRTEM micrograph of an ordered octahedral particle. The superstructure reflections (100) and (0-11), marked by red and blue circles in the corresponding FFT image (Fig.5.5(f)), indicate the formation of the L1$_0$ structure. Also, the image contrast in Fig.5.5(e) (white and black stripes) is a

typical feature for the L1$_0$ structure [79]. The particle is viewed along the <011> direction, and {111} facets are marked by yellow lines. The [001] axis (*c*-axis) lies in the image plane. The measured d-spacing corresponding to (100) and (0-11) superstructure reflections are 0.372 ± 0.005 nm and 0.274 ± 0.005 nm, respectively. The measured d-spacing corresponding to (1-11) fundamental reflection is 0.224 ± 0.005 nm.

Further proof for the existence of a chemically ordered phase in primary octahedral particles is provided by atomically resolved HAADF-STEM images. Fig.5.6(a) shows a HAADF-STEM image of the octahedral primary FePt$_2$Cu particle viewed in the <011> direction and the corresponding FFT image in the inset. The superstructure reflection (100) present in FFT image indicates the formation of the L1$_0$ structure. The magnified image of the central part of the particle is shown in Fig.5.6(b). Fig.5.6(c) shows the intensity profile obtained from the area marked by the white rectangle in Fig.5.6(b). Each peak corresponds to an atomic column. The profile clearly shows intensity modulation. Peaks of higher intensity correspond to Pt-rich atomic columns, as Pt is much heavier than Fe and Cu. Peaks of lower intensity correspond to Fe(Cu)-rich atomic columns assuming that Cu atoms preferably occupy Fe sites [181, 182]. This means that the core region of the particle presented in Fig.5.6(a) is chemically ordered.

It has to be noted that atomic columns situated at the surface of the particle presented in Fig.5.6(a) produce the HAADF-STEM contrast intensity comparable or even brighter then the atomic columns situated in the particle core. This indicates the segregation of a heavier element (in this case, Pt) to the particle surface. Pt segregation to the surface of the octahedral FePt particles was reported in reference [4].
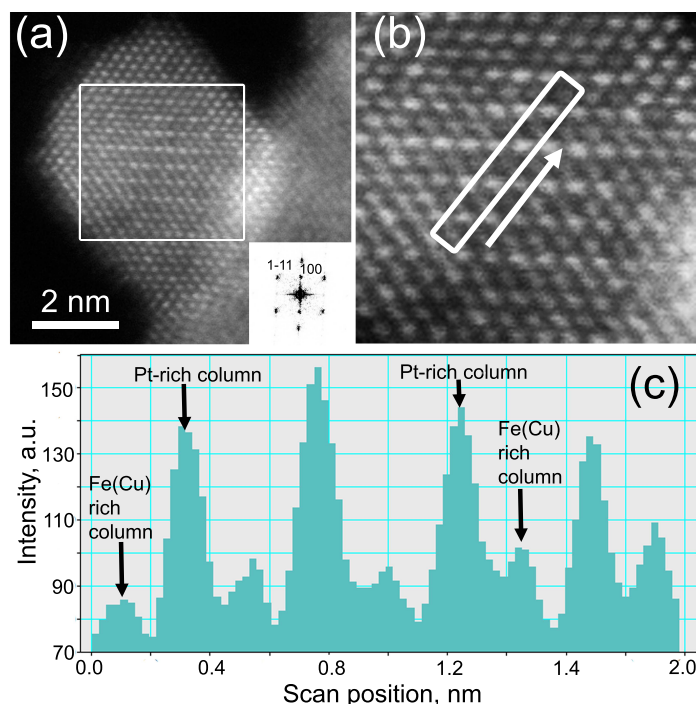
Figure 5.6: Primary FePt$_2$Cu nanoparticles. (a) HAADF-STEM image of an octahedral primary FePt$_2$Cu nanoparticle with corresponding FFT image (inset). (b) The magnified image of the area marked with the white square in image (a). (c) Intensity profile obtained from the area marked with the white rectangle in the image (b).

5.2.2 HRTEM analysis of in-flight annealed FePt$_2$Cu nanoparticles

Most of the particles in-flight annealed at 1273 K were found to be single crystalline and possess the same morphology. A small amount of particles (approximately 5%) have a twinned structure (Fig.5.8). 40% of all investigated nanoparticles showed the presence of superstructure reflections and HRTEM and HAADF-STEM contrast typical for L1$_0$ structure.

A typical in-flight annealed particle shown in Fig.5.7(a) is single crystalline and possesses the L1$_0$-ordered structure. This is indicated by the (100) and (001) superstructure reflections in the FFT image (Fig.5.7(b)). The particle is viewed along the <011> zone axis. Analysis of the orientations of the facets, marked by yellow, blue, and red lines in
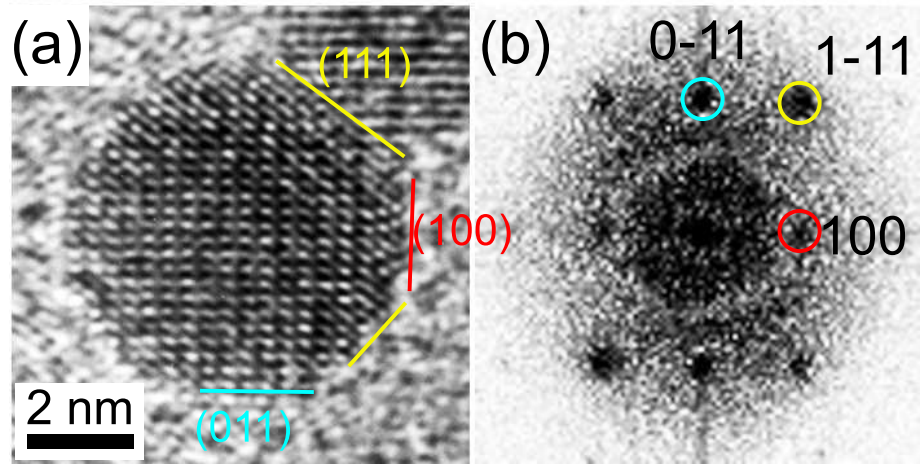
Figure 5.7: In-flight annealed FePt$_2$Cu nanoparticles. (a)Typical HRTEM image of in-flight annealed FePt$_2$Cu particle with corresponding FFT image (b).

Fig.5.7(b), reveals that the particle has a truncated cubooctahedral shape [180]. The measured d-spacing corresponding to (100) and (0-11) superstructure reflections are 0.368 $\pm$ 0.005 nm and 0.276 $\pm$ 0.005 nm, respectively. The measured d-spacing corresponding to (1-11) fundamental reflection is 0.225 $\pm$ 0.005 nm.

Fig.5.8 shows a HAADF-STEM image of several in-flight annealed FePt$_2$Cu particles. The image contrast oscillation indicates chemical ordering within particles 1 and 2 as well as the appearance of (001) and (011) superstructure reflections in the respective FFT images, hence the formation of L1$_0$ ordered phase . Particle 3 has a twinned structure.

5.3   Magnetic properties of FePt$_2$Cu nanoparticles

Fig.5.9,(a) and (b) show the temperature dependence of the zero field cooled (ZFC) and field cooled (FC) magnetization M(T) of primary and in-annealed FePt$_2$Cu nanoparticles, respectively, measured at 200 Oe in the temperature range 5-300 K.

There are two distinct points in the ZFC M(T) curve, both for primary and in-flight annealed nanoparticles. At T$_{B1prim}$ = 47 K for primary and T$_{B1annealed}$ = 80 K for in-flight
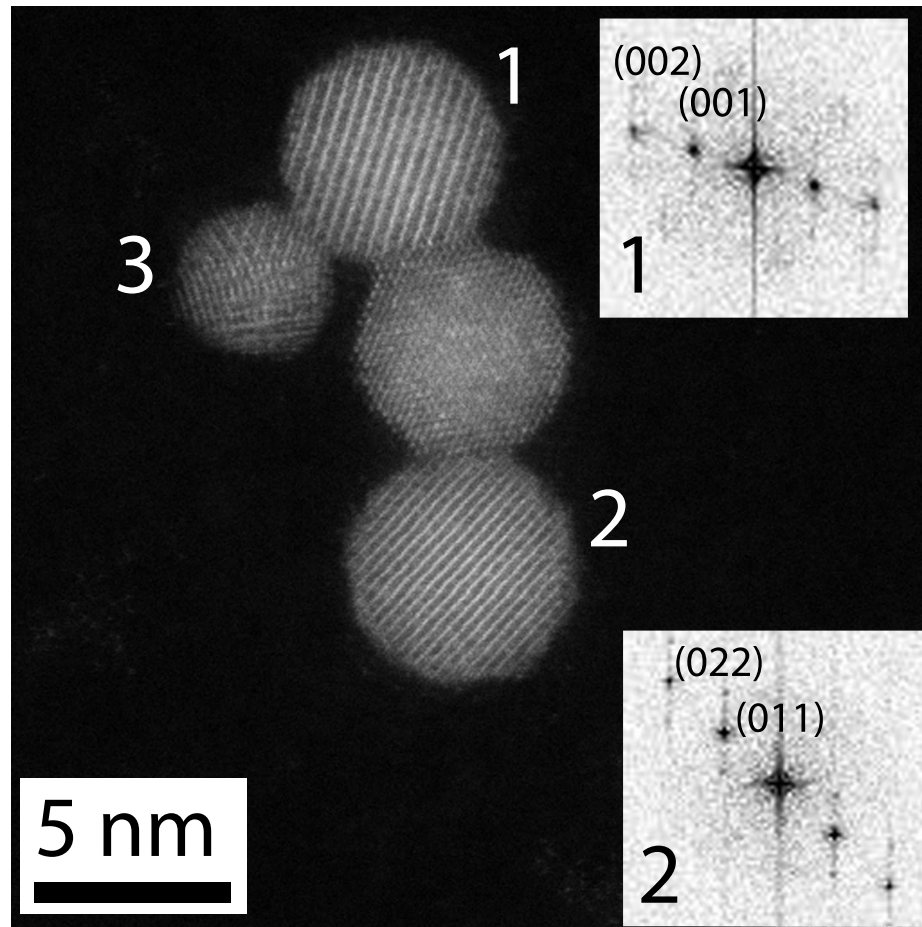
Figure 5.8: In-flight annealed FePt$_2$Cu nanoparticles. HAADF-STEM image of in-flight annealed FePt$_2$Cu nanoparticles with corresponding FFT images of nanoparticles 1 and 2.

annealed particles, the curve changes its slope. At another point, T$_{B2prim}$ = 250 K for primary and T$_{B2annealed}$ = 270 K for in-flight annealed particles, there is a local maximum. Both FC M(T) curves decrease monotonously with increasing temperature.

In Fig.5.10 normalized magnetization loops M(H)/M$_{5K}$(4T) obtained from FePt$_2$Cu primary particles are plotted. Primary particles have near zero coercivity at 300 K (Fig.5.10(a)) and small coercivity (about 163 Oe) at 5K (Fig.5.10(b)). The magnetization loop measured at 5 K has a constriction at the middle. This shape of hysteresis loops is called "wasp-waisted" [183].
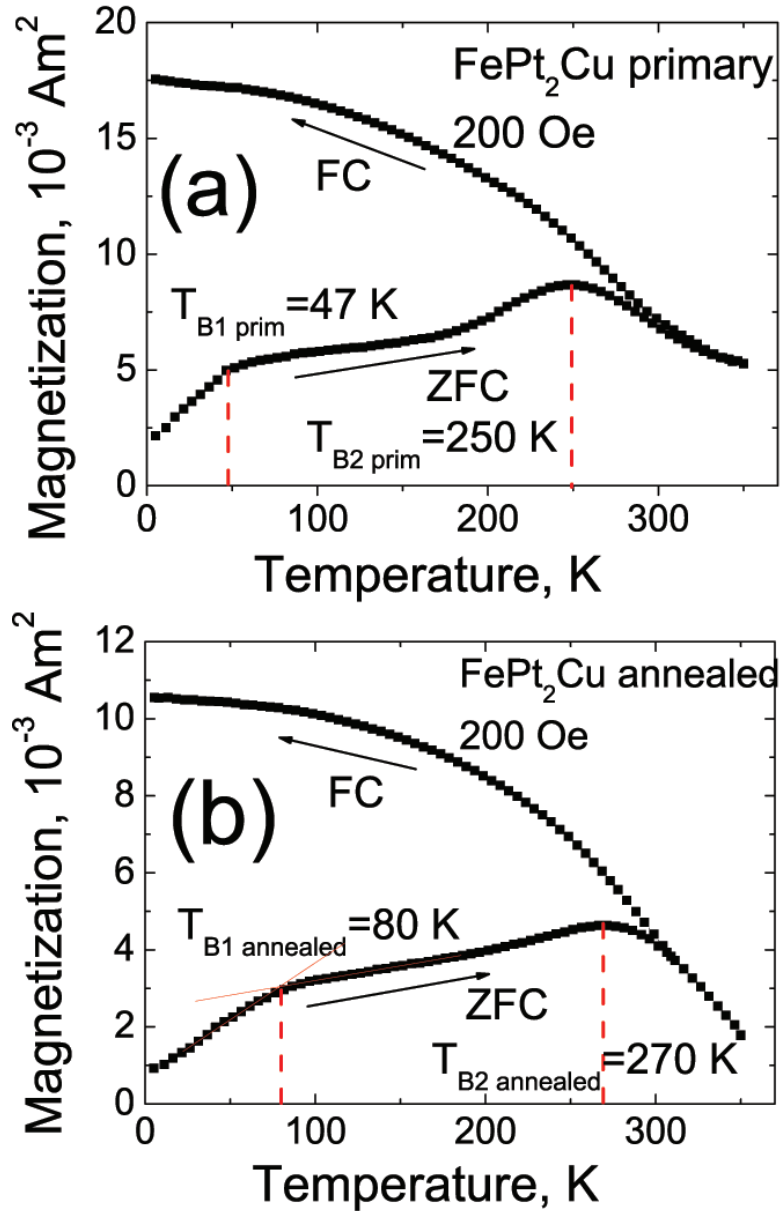
Figure 5.9: Magnetic properties of FePt$_2$Cu nanoparticles. Temperature dependence of the zero field cooled (ZFC) and field cooled (FC) magnetization M of (a) primary and (b) in-flight annealed FePt$_2$Cu nanoparticles measured at 200 Oe.

Magnetization loops of in-flight annealed FePt$_2$Cu nanoparticles were measured in the temperature range 5K $\leq$ T $\leq$ 300 K. Normalized loops M(H)/M$_{5K}$(4T) measured at 5 K
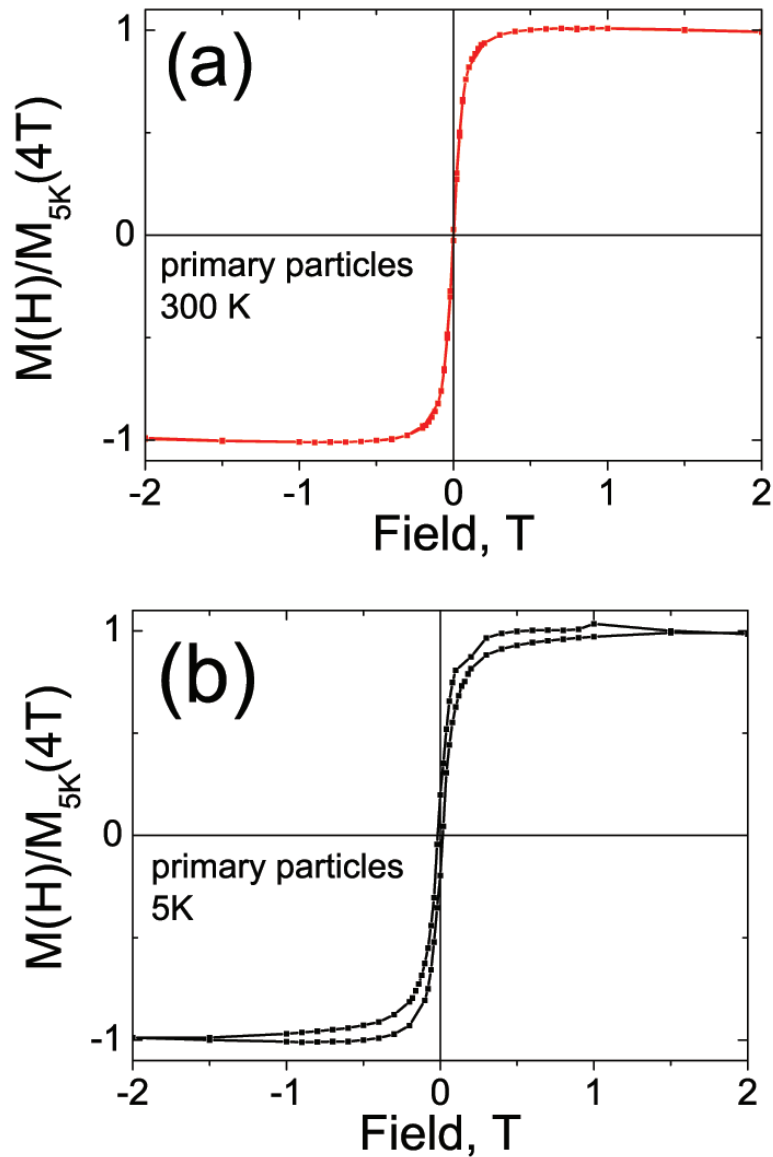
Figure 5.10: Normalized magnetization loops M(H)/M$_{5K}$(4T)of primary FePt$_2$Cu nanoparticles measured at (a) 300 K and (b) 5 K.

and 300 K are plotted in Fig.5.11(a). Up to room temperature, a "wasp-waisted" curve was observed. The temperature dependence of the coercivity is plotted in Fig.5.11(b). The coercivity decreases monotonously from 1800 Oe at 5K to 70 Oe at 300 K.
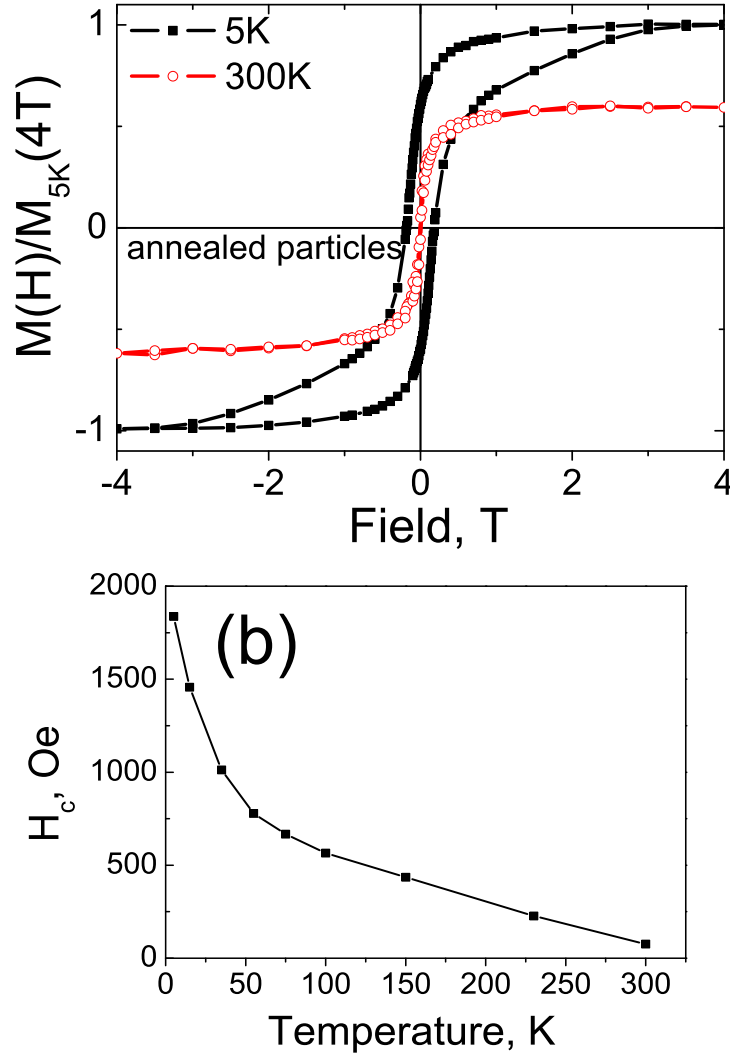
Figure 5.11: (a) Normalized magnetization loops M(H)/M$_{5K}$(4T) of in-flight annealed FePt$_2$Cu nanoparticles measured at 300 K and 5 K. (b) Temperature dependence of the coercivity.

In the case of in-flight annealed particles, the saturation magnetization decreases in the measured temperature range to M$_s$(300K) $\simeq$ 0.25 M$_s$(5K) (see Fig.5.11(b)). In primary particles, M$_s$(300 K) $\simeq$ M$_s$(5K). This indicates presence of nanoparticles fractions with

different Curie temperatures. In case of L1$_0$ FePt particles and films Curie temperature T$_c$ is known to depend on Fe and Pt concentrations ([182], [184], [185]) and ordering parameter ([186]) or, in case of partial ordering, by the presence of magnetic inhomogeneities ([187]). In case of two alloys of the same concentrations one is fully disordered, another is perfectly ordered, the Curie temperature of the ordered alloy should be higher than in disordered one. However, judging by behavior of ZFC-FC curves at high temperatures, it's not the case. This indicates that there might be a distribution of concentrations in FePt$_2$Cu nanoparticles or that nanoparticles have various degree of order.

A "wasp-waisted" shape of hysteresis loops may have various origins: presence of several magnetic phases, superposition of the magnetic behavior of (non-interacting) superparamagnetic and single domain particles [188], competition between magnetocrystalline and shape anisotropies [189], and strong surface anisotropy [190]. However, the ZFC-FC curve behavior indicates that the distribution of magnetic anisotropies is the major reason for the "wasp-waisted"shape of the magnetization loops. The shape of ZFC curve reflects the distribution of energy barriers in nanoparticles system, so the two distinct points (T$_{B1prim}$ and T$_{B2prim}$; T$_{B1annealed}$ and T$_{B2annealed}$) indicate the presence of two magnetic phases in both primary and in-flight annealed FePt$_2$Cu particles and are associated with the average blocking temperatures of each phase.

5.4 Stoner-Wohlfarth model with double distribution of magnetocrystalline anisotropy energy density

Magnetization data suggests a broad distribution of the magnetic anisotropy energy in FePt$_2$Cu particles. Traditionally, ZFC-FC susceptibility curves are used to determine the values of the magneto-crystalline anisotropy energy density K. However, this method requires the estimation of the fraction of blocked and superparamagnetic particles at each temperature and is very sensitive to the volume size distribution ([19], [20]). Instead, the
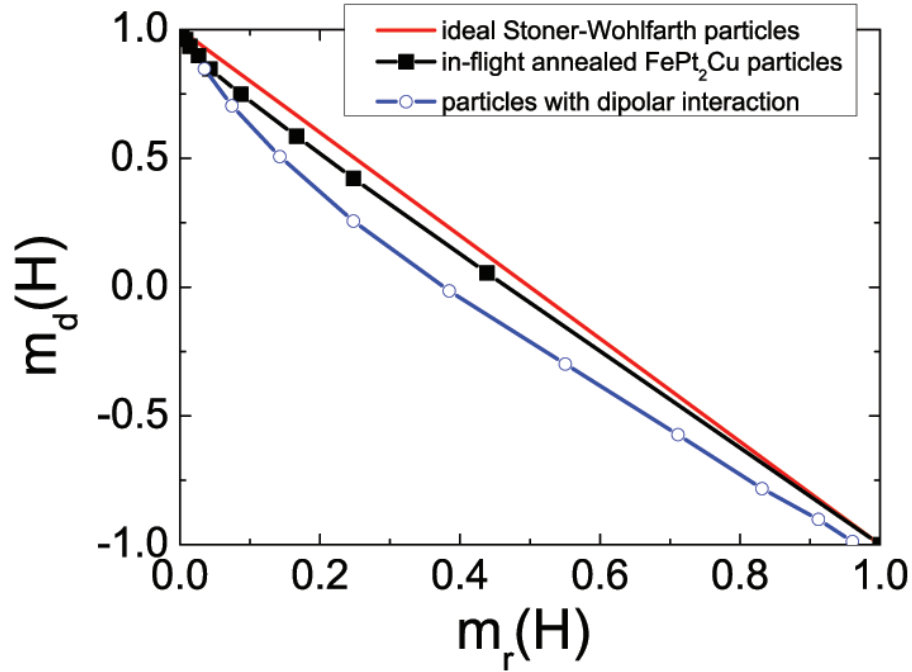
Figure 5.12: Henkel plot of the in-flight annealed FePt$_2$Cu nanoparticles (black squares) measured at 5K. Expected behavior for ideal StonerWohlfarth particles (red line) at T = 0 K. Simulated Henkel plot for particles with uniaxial magnetocrystalline anisotropy and dipolar interactions taken from [191] (empty circles).

approach used in reference [183] was adopted. This approach is based on simulating low temperature experimental magnetization loops using the Stoner-Wohlfarth model [18] (see *Appendix A*). To employ this method, it must be assumed that the FePt$_2$Cu sample is a system of particles that are

1. single-domain

2. non-interacting

3. monodisperse

4. spherical

5. with uniaxial anisotropy and random distribution of the anisotropy axis

6. surface anisotropy effects are negligible and K is simply proportional to the particle volume $K = K_{eff}$V.

Following reference [183], a bimodal Gaussian-shaped distribution of K was chosen as

$$p(K) = \frac{A}{\sigma_1\sqrt{2\pi}}e^{-\frac{(K-K_1)^2}{2\sigma_1^2}} + \frac{B}{\sigma_2\sqrt{2\pi}}e^{-\frac{(K-K_2)^2}{2\sigma_2^2}}, \tag{5.3}$$

where A and B are weights of the two Gaussian peaks centered at K_1 and K_2 with corresponding standard deviations σ_1 and σ_2.

To check the deviation of the properties of in-flight annealed FePt$_2$Cu particles from the Stoner-Wohlfarth model, the corresponding Henkel plot [192] was obtained. The Henkel plot is a combination of two measurements: isothermal remanent magnetization M_r(H) and DC-demagnetization M_d(H) [191]. To measure M_r(H), a fully demagnetized sample is cooled down in zero magnetic field. When the experiment temperature (in this case 5 K) is reached, a small external field H is applied for some time, and afterwards that the field is switched off, and the remanence magnetization M_r(H) is measured. The process is repeated with increased value of H until the sample reaches saturation (the remanence magnetization reaches the value of $M_r(\infty)$). The DC-demagnetization M_d(H) is measured in a similar way to that of M_r(H), but initially the sample is in the saturated state. A magnetic field H is then applied in the direction opposite to the sample's magnetization. Then, the magnetic field is switched off, and the remanent magnetization M_d(H) is measured. The process is repeated until the sample reaches saturation in the opposite direction. Both M_r(H) and M_d(H) are normalized to the saturation remanent magnetization M$_r(\infty)$. The normalized values m_d(H) and m_r(H) are used to construct the Henkel plot as shown in Fig.5.12.

In a perfect Stoner-Wohlfarth system m_d(H) = 1 - 2m_r(H) [192] as represented by straight red line in Fig.5.12. If, for example, nanoparticles interact with each other via dipolar interactions, the Henkel plot shows a deviation from linearity (Fig.5.12, empty circles). The exchange interactions produce the deviation from linearity with the opposite curvature.

The Henkel plot obtained for in-flight annealed FePt$_2$Cu particles is shown in Fig.5.12 (black squares). The behavior clearly deviates from an ideal Stoner-Wohlfarth model (red line). The deviation of experimental values from the values predicted by Stoner-Wohlfarth model was estimated using the chi-square parameter:

$$\chi = \sqrt{\sum_i \frac{((m_{d_i}(H))_{exp} - (m_{d_i}(H))_{SW})^2}{(m_{d_i}(H))_{SW}}}, \qquad (5.4)$$

where $(m_{d_i}(H))_{exp}$ are experimental values of DC-demagnetization, $m_{d_i}(H))_{SW}$ are the values expected for the perfect Stoner-Wohlfarth particles $(m_{d_i}(H))_{SW} = 1\text{-}2(m_{r_i}(H))_{exp})$. χ was found to be 0.22, which means that there is a 22% deviation from perfect Stoner-Wohlfarth behavior.

5.5 Distribution of magneto-crystalline anisotropy energy densities in in-flight annealed FePt$_2$Cu nanoparticles

Fig.5.13 shows the normalized experimental magnetization loops measured at 5 K (black squares) together with the model magnetization loop fitted to the experimental data (red solid line). The fitting was done by the standard Levenberg-Marquardt algorithm. Fit parameters are given in Table.5.4.

Table 5.4: Magnetic anisotropy density distribution parameters (eq.5.3) evaluated for in-flight annealed FePt$_2$Cu nanoparticles using the Stoner-Wohlfarth model

A	B	K$_1$, MJ/m^3	K$_2$, MJ/m^3	σ_1,MJ/m^3	σ_2,MJ/m^3
0.5	0.5	0.190	0.628	0.07	1.96

The magnetic anisotropy density distribution $p(K)$ described by equation 5.3 is plotted in Fig.5.14. The chi-square parameter (see equation 5.4) was determined as 0.2, which implies a 20% deviation of the fitting function from experimental data. It has to be noted that the fit was done assuming ideal Stoner-Wohlfarth behavior of the particles. Taking into consideration the deviation from the Stoner-Wohlfarth model shown by Henkel plot, the fit
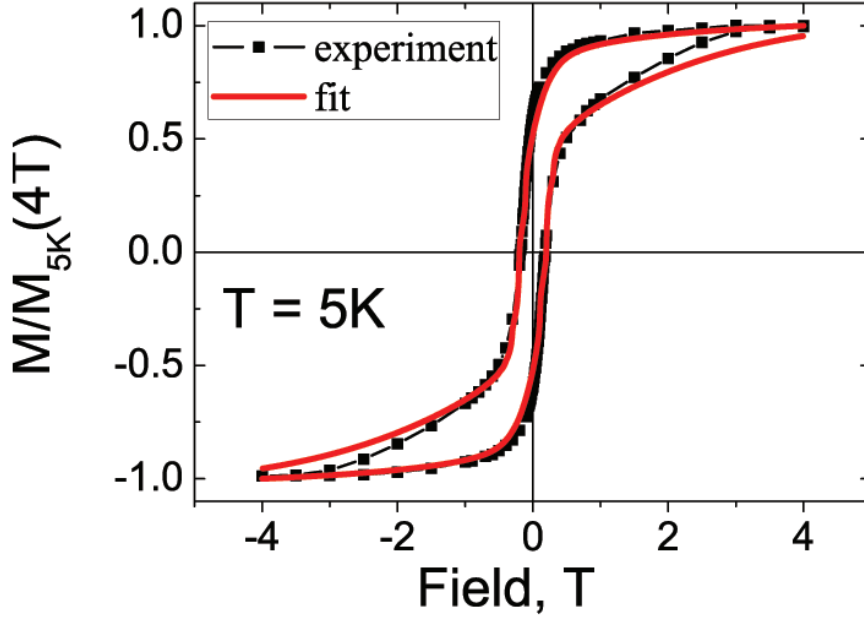
Figure 5.13: Normalized magnetization loop M(H)/M$_{5K}$(4T) of in-flight annealed FePt$_2$Cu nanoparticles measured at 5K (black squares). The solid line represents the magnetization loop calculated using the Stoner-Wohlfarth model with a bimodal Gaussian-shaped distribution of magnetic anisotropy densities p(K).

adequately describes the magnetization behavior of in-flight annealed FePt$_2$Cu nanoparticles.

The blocking temperatures T$_{K1}$ and T$_{K2}$ were calculated from corresponding peak positions K$_1$ and K$_2$ as

$$T_K = \frac{K <V>_{sint}}{\alpha k_B} \tag{5.5}$$

where $<V>_{sint} = \pi <d>_{sint}^3/6$ is the mean volume of the in-flight annealed FePt$_2$Cu particles, and k$_B$ is the Boltzmann constant. The parameter α is given by $\ln(\tau/\tau_0) \simeq 25$, where $\tau_0 \simeq 10^{-9}$ s is the characteristic time for thermal fluctuations of the magnetization in nanoparticles, and τ is the measurement time window ($\tau = 10^2$ s DC magnetometry) [19]. The estimated values of T$_{K1}$ = 76 K and T$_{K2}$ = 260 K are close (within 4-5 %) to the values
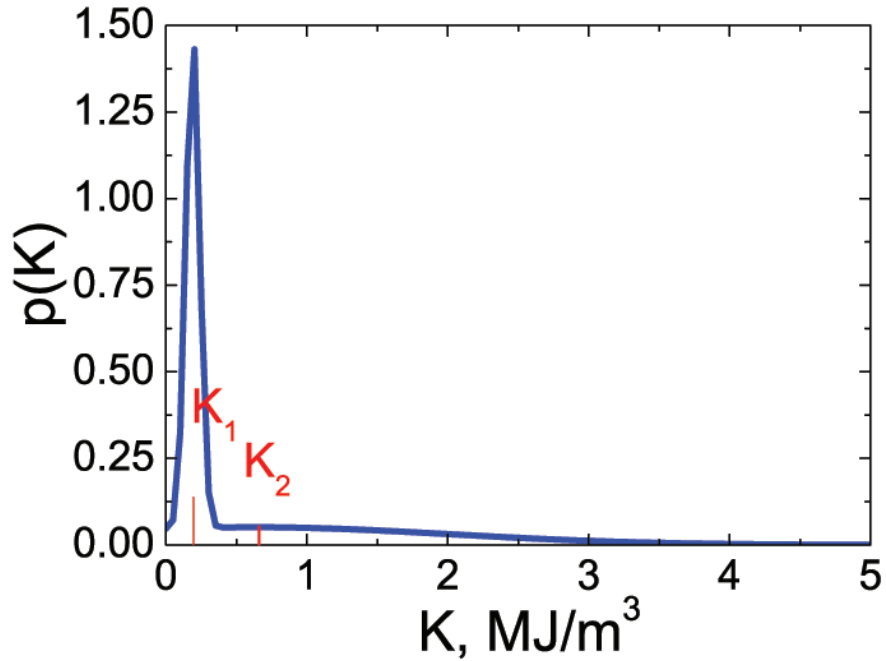
Figure 5.14: Bimodal Gaussian-shaped distribution of magnetic anisotropy densities p(K) described by equation 5.3.

of the characteristic blocking temperatures T_{B1sint} = 80 K and T_{B2sint} = 270 K obtained from ZFC curves. This also confirms that the model adequately describes the distribution of anisotropy energies in annealed FePt$_2$Cu nanoparticles.

Simulated magnetization loops corresponding to each Gaussian mode in eq.5.3 are plotted in Fig.5.15. From here, the annealed FePt$_2$Cu particles may be viewed as a system consisting of two magnetic phases. One of these is a soft magnetic phase containing particles with a Gaussian distribution of anisotropy density K centered at K_1 and standard deviation σ_1. The magnetization loop corresponding to this phase simulated at 5K shows a coercivity of 1300 Oe. The other is a hard magnetic phase corresponding to the second Gaussian peak, and has a coercivity of 8800 Oe. Summed together, two hysteresis loops produce the "wasp-waisted"shaped magnetization loop observed experimentally (Fig.5.13).
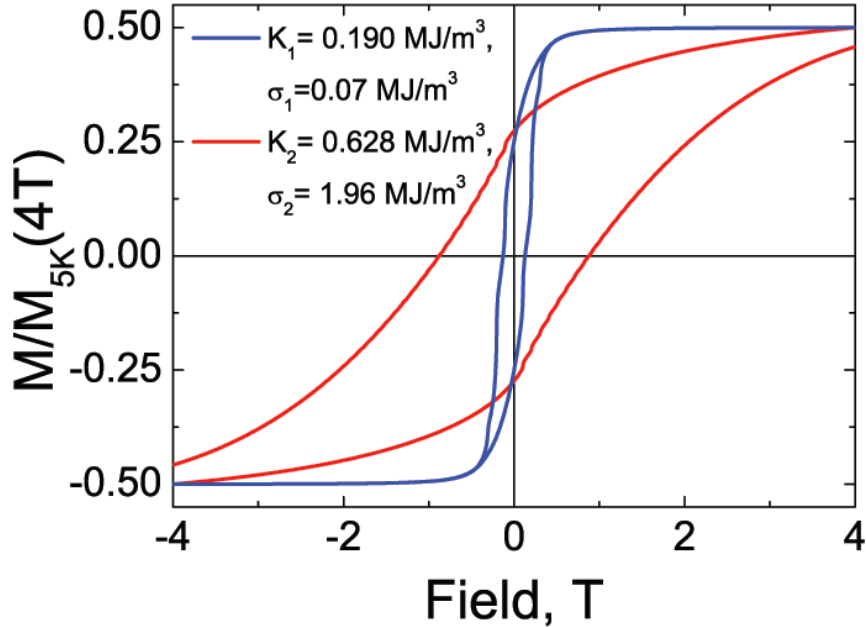
Figure 5.15: Simulated normalized magnetization loops corresponding to soft and hard magnetic phases of the in-flight annealed FePt$_2$Cu nanoparticles (see text).

5.6   Concentration distribution in in-flight annealed FePt$_2$Cu nanoparticles

One of the origins of the anisotropy energy distribution can be attributed to a variation of the relative Fe, Pt and Cu concentrations from particle to particle. Compositions of 50 individual in-flight annealed nanoparticles were measured, and the results are plotted in a Fe-Pt-Cu ternary diagram at 1273 K (Fig.5.16). The composition range covers different areas of phase diagram: region **I**, where the stable ordered L1$_0$ structure is formed, region **II**, where both L1$_0$ and disordered fcc (Cu and Pt-rich) phases exist, and region **III**, where Fe-Pt-Cu only has the disordered Pt-rich fcc structure.

Though, the actual relation between structure and concentration may be different for gas-phase nanoparticles, as they do not have enough time to reach an equilibrium state
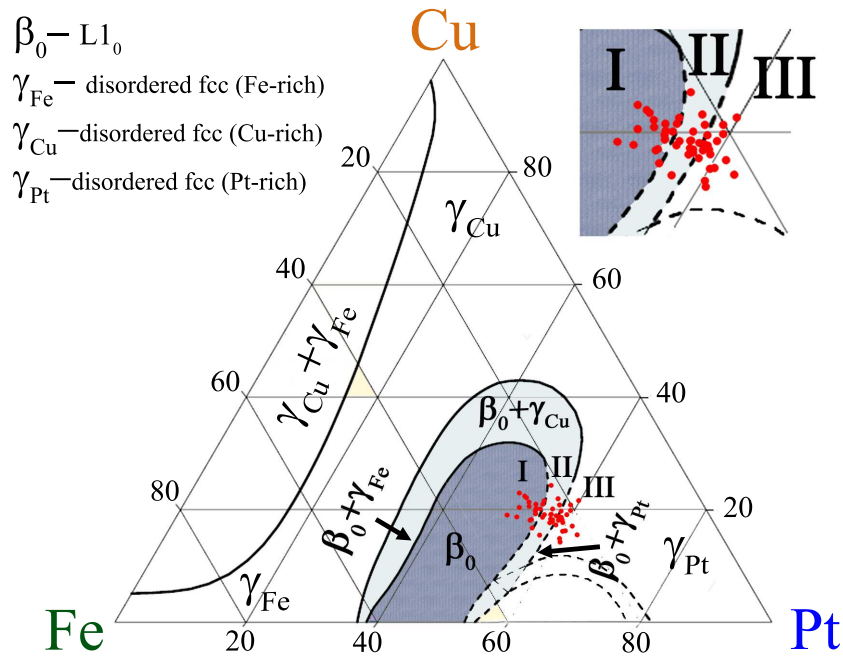
Figure 5.16: Concentrations of individual in-flight annealed FePt$_2$Cu nanoparticles (in at.%) plotted on Fe-Pt-Cu ternary phase diagram [102] (isothermal section at 1273 K).

during formation, the non-uniformity in the concentration leads to a non-uniformity in the ordering parameter. Hence, there is a magnetic anisotropy energy distribution and a co-existence of hard and soft magnetic phases.

The reason for this is that the plasma density is non-uniform. Plasma density and shape defines the conditions of the particles' nucleation and growth and is strongly correlated with the distribution of magnetic flux. The latter strongly depends on the magnetic permeability of the sputtering target and its configuration, as illustrated in Fig.1.25 [59]. A change in the target's magnetic permeability leads to a change in the magnetic flux distribution and plasma density. In the case of a Cu-patched FePt target, the plasma shape becomes complex and non-uniform due to different magnetic permeabilities of Cu and FePt. This means that atoms are sputtered with different probabilities from different areas of the target leading to the formation of particles with various elemental concentrations.

An additional complication comes from the fact that the plasma density distribution also defines the plasma temperature gradient. This means that in case of a non-uniform plasma, the different fractions of particles will form in different thermal environments, so even particles with the same elemental concentration may have a different degree of order. Though the particles are annealed in the furnace after they exit the plasma, the annealing time is too short (0.16 s) and is not sufficient for complete ordering.

5.7   Fe-Pt-Cu nanoparticles: summary

Fe-Pt-Cu nanoparticles prepared in this work were compared to FePt particles prepared using the same setup under identical preparation conditions ([60]). Both primary and in-flight annealed FePt particles were fcc multi-twinned icosahedral crystals. Adding 5 and 7 at.% of Cu had no significant effect on structure and morphology of Fe-Pt-Cu particles which remained multi-twinned icosahedra. Adding 11 at.% of Cu produced a small amount of double-twinned L1$_0$ ordered particles, but the majority of them also remained icosahedral.

However, adding higher concentration of Cu (about 25 at.%) had a significant effect on structure and morphology in both primary and in-flight annealed Fe-Pt-Cu particles as compared to Fe-Pt nanoparticles prepared under the same conditions. Primary particles with three different morphologies are found: single-crystal octahedra (some of which exhibited L1$_0$ ordered structure in particle core), single crystal truncated octahedra and multi-twinned fcc icosahedra. After annealing at 1273 K, 95% of FePt$_2$Cu particles become single-crystalline, and at least 40% of them possess the ordered L1$_0$ structure. This result shows that under chosen preparation conditions, sufficient amount of Cu is capable of suppressing the formation of twinned structures and to induce chemical L1$_0$-type ordering.

Analysis of magnetization measurements revealed a wide distribution of magneto-crystalline anisotropy energy densities and co-existence of hard and soft magnetic phases in primary and in-flight annealed FePt$_2$Cu nanoparticles.

Chapter 6

Conclusions

This work has been devoted to the investigation of three types of multi-metallic particles: (1) Fe-Cu, (2) Fe-Ag and (3) FePt-Cu.

Fe-Cu nanoparticles. Fe-Cu nanoparticles with three different average concentrations of Fe(Cu) $C_{Fe(Cu)}$ = 25(75), 60(40) and 75(25) at.% were investigated. For each concentration two samples were prepared: the primary particles, produced without in-flight annealing, and particles annealed in-flight at 1273 K (see *Chapter 3*).

The majority of primary Fe-Cu particles consist of a single-crystal core and polycrystalline (oxide) shell. 90% of the $Fe_{75}Cu_{25}$ and $Fe_{60}Cu_{40}$ particles have spherical shape and the rest 10% are cubic. All particles consist of both Fe and Cu uniformly distributed in the core forming a metastable alloy. The crystal structure depends on the Fe(Cu) content. Iron-rich $Fe_{75}Cu_{25}$ nanoparticles have a bcc alloy core, while copper-rich $Fe_{25}Cu_{75}$ particles are fcc. The majority of $Fe_{60}Cu_{40}$ particles possess a bcc alloy structure. This result is in agreement with the phase diagrams of Fe-Cu metastable alloys [25].

The distribution of Fe and Cu in $Fe_{75}Cu_{25}$ and $Fe_{25}Cu_{75}$ primary particles is uniform, except for thin oxide shell. In spherical primary $Fe_{60}Cu_{40}$ particles a distinct local composition variation caused by spinodal decomposition is observed. For cubic particles the elemental distribution is uniform. Cubic particles are most likely formed in areas with higher cooling rate which reduces segregation.

Thermal treatment promotes phase segregation, which also depends on Cu concentration. In the in-flight annealed $Fe_{25}Cu_{75}$ particles complete segregation of iron and copper is observed. In $Fe_{60}Cu_{40}$ and $Fe_{75}Cu_{25}$ samples iron and copper segregate via spinodal decomposition into $Fe_{rich}Cu$ and $FeCu_{rich}$ regions. The $Fe_{75}Cu_{25}$ alloy is more stable to annealing and preserves the bcc structure, while in $Fe_{60}Cu_{40}$ particles Fe_{rich} and Cu_{rich} regions become more pronounced and both fcc and bcc structures are formed. The thermal stability of Fe-Cu nanoalloys decreases with increasing Cu concentration, because of the higher iron diffusion rate in Fe-Cu alloy for higher copper concentration.

Fe-Ag nanoparticles. Two types of Janus Fe-Ag with different morphologies - dumbbell and "raspberry"- were prepared (see *Chapter 4*). The dumbbell nanoparticles consist of a faceted Ag part sitting on a $Fe@Fe_xO_y$ core-shell particle of spherical shape. The "raspberry" nanoparticles have several (3-4) smaller Ag pieces sitting on a spherical $Fe@Fe_xO_y$ particle. Ageing of both types of particles induced changes of their structure and morphology. For the dumbbell Fe-Ag particles, part of the faceted Ag piece evolved into a spherical Ag_2O particle which in some cases was separated entirely from the rest of the composite. The $Fe@Fe_xO_y$ part oxidized completely into a hollow oxide shell particle and encapsulated the rest of the silver inside. The "raspberry" particles aged in a similar fashion, only silver was fully encapsulated by an iron oxide shell. The following possible explanation for ageing of Fe-Ag particles is proposed. The main driving force for ageing is the minimization of surface energy and mass transport at Ag/iron oxide interface. As the iron/iron oxide part oxidizes, the voids are formed within the particle and silver starts diffusing inside through the void/Fe(Fe-oxide) interface. When a particle is fully oxidized, small voids coalesce into a large one in the centre of the particle and silver is encapsulated inside. In the dumbbell particles not only silver diffuses into voids in the iron part, but small pores appear in silver as well. These pores create the route for surface diffusion of iron oxide inside the silver part and finally the silver piece is "cut" in two halves. One half is encapsulated inside the oxide shell, another remains outside and in some cases completely separates from the rest of the composite to minimize interfacial energy. The outer silver part then oxidizes,

while encapsulated silver is protected from oxidation by the iron oxide shell.

FePt-Cu nanoparticles. FePt-Cu particles with 5 and 7 at.% Cu have the same structure and morphology as the FePt particles prepared under identical conditions [137]: fcc disordered multi-twinned icosahedra. Small amount (approximately 10%) of in-flight annealed nanoparticles with average Cu concentration of 11 at.% possess double-twinned morphology and $L1_0$ structure, the rest are also fcc icosahedral particles.

Adding approximately 25 at.% Cu to FePt changes the structure and morphology of particles, both in-flight annealed and primary.

In the primary FePt-Cu sample three different morphologies are found: one third of them are single-crystal partially $L1_0$ ordered octahedra, the rest are single crystal fcc disordered cubooctahedra and multi-twinned fcc disordered icosahedra. After annealing at 1273 K approximately 95% particles become single-crystal and at least 40 % of them possess the ordered $L1_0$ structure.

The magnetization measurements revealed the presence of two magnetic phases in both primary and in-flight annealed nanoparticles and a broad distribution of magnetic anisotropy energies. The primary particles have near zero coercivity at 300 K and small coercivity (about 160 Oe) at 5K. In-flight annealed particles have a small coercivity at room temperature (70 Oe) and coercivity of 1800 Oe at 5K. The hysteresis loops of primary and in-flight annealed particles have the "wasp-waisted" shape. The Stoner-Wohlfarth model with a double Gaussian distribution of magnetic anisotropy energy density was applied to fit the hysteresis loop of the in-flight annealed particles measured at 5K and was shown to adequately describe their magnetic behavior. The distribution of magnetic anisotropy energies is a result of the concentration distribution between individual FePt-Cu particles (see *Chapter 5*).

Summarizing, a detailed TEM spectroscopic and structural analysis of gas-phase synthesized Fe-Cu, Fe-Ag and FePt-Cu nanoparticles with different compositions has been presented here.

Appendix A

Stoner-Wohlfarth model with double Gaussian distribution of anisotropy energy density K

Here, the procedure and source code for fitting the experimental low temperature hysteresis loop with Stoner-Wohlfarth model with double Gaussian distribution of anisotropy energy density K are presented. The code was written in GNU Octave language. In case of a Stoner-Wohlfarth nanoparticle [18] with uniaxial anisotropy the magneto-crystalline energy is given to a first approximation by

$$E_C = K \sin^2 \phi, \tag{A.1}$$

where ϕ is the angle between the magnetization vector I_0 and easy axis. (Note: angle symbols are different from the original ones in [18]) The total energy of the particle can be written as

$$E = K \sin^2 \phi - H I_0 cos\theta, \tag{A.2}$$

where H is external magnetic field, and θ is the angle between magnetic field and mag-

netization vector. It can be easily seen that $\phi = \theta - \psi$, where ψ is the angle between magnetic field and easy axis of magnetization. Thus equation A.2 becomes:

$$E = K \sin^2(\theta - \psi) - HI_0 cos\theta. \tag{A.3}$$

It's convenient to express equations using non-dimensional parameters by dividing throughout by 2K giving the reduced energy η:

$$\eta = \frac{E}{2K} = \frac{1}{2}\sin^2(\theta - \psi) - hcos\theta, \tag{A.4}$$

$$\eta(h, \theta, \psi) = \frac{1}{4} - \frac{1}{4}\cos(2(\theta - \psi)) - h\cos\theta, \tag{A.5}$$

where h = $\frac{HI_0}{2K}$. (For a normalized loop I_0=1).

Treating h and ψ as fixed:

$$\frac{\partial\eta}{\partial\theta} = \frac{1}{2}\sin(2(\theta - \psi)) + h\sin\theta. \tag{A.6}$$

In the first part of the code angle ψ is varied from 0.1 to 89.9 rad with 0.1 rad step. For each step the value of h was varied from 0 to $h_{(max)}$=20. For each h the equation:

$$0 = \frac{1}{2}\sin(2(\theta - \psi)) + h\sin\theta \tag{A.7}$$

is solved. For each $\psi=\psi'$ the file named ψ'.txt is created. For a given value of ψ the critical values of h and θ, h_{crit} and θ_{crit}, for which the change in the direction of magnetization becomes discontinuous as the field changes continuously, are such that the fist partial derivative of η with respect to θ being zero, the second passes through zero from positive to negative value. Solving equations A.7 and equation

$$\frac{\partial^2\eta}{\partial\theta^2} = 0 = \cos(2(\theta - \psi)) + h\cos\theta. \tag{A.8}$$

simultaneously and eliminating h (see [18]) one gets:

$$\theta_{crit} = \psi + \tan^{-1}(\tan^{\frac{1}{3}}\psi). \tag{A.9}$$

Repeating the same procedure, but eliminating θ, one gets

$$h_{crit} = (\sin^{\frac{2}{3}}\psi + \cos^{\frac{2}{3}}\psi)^{-\frac{3}{2}} \tag{A.10}$$

file "SW1.txt":

```
for ang:0.1 thru 89.9 step 0.1 do batch("SW1.txt");
disp ( ang ) ;
np : 100;
H : 20;
array(hp,np);
array(hn,np);
array(mp,np);
array(mn,np);
psi : ang*%pi/(180.0);
 w : 0.5* sin (2*(theta - psi)) + h * sin ( theta);
hk : float ( ((sin (psi))^(2/3) + ((cos (psi))^(2/3) ))^(-3/2) );
thetacrit : float(psi + atan(tan(psi)^(1/3)));
/*hp[1] : 0.;
mp[1] : float(cos(psi));
hn[1] : 0.;
mn[1] : float(cos(%pi - psi));*/
hn[np] : hk;
mn[np] : float(cos(thetacrit));
 for i:1 thru np do
block (
hp[i] : (i-1)*H/(np-1),
h : hp[i],
theta_plus : find_root(w = 0, theta , 0, thetacrit),
mp[i] : float(cos(theta_plus)) );
for i:1 thru np-1 do
```

```
block (
 hn[i] : (i−1)*hk/(np−1),
 h : −hn[i],
 theta_min : find_root(w = 0, theta, 0 , thetacrit),
 mn[i] : float(cos(theta_min))
);


file_output_append : true ;
f_name : sconcat ("/home/tis/SW/psy",ang,".txt");
f : openw (f_name);
for i:1 thru np do printf(f,"~f ~f ~&",hp[i],mp[i]*sin(psi)) ;
for i:1 thru np do printf(f,"~f ~f ~&",−hn[i],mn[i]*sin(psi)) ;
close (f);
kill (allbut (ang));
```

Next part of the code the Stoner-Wohlfarth loop for the particles with easy axes distribution is calculated by averaging hysteresis loops obtained for each ψ.

file "SW2.txt":

```
clear all
list = glob("psy*.txt");

points = 2000;
h_max = 20;
angle_step = 0.0174533;
for i = 1:points
xi(i) = (−h_max + i*(2*h_max/points));
yi(i,1:size(list)(1)) = 0;
endfor

for k = 1:size(list)(1)
texte=load(char( list(k,1)));
texte = sort (texte);
yi(1:size(yi)(1),k)=interp1(texte(2:size(texte)(1),1),texte(2:size(texte
```

```
   )(1) ,2) , xi , ' l i n e a r ' ) ;
clear texte ;
endfor




for k = 1: s i z e ( l i s t ) ( 1 )
for i = 1: s i z e ( yi ) ( 1 )
if ( isnan ( yi ( i , k ) ) )
yi ( i , k ) = −yi ( s i z e ( yi ) (1)−i +1 ,k ) ;
endif
endfor
endfor




y_avg (1: s i z e ( yi ) ( 1 ) ,1) = 0;
for k = 1: s i z e ( l i s t ) ( 1 )
y_avg (1: s i z e ( yi ) ( 1 ) ,1) = y_avg (1: s i z e ( yi ) ( 1 ) ,1) + yi (1: s i z e ( yi ) ( 1 ) ,k ) ;
endfor
y_avg=y_avg∗angle_step ;
plot ( xi , y_avg , −xi , −y_avg ) ;




fid = fopen ( " h y s t e r e s i s . dat " , "w" ) ;
for i = 1: s i z e ( y_avg ) ( 1 )
f p r i n t f ( f i d , "%f %f \n" , xi ( i ) , y_avg ( i ) ) ;
endfor
f c l o s e ( f i d ) ;
clear all
```

The next step is fitting experimental data. The experimental hysteresis loop must be normalized to saturation value. In the first part of code in the file **SW3.txt** data is fitted by function **linefunc** using Octave package **leasqr**. The magneto-crystalline anisotropy energy density K is varied in the range from $K_1 = 0.1 \frac{MJ}{m^3}$ to maximum possible value for FePt - $K_{max} = 7 \frac{MJ}{m^3}$. Initial fitting parameters are set in the array **pin**, the resulting fitting

parameters are stored in the array **p**. In the second part the hysteresis loop for the Stoner-Wohlfarth particles with double Gausssian distribution (with distribution parameters obtained from the fit) is calculated. This is done in the following way: for each experimental value of the magnetic field H the value of magnetization $M^H{}_{Fit}$ is calculated as:

$$M_{Fit}^H = M_{K_1} + M_{K_2} + ... M_{K_n} ... + M_{K_{max}},$$ (A.11)

where $M_{K_n} = M_{SW}(h = \frac{H}{2K})p(K)$, where M_{SW} is taken from the Stoner-Wohlfarth loop calculated in **SW2.txt**, and p(K) - is double Gaussian distribution (Eq.5.3). The resulting curve is written in file **SIMhysteresis.dat**.

    file "SW3.txt":

```
% Part 1 start here
clear all;


function [y]=line_func(x,par)
y_avg = load ("hysteresis.dat");
y = 0;
y1 = 0;
for i = 1 : 70
K =   0.1*i ;
k_i = 1/(abs(par(1))*sqrt(2*pi))*exp(-0.5*((K-abs(par(2)))/abs(par(1)))
    ^2) + 1/(abs(par(3))*sqrt(2*pi))*exp(-0.5*((K-abs(par(4)))/abs(par
    (3)))^2);


y =y + interp1(y_avg(1:size(y_avg)(1),1),y_avg(1:size(y_avg)(1),2),x/(2*
    K),'spline')*k_i;


y1 = y1 + interp1(y_avg(1:size(y_avg)(1),1),y_avg(1:size(y_avg)(1),2),2/
    K,'spline')*k_i;


endfor


y = y/y1;
```

```
clear y1 K y_avg i k_i


end



a=load("ExperimentalData.dat" );
x = a(1:size(a)(1),1);
y = a(1:size(a)(1),2);
clear a;


% Perform the fit
pin=[0.1,0.11,0.1,0.6,1,1];
[f,p,cvg,iter,corp,covp]=leasqr(x,y,pin,"line_func",.00001,100);




p
% Part 1 ends here


% Part 2 starts here
y_avg = load ("hysteresis.dat");
#                                                      k



w_1 = p(1);
K_1 = p(2);
w_2 = p(3);
K_2 = p(4);
A = p(5);
B = p(6);


for i = 1 : 70
K =   0.1*i ;
k_i(i) = A/(w_1*sqrt(2*pi))*exp(−2*((K−K_1)/w_1)^2) + B/(w_2*sqrt(2*pi))
```

```
    *exp(-2*((K-K_2)/w_2)^2);
endfor


for j = 1 : 800
M(j,2) = 0;
H_ext = (-400+j)/100;
M(j,1) = H_ext;
 for i = 1 : 70
K = 0.1*i ;
M(j,2)=M(j,2)+interp1(y_avg(1:size(y_avg)(1),1),y_avg(1:size(y_avg)(1)
    ,2),H_ext/(2*K),'linear')*k_i(i);
 endfor


 endfor


M(1:size(M)(1),2)=M(1:size(M)(1),2)/M(size(M)(1),2);
a = load("ExperimentalData.dat");
plot(M(1:size(M)(1),1),M(1:size(M)(1),2),a(1:size(a)(1),1),a(1:size(a)
    (1),2),'+')


b = interp1(M(1:size(M)(1),1),M(1:size(M)(1),2),a(1:size(a)(1),1));
chi = 0;
for i = 1:size(b)(1)-1
chi = chi + (b(i)-a(i,2))^2/abs(a(i,2));
endfor


fid = fopen ("SIMhysteresis.dat", "a");
fprintf(fid,"# y_0 = %f, A = %f, w_1 = %f, K_1 = %f, B = %f, w_2 =
    %f, K_2 = %f \n",y_0, A, w_1, K_1, B, w_2, K_2);
for i = 1:size(M)(1)
fprintf(fid,"%f %f\n",M(i,1),M(i,2));
endfor
fclose(fid);
```

```
clear all

% Part 2 ends here
```

Bibliography

[1] M.T. Swihart. Vapor-phase synthesis of nanoparticles. *Current Opinion in Colloid and Interface Science*, 8:127–133, 2003.

[2] Boris M. Smirnov. *Cluster processes in gases and plasmas*. Wiley-VCH Verlag GmbH & Co. KGaA, 2010.

[3] T.B. Massalski. *Binary Alloys Phase Diagrams*, volume II. ASM International, Materials Park, Ohio, 1990.

[4] J. Lyubina, B. Rellinghaus, O. Gutfleisch, and M. Albrecht. *Handbook of Magnetic Materials*, volume 19. Elsevier, 2011.

[5] M. Mueller and K. Albe. Structural stability of multiply twinned FePt nanoparticles. *Acta Materialia*, 55(19):6617 – 6626, 2007.

[6] R. C. Flagan and M. M. Lunden. Particle structure control in nanoparticle synthesis from the vapor phase. *Materials Science and Engineering A*, 204:113 – 124, 1995.

[7] X. Liu and J.-P. Wang. Fabrication and morphologies of large directly ordered L10 FePt nanoparticles in gas phase. *Journal of Applied Physics*, 105(7):07A722(3), 2009.

[8] X. Liu. *Gas-phase synthesis of magnetic nanocomposite materials and its application inch anisotropic-echange-spring magnets.* PhD thesis, University of Minnesota, 2009.

[9] A.T. Dinsdale. SGTE data for pure elements. *CALPHAD*, 15:317–425, 1991.

[10] T.B. Massalski. *Physical Metallurgy*, volume I. Elsevier Science B.V., Amsterdam, 1996.

[11] J. A. Alonso and S. Simozar. Prediction of solid solubility in alloys. *Phys. Rev. B*, 22 (12):5583–5589, 1980.

[12] A.R. Miedema, P.F. de Chadel, and F. R. de Boer. Cohesion in alloys - fundamentals of a semi-empirical model. *Physica B.*, 100:1–28, 1980.

[13] J.A. Alonso. The factors influencing solid solubility in metallic alloys. *Revista Latinoamericana de Metalurgia y Materiales*, 5:3–13, 1985.

[14] J.M. López and J. A. Alonso. A comparison of two parametrizations of solid solubility in alloys: thermochemical coordinates versus orbital radii coordinates. *Physica B*, 113(1):103–112, 1982.

[15] D.H. Kim, W.T. Kim, E.S. Park, N. Mattern, and J. Eckert. Phase separation in metallic glasses. *Progress in Materials Science*, 58 (8):1103–1172, 2013.

[16] S Bedanta and W. Kleemann. Supermagnetism. *Journal of Physics D: Applied Physics*, 42(1):013001 (28), 2009.

[17] M. Knobel, W.C. Nunes, L.M. Socolovsky, E. De Biasi, J.M. Vargas, and J.C. Denardin. Superparamagnetism and other magnetic features in granular materials: A review on ideal and real systems. *Journal of Nanoscience and Nanotechnology*, 8(6):2836–2857, 2008.

[18] E.C. Stoner and P. Wohlfarth. A mechanism of magnetic hysteresis in heterogeneous alloys. *Philos. Trans. R. Soc. London A*, 240:599–642, 1948.

[19] F. Tournus and E. Bonet. Magnetic susceptibility curves of a nanoparticle assembly I: Theoretical model and analytical expressions for a single magnetic anisotropy energy. *JMMM*, 323:1109–1117, 2011.

[20] F. Tournus and A. Tamion. Magnetic susceptibility curves of a nanoparticle assembly II. Simulation and analysis of ZFC/FC curves in the case of a magnetic anisotropy energy distribution. *JMMM*, 323:1118–1127, 2011.

[21] A. Jansson. Trita Mac 0340,Mater. Res. Center KTH, Stockholm, Sweden, 1987.

[22] E. Ma and M. Atzmon. Phase transformations induced by mechanical alloying in binary systems. *Materials Chemistry and Physics*, 39(4):249 – 267, 1995.

[23] G. Mazzone and M. V. Antisari. Structural and magnetic properties of metastable fcc Cu-Fe alloys. *Phys. Rev. B*, 54:441–446, Jul 1996.

[24] L.B. Hong and B. Fultz. Two-phase coexistence in Fe-Cu alloys synthesized by ball milling. *Acta Materialia*, 46(8):2937 – 2946, 1998.

[25] M. Qi, M. Zhu, and D.Z. Yang. On the supersaturated solution in the Fe-Cu binary system induced by high energy ball milling. *Journal of Materials Science Letters*, 13(13):966–968, 1994.

[26] K. Sumiyama, T. Yoshitake, and Y. Nakamura. Magnetic properties of metastable bcc and fcc Fe-Cu alloys produced by vapor quenching. *Journal of the Physical Society of Japan*, 53(9):3160–3165, 1984.

[27] E. F. Kneller. Magnetic and structural properties of metastable Fe-Cu solid solutions. *Journal of Applied Physics*, 35(7):2210–2211, 1964.

[28] F. Kajzar and G. Parette. Magnetic moment distribution in bcc Fe-Cu alloys. *Journal of Applied Physics*, 50(B3):1966–1968, 1979.

[29] J. Z. Jiang and X. J. Liu. *Encyclopedia of Nanoscience and Nanotechnology*, volume X. American Scientific Publishers, 2004.

[30] Q. Chen and Z. Jin. The Fe-Cu system: A thermodynamic evaluation. *Metallurgical and Materials Transactions A*, 26(2):417–426, 1995.

[31] A. Hernando, P. Crespo, A. García Escorial, J. Barandiaran, M. Urchulutegui, and M. Vittori Antisari. Contrast modulations during decomposition of Fe-Cu alloys. *Europhys. Lett.*, 32(7):585–588, 1995.

[32] E. Hornbogen. Structure and thermal stability of vapour-deposited Fe-Cu alloys. *Journal of Materials Science*, 13:666–670, 1978.

[33] Y. Nakamura, K. Sumiyama, and N. Kataoka. Thermal stability of high concentration Fe-Ag and Fe-Cu alloys produced by vapor quenching. *Hyperfine Interactions*, 28:1029–1032, 1986.

[34] J. Eckert, R. Birringer, J.C. Holzer, C.E. Krill III, and W.L. Johnson. Alloy effects and extended solubilities in binary mixtures of nanometer-sized Fe-Cu crystals. *Mat. Res. Soc. Symp. Proc.*, 238:739–744, 1992.

[35] J. Eckert, J.C. Holzer, C.E. Krill III, and W.L. Johnson. Mechanically driven alloying and grain size changes in nanocrystalline Fe-Cu powders. *Journal of Applied Physics*, 73:2794–2802, 1993.

[36] J. Eckert, J.C. Holzer, and W.L. Johnson. Thermal stability and grain growth behavior of mechanically alloyed nanocrystalline Fe-Cu alloys. *Journal of Applied Physics*, 73:131–141, 1993.

[37] P. Crespo, A. Hernando, R. Yavari, O. Drbohlav, and A. Garcia-Escorial. Magnetic behavior of metastable fcc Fe-Cu after thermal treatments. *Physical Review B*, 48:7134–7139, 1993.

[38] P. Crespo, A. Hernando, and A. Garcia-Escorial. Spinodal decomposition of Fe-Cu nanocrystals: control of atomic-magnetic-moment and magnetic properties. *Physical Review B*, 49:13227–13230, 1994.

[39] P. Crespo, N. Menéndez, J.D. Tornedo, M.J. Barro, J. Barandiaran, A. García Escorial, and A. Hernando. Mössbauer spectroscopy evidence of a spinodal mechanism for the thermal decomposition of fcc FeCu. *Acta Mater.*, 46(12):4161–4166, 1998.

[40] P. Crespo, A. Hernando, A. García Escorial, K.M. Kemner, and V.G. Harris. Extended x-ray absorption fine-structure studies of heat-treated fcc Fe50Cu50 powders processed via high-energy ball milling. *J. Appl. Phys.*, 76(10):6322–6324, 1994.

[41] L. J. Swartzendruber. The AgFe (Silver-Iron) system. *Bull. Alloy Phase Diag.*, 5:560–564, 1984.

[42] A. Perro, S. Reculusa, S. Ravaine, E. Bourgeat-Lamic, and E. Duguet. Design and synthesis of Janus micro- and nanoparticles. *J. Mater. Chem.*, 15:3745–3760, 2005.

[43] B. P. Binks. Particles as surfactants-similarities and differences. *Curr. Opin. Colloid Interf. Sci.*, 7:21–41, 2002.

[44] T. Honegger, O. Lecarme, K. Berton, and D. Peyrade. 4-D dielectrophoretic handling of Janus particles in a microfluidic chip. *Microelectron. Eng.*, 87:756–759, 2010.

[45] T. Honegger, O. Lecarme, K. Berton, and D. Peyrade. Rotation speed control of Janus particles by dielectrophoresis in a microfluidic channel. *J. Vac. Sci. Technol. B*, 28:C6I14, 2010.

[46] H. Takei and N. Shimizu. Gradient sensitive microscopic probes prepared by gold evaporation and chemisorption on latex spheres. *Langmuir*, 13:1865–1868, 1997.

[47] H. Gu, Zh. Yang, J. Gao, C.K. Chang, and B. Xu. Heterodimers of nanoparticles: Formation at a liquid-liquid interface and particle-specific surface modification by functional molecules. *J. Am. Chem. Soc.*, 127:34–35, 2005.

[48] J.-S. Choi, Y.-W. Jun, A.-I. Yeon, H.C. Kim, J.-S. Shin, and J. Cheon. Biocompatible heterostructured nanoparticles for multimodal biological detection. *J. Am. Chem. Soc.*, 128:15982–15983, 2006.

[49] Y.-S. Lin, S.-H. Wu, Y. Hung, Y.-H. Chou, C. Chang, M.-L. Lin, C.-P. Tsai, and C.-Y. Mou. Multifunctional composite nanoparticles: Magnetic, luminescent, and mesoporous. *Chem. Mater*, 18:5170 – 5172, 2006.

[50] C. Xu, J. Xie, D. Ho, C. Wang, N. Kohler, E. G. Walsh, J. R. Morgan, Y. E. Chin, and S. Sun. Au-Fe3O4 dumbbell nanoparticles as dual-functional probes. *Angew. Chem. Int. Ed.*, 47:173–173, 2008.

[51] G.P. Adams and L.M. Weiner. Monoclonal antibody therapy of cancer. *Nat. Biotech.*, 23:1147–1157, 2005.

[52] S.T. Selvan, P.K. Patra, Ch.Y. Ang, and J.Y. Ying. Synthesis of silica-coated semiconductor and magnetic quantum dots and their use in the imaging of live cells. *Angew. Chem. Int. Ed.*, 46:2448–2452, 2007.

[53] Ch. Wang, Ch. Xu, H. Zeng, and S. Sun. Recent progress in syntheses and applications of dumbbell-like nanoparticles. *Adv. Mater.*, 21:3045–3052, 2009.

[54] H. Ying, Ch. Wang, H. Zhu, S. Overbury, S. Sun, and Sh. Dai. Colloidal deposition synthesis of supported gold nanocatalysts based on Au-Fe3O4 dumbbell nanoparticlesw. *Chem. Commun.*, 36:4357–4359, 2008.

[55] J. Zhang, K. Sasaki, E. Sutter, and R. R. Adzic. Stabilization of platinum oxygen-reduction electrocatalysts using gold clusters. *Science*, 315:220–222, 2007.

[56] H. Yu, M. Chen, P.M. Rice, S.X. Wang, R.L. White, and S. Sun. Dumbbell-like bifunctional Au-Fe3O4 nanoparticles. *Nano Lett.*, 5:379382, 2005.

[57] M.-Ch. Daniel and D. Astruc. Gold nanoparticles: Assembly, supramolecular chemistry, quantum-size-related properties, and applications toward biology, catalysis, and nanotechnology. *Chem. Rev.*, 104:293–346, 2004.

[58] N. A. Frey, S. Srinath, H. Srikanth, Ch. Wang, and Sh. Sun. Static and dynamic magnetic properties of composite Au-Fe3O4 nanoparticles. *IEEE Tran. on Magn.*, 43:3094–3096, 2007.

[59] J.-P. Wang. FePt magnetic nanoparticles and their assembly for future magnetic media. *Proceedings of the IEEE*, 96(11):1847–1863, 2008.

[60] S. Stappert, B. Rellinghaus, M. Acet, and E. F. Wassermann. Gas-phase preparation of L10 ordered FePt nanoparticles. *Journal of Crystal Growth*, 252:440 – 450, 2003.

[61] J.-U. Thiele, L. Folks, M. F. Toney, and D. K. Weller. Perpendicular magnetic anisotropy and magnetic domain structure in sputtered epitaxial FePt (001) L10 films. *Journal of Applied Physics*, 84(10):5686–5692, 1998.

[62] M. R. Visokay and R. Sinclair. Direct formation of ordered CoPt and FePt compound thin films by sputtering. *Applied Physics Letters*, 66(13):1692–1694, 1995.

[63] B. E. Warren. *X-ray Diffraction*. Dover Publications, Inc, 1990.

[64] J.V. Lyubina. *Nanocrystalline Fe-Pt alloys: phase transformations, structure and magnetism*. PhD thesis, Technischen Universität Dresden, 2006.

[65] G. H. O. Daalderop, P. J. Kelly, and M. F. H. Schuurmans. Magnetocrystalline anisotropy and orbital moments in transition-metal compounds. *Phys. Rev. B*, 44:12054–12057, Dec 1991.

[66] P. Kamp, A. Marty, B. Gilles, R. Hoffmann, S. Marchesini, M. Belakhovsky, C. Boeglin, H. A. Dürr, S. S. Dhesi, G. van der Laan, and A. Rogalev. Correlation of spin and orbital anisotropies with chemical order in Fe0.5Pd0.5 alloy films using magnetic circular x-ray dichroism. *Phys. Rev. B*, 59:1105–1112, 1999.

[67] V.V. Maykov, A.Y. Yermakov, G.V. Ivanova, V.I. Khrabrov, and L.M. Magat. Vliyanie stepeni dalnego atomnogo poryadka na magnitnie svoistva monocristallov CoPt i FePd (in russian). *Fiz. Met. Metalloved.*, 67:79, 1989.

[68] S. Okamoto, N. Kikuchi, O. Kitakami, T. Miyazaki, Y. Shimada, and K. Fukamichi. Chemical-order-dependent magnetic anisotropy and exchange stiffness constant of FePt (001) epitaxial films. *Phys. Rev. B*, 66:024413(9), Jul 2002.

[69] J. B. Staunton, S. Ostanin, S. S. A. Razee, B. Gyorffy, L. Szunyogh, B. Ginatempo, and E. Bruno. Long-range chemical order effects upon the magnetic anisotropy of FePt alloys from an ab initio electronic structure theory. *Journal of Physics: Condensed Matter*, 16(48):S5623–S5631, 2004.

[70] Ch.-B. Rong, Y. Li, and J. P. Liu. Curie temperatures of annealed FePt nanoparticle systems. *Journal of Applied Physics*, 101(9):09K505(3), 2007.

[71] D. C. Berry and K. Barmak. Effect of alloy composition on the thermodynamic and kinetic parameters of the A1 to L10 transformation in FePt , FeNiPt, and FeCuPt films. *Journal of Applied Physics*, 102(2):024912(9), 2007.

[72] A. Kussmann and G. Grfn von Rittberg. Untersuchung uber die Umwandlungen im System Platin-Eisen. *Z. Metallkd.*, 41:470–477, 1950.

[73] Y. Nose, A. Kushida, T. Ikeda, H. Nakajima, K. Tanaka, and H. Numakura. Re-examination of phase diagram of Fe-Pt system. *Mater. Trans.*, 44:2723–2731, 2003.

[74] A. Dannenberg, M. E. Gruner, A. Hucht, and P. Entel. Surface energies of stoichiometric FePt and CoPt alloys and their implications for nanoparticle morphologies. *Phys. Rev. B*, 80:245438(15), Dec 2009.

[75] O. Dmitrieva, M. Acet, G. Dumpich, J. Kästner, C. Antoniak, M. Farle, and K. Fauth. Enhancement of L10 phase formation in FePt nanoparticle by nitrogenization. *Journal of Physics D: Applied Physics*, 39(22):4741–4745, 2006.

[76] J.-M. Qiu and J.-P. Wang. Tuning the crystal structure and magnetic properties of FePt nanomagnets. *Advanced Materials*, 19(13):1703 – 1706, 2007.

[77] B. Rellinghaus, S. Stappert, M. Acet, and E. F. Wassermann. Magnetic properties of FePt nanoparticles. *Journal of Magnetism and Magnetic Materials*, 266:142 – 154, 2003.

[78] B. Rellinghaus, E. Mohn, L. Schultz, T. Gemming, M. Acet, A. Kowalik, and B. F. Kock. On the L10 ordering kinetics in Fe-Pt nanoparticles. *IEEE Transactions on Magnetics*, 42(10):3048–3050, 2006.

[79] S. Stappert, B. Rellinghaus, M. Acet, and E.F. Wassermann. Multiply twinned structures in gas-phase sintered stoichiometric Fe-Pt nanoparticles. *Proc. Mat. Res. Soc., Nanoparticulate Materials*, 704:73–78, 2002.

[80] R. M. Wang, O. Dmitrieva, M. Farle, G. Dumpich, H. Q. Ye, H. Poppa, R. Kilaas, and C. Kisielowski. Layer resolved structural relaxation at the surface of magnetic FePt icosahedral nanoparticles. *Phys. Rev. Lett.*, 100:017205(4), Jan 2008.

[81] R. Wang, O. Dmitrieva, M. Farle, G. Dumpich, M. Acet, S. Mejia-Rosales, E. Perez-Tijerina, M. J. Yacaman, and Ch. Kisielowski. FePt icosahedra with magnetic cores and catalytic shells. *The Journal of Physical Chemistry C*, 113(11):4395–4400, 2009.

[82] R. Wang, H. Zhang, M. Farle, and Ch. Kisielowski. Structural stability of icosahedral FePt nanoparticles. *Nanoscale*, 1:276–279, 2009.

[83] B. Yang, M. Asta, O.N. Mryasov, T.J. Klemmer, and R.W. Chantrell. The nature of A1L10 ordering transitions in alloy nanoparticles: A Monte Carlo study. *Acta Mater.*, 54:4201 – 4211, 2006.

[84] T. Miyazaki, O. Kitakami, S. Okamoto, Y. Shimada, Z. Akase, Y. Murakami,

D. Shindo, Y. K. Takahashi, and K. Hono. Size effect on the ordering of L10 FePt nanoparticles. *Phys. Rev. B*, 72:144419(5), Oct 2005.

[85] Y. K. Takahashi, T. Ohkubo, M. Ohnuma, and K. Hono. Size effect on the ordering of FePt granular films. *Journal of Applied Physics*, 93(10):7166–7168, 2003.

[86] Y. K. Takahashi, T. Koyama, M. Ohnuma, T. Ohkubo, and K. Hono. Size dependence of ordering in FePt nanoparticles. *Journal of Applied Physics*, 95(5):2690–2696, 2004.

[87] R. Wood. The feasibility of magnetic recording at 1 terabit per square inch. *IEEE Transactions on Magnetics*, 36(1):36–42, 2000.

[88] K. Zhang, X. Hu, L. Xie, J. Yuan, J. Zhu, and Dan Wei. Anisotropy distribution of FePt nanoparticles with twinned structures. *IEEE Transactions on Magnetics*, 45(10):4427–4430, 2009.

[89] C . Antoniak, M. Spasova, A. Trunova, K. Fauth, F. Wilhelm, A. Rogalev, J. Minár, H. Ebert, M. Farle, and H. Wende. Inhomogeneous alloying in FePt nanoparticles as a reason for reduced magnetic moments. *Journal of Physics: Condensed Matter*, 21(33):336002(12), 2009.

[90] L . Castaldi, K. Giannakopoulos, A. Travlos, N. Boukos, D. Niarchos, S. Boukari, and E. Beaurepaire. Engineering of FePt nanoparticles by e-beam co-evaporation. *Nanotechnology*, 19(13):135702(6), 2008.

[91] H. Ito, T. Shima, K. Takanashi, Y.K. Takahashi, and K. Hono. Control of the size for octahedral FePt nanoparticles and their magnetic properties. *Magnetics, IEEE Transactions on*, 41(10):3373–3375, 2005.

[92] K. Elkins, D. Li, N. Poudyal, V. Nandwana, Zh. Jin, K. Chen, and J. P. Liu. Monodisperse face-centred tetragonal FePt nanoparticles with giant coercivity. *Journal of Physics D: Applied Physics*, 38(14):2306–2309, 2005.

[93] J. S. Chen, C. Y. Tan, and G. M. Chow. Microstructure and direct ordering of FePt nanoparticles produced by nanocluster beam technology. *Nanotechnology*, 18(43):435604(6), 2007.

[94] S. Stoyanov, Y. Huang, Y. Zhang, V. Skumryev, G. C. Hadjipanayis, and D. Weller. Fabrication of ordered FePt nanoparticles with a cluster gun. *Journal of Applied Physics*, 93(10):7190–7192, 2003.

[95] O. Dmitrieva. *Strukturelle und magnetische Eigenschaften von FePt-Nanopartikeln aus der Gasphase*. PhD thesis, Universität Duisburg-Essen, 2007.

[96] M. Yata, H. Rouch, and K. Nakamura. Role of oxygen adatoms in homoepitaxial growth of Cu(001). *MRS Proceedings*, 528:59, 1998.

[97] H. Landolt and R. Boernstein. *Numerical Data and Functional Relationships in Science and Technology: New Series III*, volume 42A. Springer, Berlin, 1992.

[98] D. L. Olynick, J. M. Gibson, and R. S. Averback. Impurity-suppressed sintering in copper nanophase materials. *Philosophical Magazine A*, 77(5):1205 –1221, 1998.

[99] L. Li, A. Kida, M. Ohnishi, and M. Matsui. Surfactant effect of oxygen in epitaxial gamma-Fe/Cu(001)-O. *Surface Science*, 493:120–125, 2001.

[100] A. A. Kündig, N. Abe, M. Ohnuma, T. Ohkubo, H. Mamiya, and K. Hono. Rapidly solidified (FePt)70P30 alloy with high coercivity. *Applied Physics Letters*, 85(5):789 – 791, 2004.

[101] W. Zhang, D. V. Louzguine, and A. Inoue. Synthesis and magnetic properties of Fe–Pt–B nanocomposite permanent magnets with low Pt concentrations. *Applied Physics Letters*, 85(21):4998–5000, 2004.

[102] M. Shahmiri, S. Murphy, and D.J. Vaughan. Structural and phase equilibria studies in the system Pt-Fe-Cu and the occurrence of Tulameenite (Pt2FeCu). *Mineral. Mag.*, 49(353):547–554, 1985.

[103] S. D. Willoughby, J. M. MacLaren, T. Ohkubo, S. Jeong, M. McHenry, D. E. Laughlin, S.-J. Choi, and S.-J. Kwon. Electronic, magnetic, and structural properties of L10 FePt(x)Pd(1 - x) alloys. *Journal of Applied Physics*, 91(10):8822–8824, 2002.

[104] J. Lyubina, O. Gutfleisch, and O. Isnard. Phase transformations and magnetic structure of nanocrystalline Fe-Pd and Co-Pt alloys studied by in situ neutron powder diffraction. *Journal of Applied Physics*, 105(7):07A717(3), 2009.

[105] S. D. Willoughby. Electronic and magnetic properties of Fe(1 - x)Cu(x)Pt. *Journal of Applied Physics*, 95(11):6586–6588, 2004.

[106] J.F. Hu, J.S. Chen, B.C. Lim, and B. Liu. Underlayer diffusion-induced enhancement of coercivity in high anisotropy FePt thin films. *Journal of Magnetism and Magnetic Materials*, 320(22):3068 – 3070, 2008.

[107] Y. Zhu and J. W. Cai. Low-temperature ordering of FePt thin films by a thin AuCu underlayer. *Applied Physics Letters*, 87(3):032504(3), 2005.

[108] X.-H. Xu, H.-Sh Wu, F. Wang, and X.-L. Li. The effect of Ag and Cu underlayer on the L10 ordering FePt thin films. *Applied Surface Science*, 233:1 – 4, 2004.

[109] E. B. Svedberg, J. J. Mallett, S. Sayan, A. J. Shapiro, W. F. Jr. Egelhoff, and T. Moffat. Recrystallization texture, epitaxy, and magnetic properties of electrodeposited FePt on Cu(001). *Applied Physics Letters*, 85(8):1353–1355, 2004.

[110] S. K. Chen, F. T. Yuan, and T. S. Chin. Effect of interfacial diffusion on microstructure and magnetic properties of Cu/FePt bilayer thin films. *Journal of Applied Physics*, 97(7):073902(6), 2005.

[111] Jun-ichi Ikemoto, Y. Imai, and Sh. Nakagawa. Control of Curie temperature of FePt(Cu) films prepared from Pt(Cu)/Fe bilayers. *Magnetics, IEEE Transactions on*, 44(11):3543–3546, 2008.

[112] B. Ma, C.L. Zha, Z.Z. Zhang, and Q.Y. Jin. SiO2 layer thickness effects on the (001) texture of FePtCu:SiO2 nanocomposite films. *Thin Solid Films*, 518(8):2163 – 2166, 2010.

[113] B. Wang. *Ultrahigh Density Magnetic Recording Media: Quantitative Kinetic Experiments and Models of the A1 to L10 Phase Transformation in FePt and Related Ternary Alloy Films*. PhD thesis, Carnegie Mellon University, 2011.

[114] J.-U. Thiele, K. R. Coffey, M. F. Toney, J. A. Hedstrom, and A. J. Kellock. Temperature dependent magnetic properties of highly chemically ordered Fe(55 - x)Ni(x)Pt45 L10 films. *Journal of Applied Physics*, 91(10):6595–6600, 2002.

[115] H. Kanazawa, G. Lauhoff, and T. Suzuki. Magnetic and structural properties of (Co(x)Fe(100-x))50Pt50 alloy thin films. *Journal of Applied Physics*, 87(9):6143–6145, 2000.

[116] C. L. Platt, K. W. Wierman, E. B. Svedberg, R. van de Veerdonk, J. K. Howard, A. G. Roy, and D. E. Laughlin. L10 ordering and microstructure of FePt thin films with Cu, Ag, and Au additive. *Journal of Applied Physics*, 92(10):6104–6109, 2002.

[117] T. Maeda, A. Kikitsu, T. Kai, T. Nagase, H. Aikawa, and J. Akiyama. Effect of added Cu on disorder-order transformation of L10-FePt. *Magnetics, IEEE Transactions on*, 38(5):2796–2798, 2002.

[118] K. Aimuta, K. Nishimura, H. Uchida, and M. Inoue. Change in element distributions in FePt films with Ag or Cu additives associated with their crystallographic phase transformation through thermal annealing. *Physica Status Solidi (b)*, 241(7):1727–1730, 2004.

[119] Y.K. Takahashi, M. Ohnuma, and K. Hono. Effect of Cu on the structure and magnetic properties of FePt sputtered film. *Journal of Magnetism and Magnetic Materials*, 246(12):259 – 265, 2002.

[120] R. V. Chepulskii and S. Curtarolo. First principles study of Ag, Au, and Cu surface segregation in FePt-L10. *Applied Physics Letters*, 97(22):221908(3), 2010.

[121] C. Srivastava, G. B. Thompson, J. W. Harrell, and D. E. Nikles. Size effect ordering in [FePt](100 - x)Cr(x) nanoparticles. *Journal of Applied Physics*, 99(5):054304(6), 2006.

[122] J.W. Harrell, D.E. Nikles, S.S. Kang, X.C. Sun, Z. Jia, S. Shi, J. Lawson, G. B. Thompson, C. Srivastava, and N. V. Seetala. Effect of metal additives on L10 ordering of chemically synthesized FePt nanoparticles. *Scripta Materialia*, 53(4):411 – 416, 2005.

[123] A. Kovacs and Y. Hirotsu. Structural and magnetic properties of L10 FeCoPt nanoparticles prepared by rf-sputtering. *Applied Physics A*, 93(2):543 – 547, 2008.

[124] S.-R. Lee, S. Yang, Y. K. Kim, and J. G. Na. Rapid ordering of Zr-doped FePt alloy films. *Applied Physics Letters*, 78(25):4001 – 4003, 2001.

[125] Ch.-H. Lai and Ch.-H. Ho. Improvement of magnetic properties of FePt nanoparticles by adding Mn. *Journal of Applied Physics*, 97(10):10J314(3), 2005.

[126] S. Kang, Zh. Jia, D.E. Nikles, and J.W. Harrell. Synthesis, self-assembly, and magnetic properties of [FePt](1-x)Au(x) nanoparticles. *IEEE Transactions on Magnetics*, 39(5):2753–2757, 2003.

[127] H. Kura, T. Sato, M. Takahashi, and T. Ogawa. Effect of coalescence on ordering and c-axis orientation of FePt, FePtAu, and FePtCu nanoparticles heat-treated in magnetic field. *Japanese Journal of Applied Physics*, 47(5):3466–3470, 2008.

[128] S. Kang, J. W. Harrell, and D. E. Nikles. Reduction of the fcc to L10 ordering temperature for self-assembled FePt nanoparticles containing Ag. *Nano Letters*, 2(10):1033–1036, 2002.

[129] Sh. Kang, Zh. Jia, D. E. Nikles, and J. W. Harrell. Synthesis and phase transition of self-assembled FePd and FePdPt nanoparticles. *Journal of Applied Physics*, 95(11):6744 – 6746, 2004.

[130] Y. Hirotsu, H.W. Ryu, K. Sato, and M. Ishimaru. Electron microscopy study of L10-FePtCu nanoparticles synthesized at 613 K. *Journal of Microscopy*, 236(2):94–99, 2009.

[131] S.-W. Yung, Ch.-M. Chung, and J.Y. Ding. Reduction of the fcc to L10 ordering temperature for FePt nanoparticles containing Cu. In *Nano/Micro Engineered and Molecular Systems, 2006. NEMS '06. 1st IEEE International Conference on*, pages 231–235, 2006.

[132] H. W. Ryu, H. Naganuma, K. Sato, and Y. Hirotsu. Direct synthesis of oriented high-density islands of L10-FePtCu alloy at 613 K. *Japanese Journal of Applied Physics*, 45(23):L608–L610, 2006.

[133] H. Kura and T. Sato. Synthesis of L10 - [Fe(y)Pt(100 - y)](100 - x)Cu(x) nanoparticles with high coercivity by annealing at 400 c. *Journal of Applied Physics*, 96(10):5771–5774, 2004.

[134] H. Kura and T. Sato. Preparation of non coagulated FePtCu nanoparticles with high coercivity. *Physica Status Solidi (c)*, 1(12):3499 – 3502, 2004.

[135] X. Sun, S. Kang, J. W. Harrell, D. E. Nikles, Z. R. Dai, J. Li, and Z. L. Wang. Synthesis, chemical ordering, and magnetic properties of FePtCu nanoparticle films. *Journal of Applied Physics*, 93(10):7337–7339, 2003.

[136] T.-W. Huang, T.-H. Tu, Y.-H. Huang, Ch.-H. Lee, and C.-M. Lin. X-ray scattering and absorption spectroscopy study of the order-disorder transition of (FePt)(1-x)Cu(x) nanoparticles. *Magnetics, IEEE Transactions on*, 41(2):941–943, 2005.

[137] S. Stappert. *FePt-Nanopartikel aus der Gasphase: Herstellung, Struktur und Magnetismus*. PhD thesis, Universität Duisburg-Essen, 2007.

[138] D. B. Williams and C. B. Carter. *Transmission Electron Spectroscopy*. Plenum Press, New -York, 1996.

[139] D.A. Muller. Structure and bonding at the atomic scale by scanning transmission electron microscopy. *Nature Materials*, 8:263–270, 2009.

[140] C. A. Channing and O.L. Krivanek. *EELS atlas: A reference collection of electron energy loss spectra covering all stable elements*. Gatan, Inc., Warrendale, PA, 1983.

[141] F. Hofer, P. Warbichler, and W. Grogger. Imaging of nanometer-sized precipitates in solids by electron spectroscopic imaging. *Ultramicroscopy*, 59:15–31, 1995.

[142] H.E. Swanson. *Natl. Bur. Stand. (U.S.)*, 539 (IV):3, 1955.

[143] H.E. Swanson. *Natl. Bur. Stand. (U.S.)*, 538 (I):15, 1953.

[144] E. Prince and R.G. Treuting. The structure of tetragonal copper ferrite. *Acta Crystallogr.*, 9:1025–1028, 1956.

[145] R. Restori and D. Schwarzenbach. Charge density in cuprite, Cu2O. *Acta Crystallogr., Sec. B: Structural Science*, 42:201–208, 1986.

[146] D. Lindsley. *Min. Soc. of America, Short Course Notes*. Number 3. Washington D.C., USA, 1976. http://www.minsocam.org/msa/rim/rim03.html.

[147] F. de Boer, J.H. van Santen, and E.J.W. Verwey. The electrostatic contribution to the lattice energy of some ordered spinels. *J. Chem. Phys.*, 18:1032–1034, 1950.

[148] D. Schulz, F. Larson, and G. McCarthy. Technical report, ICDD Grant-in-Aid, North Dakota State University, Fargo, ND, 1988.

[149] D. B. Butrymowicz, J. R. Manning, and M. E. Read. Diffusion in copper and copper alloys part IV. diffusion in systems involving elements of group VIII. *Journal of Physical and Chemical Reference Data*, 5(1):103–200, 1976.

[150] F. Gesmundo, Y. Niu, D. Oquab, C. Roos, B. Pieraggi, and F. Viani. The air oxidation of two-phase fe-cu alloys at 600-800o c. *Oxida*, 49:115 – 147, 1998.

[151] E.A. Owen and G.I. Williams. A low-temperature X-ray camera. *J. Sci. Instrum.*, 31:49, 1954.

[152] H.E. Swanson, N. T. Gilfrich, and G. M. Ugrimic. *Natl. Bur. Stand. Circular 539 (U.S. GPO, Washington D.C.)*, 5:27, 1955.

[153] P. Etienne and J. Massies. Basic considerations on the growth of metallic layers by molecular beam epitaxy: application to Cr/Fe, Ag/Fe and Cu/Co multilayers. *J. Phys. III France*, 3(8):1581 – 1588, 1993.

[154] J. Welton-Holzer and G. McCarthy. ICDD Grant-in-Aid, North Dakota State University, Fargo, North Dakota, 1989.

[155] A. Elsukova, Zi-An Li, C. Mller, M. Spasova, M. Acet, M. Farle, M. Kawasaki, P. Ercius, and Duden T. Structure, morphology, and aging of AgFe dumbbell nanoparticles. *Phys. Status Solidi A*, 208 (10):2437–2442, 2011.

[156] L. Signorini, L. Pasquini, L. Savini, R. Carboni, F. Boscherini, and E. Bonetti. Size-dependent oxidation in iron/iron oxide core-shell nanoparticles. *Phys. Rev. B*, 68:195423 (8), 2003.

[157] R.C. Weast and M.J. Astle. *Handbook of Chemistry and Physics*. CRC Press, West Palm Beach, Florida, 1978.

[158] P. Wynblatt. Interfacial segregation effects in wetting phenomena. *Annu. Rev. Mater. Res.*, 38:173–196, 2008.

[159] D. Pique. *Mouillabilité du fer solide par des alliages d'argent*. PhD thesis, Institut National Polytechnique de Grenoble, 1982.

[160] H. Zhu, Z. Guo, and W. Liu. Adhesion behaviors on superhydrophobic surfaces. *Chem. Commun.*, 2014. in print, doi: 10.1039/C3CC47818A.

[161] P.A. Charnavskii, N.V. Peskov, A.V. Migtasmov, and V.V. Lunin. Oxidation of metal nanoparticles: Experiment and model. *Russian Journal of Physical Chemistry B*, 1(4):394–411, 2007.

[162] C. M. Wang, D. R. Baer, L. E. Thomas, J. E. Amonette, J. Antony, Y. Qiang, and G. Duscher. Void formation during early stages of passivation: Initial oxidation of iron nanoparticles at room temperature. *J. Appl. Phys.*, 98:094308(7), 2005.

[163] A. V. Mijiritskii and D. O. Boerma. Growth, thermal stability and oxidation of Ag/Fe and Ni/Fe bilayers. *J. Magn. Magn. Mater.*, 232:9–17, 2001.

[164] Domagoj Belić. *Studies of Alloy Nanoclusters and Their Influence on Growth of Carbon Nanotubes*. PhD thesis, University of Canterbury, 2012.

[165] N. Cabrera and N.F. Mott. Theory of the oxidation of metals. *Rep. Prog. Phys.*, 12:163–184, 1949.

[166] F.P. Fehlner and N.F. Mott. Low-temperatrue oxidation. *Oxidation of metals*, 2(1):59–99, 1970.

[167] K.R. Lawless. The oxidation in metals. *Rep. Prog. Phys.*, 37:231–316, 1974.

[168] S. Linderoth, S. Morup, and M.D. Bentzon. Oxidation of nanometer-sized iron particles. *Journal of Materials Science*, 30(12):3142–3148, 1995.

[169] A. Atkinson. Transport processes during the growth of oxide films at elevated temperature. *Rev. Mod. Phys.*, 57:437–470, 1985.

[170] A.P. Grosvenor, B.A. Kobe, and N.S. McIntyre. Examination of the oxidation of iron by oxygen using X-ray photoelectron spectroscopy and QUASES(TM). *Surface Science*, 565:151–162, 2004.

[171] Q. Fu and T. Wagner. Interaction of nanostructure metal overlayers with oxide surfaces. *Surf. Sci. Rep.*, 62:431–498, 2007.

[172] D. Wu, R. A. Outlaw, and R. L. Ash. Glow-discharge enhanced permeation of oxygen through silver. *J. Appl. Phys.*, 74:4990–4994, 1993.

[173] L.G. Cabri, D.R. Owens, and J.H.G. LaFlamme. Tulameenite, a new Platinum-Iron-Copper mineral from placers in the Tulameen River Area, British Columbia. *Can. Mineral.*, 12:21–25, 1973.

[174] M. Shahmiri, D.J. Vaughan, and S. Murphy. Observation of twin-related order domains in CuFePt2. *Phys. Status Solidi A*, 95(1):63–72, 1986.

[175] P. Bayliss. Revised unit-cell dimensions, space group, and chemical formula of some metallic minerals. *Can. Mineral.*, 28(4):751–755, 1990.

[176] L.J. Cabri and A.D. Genkin. Re-examination of Pt alloys from lode and placer deposits, Urals. *Can. Mineral.*, 29:419–425, 1991.

[177] D. R. G. Mitchell and B. Schaffer. Scripting-customised microscopy tools for Digital Micrograph. *Ultramicroscopy*, 103:319–332, 2005.

[178] L. Colak and G. C. Hadjipanayis. Evolution of texture and atomic order in annealed sinter-free FePt nanoparticles. *Nanotechnology*, 19(23):235703 (5), 2008.

[179] M. Tanase, J.G. Zhu, C. Liu, N. Shukla, T.J. Klemer, D. Weller, and D.E. Laughlin. Structure optimization of FePt nanoparticles of various sizes for magnetic data storage. *Metall. Mater. Trans. A*, 38A:798–810, 2007.

[180] M.J. Yacaman, J.A. Ascenio, H.B. Liu, and J. Gardea-Torresday. Structure shape and stability of nanometric sized particles. *J. Vac. Sci. Technol. B*, 19(4):1091 – 1103, 2001.

[181] R.V. Chepulskii and S. Curtarolo. First principles study of Ag, Au, and Cu surface segregation in FePt-L10. *Appl. Phys. Lett*, 97:221908(3), 2010.

[182] Y. Hirotsu, H.W. Ryu, K. Sato, and M. Ishimaru. Electron microscopy study of L10-FePtCu nanoparticles synthesized at 613 K. *Journal of Microscopy*, 236(2):94–99, 2009.

[183] U. Wiedwald, L. Han, J. Biskupek, U. Kaiser, and P. Ziemann. Preparation and characterization of supported magnetic nanoparticles prepared by reverse micelles. *Beilstein J. Nanotechnol.*, 1:24–27, 2010.

[184] K. Barmak, J. Kim, D. C. Berry, K. Wierman, E. Svedberg, and J. K. Howard. Calorimetric studies of the A1 to L10 transformation in FePt and related ternary alloy thin films. *J. Appl. Phys.*, 95:7486 – 7488, 2004.

[185] K. Barmak, J. Kim, D. C. Berry, W. N. Hanani, K. Wierman, E. B. Svedberg, and J. K. Howard. Calorimetric studies of the A1 to L10 transformation in binary FePt thin films with compositions in the range of 47.554.4 at. *J. Appl. Phys.*, 97:024902(7), 2005.

[186] H. Zeng, S. Sun, R.L. Sandstrom, and C.B. Murray. Chemical ordering of FePt nanoparticle self-assemblies by rapid thermal annealing. *JMMM*, 266:227–232, 2003.

[187] D.E. Laughlin, K. Srinivasan, M. Tanase, and L. Wang. Crystallographic aspects of L10 magnetic materials. *Scripta Materialia*, 53:383–388, 2005.

[188] M. Solzi, Ch. Pernechele, G. Calestani, M. Villani, M. Gaboardi, and A. Migliori.

Non-interacting hard ferromagnetic L10 FePt nanoparticles embedded in a carbon matrix. *J. Mater. Chem.*, 21:18331–18338, 2011.

[189] C. Johnson and W. F. Jr. Brown. Stoner-Wohlfarth calculation on particle with both magnetocrystalline and shape anisotropy. *J. Appl. Phys.*, 30:S320–S322, 1959.

[190] H. Kachkachi and M. Dimian. Hysteretic properties of a magnetic particle with strong surface anisotropy. *Phys. Rev.B*, 66:174419(11), 2002.

[191] J. García-Otero, M. Porto, and J. Rivas. Henkel plots of single-domain ferromagnetic particles. *J. Appl. Phys.*, 87(10):7376 – 7381, 2000.

[192] O. Henkel. Remanenzverhalten und Wechselwirkungen in hartmagnetischen Teilchenkollektiven. *Phys. Stat. Sol.*, 7:919–929, 1964.

Acknowledgements

List of publications

1. E. V. Voronina, E. P. Yelsukov, A. V. Korolyov and A. E. Yelsukova. **Mössbauer spectroscopy study of spin structure and its in-field and temperature dynamics in B2 ordered Fe(Al) alloys.** *Hyperfine Interactions*, 168, 1079, (2006)

2. E.P. Elsukov, E.V. Voronina, A.S. Shuravin, A.V. Zagainov, A.V. Korolev, S.K. Godovikov, E.A. Pechina and A E. Elsukova. **Structure of the $Fe_{100-x}Al_x$ (25 $<$ x $<$ 35 at.%) annealed in a temperature range of 400-800°C and the effect of the ordering type on the magnetic properties.** *The Physics of Metals and Metallography*, 102, 55, (2006)

3. P.M. Sheverdyaeva, V.N. Prudnikov, N.S. Perov, A.S. Konstantinova , A.E. Yelsukova, C.G. Kim, A.B. Granovsky. **Effect of heat treatment on transport and magnetic properties of Co-based amorphous alloys.** *Journal of Non-Crystalline Solids*, 353, 869, (2007)

4. E.P. Elsukov, E.V. Voronina, A.V. Korolev, A.E. Elsukova and S.K. Godovikov. **On the magnetic structure of the ground state of ordered Fe-Al alloys.** *The Physics of Metals and Metallography* 104, 35, (2007)

5. E.V. Voronina, E.P. Elsukov, A V. Korolev, A.V. Zagainov and A.E. Elsukova. **Mössbauer and magnetometric studies of uncommon magnetic properties of ordered (B2 type) Fe-Al alloys.** *The Physics of Metals and Metallography*, 104, 351, (2007)

6. A.E. Elsukova, N.S. Perov, V.N. Prudnikov, A.B. Granovski, A.K. Arzhnikov, E.P. Elsukov, E.V. Voronina and E.A. Pechina. **Magnetoresistance and the Hall effect of the ordered alloys $Fe_{100-x}Al_x$ (25 $<$ x $<$ 35 at.%).** *Physics of the Solid State Volume* 50, 1071, (2008)

7. E.V. Voronina, E. P. Yelsukov, S. K. Godovikov, A.V. Korolyov and A. E. Yelsukova. **Magnetic inhomogeneities in temperature dynamics of spin structure of the ordered $Fe_{100-x}Al_x$ (25 $<$ x $<$ 35 at.%) alloys** *Journal of Physics: Conference Series*, 217, 012134, (2010)

8. E.V. Voronina, E.P. Elsukov, S K. Godovikov, A.V. Korolev and A.E. Elsukova. **Temperature and field behavior of magnetic properties of ordered alloys Fe$_{100x}$Alx (25 $<$ x $<$ 35 at.%)**. *The Physics of Metals and Metallography*, 109, 417 (2010)

9. A. Elsukova, Zi-An Li, M. Acet, M. Spasova, and M. Farle. **Segregation in metastable Fe-Cu nanoparticles**, *Journal of Physics: Conference Series*, 200, 072109 (2010)

10. A. Elsukova, Zi-An Li, C. Mller, M. Spasova, M. Acet, M. Farle, M. Kawasaki, P. Ercius, T. Duden. S**tructure, morphology, and aging of AgFe dumbbell nanoparticles**, *Physica Status Solidi*, 208, 2437, (2011)

11. Y. Gao , V. V. Shvartsman, A. Elsukova, J. Landers, H. Wende, D. C. Lupascu. **Cobalt Ferrite/Barium Titanate Core/Shell Nanoparticles**, *Ferroelectrics*, 438, 115 (2012)

12. M. Acet, M. Spasova and A. Elsukova. **Diffusion Enhancement in FePt Nanoparticles for L10 Stability**, Nanoparticles from the Gas Phase, *NanoScience and Technology Part 2*, 123 (2012)

13. Y. Gao, V. V. Shvartsman, A. Elsukova and D. C. Lupascu. **Low-temperature synthesis of crystalline BaTiO3 nanoparticles by one-step organosol-precipitation**, *Journal of Materials Chemistry*, 22, 17573 (2012)

14. Y. Gao, A. Elsukova, D. Lupascu. **Preparation of SiO$_2$-Encapsulated BaTiO$_3$ Nanoparticles with Tunable Shell Thickness by Reverse Microemulsion**, *Particle and Particle Systems Characterization*, 30, 832, (2013)

15. M. Meseth, K. Lamine, M. Dehnen, S. Kayser, W. Brock, D. Behrenberg, H. Orthner, A. Elsukova, N. Hartmann, H. Wiggers, T. Hlser, H. Nienhaus, N. Benson and R. Schmechel. **Laser-doping of crystalline silicon substrates using doped silicon nanoparticles**, *Thin Solid Films*, 548, 437, (2013)

Selected conference contributions

1. MISM 2011, Moscow A. Elsukova, M. Spasova, G. Ünlü, M. Acet, M. Farle Hard magnetic FePtCu nanoparticles from the gas-phase.

2. IV Euro-Asian Symposium "Trends in MAGnetism" EASTMAG-2010. A.Elsukova, Zi-An Li, Ch.Möller, M.Spasova, M.Acet, M.Farle, M. Kawasaki. Structure, morphology and ageing of dumbbell Ag-Fe nanoparticles.

3. DPG Spring Meeting Regensburg 2010 A.Elsukova, Zi-An Li, Ch.Möller, M.Spasova, M.Acet, M.Farle. Structure, morphology and ageing of dumbbell Ag-Fe nanoparticles.

4. International Conference on Magnetism ICM 2009, Karlsruhe A. Yelsukova, Zi-An Li, M. Acet, M. Spasova and M. Farle. Segregation in metastable Fe-Cu nanoparticles

Curriculum Vitae

I. Personal Data

Name	Anna Elsukova
Date of birth	January 17, 1984
Place of birth	Yekaterinburg, Russian Federation
Nationality	Russian
Permanent Address	Mülheimerstr. 178
	47057, Duisburg
	Duisburg
	Tel.: +49-157-372-18891
	E-Mail: anna.elsukova@uni-due.de

II. Academic Career

June, 2001	High school diploma at the school "Lyceum 30", Izhevsk, Russia
January, 2008	Diploma in Physics at the M.V. Lomonosov Moscow State University, Moscow, Russia
	Diploma Thesis "Magnetoresistance and the Hall effect of the ordered $Fe_{100-x}Al_x$ (25 < x < 35 at. %) alloys"
	Advisor: Prof. N.S. Perov

III. Experience

2001-2008	Studies of physics at the M.V. Lomonosov Moscow State University, Moscow, Russia
July, 2008- November, 2008	University Duisburg-Essen, AG Farle Duisburg, Germany Studying of magnetic properties of magnetic nanoparticles using Ferromagnetic Resonance (FMR) technique at the University Duisburg-Essen
2008-2014	Researcher at the University Duisburg-Essen
2011-2014	Service TEM measurements for Center for Nanointegration Duisburg-Essen (CENIDE)

Eklärung

Ich beantrage die Zulassung zur Promotionsprüfung zur Erlangung des Titels "Dr. rer. nat.".

Beigefügt sind fünf Ausfertigungen der Dissertation in gebundener Form inklusive der im Zusammenhang entstandenen Veröffentlichung.

Ich habe die eingereichte Dissertation selbständig verfasst, nur due angegebenen Hilfsmittel benutzt und alle wörtlich oder inhaltlich übernommenen Stellen als solche gekennzeichnet.

Die Dissertation wurde nur in diesem Promotionsverfahren eingereicht.

Anna Elsukova

List of relevant publications

1. A. Elsukova, Zi-An Li, M. Acet, M. Spasova, and M. Farle. **Segregation in metastable Fe-Cu nanoparticles**, *Journal of Physics: Conference Series*, 200, 072109 (2010)

2. A. Elsukova, Zi-An Li, C. Mller, M. Spasova, M. Acet, M. Farle, M. Kawasaki, P. Ercius, T. Duden. S**tructure, morphology, and aging of AgFe dumbbell nanoparticles**, *Physica Status Solidi*, 208, 2437, (2011)

3. M. Acet, M. Spasova and A. Elsukova. **Diffusion Enhancement in FePt Nanoparticles for L10 Stability**, Nanoparticles from the Gas Phase, *NanoScience and Technology Part 2*, 123 (2012)